4

RESULTS AND DISCUSSION

The results obtained for the research work entitled "Bioinspired Synthesis of Metallic and Non-metallic Nanoparticles and Delving their Pharmacological, Biological, Cosmetic and Nanoswitching applications" are detailed with discussion and relevant explanations in the following pages. The chosen twenty-one bio reductants for the study are mentioned below.

Bioreductants	Common name	Used part	Sample code
Terminalia bellirica	Bahera	Dry Fruit; Epicarp	TBOS
Terminalia bellirica	Bahera	Dry Fruit Mesocarp	TBIS
Terminalia bellirica	Bahera	Seed	TBS
Terminalia bellirica	Bahera	Whole dry fruit	TBP
Oryza sativa	Parboiled Rice	Washed water	IBoRW
Oryza sativa	Raw Rice	Washed water	IRaRW
Oryza sativa	Red Rice	Washed water	IRRW
Oryza sativa	Broken Rice	Washed water	IBrRW
Oryza sativa	Broken Red Rice	Washed water	IBRRW
Oryza sativa	Basmati Rice	Washed water	IBaRW
Triticum aestivum	Punjab Wheat	Washed water	IWW
Fagopyrum esculentum	Buck wheat	Washed water	BuWW
Pennisetum glaucum	Bajra	Washed water	BJWW
Cicer arietinum	White chana	Washed water	WCWW
Cajanus cajan	Toor dhal	Washed water	TDWW
Oryza sativa	Brown rice (Indonesia)	Washed water	InB
Oryza sativa	Raw rice (Indonesia)	Washed water	InW
Oryza sativa	Raw rice (Thailand)	Washed water	ThW
Oryza sativa	Raw rice (Boston)	Washed water	BoW
Garcinia cambogia	Pot tamarind	Capsules	GC
Corpus unguis	Human nail	Free edge	HN28

Phytochemical screening and analysis for the processed bioreductants (i.e., extraction, conventional washings of cereals/pulses) were initially carried out. These bioreductants were utilized for the synthesis of metallic and non-metallic nanoparticles and they were characterized. The appropriate applications of the characterized nanoparticles are also carried out. The results and discussion of the above mentioned are detailed below.

4.1 Phytochemical screening of the aqueous extracts of TB (TBOS, TBIS, TBS and TBP)

The systematic screening of the phytochemicals in the plant extracts provides an idea of the active secondary metabolites present in the plant extract, which might help in the formulation of bioactive drugs. These secondary metabolites in turn, act as reducing and stabilizing agents to reduce the metal ions during the synthesis of metallic nanoparticles such as gold, silver and zinc oxide nanoparticles. The phytochemicals in the plant extracts also help in the determination of specific bioactivity. The synergistic effect of the secondary metabolites present in the plant extract has a great influence on the synthesized nanoparticles.

Secondary metabolite screening is performed on aqueous extracts obtained from TB fruit parts. **Table 6** shows the final outcome.

Table 6. Phytochemical screening for TB extracts

Phytochemical Class	Aqueous extracts of TB			
	TBOS	TBIS	TBS	TBP
Alkaloids	-	-	-	-
Flavonoids	+	+	+	+
Sterols	-	-	-	-
Terpenoids	-	-	-	-
Anthocyanin	-	-	-	-
Proteins	-	-	-	-
Phenols	+	-	-	+
Quinones	-	-	-	-
Carbohydrates	-	-	-	-
Tannins	+	+	-	+

(+) indicates presence and (–) indicates the absence of metabolites

The phytochemical screening confirmed the presence of flavonoids, phenols, tannins in all sections of the TB fruit and absence of other metabolites such as alkaloids, sterols, terpenoids, anthocyanin, quinones and carbohydrates.

Cough is treated with a TB fruit decoction (**Deb *et al.*, 2016**). This shows that even when TBOS decoction is delivered, the effect of ingesting the decoction of the entire fruit of TB can be reached. Earlier reports on the TB whole fruit extraction shows the presence of sterols, phenols, tannins, sugar, glycosides (**Smina *et al.*, 2020**). Several secondary metabolites were isolated from the various solvent extracts of TB fruit parts **(Hazra, 2019)**.

This finding indicates that a specific solvent extraction procedure is required for successful chemical isolation from fruit components.

In this study, *Garcinia combogia* capsules (commercially available) were used for the preparation of aqueous suspension. The 800 mg capsule consist the active component (70%) Hydroxy citric acid (HCA) as reported in the label contents of the capsules. Further phytochemical/elemental analysis with the suspension was hence not done. There are reports on nanoparticle synthesis using GC extracts (**Aishwarya and Gayathri, 2018**). *There are no reports with the commercially available GC capsules with HCA for the synthesis of nanoparticles and hence it was focused in the present study.*

4.2 Nutritional analysis of the cereals and pulses washed water

The nutritional analysis of the washed water of cereals and pulses leached out from the cereals and pulses during the domestic washing process are tabulated below (**Table 7**). These results were certified by ALPHA LABS, (NABL accredited & ISO 9001 certified laboratory).

Table 7. Nutrients present in cereals and pulses washed water

Sample code	Moisture (g)	Total ash (g)	Fat (g)	Total Protein (g)	Carbohydrate (g)	Energy (KCal)	Fibre (g)	Vitamin B_6 (mg)
IBoRW	**98.85**	**0.08**	**0.08**	**0.60**	**0.39**	**4.73**	**0.11**	**23.78**
IRaRW	98.81	0.03	0.07	0.52	0.57	5.05	0.07	20.24
IBaRW	98.98	0.02	0.01	0.17	0.82	4.11	0.02	15.99
IRRW	**98.85**	**0.04**	**0.08**	**0.55**	**0.48**	**4.90**	**0.05**	**24.56**
IBrRW	98.75	0.04	0.07	0.23	0.91	5.26	0.05	17.87
IBRRW	**98.83**	**0.05**	**0.06**	**0.39**	**0.67**	**4.84**	**0.09**	**21.25**
BJWW	98.98	0.01	0.02	0.10	0.89	4.20	0.07	14.29
IWW	98.96	0.04	0.01	0.11	0.88	4.11	0.12	15.97
BuWW	98.96	0.01	0.06	0.12	0.85	4.48	0.12	16.08
TDWW	**98.20**	**0.13**	**0.06**	**0.62**	**0.99**	**7.07**	**0.21**	**35.024**
WCWW	98.74	0.07	0.06	0.26	0.87	5.13	0.11	15.24
Vitamin B_{12} is under LOQ in all the samples								

LOQ- Limit of quantitation; Samples with high nutrient contents

All the samples are in aqueous form, the moisture content in the samples is comparatively higher. TDWW samples have higher ash content (0.13g), energy, Vitamin B_6 and carbohydrate compared to other samples which may be due to leaching of significant amount of nutrients from toor dhal to the washed water. Obviously as the whole toor dhal contains higher amount of proteins (25.1g), fat (0.7g) and carbohydrates (59g) (**Rao *et al.*, 1989**) it justifies the results of the present study. Nutrient contents are also higher in IRRW, IBoRW and IBRRW samples. The significant nutrient loss from these samples might be due to the sample processing like parboiling and polishing after harvesting of the crops.

4.3 Elemental analysis and physico-chemical studies of cereals/pulses washed water and elemental analysis of HN28

The elemental analysis of the cereals and pulses washed water was determined using EDS analysis. From the analysis, it is clear that all the samples contain C, O, Na, Mg, P and Ca content (**Table 8**). IBaRW sample contains a higher percentage of Ca compared to other samples. It is reported that Basmathi rice is grown in India's desert region, therefore it has potential minerals such as Ca, Zn and Fe (**https://manjilas.com/blog/health-benefits-of-basmati-rice/**). BuWW and WCWW are the only samples with Fe. TDWW has the highest weight % of Mo. Mo is an essential element in processing DNA and proteins. The element is utilized by the human body to break down toxic chemicals and drugs (**https://ods.od.nih.gov/factsheets/Molybdenum-Consumer/).**

The physical appearances of the samples are determined by the colour of the washed water. The colour of the sample depends on the cereals or pulses chosen. The colour of the samples and turbidity of the samples (**Table 9**) are closely associated.

From the data it is clear that the rice varieties have higher turbidity, which means more particles are leaching out from the grains; eventually the colour becomes pale white or milky in appearance. IWW and BJWW have less turbidity as they have fewer particles leaching out during washing. Samples are weakly acidic in the pH range 5.6-6.8 except BuWW sample (pH-2.7). The acidity of the BuWW might be because of the origin of the buckwheat, the geographic region where it is cultivated and also the nature of the soil. The pH values are closely associated with the previous reports on rice-soaked water and rice-boiled water (**Marto *et al.*, 2018**).

The EDS of HN28 shows the presence of C, O, Au, Ca and Na. Trace presence of Au might be due to the sputtered gold (**Figure 11**). The percentage of C in the sample may also be due to the carbon tape on which HN28 is coated. From the spectrum, it is noted that Ca from the free edge of the nail, leaches out when dispersed by the sonication method. Calcium, zinc, magnesium, copper and iron in the fingernails are present in human nail (**Harrison and Tyree, 1971**). But there are no reports on the elemental distribution of free edge of human nail dispersed water

Table 8. Elemental composition in cereals and pulses washed water

Sample code	Weight (%) of Elements												
	C	O	Na	Mg	Al	P	S	Cl	K	Ca	Cu	Fe	Mo
IBoRW	55.1	35.7	1.61	1.9	-	1.45	-	1.07	1.65	0.61	-	-	0.32
IRaRW	60.9	33.8	0.74	0.94	0.45	0.63	-	0.42	0.63	0.33	0.53	-	-
IBaRW	58.7	34.5	1.14	1.05	0.31	0.74	0.28	0.94	0.97	0.71	-	-	-
IRRW	48.6	36.4	2.82	1.71	-	2.52	0.34	2.53	4.14	0.39	-	-	-
IBrRW	44.3	48.6	3.19	0.78	-	0.66	-	0.59	0.97	0.24	-	-	-
IBRRW	51.3	35.4	3.06	1.69	-	1.72	-	2.17	3.3	0.48	-	-	0.13
BJWW	64.9	29.7	0.93	0.46	0.33	0.45	0.22	0.99	1.78	0.24	-	-	-
IWW	64.8	28.4	1.07	0..49	-	0.24	-	1.52	2.18	0.38	-	-	0.32
BuWW	64.8	31.3	0.9	-	0.38	0.24	0.24	0.44	-	0.19	0.22	0.26	-
TDWW	45.0	35.9	2.47	1.19	-	1.48	-	1	10.2	0.53	-	-	1.36
WCWW	59.6	24.8	0.55	0.52	-	0.24	-	4.92	6.72	0.53	-	0.36	-

(-) absence of the element

Table 9. Physico-chemical characterization of cereals and pulses washed water

Sample code	Colour	pH	Turbidity (NTU)
IBoRW	Pale white	5.8	311
IRaRW	Pale white	6	533
IBaRW	Pale white	6.1	542
IRRW	Pale pink	5.8	522
IBrRW	Pale white	6	589
IBRRW	Pale pink	6.8	570
BJWW	Colourless	5.6	035
IWW	Colourless	5.6	029
BuWW	Pale yellow	2.7	254
TDWW	Pale yellow	6.2	090
WCWW	Pale yellow	5.7	050

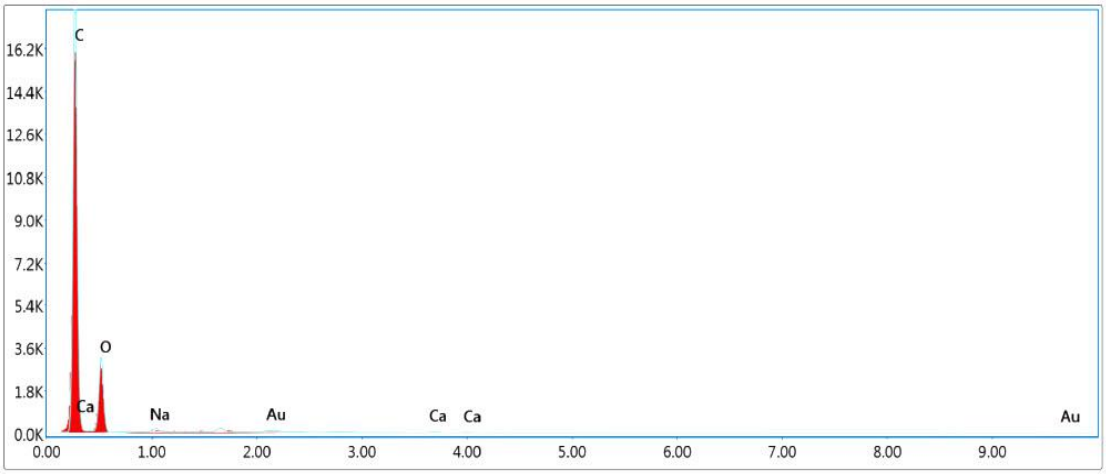

Figure 11. EDS spectrum of HN28

The determination of phytochemicals in the plant extracts, the nutrient analysis and elemental composition of cereals/pulses washed water and Corpus unguis, helps to understand the active components in the bioreductants which is being utilized for the reduction of metal ions and graphene oxide for the synthesis of metallic nanoparticles and reduced graphene oxide respectively. These active constituents in the bioreductants are responsible for the rapid formation of the nanoparticles, the particle size, and shape of the nanoparticle and the potential characteristics of the metallic nanoparticles and reduced graphene oxide particles.

4.4 Physico-chemical synthesis of metallic and non-metallic nanoparticles

In this research, work metallic nanoparticles are synthesized using;

- ✓ TB fruit part aqueous extracts
- ✓ GC capsule aqueous suspension
- ✓ cereals and pulses washed water
- ✓ HN28 aqueous dispersion

To optimize the synthesis, method of synthesis and concentrations of the bioreductants are varied. The result obtained in each reaction conditions are explained in detail in this section. Relevant supporting information for the results obtained is also mentioned.

4.4.1 Physico-chemical synthesis of Gold nanoparticles

4.4.1.1 Synthesis of GNPs using TB fruit parts as bioreductants at room temperature

The reduction of Au^{3+} to Au^{0} was done using the aqueous extracts of *Terminalia bellirica* fruit parts (TBOS, TBIS, TBS & TBP). The change in color of the colloidal solution (**Table 10**) is a preliminary indication of GNP formation.

Table 10. Color and time of formation of TB fruit parts-mediated GNPs

Sample code	Concentration of gold chloride: extract	Colour of GNPs	Time required for the formation of GNPs (s)
TBOSGNP	1:1	Navy Blue	3
TBISGNP	1:1	Green	3
TBSGNP	1:1	Greyish Blue	261 (4.35 min)
TBPGNP	1:1	Pink	2

Samples which require less time for the formation of GNPs

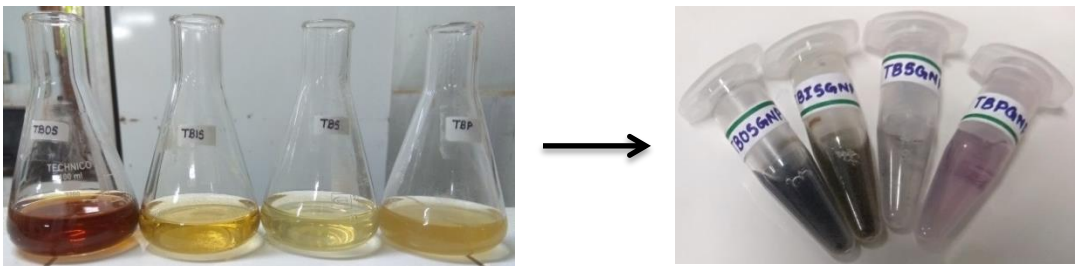

Figure 12. Synthesized GNPs using TB fruit parts extract

According to the results, at RT, GNPs can be synthesized from all the parts of TB with vivid colours. At normal (room) temperature, GNPs can be synthesized instantly from TB fruit sections. The size and shape of the NPs account for the colour variance (**Figure 12**). The fabrication of GNPs using TBS extract requires 4-5 min compared to other extracts. This could be because the components in the seed extract are less effective at reducing the gold ions (**Table 6**). For all other aqueous extracts, the period of fabrication at RT is instantaneous hence; further optimization of method/concentration was not carried out. Furthermore, each extract has a unique set of metabolites. The metabolite activity in the aqueous extracts is responsible for the conversion of Au^{3+} to Au^{0}.

However instant synthesis of GNPs was reported with sucrose and ascorbic acid as reducing agents without stirring or shaking at RT with good optical properties (**Britto Hurtado *et al.*, 2016**). TB fruit preparations have yielded several powerful compounds like termilignan, thannilignan, 7-hydroxy-3',4'-(methylenedioxy) flavones, anolignan B 5, gallic acid, ellagic acid, ß-sitosterol **(Kumari *et al.*, 2017; Nandy *et al.*, 1989; Row and Murty, 1970)**. These chemicals could be the cause of a reduction of gold ions.

4.4.1.2 Synthesis of GNPs from cereals and pulses washed water at room temperature

Simple mixing of the $HAuCl_4$ and cereals and pulses washed water at room temperature reveals the visual colour change of the colloidal solution ensuring the formation of the GNPs (**Table 11**).

Table 11. Time of formation of GNPs at RT method using cereals and pulses washed water

Sample code of NPs	Time of formation of GNPs at RT and colour of nanoparticle at different concentrations of cereals and pulses washed water				
	$HAuCl_4$ + washed water (µL)				
	100 + 100	**100 + 200**	**100 + 300**	**100 + 400**	**100 + 500**
IBoRWRT	110 min Purple	90 min Pink	90 min Pink	75 min Pink	75 min Pink
IRaRWRT	3h 20 min Purple	1h 42min Purple	1h 28min Purple	50 min Purple	50 min Purple
IBaRWRT	3h 9 min Purple	2h 38 min Purple	2h 38 min Purple	1h 20 min Purple	1h 20 min Purple
IRRWRT	110 min Violet	90 min Violet	90 min Violet	85 min Violet	85 min Violet
IBrRWRT	3h 52 min Greyish purple	3h 48 min Greyish purple	2h 37 min Greyish purple	2h 37 min Greyish purple	1h 50 min Greyish purple
IBRRWRT	1h Purple	50 min Purple	50 min Purple	50 min Purple	50 min Purple
BJWWRT	After 7h Purple	After 7h Purple	After 7h Purple	After 7h Purple	3h 28 min Purple
IWWRT	After 9h Violet	After 9h Violet	After 9h Violet	1h 52 min Violet	1h 40min Violet
BuWWRT	After 9h Violet	After 9h Violet	After 9h Violet	After 9h Violet	5h Violet
TDWWRT	1h	1h 28 min	1h 32 min	1h 48 min	3h 28 min

WCWWRT	Violet 1h 38 min Violet	Pink 1h 19 min Violet	Pink 1h 17 min Purple	Pink 58 min Pink	Pale pink 42 min Pink

Samples which require less time for the formation of GNPs
Sample which deviates from the trend followed by other samples

At RT it takes 40 min to 9h for GNP formation which shows that the washed water as reducing agents requires an external activation to reduce the Au ions. Except TDWW all the other samples of washed water require comparatively less time with increase in concentration. This might be due to the higher amounts of nutrients and elements at higher concentrations of washed water that quickly reduce the Au ions. The results from the nutrient analysis show that TDWW contain higher quantity of Vitamin B_6 and carbohydrates compared to the other samples. Synergistic effects of the nutrients help TDWW to reduce Au ions even in lowest concentration (100 µL).

Unlike TB extract aided GNP synthesis, cereals and pulses washed water aided GNP synthesis takes more than 40 min and hence to optimize the method of synthesis three other methods:

- ✓ Solar irradiation
- ✓ Sonication
- ✓ Microwave heating were employed.

❖ **Synthesis of GNPs from cereals/pulses washed water by solar irradiation method**

The time required for the formation of GNPs for the solar exposed mixture of cereals and pulses washed water and $HAuCl_4$ (**Table 12**).

Table 12. Time of formation of GNPs in solar irradiation method using cereals and pulses washed water

Sample code of NPs	Time of formation of GNPs at solar irradiation method and colour of nanoparticle at different concentrations of cereals and pulses washed water				
	$HAuCl_4$ + washed water (µL)				
	100 + 100	100 + 200	100 + 300	100 + 400	100 + 500
IBoRWSu	25 min Purple	20 min Purple	20 min Purple	10 min Purple	10 min Purple
IRaRWSu	36 min Purple	35 min Purple	28 min Purple	27 min Purple	27 min Purple
IBaRWSu	32 min Purple	28 min Purple	27 min Purple	27 min Purple	26 min Purple
IRRWSu	15 min Violet	15 min Pink	20 min Pink	30 min Rose Pink	30 min Rose Pink

IBrRWSu	20 min purple	18 min Purple	17 min purple	17 min Purple	15 min purple
IBRRWSu	6 min Wine red	5 min Purple	5 min Purple	4 min Wine red	3 min Wine red
BJWWSu	42 min Violet	39 min Purple pink	36 min Purple pink	28 min Purple	15 min Violet
IWWSu	1h 52s Violet	30 min Violet	15 min 9s Violet	8 min 32s Violet	6 min 26s Purple
BuWWSu	1h 52 s bluish Violet	35 min bluish Violet	25 min bluish Violet	15 min bluish Violet	10 min 3s Violet
TDWWSu	15 min Violet	15 min Purple	15 min Purple	20 min Pink	25 min Pink
WCWWSu	20 min Violet	15 min Violet	11 min Violet Pink	8 min Pink	8 min Pink

Samples which require less time for the formation of GNPs, Sample which deviates from the trend followed by other samples

Formation of GNPs using rice, pulses, wheat washed water by solar irradiation method yielded GNPs within 3-36 min; whereas, wheat and pulses washed water requires more time for the formation of GNPs. Among rice washed water, IBRRW forms GNPs in 3-6 min under solar irradiation compared to an hour at room temperature. This might be due to the synergistic effect of active constituents such as carbohydrates, Vitamin B_6 and proteins in IBRRW helped for the formation of GNPs quickly under solar irradiation. The optimization studies reveals that as concentration of washed water increases the time required for the formation of GNPs decreases in all the samples except TDWW. This might be in TDWW at higher concentration, the concentration of carbohydrates and other nutrients are high, which requires more activation energy to interact with Au ions.

Solar energy is a highly abundant and renewable source of carbon-neutral energy. It is not only cost-effective but is also environmentally friendly and leaves no trace in chemical processes. One interesting use of solar energy is in the production of metal nanoparticles. These nanoparticles can be stabilized using biocompatible capping agents, making them even more useful in a variety of applications (**Elsupikhe *et al.*, 2016; Reddy *et al.*, 2015; Santos *et al.*, 2019**). When synthesizing nanoparticles in presence of solar light, a trace amount of gold seed particle is formed in the mixture of gold salt solution and reducing agent which is exposed to light. The solar light enhances the growth of the seed particles, which can be observed visually by a color change. The seed particles grow rapidly under the influence of solar light due to their reactive surface, acting as an autocatalytic growth site that boosts the reduction process of Au ions. When the absorption band of small seed particles falls in the

wavelength of the incoming light source, such as solar light, it leads to the rapid formation of gold nanoparticles (**Zhao *et al.*, 2019; Kim *et al.*, 2014**). Gold seed particles were prepared via sunlight driven photochemical synthesis (**Dong *et al.*, 2004**). ***In this study, time required for the formation of GNPs compared to room temperature is less in solar irradiation method.***

❖ **Synthesis of GNPs from cereals and pulses washed water by sonication method**

Sonic wave induced synthesis of GNPs was attempted with cereals and pulses washed water as reducing agent owing to green synthetic route. Except BJWW sample, nano gold formation was observed within 5 min to 45 min for all the samples (**Table 13**). The sonic waves might have broken down the active components in BJWW. This might lead more time for GNP formation. Whereas, in all other samples; the activation energy in terms of sonic waves helps in the fast formation of GNPs.

Table 13. Time of formation of GNPs in sonication method using cereals and pulses washed water

Sample code of NPs	Time of formation of GNPs at sonication method and colour of nanoparticle at different concentrations of cereals and pulses washed water				
	$HAuCl_4$ + washed water (µL)				
	100 + 100	100 + 200	100 + 300	100 + 400	100 + 500
IBoRWSo	25 min Pink	5 min Pink	5 min Pink	5 min Pink	5 min Pink
IRaRWSo	45 min Purple	40 min Purple	40 min Purple	40 min Purple	35 min Purple
IBaRWSo	35 min Purple	30 min Purple	30 min Purple	30 min Purple	25 min Purple
IRRWSo	10min Pink	15 min Pink	15 min Pink	15 min Pink	20 min Pink
IBrRWSo	20 min Purple	20 min purple	15 min purple	15 min Magenta	15 min Magenta
IBRRWSo	15 min Purple	10 min Purple	10 min Wine red	10 min Wine red	5 min Wine red
BJWWSo	3h 20 min Purple	2h 20 min Purple	2h 20 min Purple	1h 40 min Purple	1h Purple
IWWSo	45 min Greyish blue	40 min Blue	40 min Violet	25 min Violet	15 min Purple
BuWWSo	65 min Greyish Violet	45 min Greyish Violet	45 min GreyishViolet	25 min Greyish Violet	25 min Greyish Violet
TDWWSo	11 min Violet	16 min Purple	22 min Pink	30 min Pink	34 min Pink
WCWWSo	15 min Violet	15 min Violet	10 min Pink	5 min Pink	5 min Pink

Samples which require less time for the formation of GNPs, Sample which deviates from the trend followed by other samples

The mechanism behind the quick formation of GNP by sonication method would be acoustic cavitation, which is the driving factor underlying all sonochemical reactions. Cavitation bubbles that are created, grow, and collapsed when ultrasonic energy is applied to a liquid media. By precisely regulating ultrasonic parameters such as frequency, power, and sonication duration, the size and shape of NPs can be customized (**Bhangu *et al.*, 2021)**. Citrate stabilized sonication-aided synthesis of GNP are reported (**Lee *et al.*, 2012b; Ali Dheyab *et al.*, 2012**).

Compared to solar irradiation method, time required for the formation of GNPs is more in sonication method. Sonication might have broken the active components in the cereals and pulses washed water, this might have lead more time of formationof GNP compared to solar irradiation method.

❖ **Synthesis of GNPs from cereals and pulses washed water by microwave oven heating**

Conventional microwave oven heating was carried out for the synthesis of GNPs with cereals and pulses washed water (**Figure 13**). All the samples require just 2-3 min to reduce Au ions compared to room temperature, solar irradiation and sonication for all the samples at all the concentration for the formation of GNPs (**Table 14)**.

Table 14. Time of formation of GNPs in microwave heating method using cereals and pulses washed water

Sample code of NPs	Time of formation of GNPs by microwave heating method and colour of nanoparticle at different concentrations of cereals and pulses washed water				
	$HAuCl_4$ + washed water (µL)				
	100 + 100	100 + 200	100 + 300	100 + 400	100 + 500
IBoRWM	50s Pink	50s Pink	40s Pink	40s Pink	40s Pink
IRaRWM	1 min Purple	1 min Purple	40s Purple	40s Purple	30s Purple
IBaRWM	1 min Purple	1 min Purple	50s Purple	40s Purple	30s Purple
IRRWM	1min 10s Purple	1 min Purple	1 min Purple	1 min Purple	1 min Purple
IBrRWM	30s purple	30s Purple	30s Magenta	30s Magenta	30s Magenta
IBRRWM	1 min 10s Purple	30s Purple	30s Wine red	30s Wine red	30s Wine red

BJWWM	1 min 30s Greyish violet	1min 10s Purple	1min Pink	50s Pink	40s Pink
IWWM	2 min 30s Violet	2min Violet	1 min 30s Violet	1 min 20s Violet	1 min Purple
BuWWM	30s Pink	30s Purple	1min Greyish purple	1 min 30s brown	1 min 50s Brown
TDWWM	1min 30s Violet	1 min 50s Pink	1 min 50s Pink	2 min 10s Pink	2 min 45s Pink
WCWWM	50s Violet	50s Violet	50s Purple	40s Purple	40s Purple

Samples which require less time for the formation of GNPs,
Sample which deviates from the trend followed by other samples

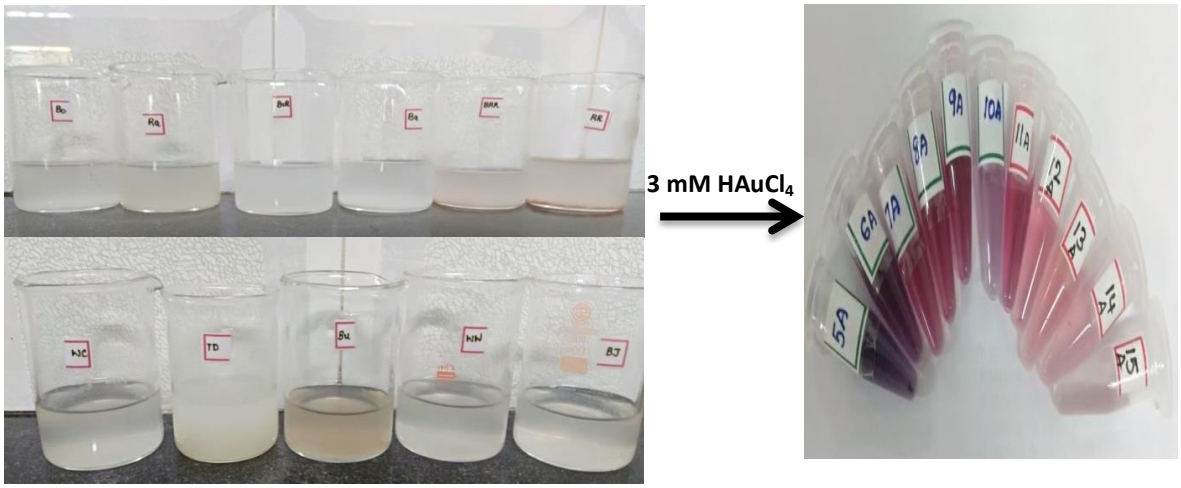

Figure 13: Microwave oven synthesized GNPs using cereals and pulses washed water

Compared to all the other methods, TDWW sample requires only 1-25 min and IBrRW requires only 30s at all concentration for the formation of GNPs. As the concentration of the sample increases, time require for the formation of GNPs decreases in all the samples except TDWW and BuWW. Rapid heating can happen when using microwave radiation as a heating source for stimulating a chemical reaction in water or in an organic solvent with a high dipole moment, these results in homogeneous energy transfer into the solution. Numerous non-thermal effects of microwave radiation have also been theorized in the past, such as an increase in the potential of a molecule colliding with another, and a decrease in the activation energy brought on by the direct interaction of certain molecules in the reactants with the electric fields, which may promote reactions **(Gerbec *et al*., 2005, Seol *et al*., 2013)**.

The microwaving of food materials in general will denature/destabilizes the active proteins, depletes Vitamins and amino acids are converted into inactive related substance (**Kopp, 1996**). This might be the reason for TDWW and BuWW samples require more time for the formation of GNPs at higher concentration. When starch is heated it becomes thick paste (gelatinization). Gelatinization occurs as a result of H bond breaking, losing the association and separation of double helix in starch. The microwave doesn't affect the total starch content (**Kaasova *et al.*, 2002**). Additionally, microwave treatment will totally destroy the particles as opposed to conventional heating, which only causes the particle surface to gelatinize. This is because the microwave energy will affect the water molecules present in the crystalline area of the starch particles, enhancing the cracking process (**Kärkkäinen *et al.*, 2011**). ***But in this study rice washed water which contains carbohydrates (starch) are not denatured, thus results in the rapid formation of GNPs by microwave heating method.***

- **Comparison of various methods of GNP formation using cereals and pulse washed water**

The samples which are capable to reduce Au ions in rapid manner are detailed below in **Table 15**.

Table 15. Comparison of time of formation of GNPs at different method of synthesis among cereals and pulses washed water

Sample variety	Time of formation of GNP and optimized concentration ($HAuCl_4$ + washed water (µL))			
	Room temperature	**Solar irradiation**	**Sonication**	**Microwave heating**
Rice/Millet washed water	IBRRW (100+500) **50 min**	IBRRW (100+500) **3 min**	IBRRW, IBoRW (100+500) **5 min**	IBRRW (100+500) **30s**
Wheat washed water	IWW (100+500) **1h 40 min**	IWW (100+500) **6 min 26s**	IWW (100+500) **15 min**	IWW (100+500) **1 min**
Pulses washed water	WCWW(100+500) **42 min**	WCWW(100+500) **8 min**	WCWW(100+500) **5 min**	WCWW(100+500) **40s**

There are no past reports on the utilization of cereals and pulses washed water for the synthesis of NPs. From the method of synthesis domestic microwave oven method was found to be an effective method which forms GNPs within seconds. All the bioreductants utilized in the study are capable of reducing Au into GNPs. The nutrients and elements present in the

samples (IBRRW, IWW and WCWW) helps to better stabilization and formation of GNPs rapidly in all the four methods of synthesis.

The representative image of GNPs synthesized from all the four methods are provided in **Figure 14**.

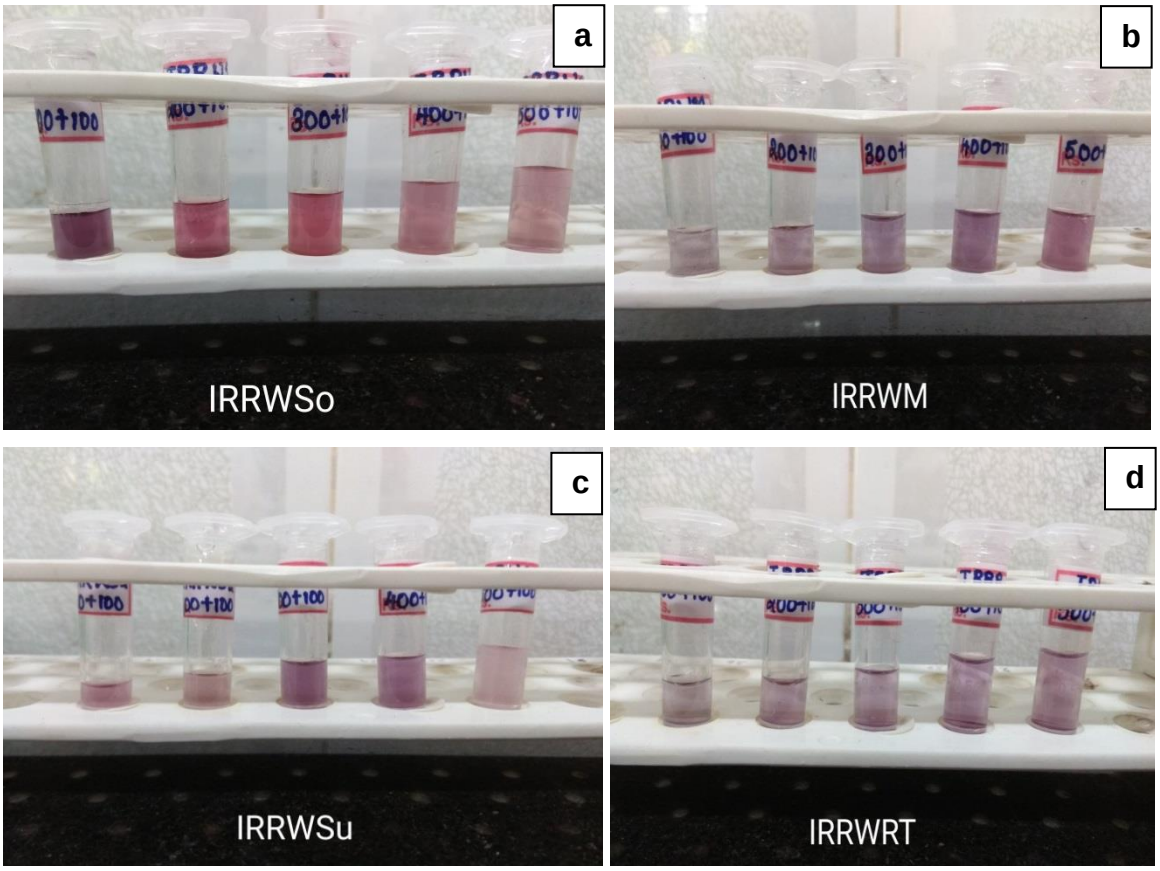

Figure 14: Representative image of GNPs synthesized using IRRW (a) sonication, (b) microwave oven heating, (c) solar irradiation and (d) room temperature method

As Indian varieties of cereals/pulses washed water are successful in synthesizing GNPs, the efficiency of rice washed water of rice varieties from Boston, Thailand and Indonesia was also determined for their efficiency in reducing the Au ions. There is no particular rationale in choosing these three international places, but for the availability of rice samples. From the results of optimization studies with the cereals/pulses washed water of Indian varieties it was noted that microwave oven heating method yielded GNPs in less time. Therefore washed water of foreign rice varieties with gold salt solution were heated in microwave oven in this study. Synthesis was optimized by varying the concentration of rice washed water. As the concentration of rice washed water increases the

time required for the synthesis of NPs decreases except BoWW (**Table 16**). The variation in the trend in BoWW might be due the constituents in it. Among the foreign rice varieties, Indonesian rice washed water; InB and InW requires only 40s – 1min 30s for the formation of GNPs. ThW and BoW samples require more time to reduce Au ions.

Table 16. Time of formation of GNPs in microwave heating method using foreign rice varieties

Sample code of NPs	Time of formation of GNPs by microwave heating method and colour of nanoparticle at different concentrations of cereals and pulses washed water				
	$HAuCl_4$ + washed water (µL)				
	100 + 100	100 + 200	100 + 300	100 + 400	100 + 500
InBAu	1 min 30s Violet	1 min 30s Violet	1 min 20s Violet	50s Violet	40s Pink
InWAu	1 min 30s Violet	1 min 10s Violet	50s Violet	50s Violet	50s Pale pink
ThWAu	2 min Violet	2 min Purple	1 min 50s Purple	1 min 50s Pale pink	1 min 40s Pale pink
BoWAu	1 min 40s Violet	1 min 40s Pink	2 min Pink	2 min 10s Pink	2 min 30s Pink

Samples which require less time for the formation of GNPs,
Sample which deviates from the trend followed by other samples

Indonesian rice varieties such as Melik Java, Cempoireng, and Toraja were reported to have fat, protein, carbohydrate and amylose and the black rice variety (Toraja) is rich in anthocyanin (**Putri *et al.*, 2022**).

4.4.1.3 Synthesis of gold nanoparticles using GC (commercial capsule) aqueous extract

The optimization studies with washed water of cereals and pulses reveals that microwave oven heating method requires less time for the formation of GNPs. Therefore phyto-reduction of gold (III) chloride was carried out using GC by microwave oven heating method. The rapid colour change of the GC to various colours ensured the formation of GNPs. **Table 17** shows the time of formation of GNP and the concentration.

Table 17. GC-mediated GNP synthesis-variation of time of formation of GNPs with concentration of GCA

Volume of GCA (µL)	Volume of $HAuCl_4$ (µL)	Time of formation of GNP(s)	Colour	Sample code of NPs
100	100	68	Violet	GCAu1
200	100	55	Violet	GCAu2

300	100	49	Purple	GCAu3
400	100	42	Pink	GCAu4
500	100	30	Pink	GCAu5

Samples which require less time for the formation of GNPs

It evident from the **Table 17** that the increasing the concentration of extract will aggrandizes and decreases the time required for NP formation. The colour of the NPs also changes depending on the concentration of GCA (**Figure 15**). From the results, it is clear that instant synthesis of NP is possible with GCA. As the volume of GCA increases by five times, the time required for the formation of GNPs decreases twice.

It is also evident that by increasing GCA's volume, the time taken for the synthesis of GNPs is less. The rapid reduction of GNPs is possibly due to the potential phyto compound hydroxycitric acid in GCA.

Figure 15. GC mediated synthesized GNPs

There are reports on the synthesis of NP using GCA aqueous extract by stirring **(Kureshi *et al.*, 2020**) and RT method (**Nithya and Jayachitra, 2016**), the study focus on the efficiency of microwave oven heating method for the synthesis of the nanoparticles

4.4.1.4 Synthesis of gold nanoparticles using HN28 dispersed water

Among all the other methods, by microwave heating of the $HAuCl_4$ and HN28 suspension provides visible colour change, but stable colloidal solution was not obtained hence solar irradiation method was adopted for GNP synthesis with HN28. **Figure 16** shows the optimization of concentration of HN28 revealed as the concentration increases time of

formation of GNP decreases **(Table 18)**. Human nail consist of calcium (**Vecht-Hart *et al.*, 1995**), cysteine (**Towler *et al.*, 2007**), alpha keratin (**Saeedi *et al.*, 2018**) as the major components. The abundance of cysteine, an amino acid that contains sulphur necessary for the disulfide bonds, distinguishes keratin from other proteins. The proteins that constitute nails mainly comprise carbon, nitrogen, oxygen, sulphur, and hydrogen. There are reports on the utilization of human nails for the synthesis of CNTs (**Chatzimitakos *et al.*, 2018**).

Table 18. Time of formation of GNPs using HN28 under solar irradiation method

Volume of HN28 (µL)	Volume of $HAuCl_4$ (µL)	Time of formation of gold nanoparticles (min)	Colour of GNPs (HN28Au)
100	100	28	Pale pink
200	100	23	Violet
300	100	19	Pale pink
400	100	17	Pink
500	100	16	Pale pink

Samples which require less time for the formation of GNPs

Figure 16: Synthesized GNPs using HN28

- **Comparison of time of formation of GNP by the chosen bioreductants for the study**

The comparison of the time of formation of GNP by all the chosen bioreduction at different reaction conditions shows that the microwave oven heating was best method for the synthesis of GNP using cereals and pulses washed water. TB samples show the efficacy to synthesise GNP at room temperature. This might be due to the potential phytoconstituents in the TB aqueous extracts. For HN28 solar irradiation method was found to be best method.

From the optimization studies, the samples which show less time of formation of GNP are tabulated in **Table 19**.

Table 19. Comparison of time required for the formation of GNPs by chosen bioreductants

Sample variety	Time of formation of GNP at optimized concentration			
	Room temperature	Solar irradiation	Sonication	Microwave heating
TB	TBPGNP- **2s**	-	-	-
Cereals/Pulses washed water	WCWWRT **42 min**	IBRRWSu **3 min**	IBRRWSo,IBoRWSo, WCWWSo- **5min**	IBRRWM- **30s**
GC	-	-	-	GCAu5-**30s**
HN28	*	HN28Au **16 min**	-	*

(-) studies not carried out, (*) NP formed which are unstable

❖ **Mechanism of GNP synthesis by bioreductants**

The bioreductants chosen in the study contains different nutrients/phytochemical that capable of reducing the ions in gold salt solution/stabilizes/reduces the formed GNPs. The reduced Au^0 ions will nucleation and growth phases and the potent stabilizing/capping agents would stabilize the resulting GNPs (**Figure 17**).

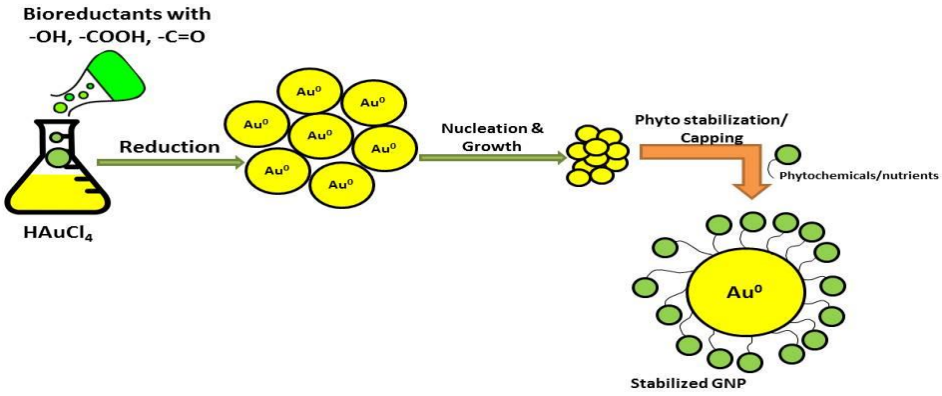

Figure 17. Proposed mechanism of GNP formation

Effective and safe production of NPs is essential for their use in biomedical applications. To achieve this, capping and stabilizing compounds are necessary to reduce toxicity, increase biocompatibility, and improve the bioavailability of NPs in living cells. Capping agents play a crucial role in the precise control of NP development, aggregation, and physicochemical properties in colloidal dispersions. With an amphiphilic nature, capping agents consist of a polar head group and a non-polar hydrocarbon tail, making them highly functional and compatible with different phases. The non-polar tail interacts with the

surrounding medium, while the polar head interacts with the metal atom in the nano system.

These compounds also prevent unwanted particle aggregation, improve colloidal stability, and regulate the growth of metal and metal oxide NPs. Moreover, the choice of capping agents can influence particle size, shape, and properties like magnetism, optics, and catalysis. The bio-conjugation of NPs is a critical aspect of their use in biological applications, such as cancer therapy and antibacterial properties. Therefore, it is important to use biocompatible, non-toxic, and biodegradable moieties as potential capping agents to ensure the safety and efficacy of NPs in medical research (**Javed *et al.*, 2020**).

4.4.2 Synthesis of silver nanoparticles

In the synthesis of GNP using TB extract room temperature yield GNPs in 2s. Hence same method was followed for SNP synthesis. The formed SNP was oxidized and black solution was obtained hence solar irradiation method is done.

4.4.2.1 Synthesis of SNPs using TB fruit part extracts- Solar irradiation method

The equal concentration of extract of TB fruit showed a colour change pale yellow to brown within 2-3 s (**Table 20**) which ensures the formation of SNPs (**Figure 18**).

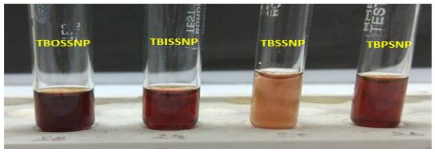

Figure 18. Synthesized SNP using TB extracts

Table 20. Sample code and details of TB dry fruit parts aided SNPs by solar irradiation method

Sample code of NPs	Extract:$AgNO_3$	Colour of SNPs	Time of formation of SNPs (s)
TBOSSNP	1:1	Brown	3
TBISSNP	1:1	Reddish brown	2
TBSSNP	1:1	Golden brown	3
TBPSNP	1:1	Reddish brown	2

Secondary metabolites in TB fruit parts as it is evident from the phytochemical analysis reduce the silver ions. The secondary metabolites in plants act as the reducing agents and thus in turn reduce the Ag^+ ions. The photo reduction is one of the green synthetic routes for the synthesis of metal NPs like SNPs. The confirmation of the formation of SNPs was initially through the colour change from pale yellow to brown. TBISSNP and TBPSNP were formed quickly compared to the other two samples (**Figure 18**). This might be due to the

secondary metabolites like tannins and phenols. It was reported that TBIS and TBP aqueous extracts shows the presences of flavonoids, tannins and phenols. ***These components help for the rapid formation of SNPs under solar irradiation method.***

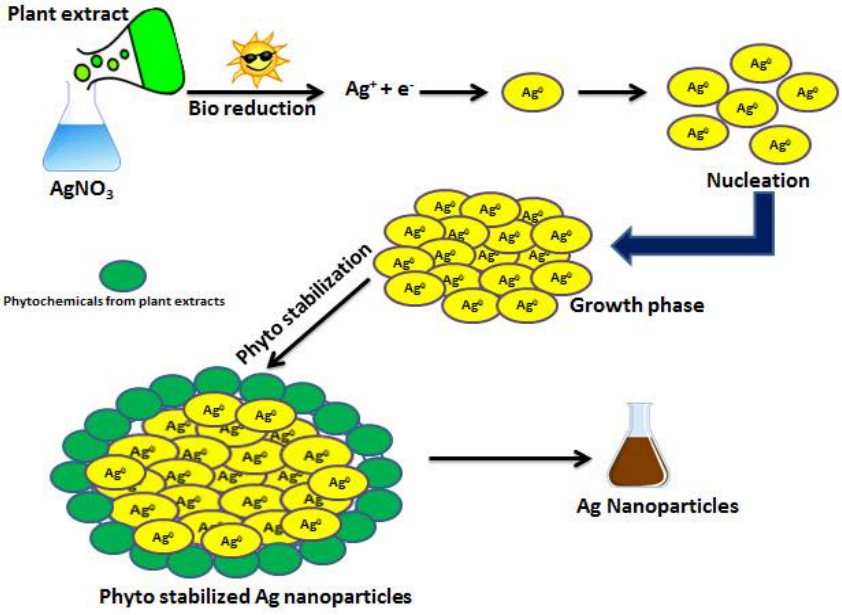

Figure 19. Proposed mechanism of SNP formation

As depicted in the **Figure 19** in the presence of sunlight the reduction of Ag^+ into Ag^0 occurs. The formed SNPs are stabilized by the secondary metabolites present in the plant extracts. According to research, adding metal salts to plant extract causes silver ions to bind to proteins and water-soluble substances via the -OH and -COOH groups. This causes conformational changes in the protein molecule, which help the captured metal ion turn into a SNPs **(Huang *et al*., 2015; Singh *et al*., 2018)**.

For the synthesis of SNPs, alkanes, amines, phenols, polyphenols, arabinose, galactose, aldehyde, ketones, alcohols, alkaloids, lignans, terpenoids, and flavonoids can serve as "capping" agents. Fructose and sucrose also act as reducing and stabilizing agent during the NP formation **(Von White *et al*., 2012)**. It appears that "capping" agents have the potential to selectively bind to various facets on a nano crystal in order to alter their particular surface free energies and, consequently, their area proportions **(Xia *et al*., 2015)**. Thus, NP "capping" can carry out a number of crucial tasks, including preventing NP agglomeration, lowering toxicity, and improving antibacterial characteristics. Additionally, these molecules can boost the potential of association and the effect of SNPs on bacterial cells **(El-Rafie *et al*., 2011, Roy *et al*., 2019)**.

4.4.2.2 Synthesis of SNPs using cereals and pulses washed water- solar irradiation method

The optimization of concentration of cereals and pulses washed water reveals that as concentration increases, the time required for the formation of SNPs increases. **Table 21** represents the time of formation of SNPs by the reduction of Ag^+ ions by the cereals and pulses washed water.

Table 21. Time of formation of SNPs by solar irradiation method using cereals and pulses washed water

Sample code of SNPs	Time of formation (min) of SNPs by solar irradiation method at different concentrations of cereals and pulses washed water				
	$AgNO_3$ + washed water (µL)				
	100 + 100	100 + 200	100 + 300	100 + 400	100 + 500
IBoRWAgSo	8.32	15.3	20.42	27.34	35.9
IRaRWAgSo	5.9	13.8	19.27	28.3	32.10
IBaRWAgSo	12	12.39	15.8	25.9	30.28
IRRWAgSo	1.52	9.52	18.14	24.2	32.56
IBrRWAgSo	1.8	5.9	17.8	22.17	29.11
IBRRWAgSo	10	12.50	14.9	19.28	25.22
BJWWAgSo	11.3	8.30	5.8	4.28	2.8
IWWAgSo	3.29	5.28	6.55	7.16	8.10
BuWWAgSo	3	4.8	5.29	7.58	8.19
TDWWAgSo	9	15	22	29	40
WCWWAgSo	10	8	5	5	3
InBAg	0.30	0.39	0.48	0.53	1.8
InWAg	2.48	5.9	8.4	10.42	12.8
ThWAg	1.38	1.53	3.9	4.38	7.42
BoWAg	0.50	1.20	3.8	15	19

All the samples were efficient in synthesizing SNPs via solar irradiation method. The time required for the SNP formation and colour of the particle (**Figure 20**) alone varies. Except BJWW and WCWW all other samples in same ratio of washed water and $AgNO_3$ took less time for the formation of SNPs. In WCWW and BJWW, 1:5 concentrations of $AgNO_3$ and washed water nano silver formation become faster. This implies that the higher concentration of the bio constituents in WCWW and BJWW are capable of reducing the Ag^+ ions by solar irradiation faster.

Figure 20. Synthesized silver nanoparticles using cereals and pulses washed water (Indian varieties)

Among the all the samples WCWW formed SNP in 3 min. This might be due to the nutrients present in WCWW such as fat, carbohydrates and Vitamin B_6. These constituents might have promoted the reduction of the metal ions.

Literature reports on waste materials such as onion peel **(Santhosh *et al.*, 2021**), vegetable peel waste of peas and bitter gourd (**Deepa *et al.*, 2022)** and electronic scrap (**Najafi *et al.*, 2021)** efficiently reduced Ag^+ ions and formed SNPs. ***But this is the first research study on determining the reducing power of cereals and pulses washed water (which is often discarded and considered as waste water). The potent nutrients in the washed water of cereals and pulses proved their efficiency in solar irradiation aided SNP synthesis.***

4.4.3 Synthesis of ZnONPs using cereals and pulses washed water as reducing agents

In this study, ZnONPs were synthesized using the cereals and pulses washed water as bioreductants. As there are no previous reports on utilizing cereals and pulses washed water for synthesis of NPs, we have not optimized the synthesis with different synthesis procedures. Sol-gel method is executed in this study.

The white powder obtained as a result of the reaction between $ZnSO_4$ and bioreductants are considered to be the cereals and pulses washed water mediated ZnONPs (**Figure 21**).

Figure 21. Synthesized ZnONPs using cereals and pulses washed water

Table 22: Sample code of synthesized ZnONPs

S.No.	Sample code of ZnONPs	Colour of ZnONPs
1	RaZn	**White**
2	BoZn	
3	BaZn	
4	BRRZn	
5	BrRZn	
6	RRZn	
7	IWWZn	
8	BuZn	
9	BJZn	
10	TDZn	
11	WCZn	

In this study, bottom-up method of synthesis is followed. The nutrients present in the cereals and pulses washed water such as carbohydrates, fats and Vitamin B_6 act as reducing agents. Synergistic effect of all the components in the washed water helps for the rapid reduction of $ZnSO_4$. As visible colour change cannot confirm the formation of ZnONPs, characterization techniques can only determine the characteristics of synthesized ZnONPs.

The co-precipitation or controlled precipitation makes it possible to generate a product with predictable qualities; it is frequently used technique of creating ZnONPs. In order to prevent the formation of particles with certain dimensions, the technique entails quickly and spontaneously reducing a zinc salt solution using a reducing agent, followed by the precipitation of a precursor of ZnO from the solution. Temperature (drying of the NP),

pH, and precipitation time are all factors that affect the precipitation process **(Basnet *et al.*, 2018**). ZnONPs was synthesized by utilizing the polymeric capping agents such as PVA, PVP, ethylene glycol and gelatin (**Akhil *et al.*, 2016)**. Utilization of onion peel waste (**Modi *et al.*, 2022**), citrus peel waste (**Okpara *et al.*, 2020**) as capping/reducing agents for the synthesis of ZnONPs was reported. There are no reports on the utilization of cereals and pulses washed water for the synthesis of ZnONPs.

❖ Mechanism of formation of ZnONP stabilized by bioreductants

Several factors affect the synthesis of ZnONPs. In the sol-gel method the Zn precursor and bioreductants are stirred well for hours. To precipitate the gel pH of the reaction should be basic for which NaOH is added to the system. The crystallinity, morphology and surface area of the ZnONP depends on the (+) ve and (–) ve ions present in the media during the synthesis. One of the reasons why solution pH is important is due to its ability to change the electrical charge of molecules, which in turn affects their reduction. In acidic medium the presence of OH^- will be less, but in alkaline OH^- will be more and they will interact with Zn^+ and form nano sized ZnO with improved crystallinity (**Jay Chithra *et al.*, 2015**). This is how the alkaline pH helps in the formation of ZnONP.

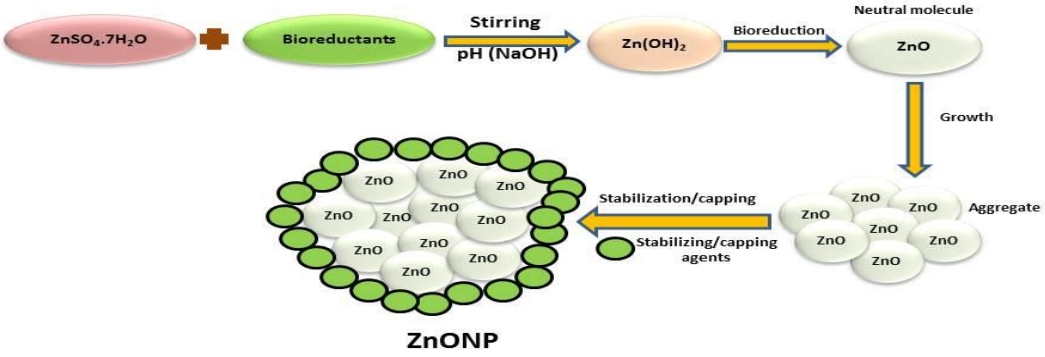

Figure 22. Proposed mechanism of formation of ZnONP

The size of ZnONPs' crystallites is impacted by both the reaction temperature and the synthesis process. It is essential to consider both factors when attempting to control the crystallite's size. Calcination is a crucial step in material processing that involves heating the material to a specific temperature in a controlled environment. It triggers a fascinating phenomenon called particle coarsening, where the primary crystallite size increases as the particles fuse together. This effect is particularly noticeable in solid or liquid solutions, where

smaller crystals merge into larger ones, reducing the number of smaller particles while larger particles continue to grow. In other words, the process allows for the creation of larger and more stable NPs with increased energy and stability. Even at room temperature, particle coarsening can occur, but it is much slower compared to the heating process. Understanding the role of calcination and particle coarsening in material science is crucial to developing new and innovative materials with superior properties (**Ruys, 2019**).

The capping agent plays a crucial role in controlling the growth rate, particle size, and preventing particle aggregation, as mentioned by **Bakshi (2015)**. According to **Al-Hada *et al.*, (2014)**, nanoparticles can also be stabilized through immobilization with organic/polymeric moieties. It is important to note that the capping agents should be stable and heat-resistant enough to prevent nanoparticle agglomeration at synthesis temperatures, as highlighted by **Gulati *et al.*, (2018)**. Thus the effect of each factor emphasizes on the characteristics of synthesized ZnONPs (**Figure 22**).

4.5 Synthesis of reduced graphene oxide particles using cereals and pulses washed water

Waste management, particularly the management of waste water, is an ongoing issue that requires creative and permanent solutions. In this research study cereals and pulses washed waste water was utilized for the reduction of GO to RGO. The change in colour of the solution to black indicates the formation of reduced graphene oxide (**Figure 23 and Table 23**).

Table 23. Sample code of synthesized RGOs

S.No.	Sample code of RGOs	Colour of RGOs
1	IBoRWRGO	**Black**
2	IRaRWRGO	
3	IBaRGO	
4	IRRRGO	
5	IBrRWRGO	
6	IBRRWRGO	
7	BJRGO	
8	IWWRGO	
9	BuRGO	
10	TDRGO	
11	WCRGO	

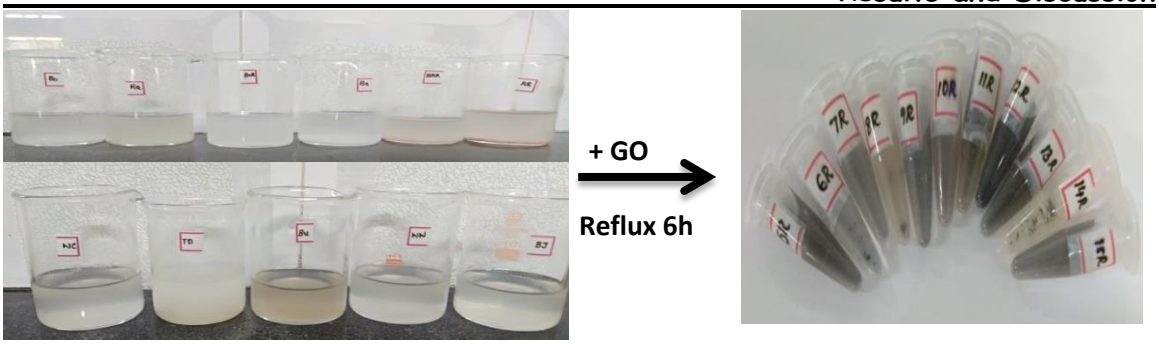

Figure 23. Synthesized RGO using cereals and pulses washed water

Previous reports also have discussed about the reduction of GO. GO was reduced to reduced graphene oxide using a green process using green reducing agents with thermal treatment can yield RGO. GO is exfoliated initially and then reduced by a reducing agent. Reduced graphene oxide is an immensely valuable material due to its unique composition and heterogeneous structure, which consists of a graphene-like basal plane that is decorated with structural defects and areas containing oxidised chemical groups. These exceptional characteristics give it exceptional mechanical, optoelectronic, and conductive properties that are comparable to pristine graphene. As a result, reduced graphene oxide is highly sought after for use in a wide range of applications, including sensors, biological and environmental systems, catalytic processes, optoelectronics, and storage devices.

Producing large amounts of GO quickly and affordably is a definite possibility. GO shares a two-dimensional design with graphene, having a single layer of carbon atoms that are covalently functionalized with oxygen-containing groups, such as hydroxyl, epoxide, carbonyl, etc., on both the basal plane and edges. These functional groups make processing GO in dispersions, provide excellent colloidal stability in water, and give rise to a unique set of mechanical, colloidal, or optical properties (**Tarcan *et al.*, 2020)** . Upon reduction of GO, the carbon networks of the material are rebuilt to form sp^2-bonds. However, these networks lack the precise crystallinity of unaltered graphene. As a result, disordered areas are created which can be best described as clustered topological defects. These defects cause strain and deformations in both the in-plane and out-of-plane of the surrounding RGO. There are also isolated topological defects, known as dislocations, which may have originated due to the strain. It is important to consider the consequences of these faults when examining the qualities of the material. Understanding these faulty structures may help in finding ways to

eliminate them or even lead to creative applications that take advantage of their presence **(Gómez-Navarro *et al.*, 2010).**

There are previous reports on TB fruit aided RGO and bacterial applications (Sethumadhavan et al., 2022). Thus we focus on cereals and pulses washed water which is good carbon source for the synthesis of RGO.

4.6 Characterization of synthesized nanoparticles

The nanoparticles synthesized were characterized by the following analytical and spectral techniques (**Table 24**).

Table 24. List of characterization carried out for the synthesized nanoparticles

S.No	Sample code of synthesized NPs	Characterization carried out						
		UV	FT-IR	XRD	Zeta potential	FE-SEM & EDX	TGA	Raman
1	TBOSGNP	✓	✓	✓	-	✓	-	-
2	TBISGNP	✓	✓	✓	-	✓	-	-
3	TBSGNP	✓	✓	✓	-	✓	-	-
4	TBPGNP	✓	✓	✓	-	✓	-	-
5	IBoRWM	✓	✓	✓	-	-	-	-
6	IRaRWM	✓	✓	✓	-	✓	-	-
7	IBaRWM	✓	✓	✓	-		-	-
8	IRRWM	✓	✓	✓	-	✓	-	-
9	IBrRWM	✓	-	✓	-	✓	-	-
10	IBRRWM	✓	✓	✓	✓	-	-	-
11	BJWWM	✓	✓	✓	✓	-	-	-
12	IWWM	✓	✓	✓	-	-	-	-
13	BuWWM	-	✓	✓	-	-	-	-
14	TDWWM	✓	✓	✓	-	-	-	-
15	WCWWM	✓	✓	✓	✓	-	-	-
16	InWAu	✓	✓	-	-	-	-	-
17	InBAu	✓	✓	-	-	-	-	-
18	BoWAu	✓	✓	-	-	-	-	-
19	ThWAu	✓	✓	-	-	-	-	-
20	GCAu	✓	✓	-	-	✓	-	-
21	HN28Au	✓	✓	-	-	✓	-	-
22	TBOSSNP	✓	✓	✓	-	✓	-	-
23	TBISSNP	✓	✓	✓	-	✓	-	-
24	TBSSNP	✓	✓	✓	-	✓	-	-
25	TBPSNP	✓	✓	✓	-	✓	-	-
26	IBoRWAgSo	✓	✓	✓	-	-	-	-
27	IRaRWAgSo	✓	✓	✓	✓	✓	-	-
28	IBaRWAgSo	-	✓	✓	-	-	-	-
29	IRRWAgSo	✓	✓	✓	-	-	-	-
30	IBrRWAgSo	✓	✓	✓	-	-	-	-
31	IBRRWAgSo	✓	✓	✓	-	-	-	-
32	BJWWAgSo	✓	✓	✓	✓	✓	-	-

33	IWWAgSo	✓	-	✓	-	-	-	-
34	BuWWAgSo	-	-	✓	-	-	-	-
35	TDWWAgSo	✓	✓	✓	-	-	-	-
36	WCWWAgSo	✓	✓	✓	✓	✓	-	-
37	InBAg	✓	✓	-	-	-	-	-
38	InWAg	✓	✓	-	-	-	-	-
39	ThWAg	✓	✓	-	-	-	-	-
40	BoWAg	✓	✓	-	-	-	-	-
41	BoZn	✓	✓	-	-	-	✓	-
42	RaZn	✓	✓	✓	-	✓	✓	-
43	BaZn	✓	-	-	-	-	✓	-
44	RRZn	-	✓	✓	-	-	-	-
45	BrZn	✓	✓	✓	-	-	-	-
46	BRRZn	✓	-	-	-	-	-	-
47	BJZn	✓	-	-	-	✓	-	-
48	IWZn	✓	-	-	-	-	✓	-
49	BuZn	✓	✓	✓	-	-	-	-
50	TDZn	✓	✓	✓	-	-	-	-
51	WCZn	-	✓	✓	-	✓	-	-
52	IBoRWRGO	-	✓	✓	-	-	✓	-
53	IRaRWRGO	-	✓	✓	-	✓	✓	✓
54	IBaRGO	-	✓	-	-	-	✓	-
55	IRRRGO	-	✓	✓	-	✓	✓	-
56	IBrRWRGO	-	✓	✓	-	-	✓	-
57	IBRRWRGO	-	✓	-	-	-	-	-
58	BJRGO	-	✓	✓	-	✓	✓	✓
59	IWWRGO	-	✓	-	-	-	✓	-
60	BuRGO	-	✓	✓	-	✓	✓	-
61	TDRGO	-	✓	-	-	-	✓	-
62	WCRGO	-	✓	✓	-	-	✓	-

(-) characterization not carried out

Transmission Electron Microscopic (TEM) analysis was not carried out for any of the synthesized NPs as FE-SEM images shows better morphology of the sample with shape. In the case of RGO samples, the solubility/dispersion in water was not attained, thus the recorded UV spectra with the partially dispersed RGO samples shows noise. Therefore it is not included in this thesis. For the NPs synthesized with foreign rice washed water, only UV and FT-IR was done and compared as those samples are prepared only for comparison with Indian varieties, further characterization was not done. ZnONP and RGO which shows better visual stability (particle agglomeration was not observed visually for samples) was only taken up for the XRD analysis. Representative samples from GNP and SNP prepared from cereals/pulses washed water were taken for the zeta potential analysis, as biological activities with these samples are proposed in objectives. TGA (thermal stability) upto 1000^{o}C was carried out for representative ZnONPs and RGOs which shows better UV, FT-IR and XRD spectra. TGA analysis requires minimum 4 mg of sample. The yield of GNP and SNP upto 4

mg is laborious and expensive. Therefore TGA not done for synthesized SNPs and GNPs. The representative samples from synthesized RGO were chosen for Raman analysis.

4.6.1 UV-Visible spectral characterization for synthesized nanoparticles

UV-Visible spectrophotometer is a common instrument even in not-so-well equipped laboratories, making it an unbeatable tool for the characterization of NPs. When characterizing the nanoparticles, it is important to consider the limitations, strengths, and weaknesses of the techniques to be applied. The UV-Visible spectrum is one of the basic analytical tools for the characterization of GNPs.

4.6.1.1 UV-Visible spectral characterization for synthesized GNP

The SPR is a critical parameter that defines the unique properties of gold nanoparticles in the 520-580nm range. A higher concentration of gold nanoparticles is indicated by the higher OD values in our results. All samples, including cereals/pulses washed water-aided GNP, exhibit excellent SPR, unequivocally confirming the formation of gold nanoparticles. These findings underscore the importance of SPR in the formation and concentration of gold nanoparticles, and its potential for various applications in the field of nanotechnology. The UV-Visible spectra of the GNP's are given below (**Figure 24**).

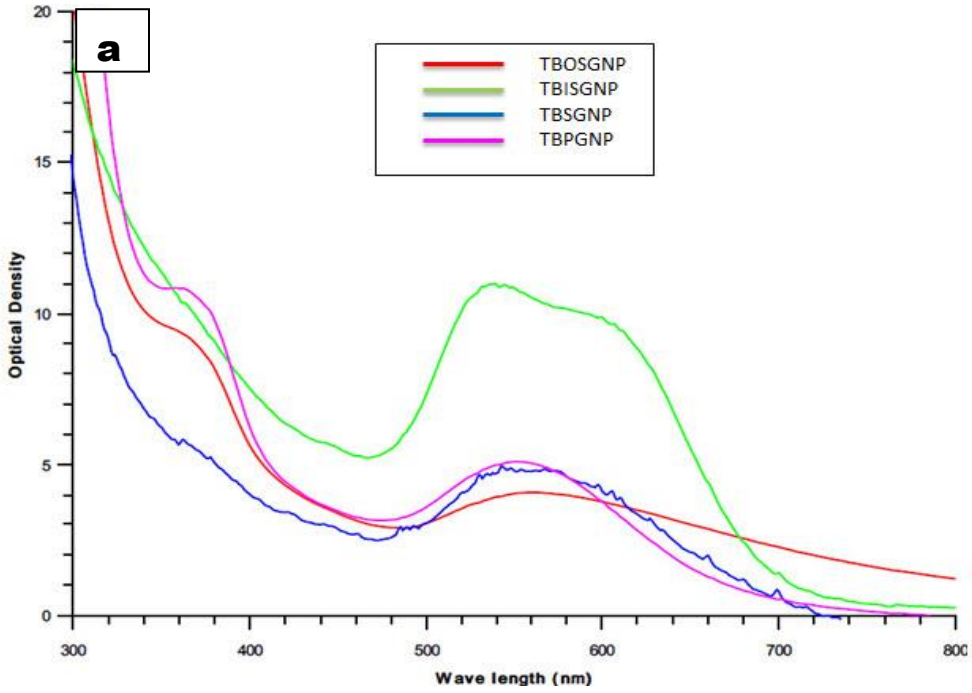

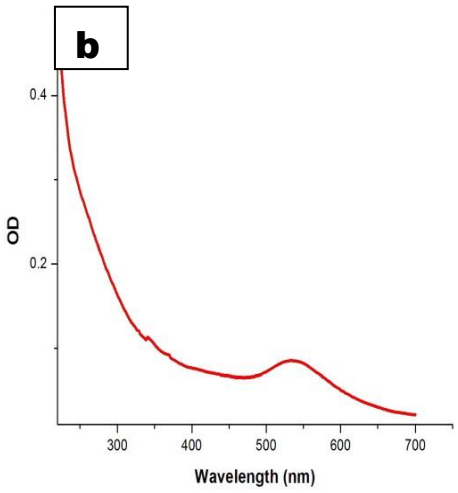
b
OD
0.4
0.2
300
400
500
600
700
Wavelength (nm)

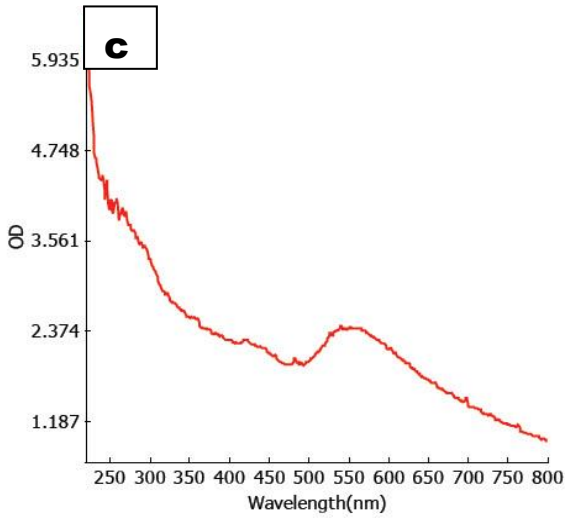
c
OD
5.935
4.748
3.561
2.374
1.187
250 300 350 400 450 500 550 600 650 700 750 800
Wavelength(nm)

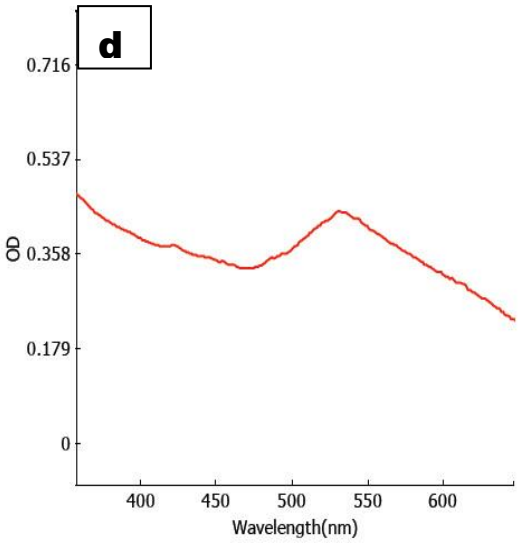
d
OD
0.716
0.537
0.358
0.179
0
400
450
500
550
600
Wavelength(nm)

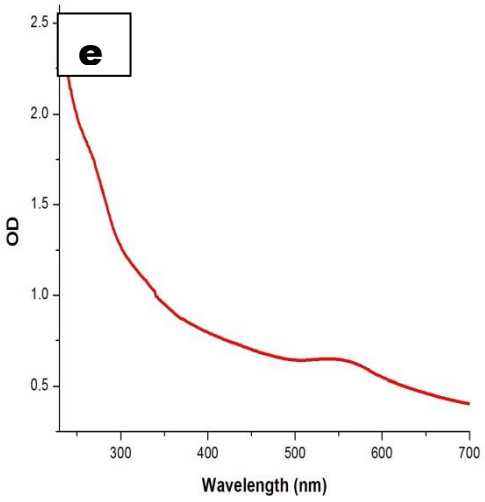
e
OD
2.5
2.0
1.5
1.0
0.5
300
400
500
600
700
Wavelength (nm)

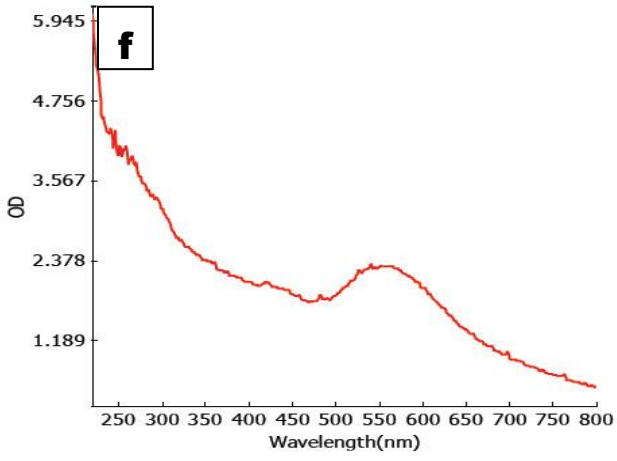
f
OD
5.945
4.756
3.567
2.378
1.189
250 300 350 400 450 500 550 600 650 700 750 800
Wavelength(nm)

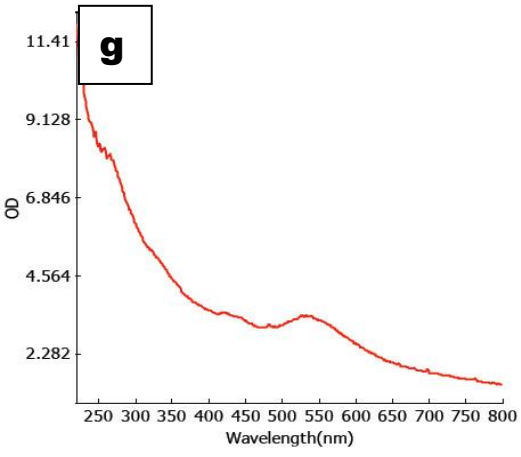
g
OD
11.41
9.128
6.846
4.564
2.282
250 300 350 400 450 500 550 600 650 700 750 800
Wavelength(nm)

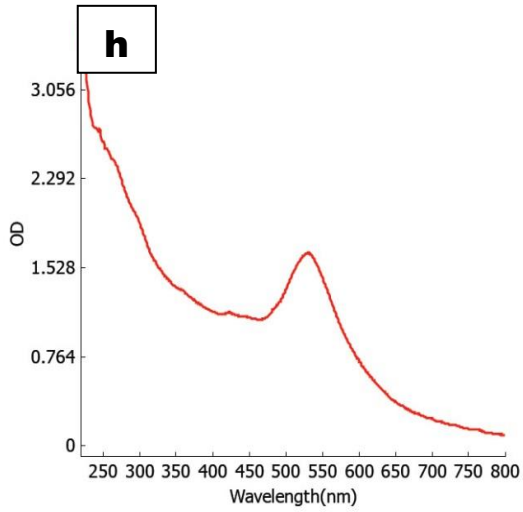
h
3.056
2.292
1.528
0.764
0
OD
250 300 350 400 450 500 550 600 650 700 750 800
Wavelength(nm)

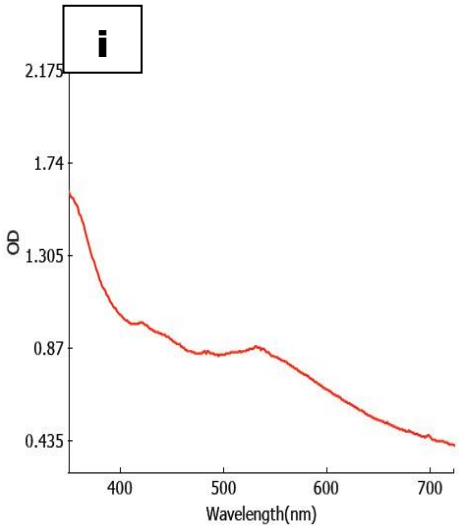
i
2.175
1.74
1.305
0.87
0.435
OD
400 500 600 700
Wavelength(nm)

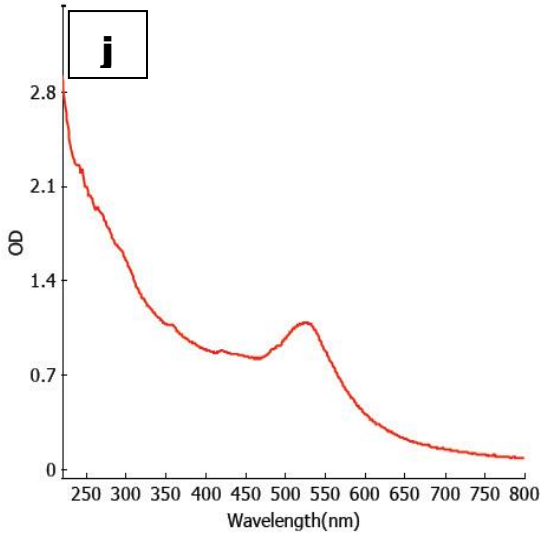
j
2.8
2.1
1.4
0.7
0
OD
250 300 350 400 450 500 550 600 650 700 750 800
Wavelength(nm)

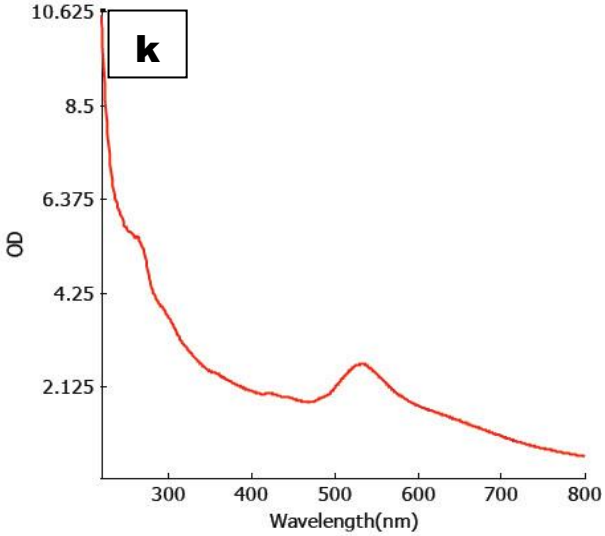
k
10.625
8.5
6.375
4.25
2.125
OD
300 400 500 600 700 800
Wavelength(nm)

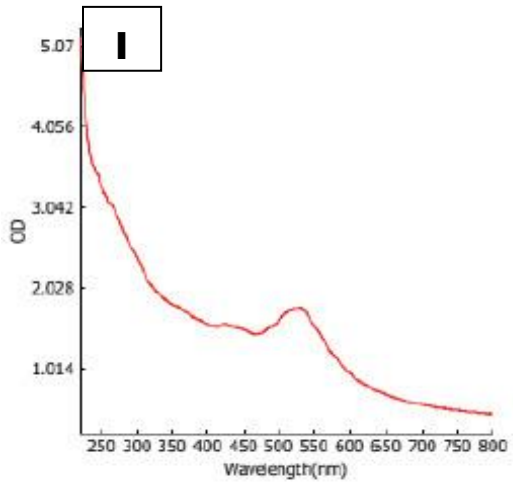
l
5.07
4.056
3.042
2.028
1.014
OD
250 300 350 400 450 500 550 600 650 700 750 800
Wavelength(nm)

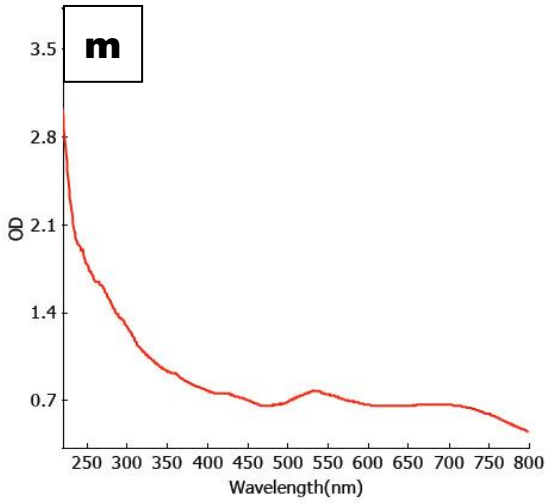
m
3.5
2.8
2.1
1.4
0.7
OD
250 300 350 400 450 500 550 600 650 700 750 800
Wavelength(nm)

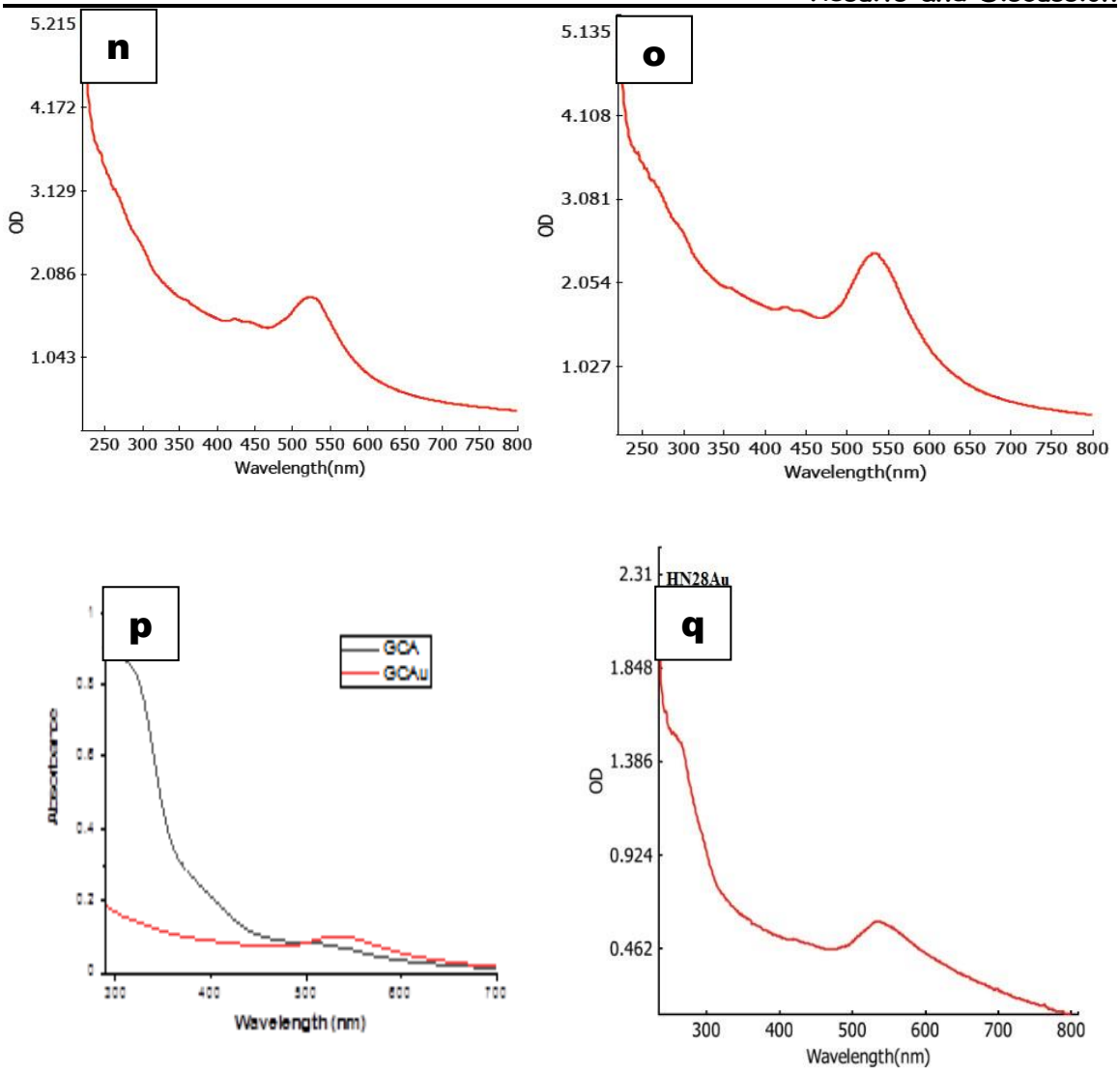

Figure 24. UV-Visible spectra of synthesized GNP (a)TBOSGNP, TBISGNP, TBSGNP and TBPGNP, (b)IBoRWM, (c)IRaRWM, (d)IBaRWM, (e)IRRWM, (f)IBrRWM, (g)IBRRWM, (h)BJWWM, (i)IWWM, (j)TDWWM, (k)WCWWM, (l)InWAu, (m)InBAu, (n)BoWAu, (o)ThWAu, (p)GCAu and (q)HN28Au

GNPs have become an indispensable tool in various fields of science and technology due to their unique optical and spectroscopic properties. Their size and surface characteristics can be finely controlled to achieve specific electrical, optical, and chemical properties that are essential in chemical, bioanalytical, and biomedical applications. Recent studies have shown that the absorbance or wavelength changes of the surface plasmon resonance band can

provide precise information on particle size, shape, concentration, and dielectric medium properties. Therefore, the use of gold nanoparticles can significantly enhance the accuracy and effectiveness of various scientific applications (**Njoki *et al*., 2007**).

Synthesis of GNPs using the leaf extract of *Ziziphus zizyphus* shows an SPR at 535 nm (**Aljabali *et al.* 2018**) and *Platycodon grandiflorum* extract aided GNPs shows SPR at 545nm (**Anbu *et al*., 2020**). ***These results correlate with the results of the present study and thus confirmed the synthesized product is GNPs.***

4.6.1.2 UV-Visible spectral characterization of SNP

The synthesized NPs shows absorption maximum at 375 nm (TBOSSNP), 371 nm (TBISSNP), 446 nm (TBSSNP) and 382 nm (TBPSNP). The SNPs synthesized using cereals and pulses washed water aided SNPs (**Figure 25**) shows SPR between 420nm-480nm.

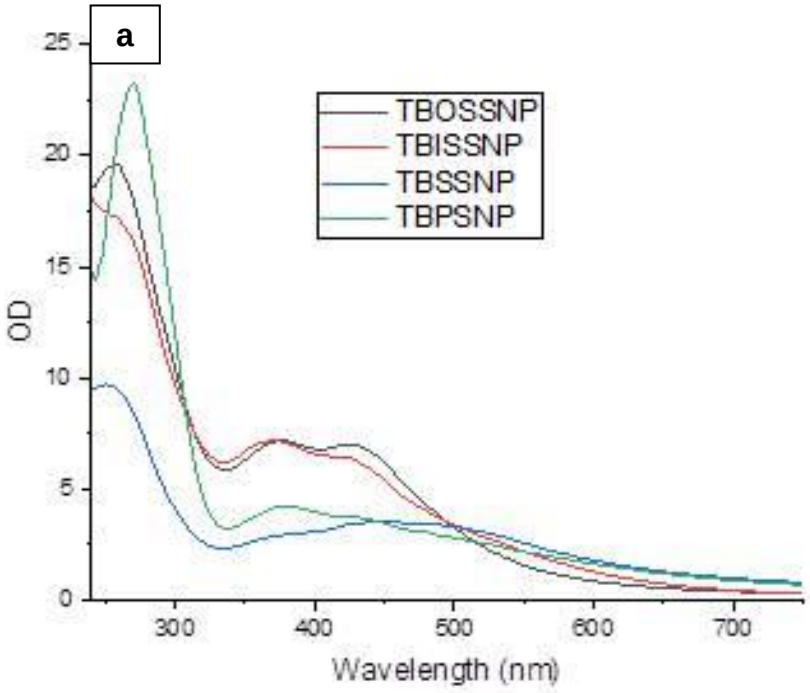

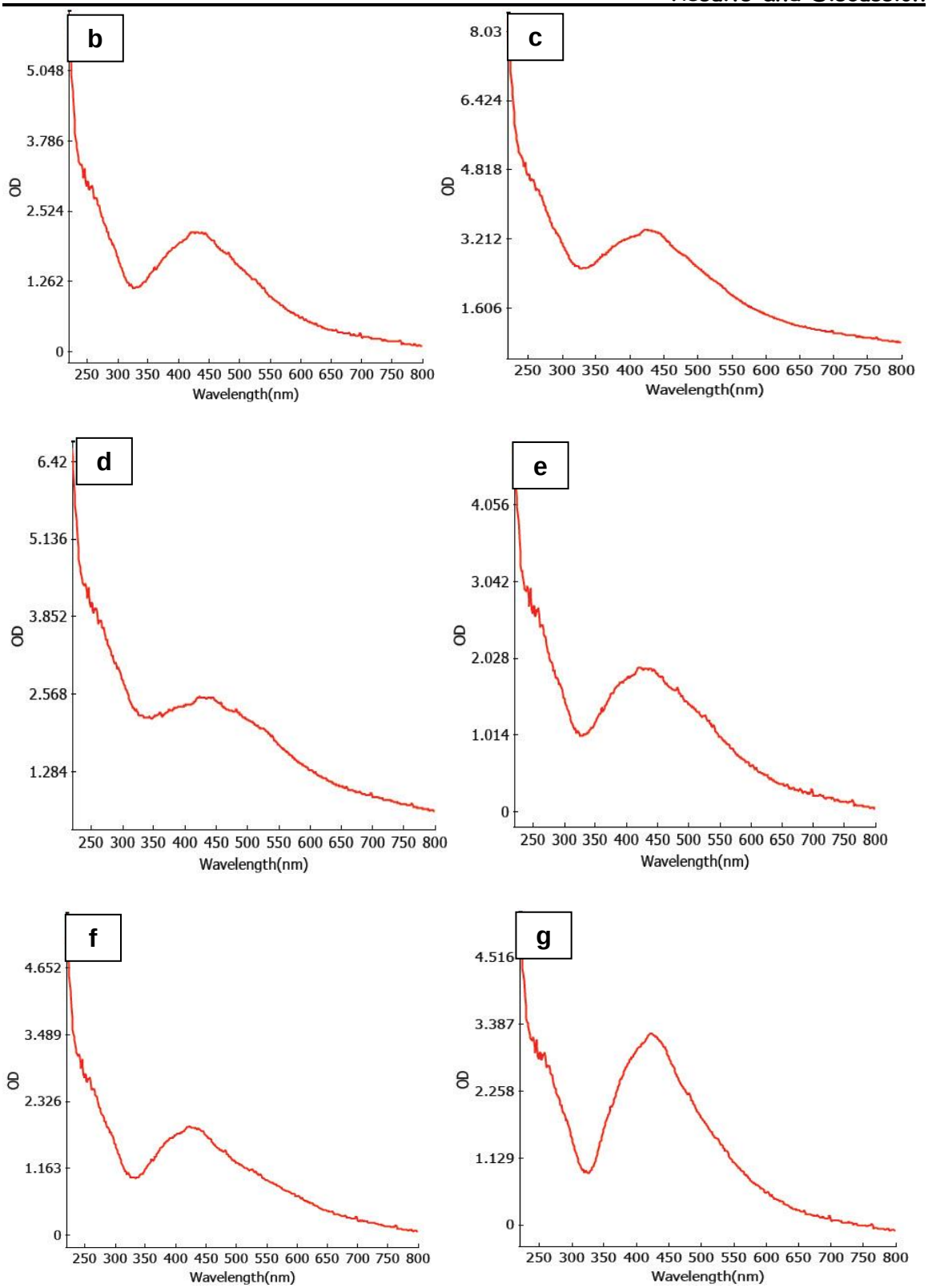
b
5.048
3.786
2.524
1.262
0
OD
250 300 350 400 450 500 550 600 650 700 750 800
Wavelength(nm)
c
8.03
6.424
4.818
3.212
1.606
OD
250 300 350 400 450 500 550 600 650 700 750 800
Wavelength(nm)
d
6.42
5.136
3.852
2.568
1.284
OD
250 300 350 400 450 500 550 600 650 700 750 800
Wavelength(nm)
e
4.056
3.042
2.028
1.014
0
OD
250 300 350 400 450 500 550 600 650 700 750 800
Wavelength(nm)
f
4.652
3.489
2.326
1.163
0
OD
250 300 350 400 450 500 550 600 650 700 750 800
Wavelength(nm)
g
4.516
3.387
2.258
1.129
0
OD
250 300 350 400 450 500 550 600 650 700 750 800
Wavelength(nm)

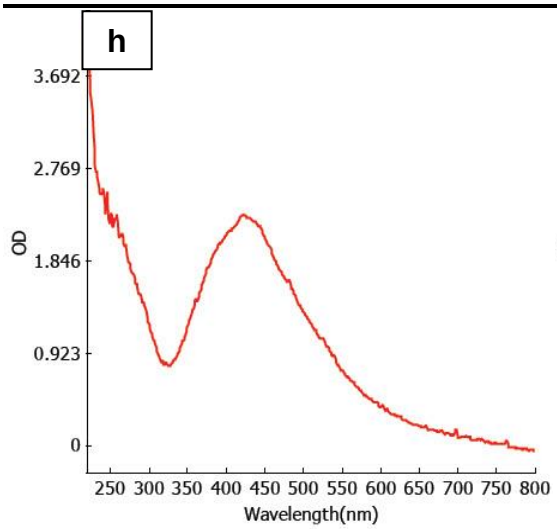
h
3.692
2.769
1.846
0.923
0
OD
250 300 350 400 450 500 550 600 650 700 750 800
Wavelength(nm)

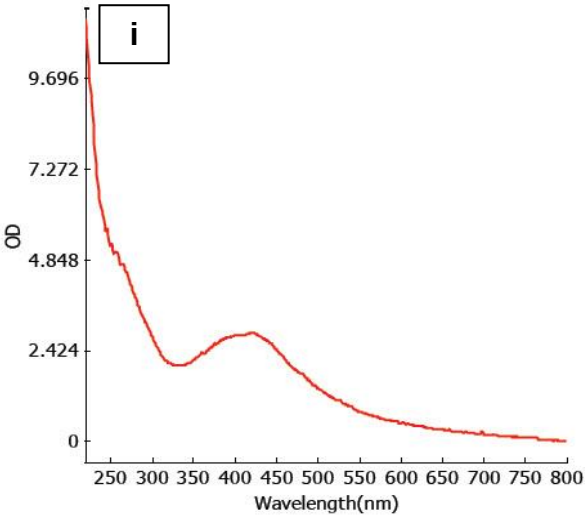
i
9.696
7.272
4.848
2.424
0
OD
250 300 350 400 450 500 550 600 650 700 750 800
Wavelength(nm)

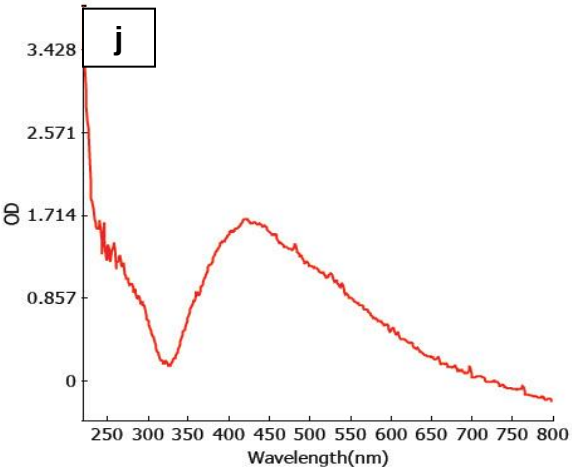
j
3.428
2.571
1.714
0.857
0
OD
250 300 350 400 450 500 550 600 650 700 750 800
Wavelength(nm)

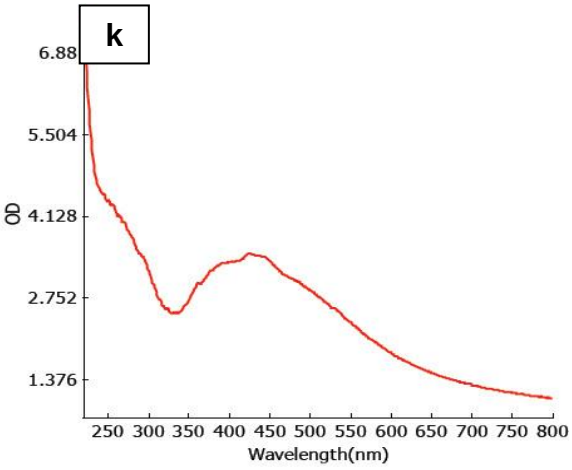
k
6.88
5.504
4.128
2.752
1.376
OD
250 300 350 400 450 500 550 600 650 700 750 800
Wavelength(nm)

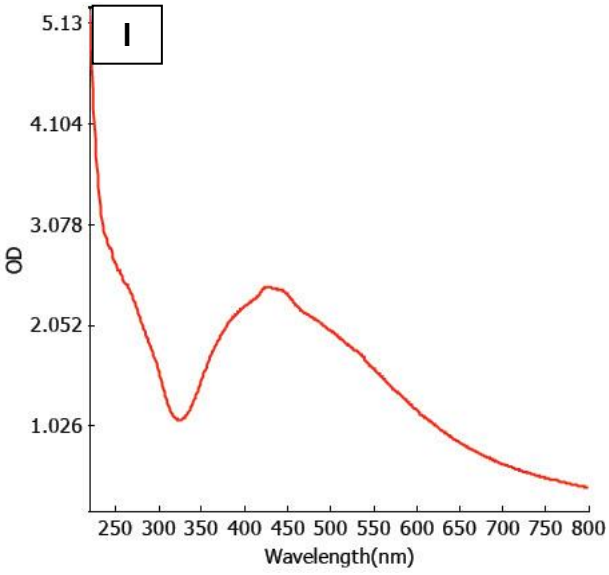
l
5.13
4.104
3.078
2.052
1.026
OD
250 300 350 400 450 500 550 600 650 700 750 800
Wavelength(nm)

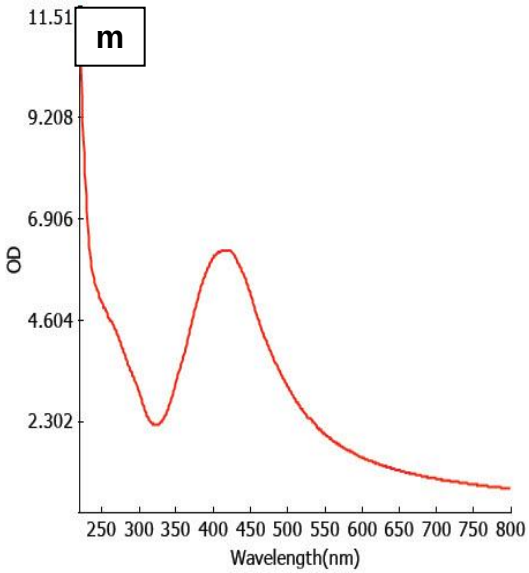
m
11.51
9.208
6.906
4.604
2.302
OD
250 300 350 400 450 500 550 600 650 700 750 800
Wavelength(nm)

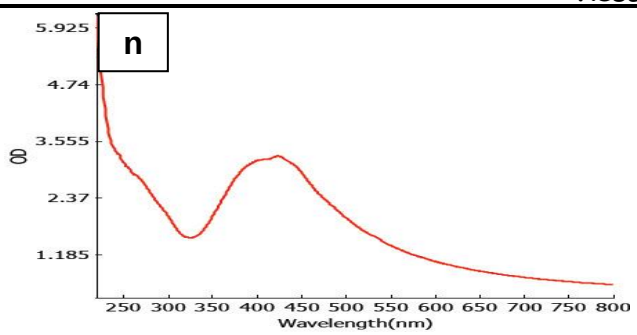

Figure 25. UV-Visible spectra of synthesized SNP (a)TBOSSNP,TBISSNP,TBSSNP and TBPSNP, (b)IBoRWAgSo, (c)IRaRWAgSo, (d)IRRWAgSo, (e)IBrRWAgSo, (f)IBRRWAgSo, (g)BJWWAgSo, (h)IWWAgSo, (i)TDWWAgSo, (j)WCWWAgSo, (k)InWAg, (l)InBAg, (m)BoWAg and (n) ThWAg

The high intensity of the SPR indicates that, the formation of SNPs. With increase in OD, SPR also found to be increased. All the SNPs was observed for a period of 2 years (2020-2022) and no discoloration of the colour or agglomeration was observed which also ensures the stability of the synthesized SNPs. The perfect SPR observed confirms the formation of SNPs. In figure 24j, the noise observed in the sample might be due to the fat content in the WCWW causes instability. In TB aided synthesized SNPs shows an excellent UV spectra with SPR, this indicates the secondary metabolite stabilized NPs.

SNPs comparatively exhibit a sharper and more powerful plasmonic resonance in the visible spectrum as the interband transitions in Ag begin at 320 nm have very little overlap, leading to distinct dielectric characteristics **(Amendola *et al.*, 2010)**. The results of this study also associates with the previously reported studies such as SNPs synthesized from *Cucumis prophetarum* aqueous leaf extract shows SPR at 420 nm **(Hemlata *et al.*, 2020)**, and the SPR of SNP synthesized from leaf extracts of banana, neem, tulsi were in the range of 425-475nm (**Banerjee *et al.*, 2014**). ***The results from the UV-visible spectra confirm the formation of SNPs.***

4.6.1.3 UV-Visible spectral characterization of synthesized ZnONP

In UV-visible spectra, the absorbance between 320-380nm (**Figure 26)** ensures the formation of ZnONPs. In this study, all the synthesized samples show the absorbance in the range (320-390nm). There are no other absorption peaks, confirming the pure and crystalline nature of ZnONPs.

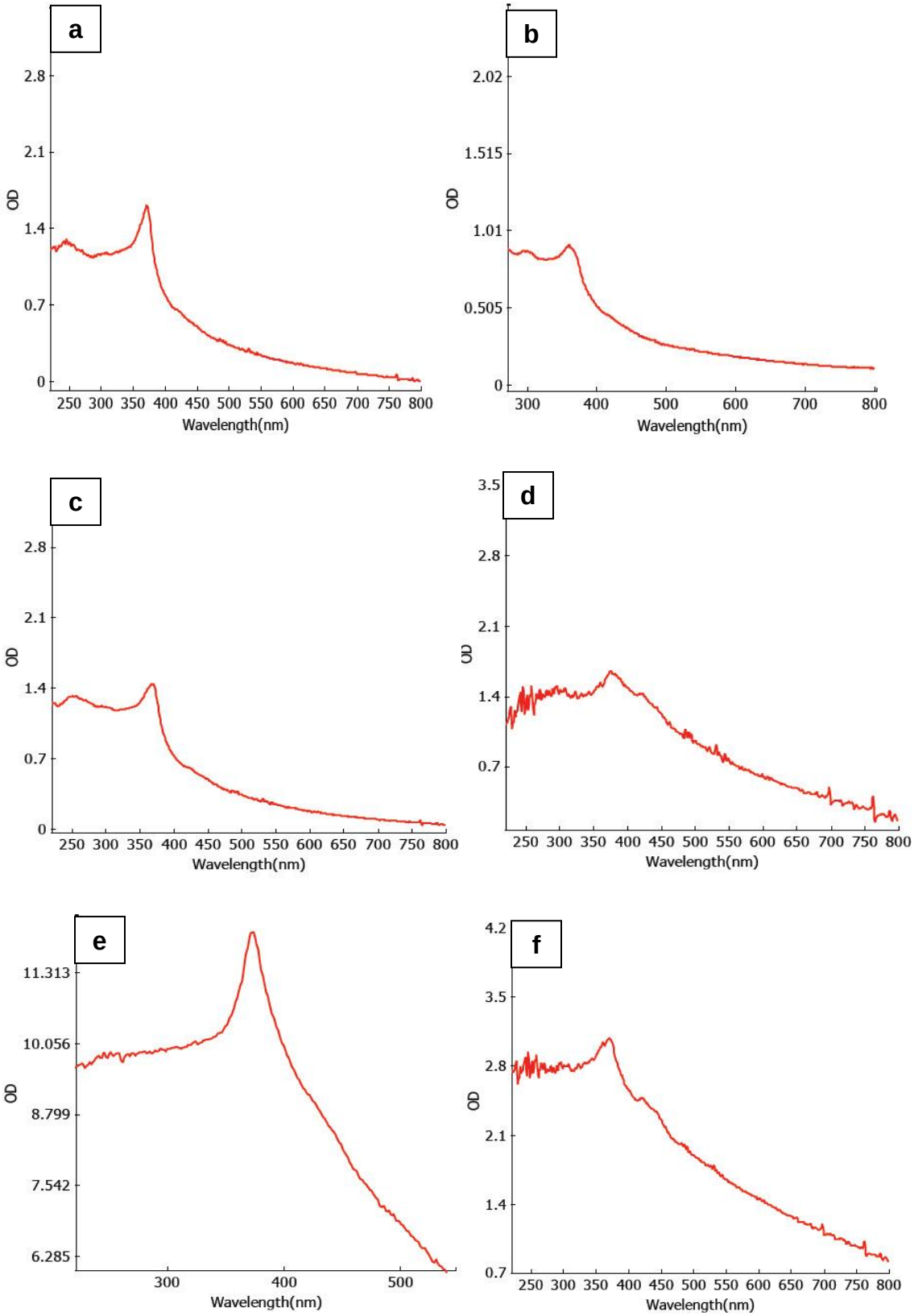
a
2.8
2.1
1.4
0.7
0
OD
250 300 350 400 450 500 550 600 650 700 750 800
Wavelength(nm)
b
2.02
1.515
1.01
0.505
0
OD
300 400 500 600 700 800
Wavelength(nm)
c
2.8
2.1
1.4
0.7
0
OD
250 300 350 400 450 500 550 600 650 700 750 800
Wavelength(nm)
d
3.5
2.8
2.1
1.4
0.7
OD
250 300 350 400 450 500 550 600 650 700 750 800
Wavelength(nm)
e
11.313
10.056
8.799
7.542
6.285
OD
300 400 500
Wavelength(nm)
f
4.2
3.5
2.8
2.1
1.4
0.7
OD
250 300 350 400 450 500 550 600 650 700 750 800
Wavelength(nm)

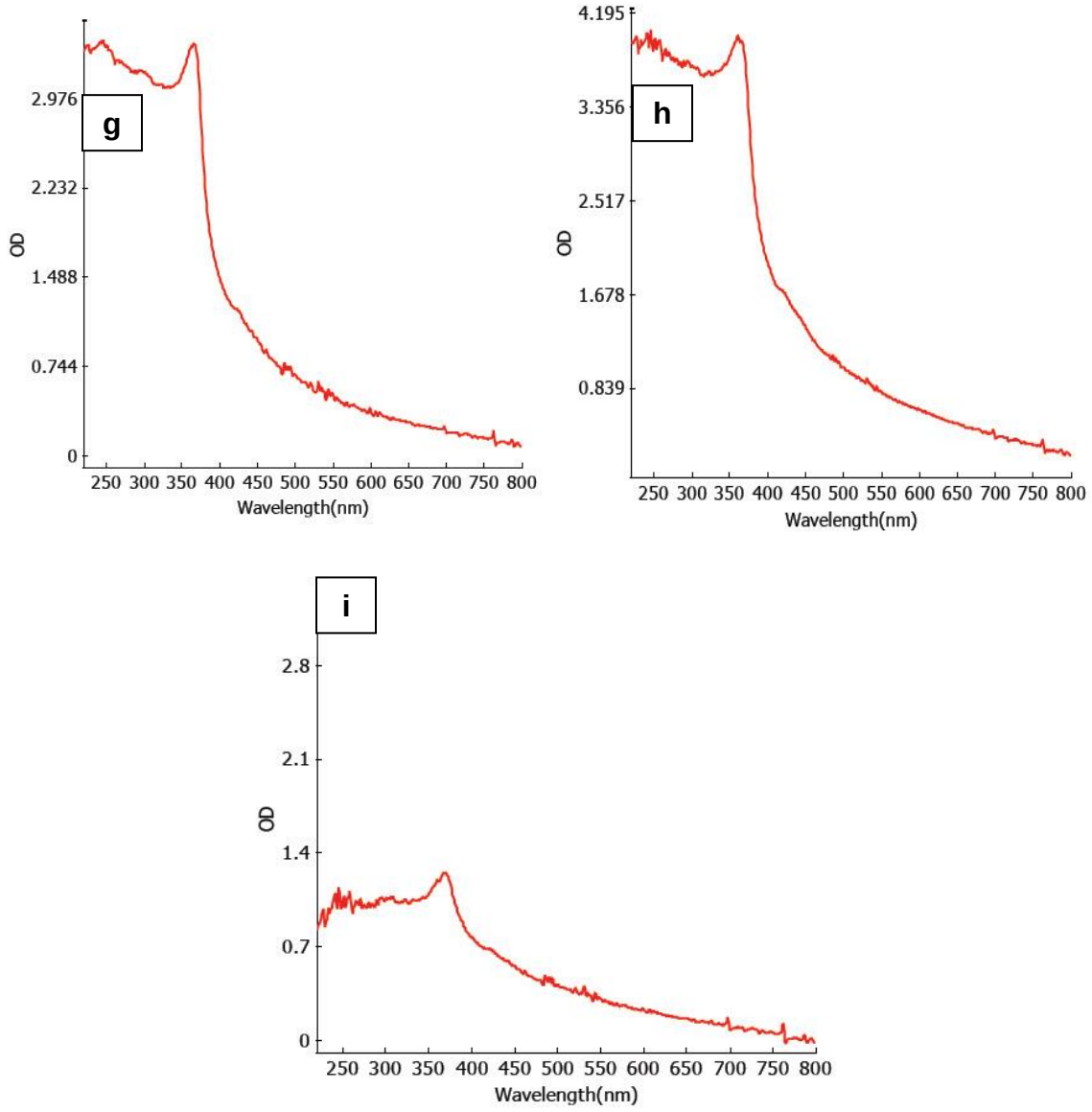

Figure 26. UV-Visible spectra of synthesized ZnONP (a)BoZn, (b) RaZn, (c)BaZn, (d)BrRZn, (e)BRRZn, (f)BJZn, (g)IWZn, (h)BuZn and (i) TDZn

The UV absorption of all the synthesized ZnONPs is in the range between (320-390nm), this shows the intrinsic (band gap) absorption of Zn-O. The absorption maximum in the UV region further ascertains the synthesized NPs can be used for pharma application and sunscreen lotions. As Bio-spec spectrophotometer is utilized in the study to record UV spectra, unlike double beam spectrophotometer it is sensitive to particles and hence shows noise in the spectra, when particles are not completely soluble.

ZnONPs synthesized using *Limonium pruinosum and Cymbopogon citratus* extract has absorption at 370nm (**Naiel *et al.*, 2022**) and 369-374nm (**Mohammed *et al.*, 2023**) respectively. These results are comparative with the present study.

The UV-visible spectrum of GNP, SNP and ZnONP reveal SPR in respective SPR region and confirms the formation of NPs. As the synthesized RGO particles are not soluble/ dispersed in water, the poor solubility/dispersion yields noise in spectra and hence it is not included in the thesis.

4.6.2 FT-IR spectral characterization of synthesized nanoparticles

4.6.2.1 FTIR analysis of GNPs

The FT-IR spectra reveal crucial information regarding the functional groups present in the materials. The GNPs' spectra, in particular, offer significant insight into the functional groups involved in reducing Au (III) to Au (0).

Upon careful examination of **Figure 27**, the FT-IR spectra of TBOSGNP show absence of C-O stretching (weak bands at 1126 cm^{-1} and 1381 cm^{-1}). This indicates the involvement of primary alcoholic functional groups in GNP formation. Additionally, comparing the TBIS and TBISGNP, reveals that the high-intensity peak at 1643 cm^{-1} in the TBIS spectra corresponds to the C=C of the monosubstituted group. However, it is worth mentioning that both TBS and TBSGNP spectra display a similar peak at 1635 cm^{-1} and 3556 cm^{-1}, respectively corresponding to C=O (Str) and O-H (Str). These findings suggest that the phenolic and flavonoid groups, which are the predominant secondary metabolites found in the extracts, have acted as capping and stabilizing agent in the surface of NPs. It is essential to note that a metal peak in the 400 to 500 cm^{-1} range is necessary to ensure the formation of GNPs.

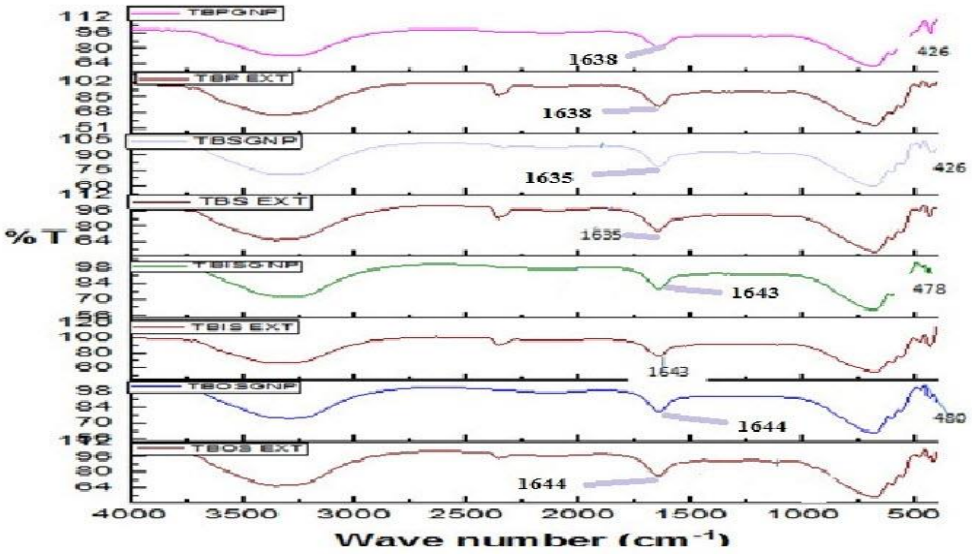

Figure 27. FT-IR spectra of aqueous fruit extracts of TB and Gold nanoparticles

The previous reports on TB whole fruit aided GNP defines the TB extract act as capping agent (**Kesarla *et al.*, 2012; Smina *et al.*, 2020**). These results endorse the results of the present study.

Determination of functional groups in GCA and GCA-mediated gold nanoparticles was determined by FT-IR spectroscopy. The broad peak at 3350 cm^{-1} corresponds to –OH group, which is possible because of the aqueous nature of samples. The sharp peak at 1643 cm^{-1} corresponds to C=O peak, which might be due to the hydroxy citric acid moiety. The peak at 462 cm^{-1} corresponds to the metal peak, which is absent in GCA and present in GCAu samples, confirming the formation of GNPs (**Figure 28**).

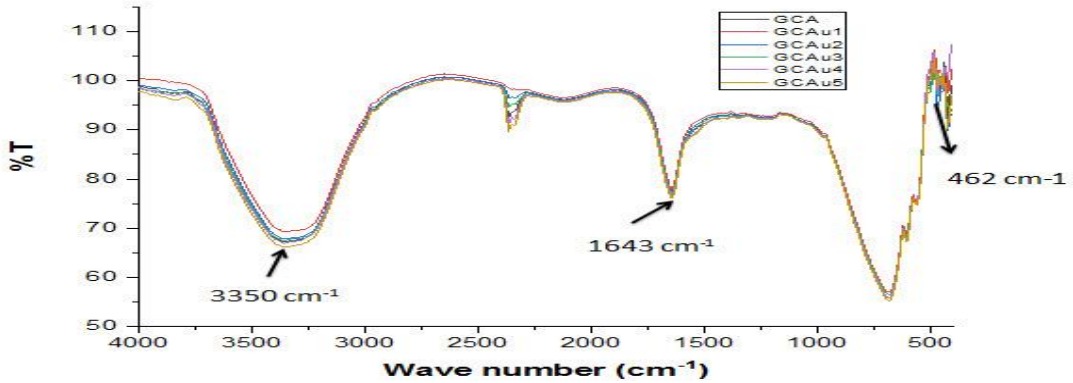

Figure 28. FT-IR spectra of GCAu

The strong band at 686 cm^{-1} corresponds to aliphatic C-H stretching, characteristic of hydroxy acids, citric acid, hydroxy citric acid etc. GC capsules (commercial) contain 70 % HCA, the other 30% may be having other molecules which corresponds to other encapsulating agents. The broad peak at 3350 cm^{-1} corresponds to N-H stretching vibrations. Peak at 1643 cm^{-1} corresponds to C=O (**Figure 28**). The peaks observed in GCA are observed in GCAu. This ensures that the functional groups in the GCA have capped the Au surface and hence stabilizes the NP. Similar observation was reported by GC fruit extract aided GNP synthesis (**Kureshi *et al.*, 2020**).

In all the FTIR spectra of GNPs synthesized from cereals and pulses washed water, the broad peak near 3330 cm^{-1} is due to O-H group and near 1640 cm^{-1} corresponds to C=O group. The peak near 430 cm^{-1} attributes to C-metal peak, which indicates GNP formation (**Figure 29**).

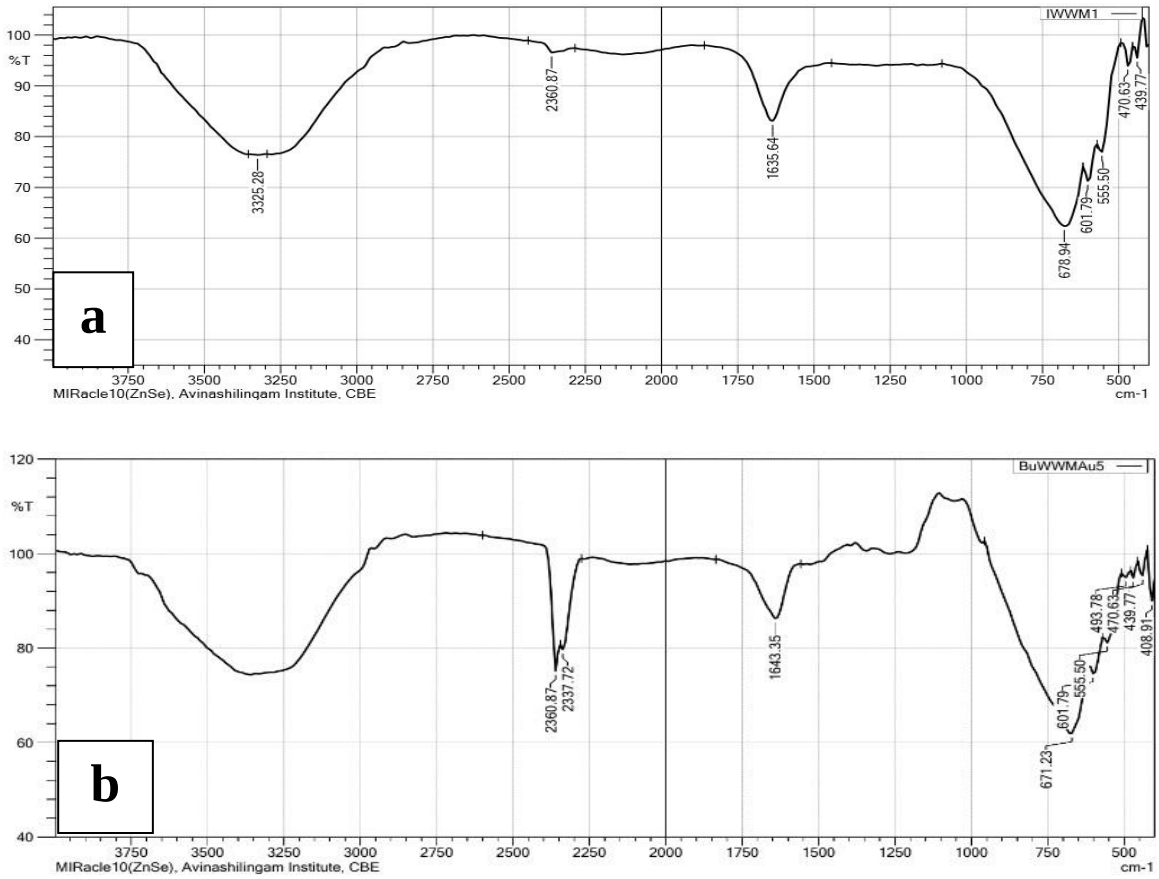

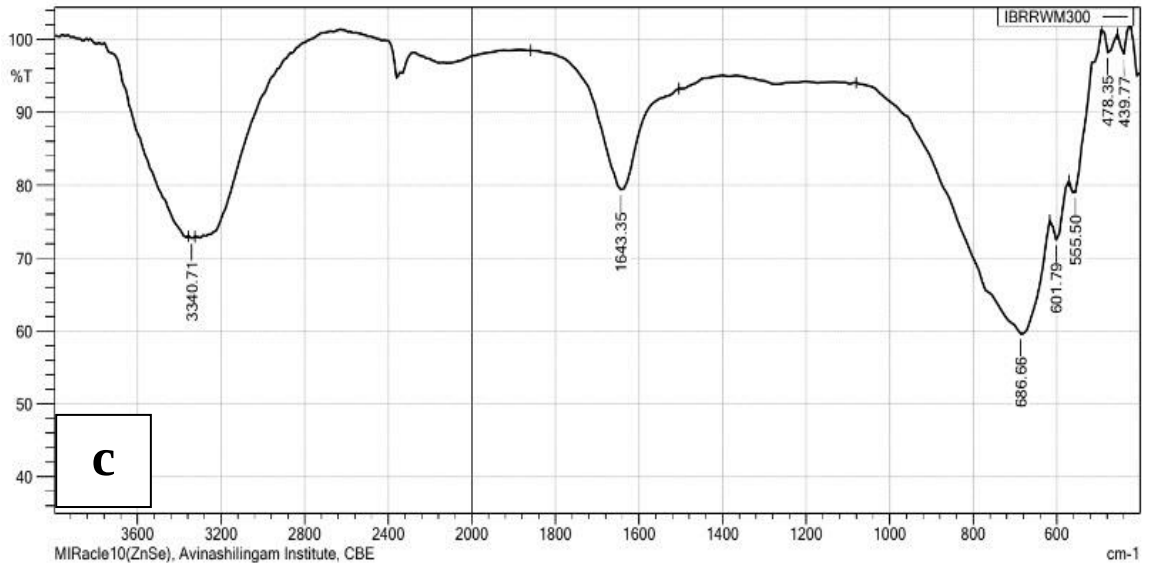
IBRRWM300
%T
3340.71
1643.35
686.66
601.79
555.50
478.35
439.77
c
MIRacle10(ZnSe), Avinashilingam Institute, CBE
cm-1

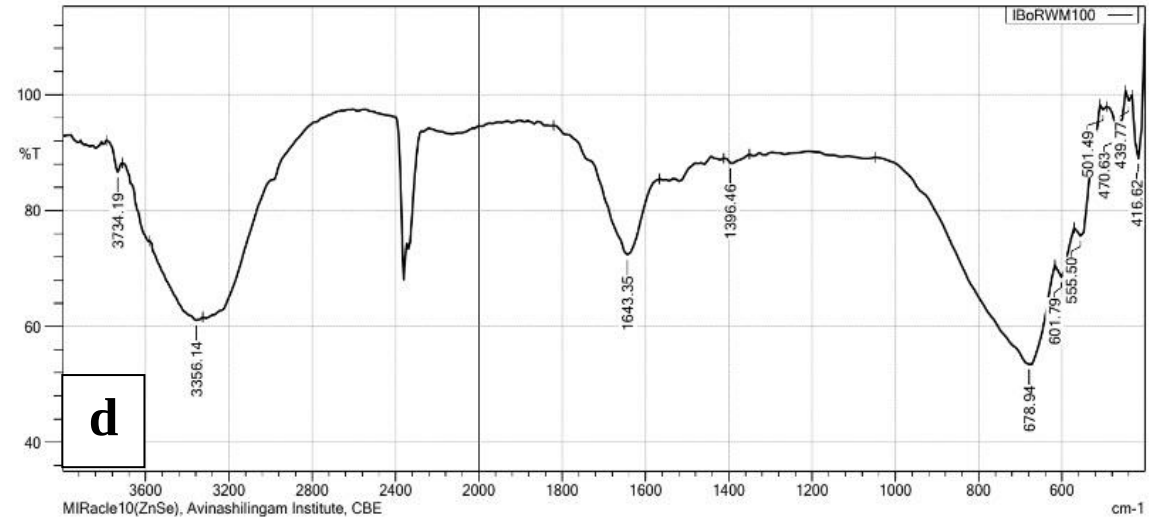
IBoRWM100
%T
3734.19
3356.14
1643.35
1396.46
678.94
601.79
555.50
501.49
470.63
439.77
416.62
d
MIRacle10(ZnSe), Avinashilingam Institute, CBE
cm-1

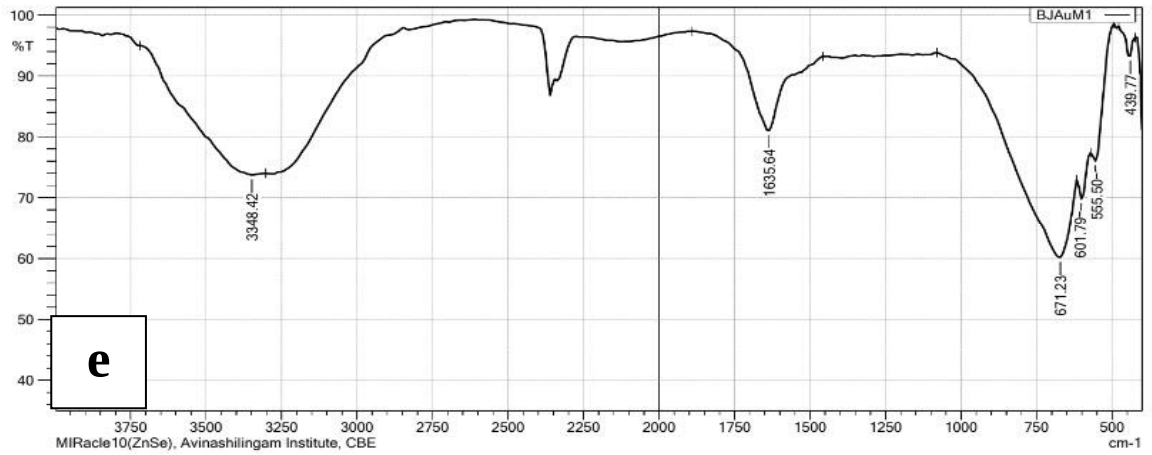
BJAuM1
%T
3348.42
1635.64
671.23
601.79
555.50
439.77
e
MIRacle10(ZnSe), Avinashilingam Institute, CBE
cm-1

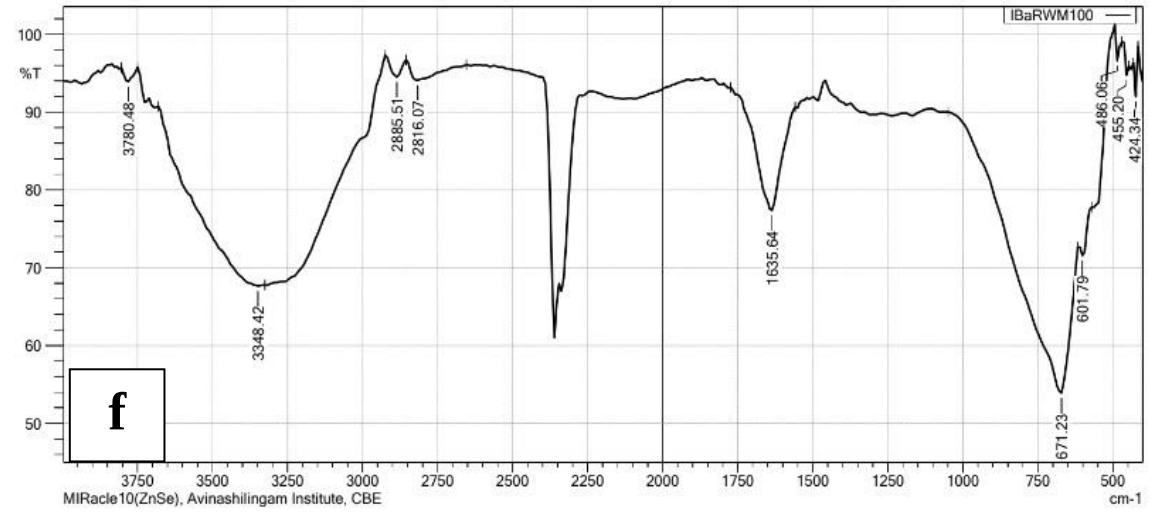
IBaRWM100
%T
3780.48
3348.42
2885.51
2816.07
1635.64
671.23
601.79
486.06
455.20
424.34
f
MIRacle10(ZnSe), Avinashilingam Institute, CBE
cm-1

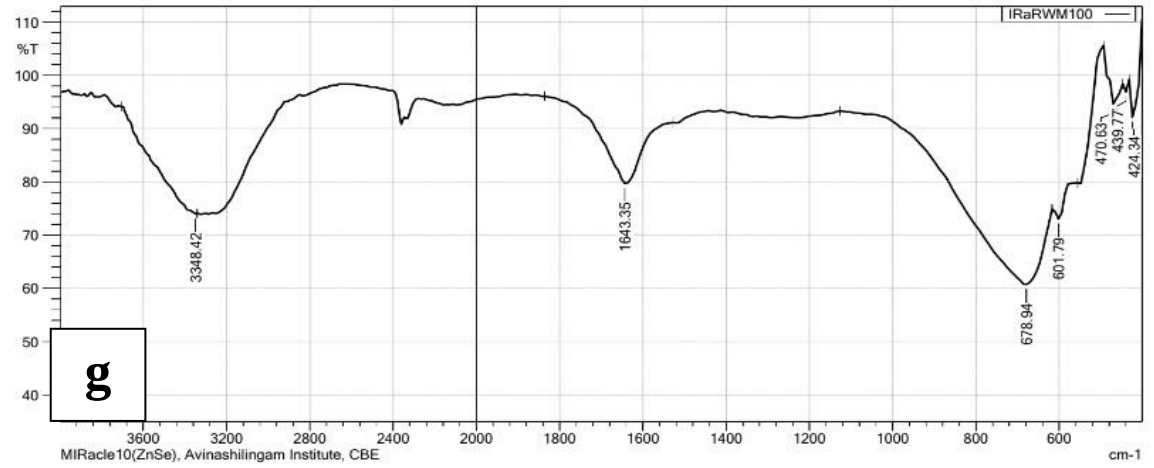
IRaRWM100
%T
3348.42
1643.35
678.94
601.79
470.63
439.77
424.34
g
MIRacle10(ZnSe), Avinashilingam Institute, CBE
cm-1

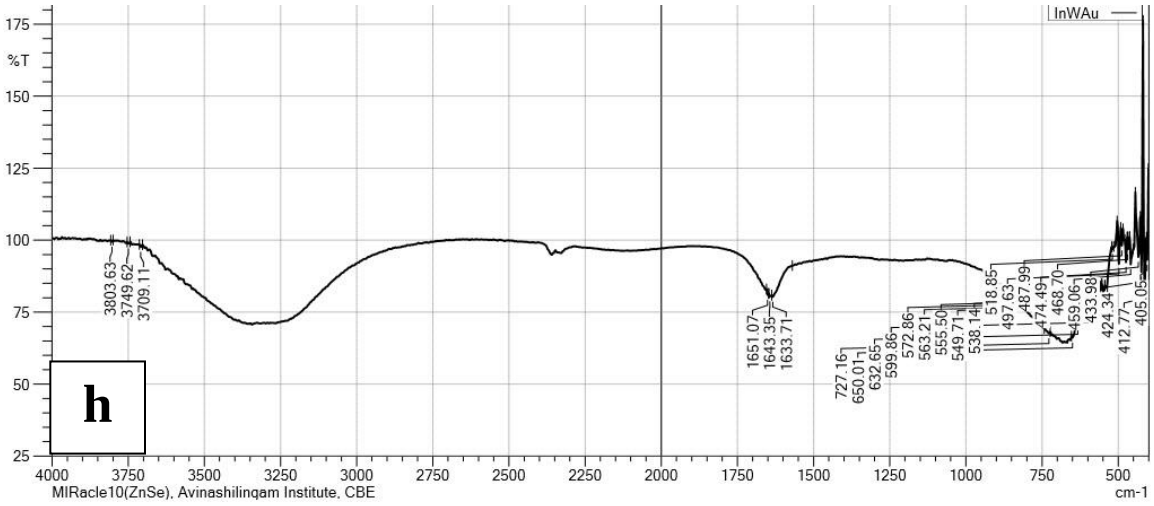
InWAu
%T
3803.63
3749.62
3709.11
1651.07
1643.35
1633.71
727.16
650.01
632.65
599.96
572.86
563.21
555.50
549.71
538.14
518.85
497.63
487.99
474.49
468.70
459.06
433.98
424.34
412.77
405.05
h
MIRacle10(ZnSe), Avinashilingam Institute, CBE
cm-1

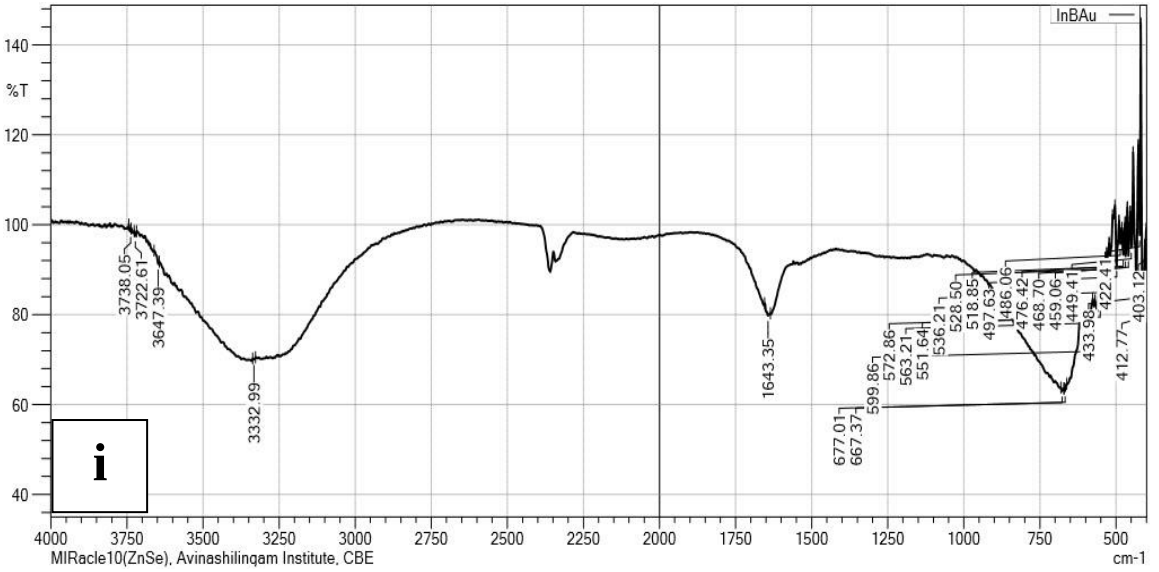
InBAu
%T
3738.05
3722.61
3647.39
3332.99
1643.35
677.01
667.37
599.86
572.86
563.21
551.64
536.21
528.50
518.85
497.63
486.06
476.42
468.70
459.06
449.41
433.98
422.41
412.77
403.12
i
MIRacle10(ZnSe), Avinashilingam Institute, CBE
cm-1

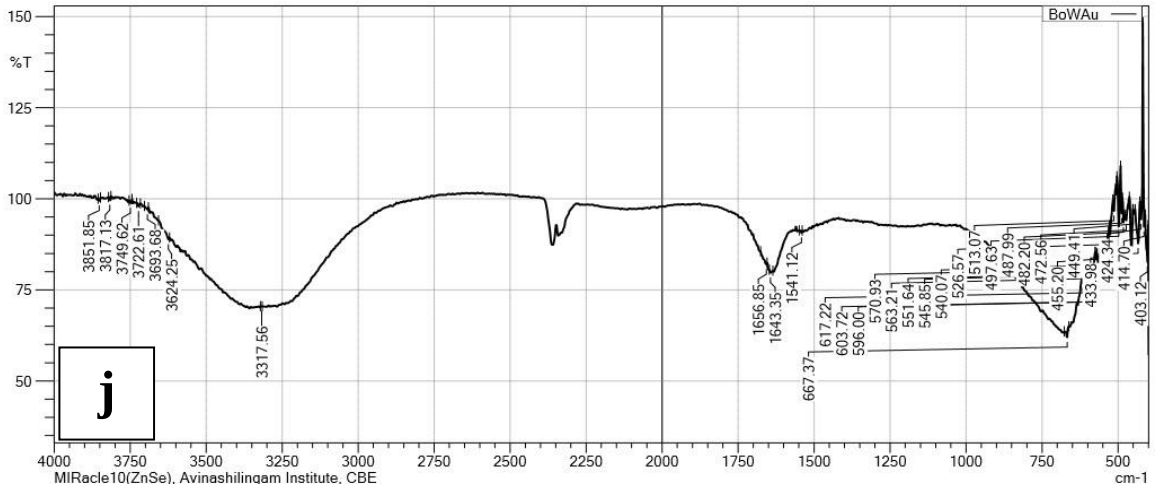
BoWAu
%T
3851.85
3817.13
3749.62
3722.61
3693.68
3624.25
3317.56
1656.85
1643.35
1541.12
667.37
617.22
603.72
596.00
570.93
563.21
551.64
545.85
540.07
526.57
513.07
497.63
487.99
482.20
472.56
455.20
449.41
433.98
424.34
414.70
403.12
j
MIRacle10(ZnSe), Avinashilingam Institute, CBE
cm-1

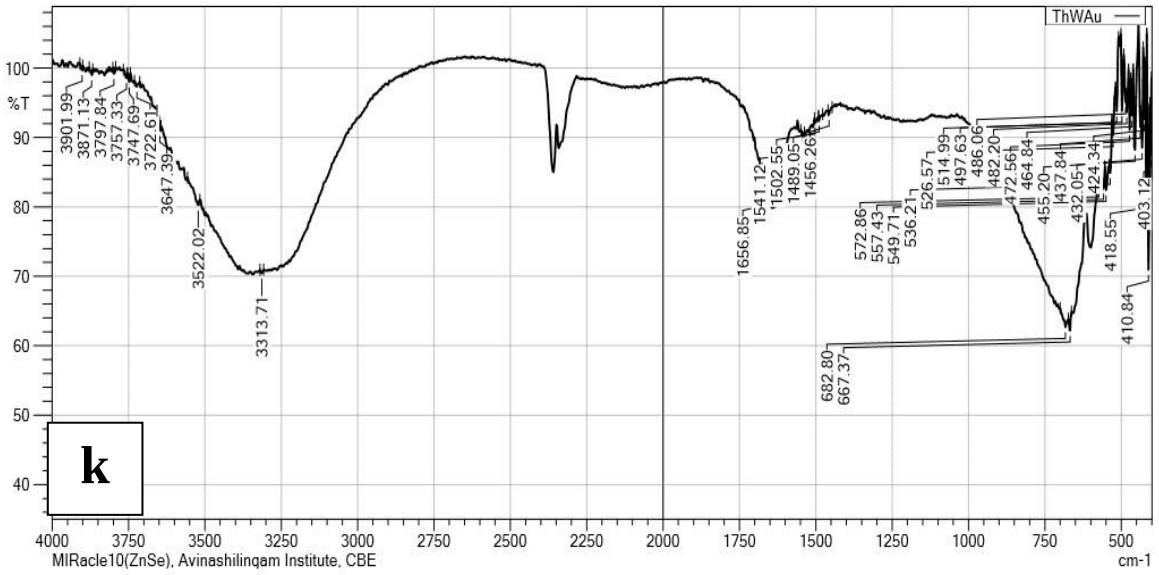
ThWAu
%T
3901.99
3871.13
3797.84
3757.33
3747.69
3722.61
3647.39
3522.02
3313.71
1656.85
1541.12
1502.55
1489.05
1456.26
682.80
667.37
572.86
557.43
549.71
536.21
526.57
514.99
497.63
486.06
482.20
472.56
464.84
455.20
437.84
432.05
424.34
418.55
410.84
403.12
k
MIRacle10(ZnSe), Avinashilingam Institute, CBE
cm-1

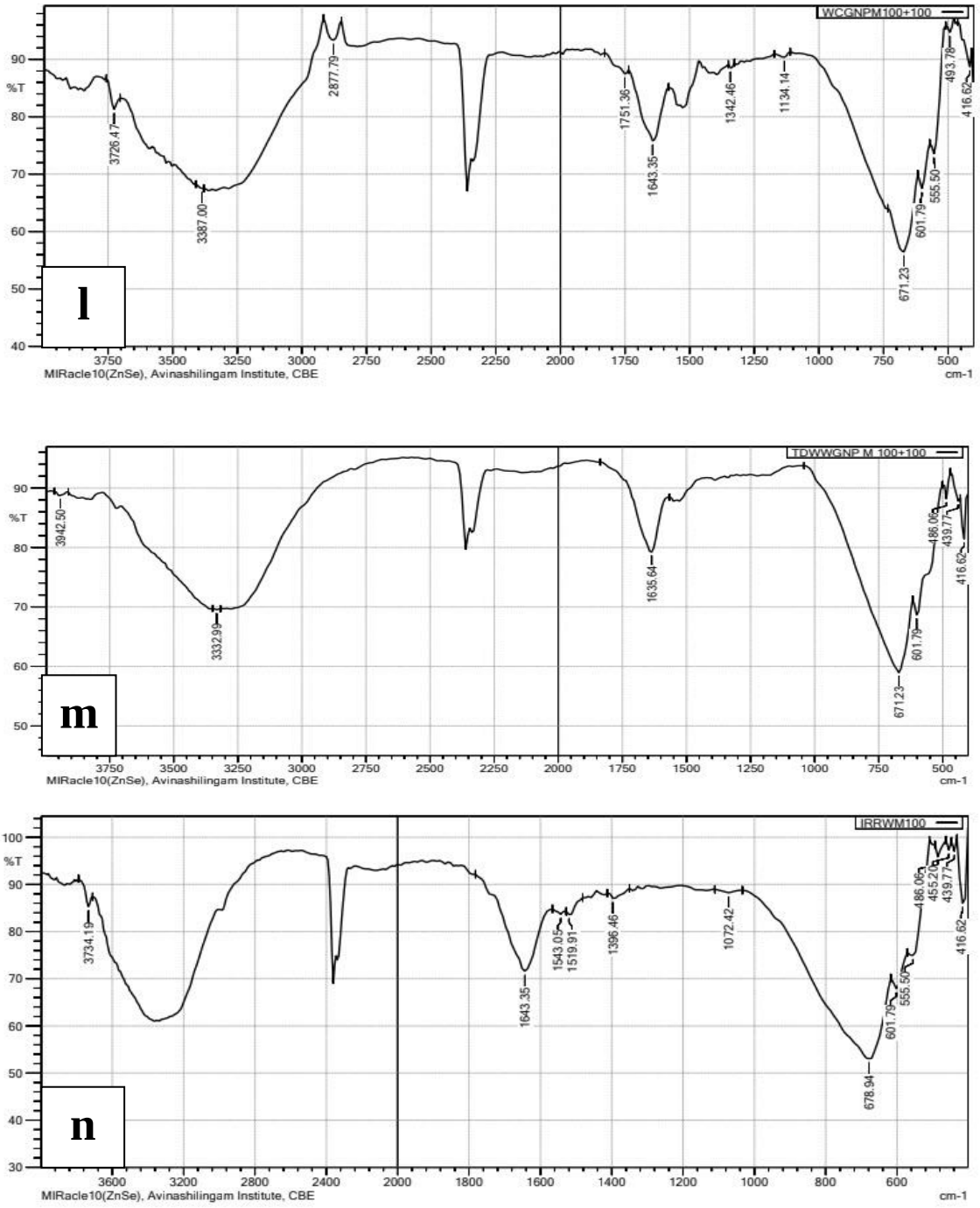

Figure 29. FT-IR spectra of GNP synthesized using cereals and pulses washed water (a) IWWM, (b) BuWWM, (c)IBRRWM, (d)IBoRWM, (e)BJWWM, (f)IBaRWM, (g)IRaRWM, (h)InWAu, (i)InBAu, (j)BoWAu, (k)ThWAu, (l) WCWWM, (m)TDWWM and (n)IRRWM

The FT-IR spectra shows that the nutrients present in cereals and pulses washed water might have acted as stabilizing and reducing agents during the formation of GNPs. The C-metal peak in the region 500 cm^{-1} to 400 cm^{-1} further confirms the formation of GNPs.

The peak at 3325 cm^{-1} is assigned to –OH group, 1635 cm^{-1} (C=O str) of amide (**Jiang *et al.*, 2022**), 432 cm^{-1} corresponds to C-metal peak in HN28Au sample (**Figure 30**). The stabilized HN28Au was due to the protein or keratin in the free edge of HN28. However the morphology of the nanoparticle can help to further understand the nature and stability of the NPs.

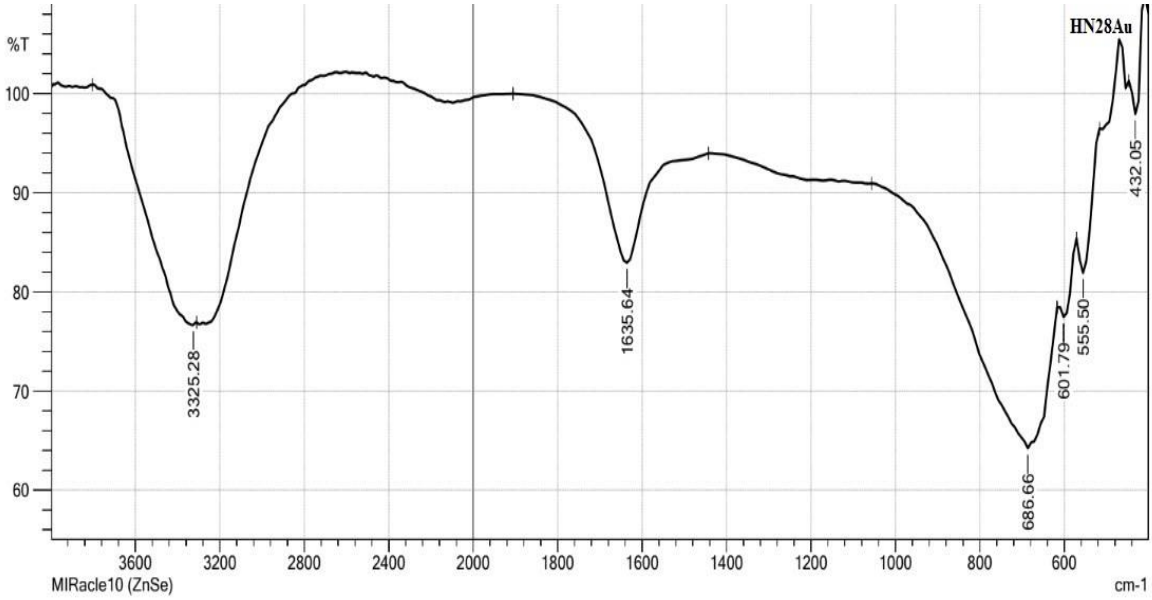

Figure 30. FT-IR of synthesized HN28Au

From the FT-IR spectra of synthesized GNPs, the functional group present in the GNP which is responsible for the stabilization/capping/ or reducing the metal ions were identified. Noise free FT-IR spectra obtained also indicates the stability of samples.

4.6.2.2 FT-IR analysis of synthesized SNPs

From FT-IR spectra of the synthesized TB aided SNPs the upward peak in the region 400 cm^{-1} to 500 cm^{-1} show the C-metal peak, which is observed in all the synthesized SNPs. It is well evident that the peaks observed in the FTIR of TB fruit part aided SNP are of functional groups O-H and C=O which are attributed to the functional groups of secondary metabolites in TB extracts (**Figure 31**). The functional groups present in the phytoextracts

are probably responsible for the reduction of Ag ions and acts as a capping agent in the synthesis of SNPs and therefore helps the SNP without aggregation and improves stability.

The FTIR spectra of all SNPs prepared using cereals and pulses washed water (**Figure 32**) reveals strong peaks at 2927, 1643, and 1265 cm^{-1} and few other minor peaks in the finger print region which may be assigned to C-H stretching, carbonyl and C-O vibrations respectively. Similar observations are reported by earlier workers **(Marimuthu *et al*., 2011).**

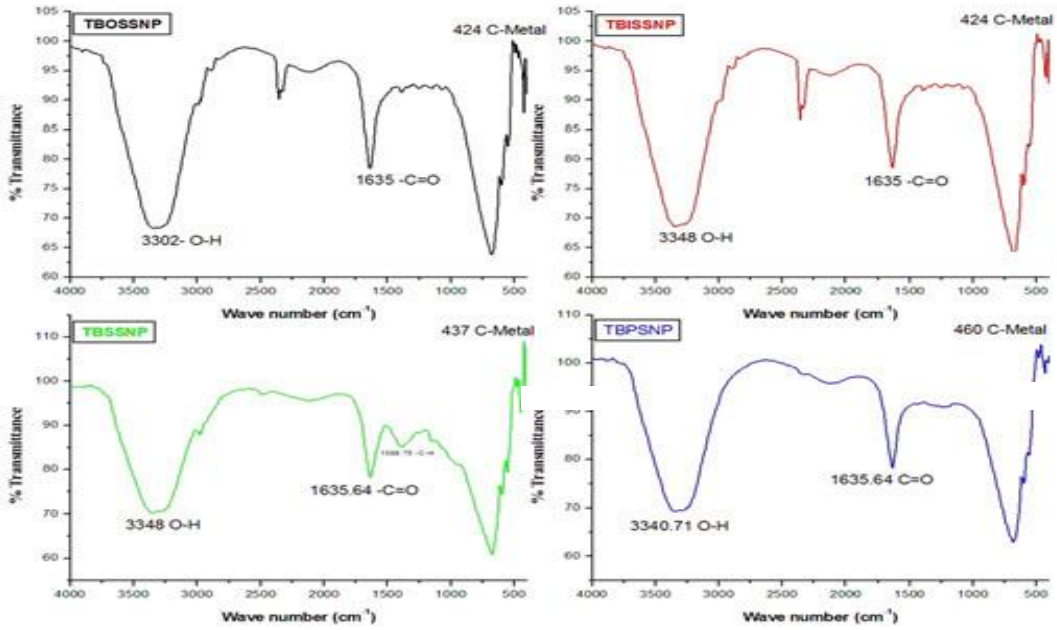

Figure 31. FT-IR spectra of TB fruit parts aided SNP

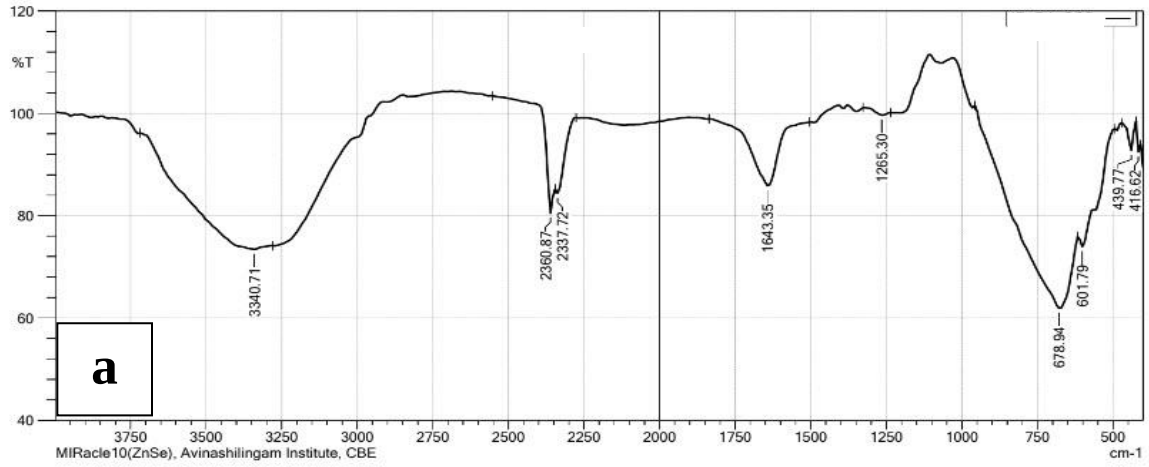

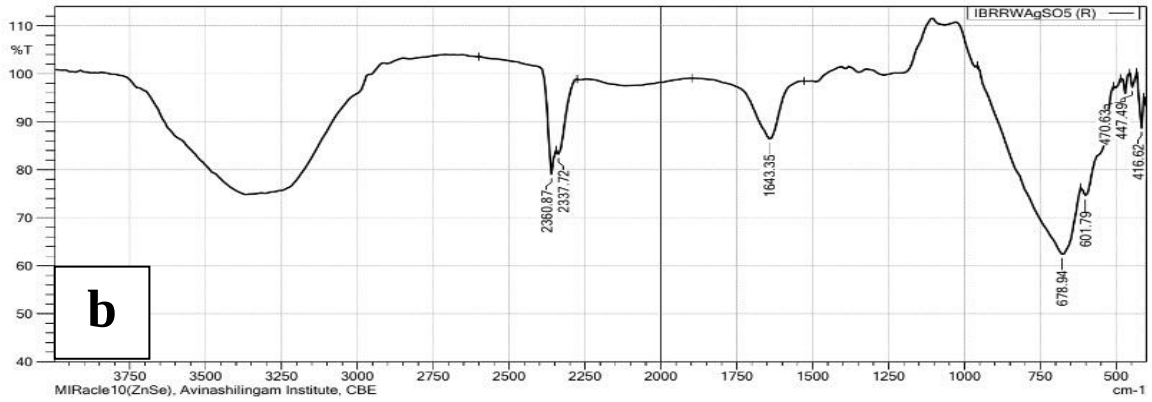
IBRRWAgSO5 (R)
%T
2360.87
2337.72
1643.35
678.94
601.79
470.63
447.49
416.62
b
MIRacle10(ZnSe), Avinashilingam Institute, CBE
cm-1

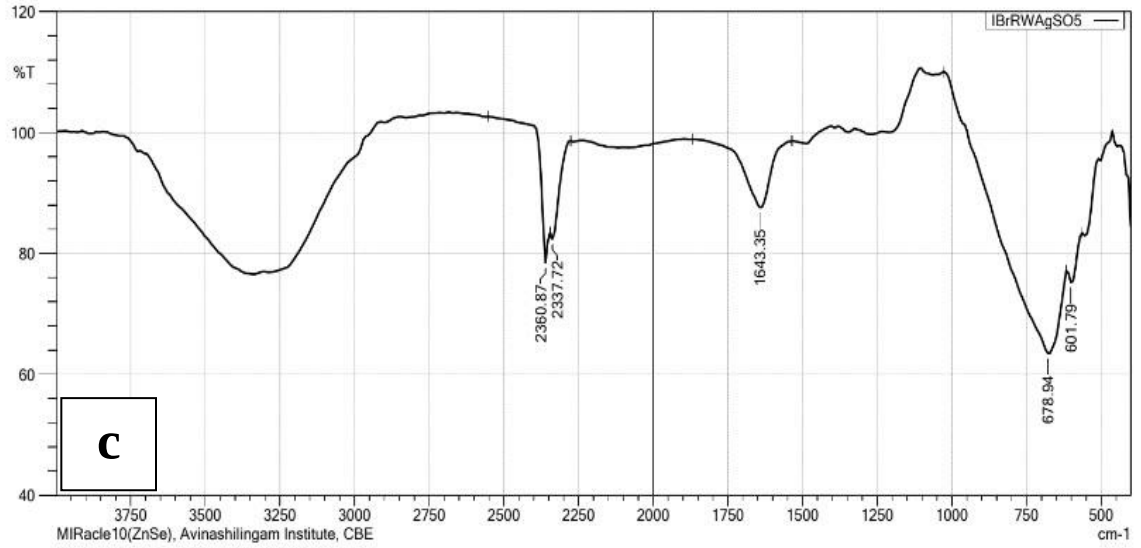
IBrRWAgSO5
%T
2360.87
2337.72
1643.35
678.94
601.79
c
MIRacle10(ZnSe), Avinashilingam Institute, CBE
cm-1

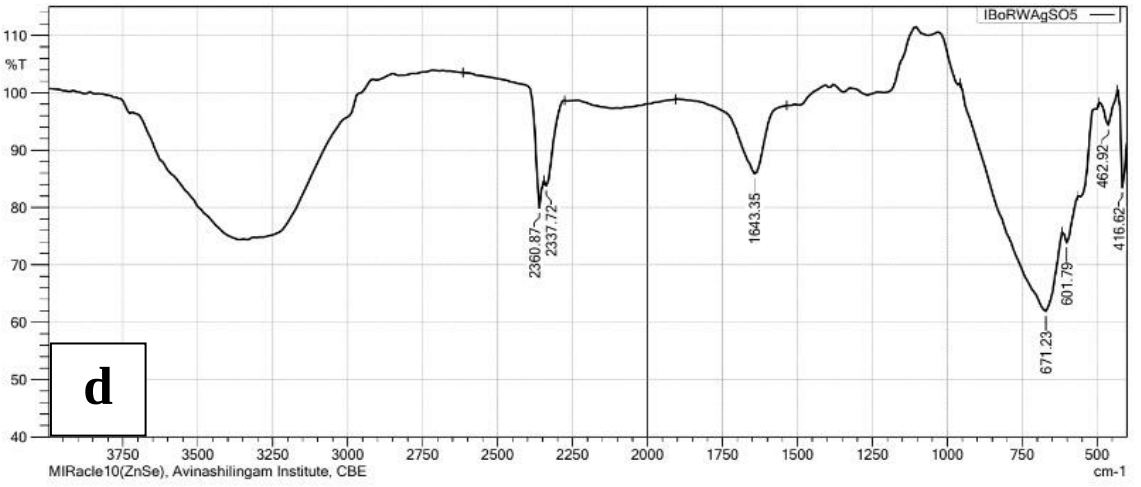
IBoRWAgSO5
%T
2360.87
2337.72
1643.35
671.23
601.79
462.92
416.62
d
MIRacle10(ZnSe), Avinashilingam Institute, CBE
cm-1

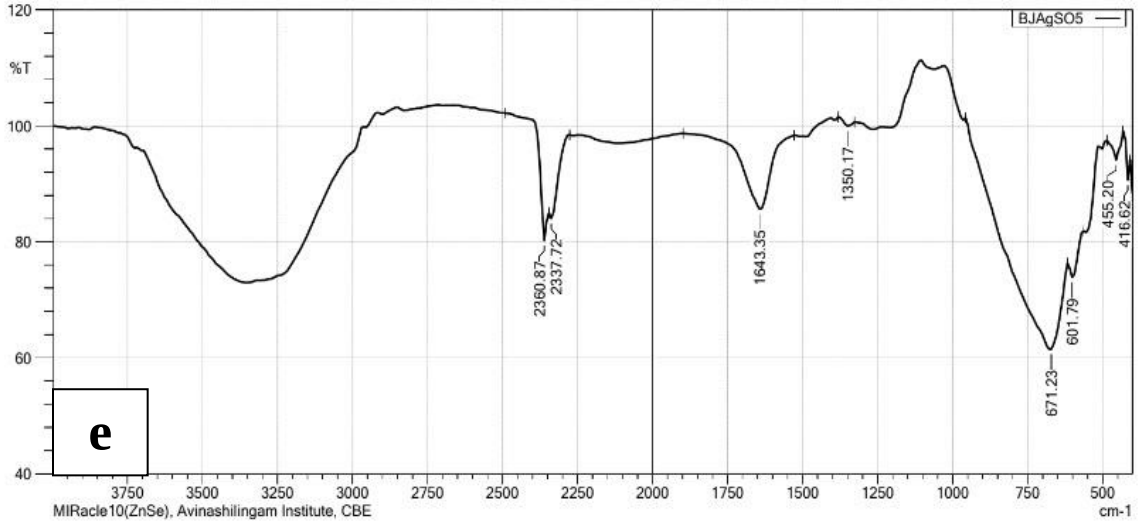
BJAgSO5
%T
2360.87
2337.72
1643.35
1350.17
671.23
601.79
455.20
416.62
e
MIRacle10(ZnSe), Avinashilingam Institute, CBE
cm-1

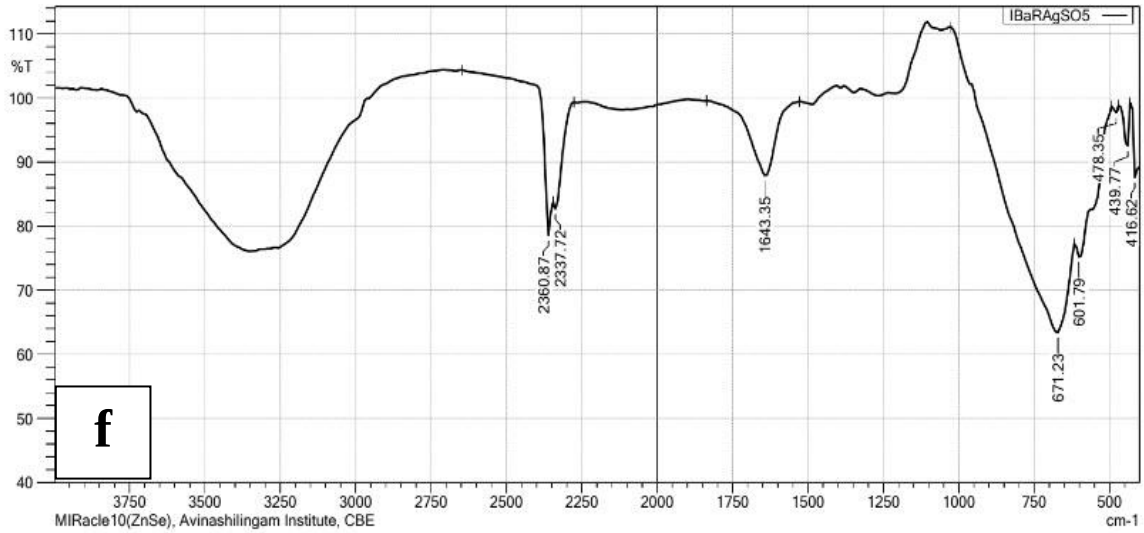
IBaRAgSO5
%T
2360.87
2337.72
1643.35
671.23
601.79
478.35
439.77
416.62
f
MIRacle10(ZnSe), Avinashilingam Institute, CBE
cm-1

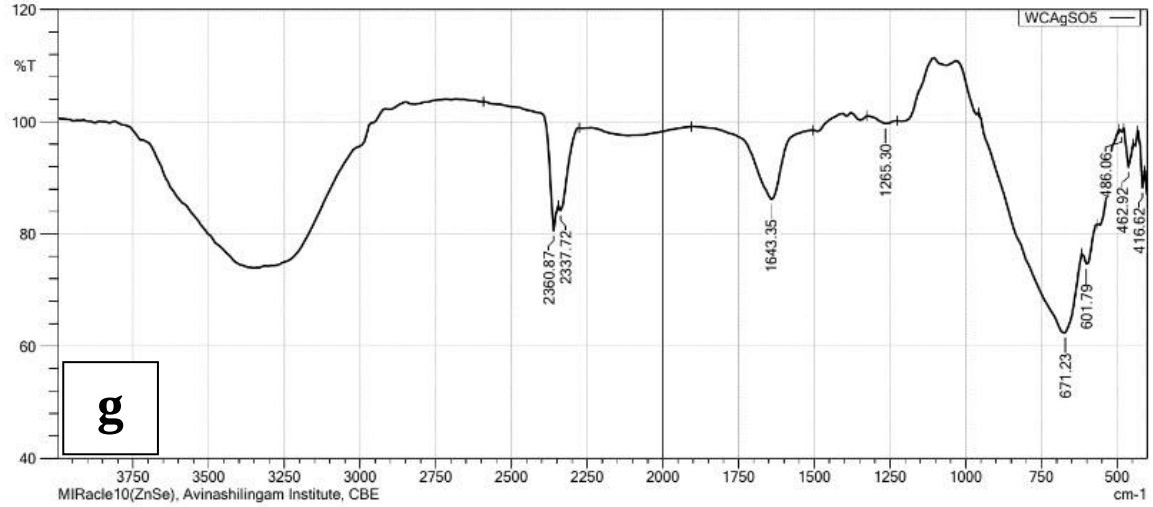
WCAgSO5
%T
2360.87
2337.72
1643.35
1265.30
671.23
601.79
486.06
462.92
416.62
g
MIRacle10(ZnSe), Avinashilingam Institute, CBE
cm-1

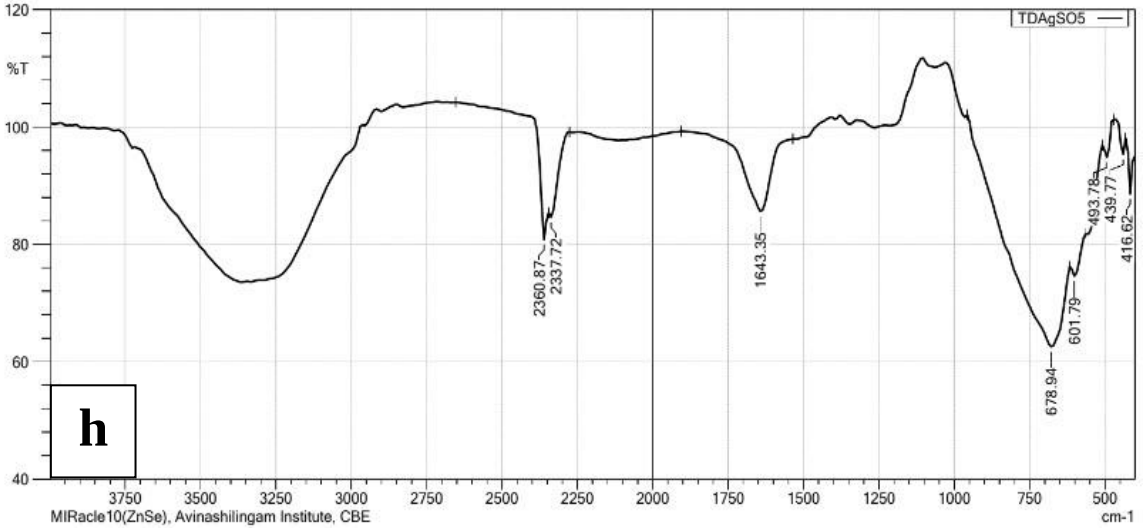
TDAgSO5
%T
2360.87
2337.72
1643.35
678.94
601.79
493.78
439.77
416.62
h
MIRacle10(ZnSe), Avinashilingam Institute, CBE
cm-1

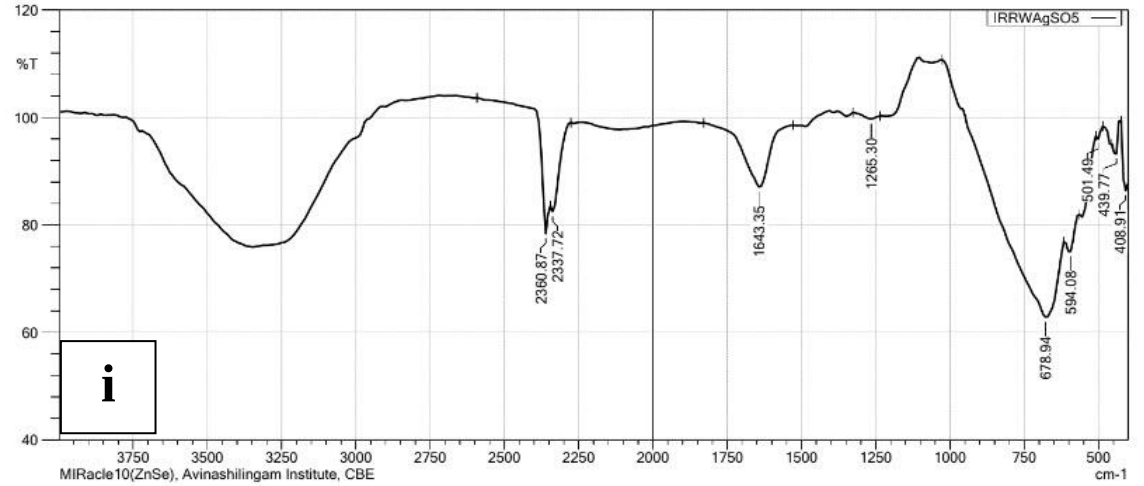
IRRWAgSO5
%T
2360.87
2337.72
1643.35
1265.30
678.94
594.08
501.49
439.77
408.91
i
MIRacle10(ZnSe), Avinashilingam Institute, CBE
cm-1

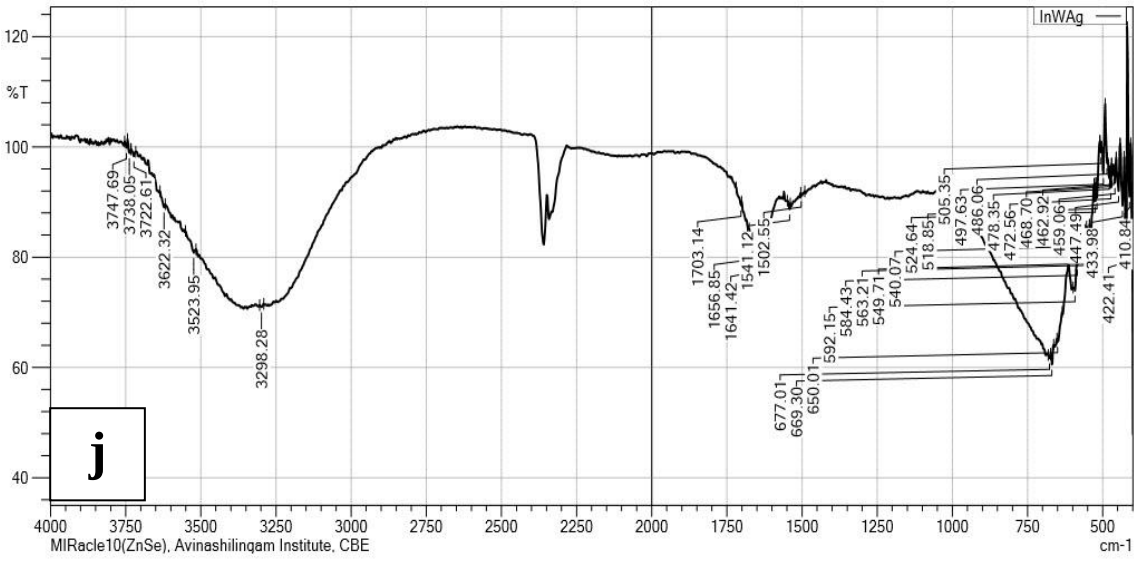
InWAg
%T
3747.69
3738.05
3722.61
3622.32
3523.95
3298.28
1703.14
1656.85
1641.42
1541.12
1502.55
677.01
669.30
650.01
592.15
584.43
563.21
549.71
540.07
524.64
518.85
505.35
497.63
486.06
478.35
472.56
468.70
462.92
459.06
447.49
433.98
422.41
410.84
j
MIRacle10(ZnSe), Avinashilingam Institute, CBE
cm-1

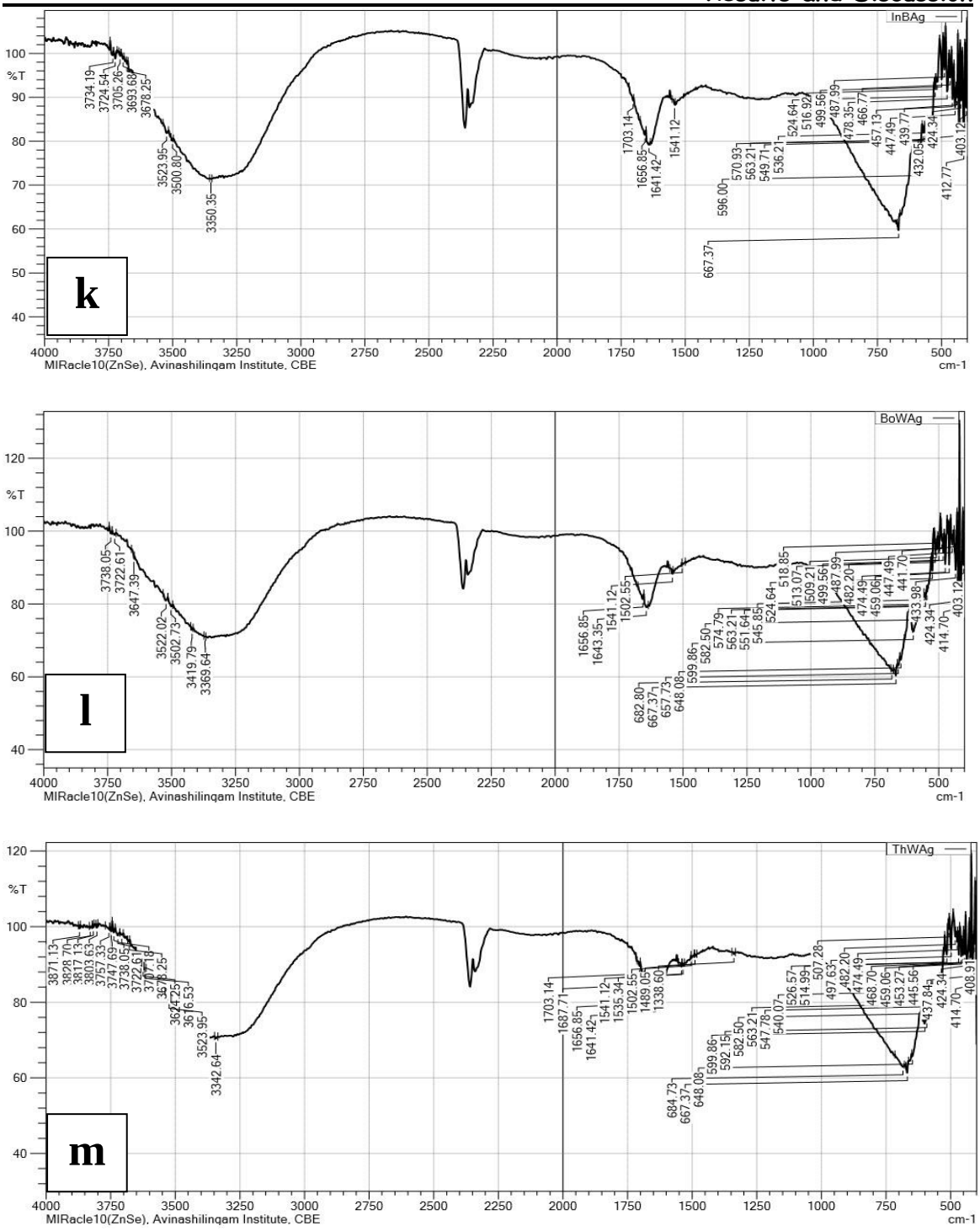

Figure 32. FT-IR spectra of cereals and pulses washed water aided synthesized SNP (a) IRaRWAgSo, (b) IBRRWAgSo, (c) IBrRWAgSo, (d)IBoRWAgSo, (e) BJAgSo, (f) IBaRWAgSo,(g) WCWAgSo, (h) TDAgSo, (i) IRRWAgSo, (j) InWAg, (k) InBAg, (l) BoWAg and (m)ThWAg

FT-IR is an indispensable tool for investigating nano-scaled materials. It enables the confirmation of functional molecules covalently grafted onto materials like silver, carbon nanotubes, graphene, and gold nanoparticles. Additionally, it helps us understand the interactions taking place between enzymes and substrates during catalytic processes. By utilizing FT-IR, we can obtain valuable insights into the properties and behavior of these materials at a molecular level **(Zhang *et al*., 2016)**.

Thus the FT-IR spectra of TB aqueous extracts and cereals/pulses washed water aided SNPs show the functional group responsible for the stabilization, capping/reduction of the Ag ions. However further characterization helps to better understand the morphology of the synthesized NPs.

4.6.2.3 FTIR analysis of ZnONPs synthesized from cereals and pulses washed water

The absorption of infrared light by a substance is measured and plotted vs wavelength using FTIR approach. The dried powder was used in the FT-IR spectroscopy for synthesized ZnONPs. It's important to note that in the presence of metal oxide, the Zn-O stretching vibration causes stretching wings of alcohols/carboxylic at 656-432 cm^{-1}. These peaks are commonly observed in the synthesized ZnONPs in the study (**Figure 33**).

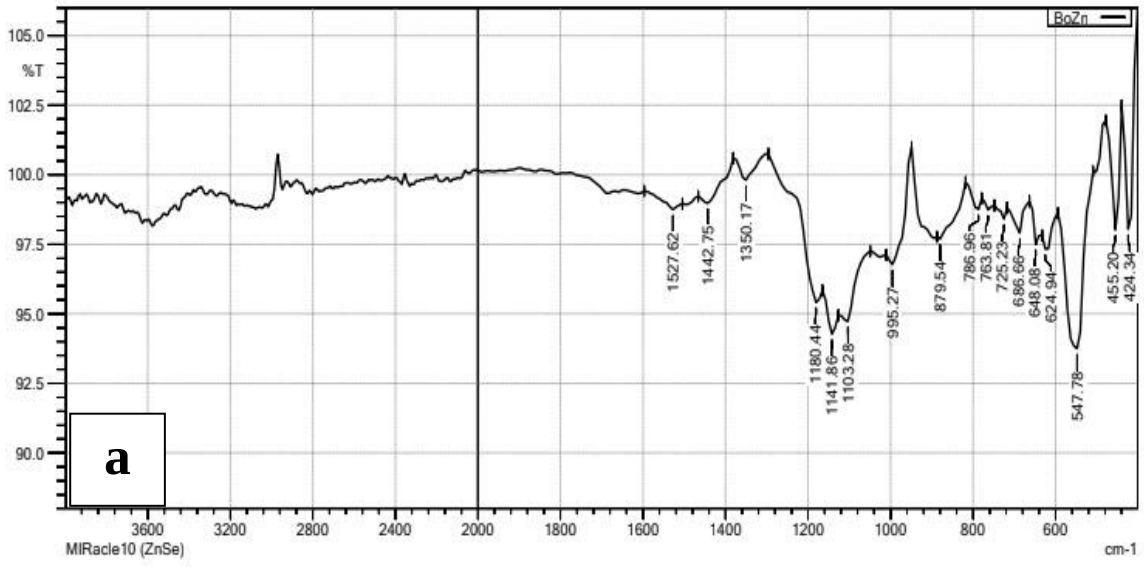

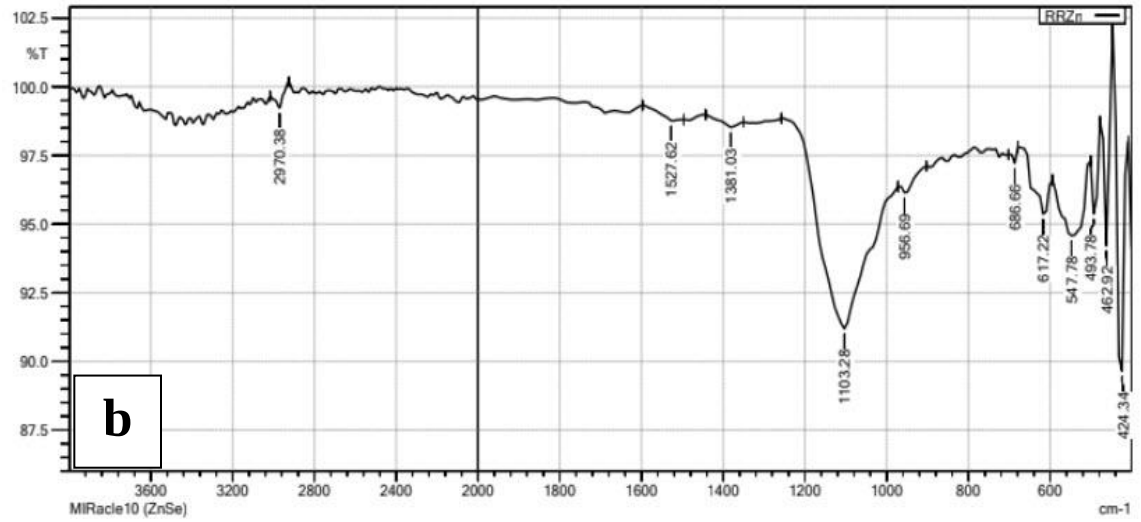
RRZn
%T
2970.38
1527.62
1381.03
1103.28
956.69
686.66
617.22
547.78
493.78
462.92
424.34
b
MIRacle10 (ZnSe)
cm-1

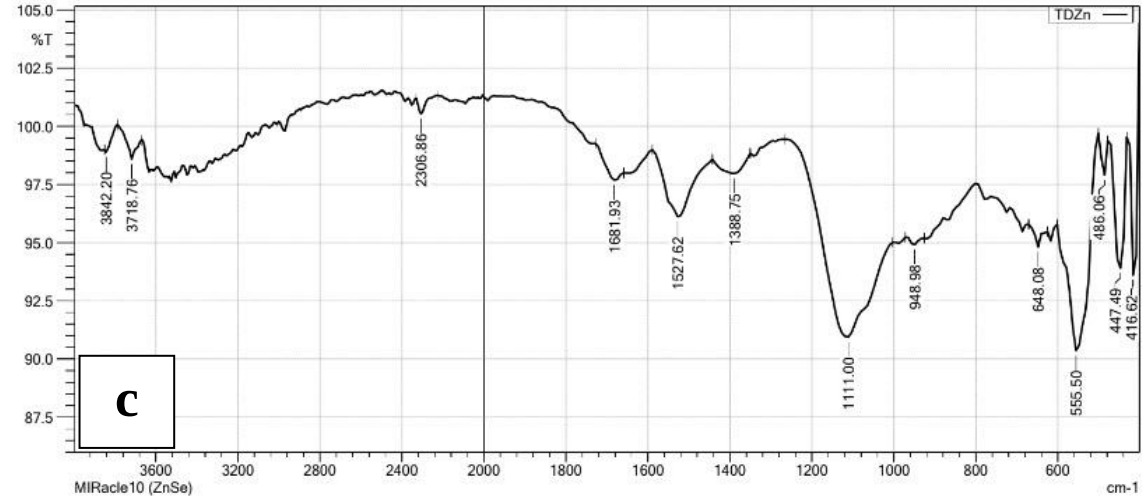
TDZn
%T
3842.20
3718.76
2306.86
1681.93
1527.62
1388.75
1111.00
948.98
648.08
555.50
486.06
447.49
416.62
c
MIRacle10 (ZnSe)
cm-1

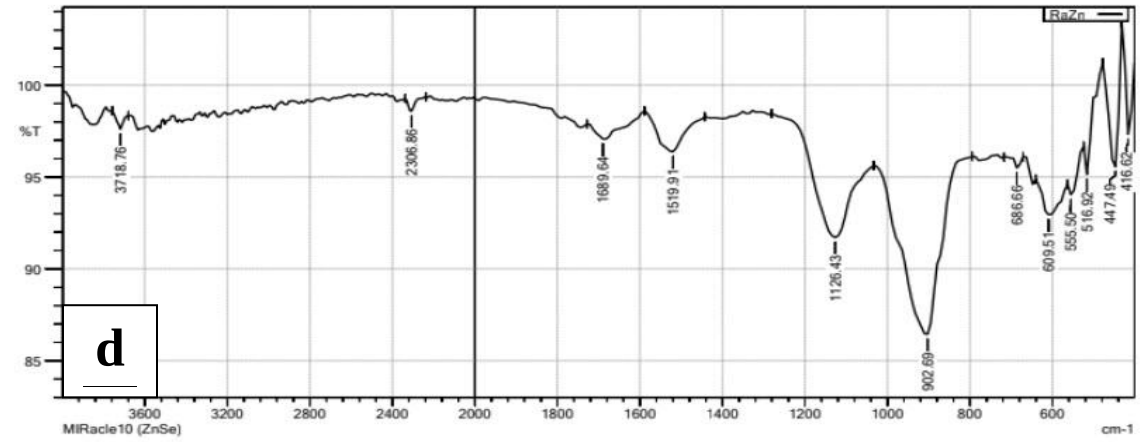
RaZn
%T
3718.76
2306.86
1689.64
1519.91
1126.43
902.69
686.66
609.51
555.50
516.92
447.49
416.62
d
MIRacle10 (ZnSe)
cm-1

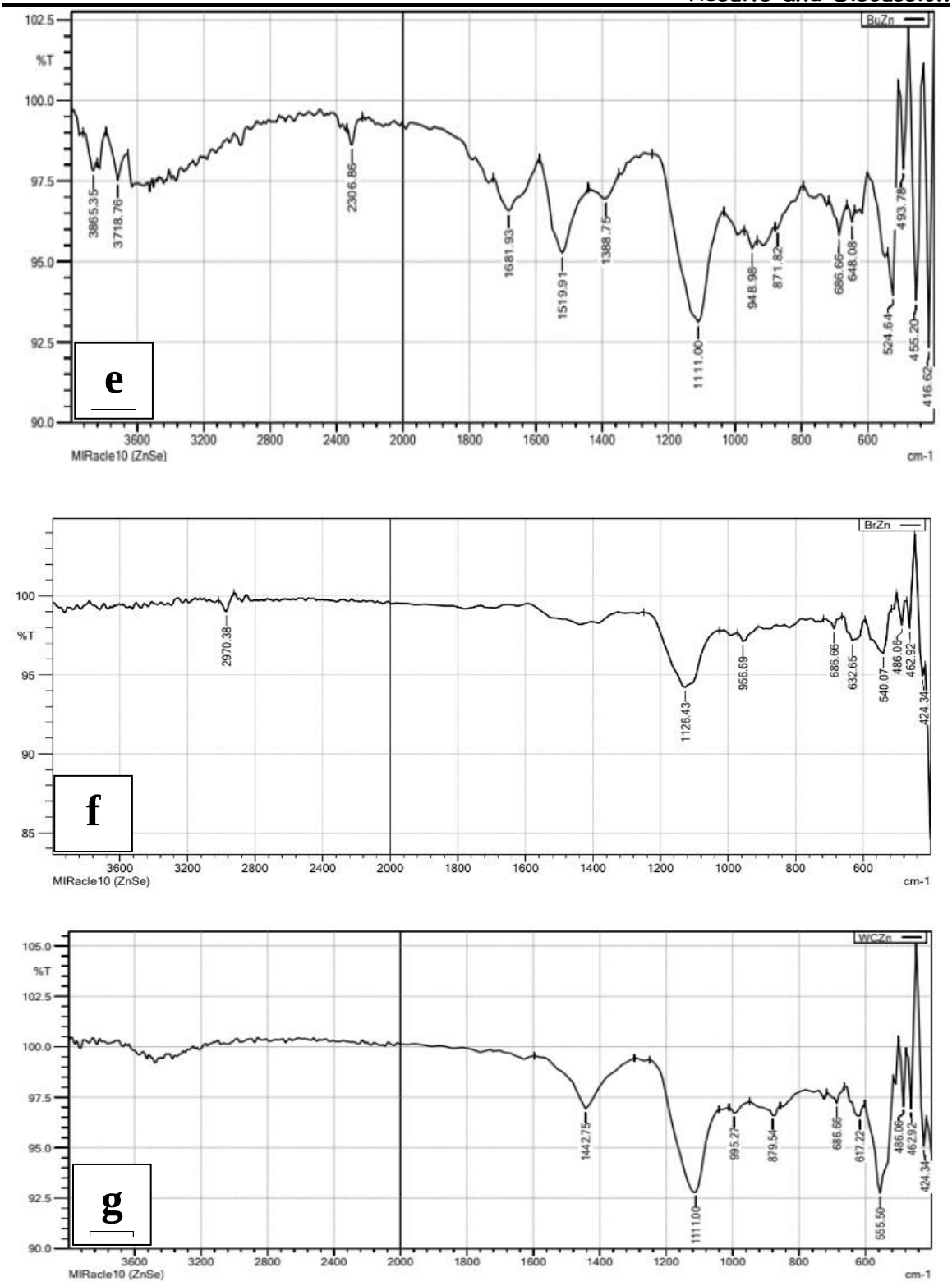

Figure 33. FT-IR spectra of ZnONPs (a) BoZn, (b) TDZn, (c) RRZn, (d) RaZn, (e) BuZn, (f) BrZn, and (g) WCZn

The other bands obtained in the spectra are assigned to the constituents of cereals and pulses. The fundamental mode of the hydroxyl alcohol group (O-H) vibrates at 3407 cm^{-1}, while the carboxylic acid group carbon (C-C) vibrates at 2173 cm^{-1}. Additionally, symmetric alkenes (C-C) vibrate at 1565 cm^{-1}, and the rocking structure of alkenes is at 1409 cm^{-1} (C-H). The C-O aromatic stretching occurs at 1081 cm^{-1}.

Characterization tools are especially utilized to differentiate ZnONPs based on their appearance, size, distribution, shape, morphology, specific surface area, and all parameters relevant to physicochemical property evaluation (**Lopez-Carrizales *et al.*, 2022**). Interpretation and linkage of chemical ingredients in the sample and absorption bands (vibrational bands) are essential for IR spectra (**Ogunyemi *et al.*, 2019; Poovizhi *et al.*, 2015**). **Alahmdi *et al.*, 2022** used FT-IR to detect the chemical composition of functional groups in green-synthesized ZnO-NPs and obtained peaks at 3455, 1640, 1400, 1070.1, 960, and 846 cm^{-1}. According to **Somu *et al.*, 2022**, the bands for ZnO at 448.6cm^{-1} were ascribed to ZnO stretching vibrations, and there were bands related to -C-O stretching (1026.6 cm^{-1}), hydroxyl groups (1358.2 cm^{-1}), and C-H stretching (2889.1 cm^{-1}).

The FT-IR results of all the synthesized ZnONPs shows Zn-O (str) peaks which is considered to be the characteristic of ZnONP which is reported in the previous reports. This ensures the formation of ZnONPs using cereals/pulses washed water as bioreductants.

4.6.2.4 FT-IR analysis of reduced graphene oxide

The FTIR spectra of GO and the synthesized RGO's using cereals and pulses washed water are given in **Figure 34**.

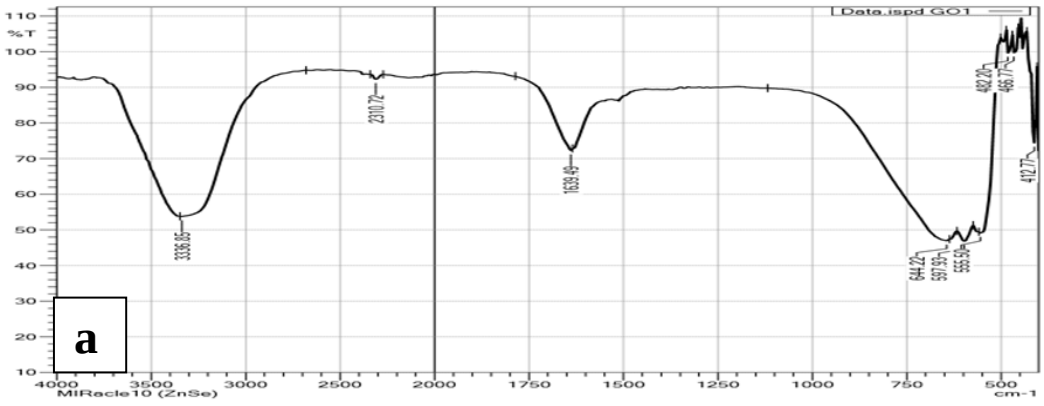

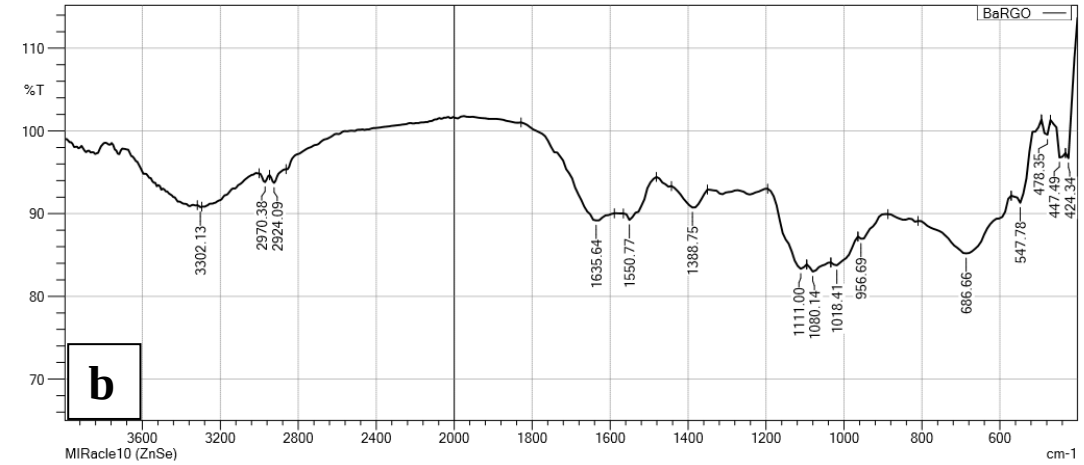
BaRGO
%T
3302.13
2970.38
2924.09
1635.64
1550.77
1388.75
1111.00
1080.14
1018.41
956.69
686.66
547.78
478.35
447.49
424.34
b
MIRacle10 (ZnSe)
cm-1

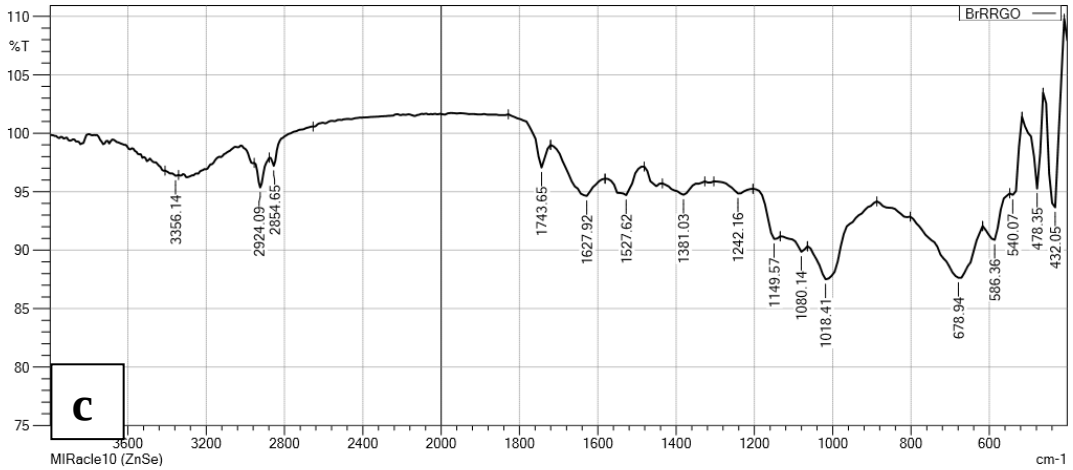
BrRRGO
%T
3356.14
2924.09
2854.65
1743.65
1627.92
1527.62
1381.03
1242.16
1149.57
1080.14
1018.41
678.94
586.36
540.07
478.35
432.05
c
MIRacle10 (ZnSe)
cm-1

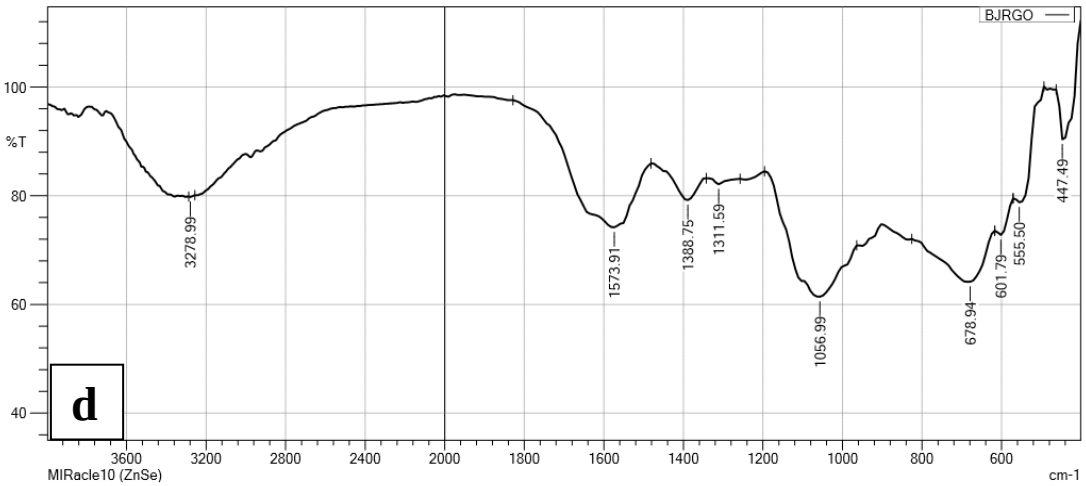
BJRGO
%T
3278.99
1573.91
1388.75
1311.59
1056.99
678.94
601.79
555.50
447.49
d
MIRacle10 (ZnSe)
cm-1

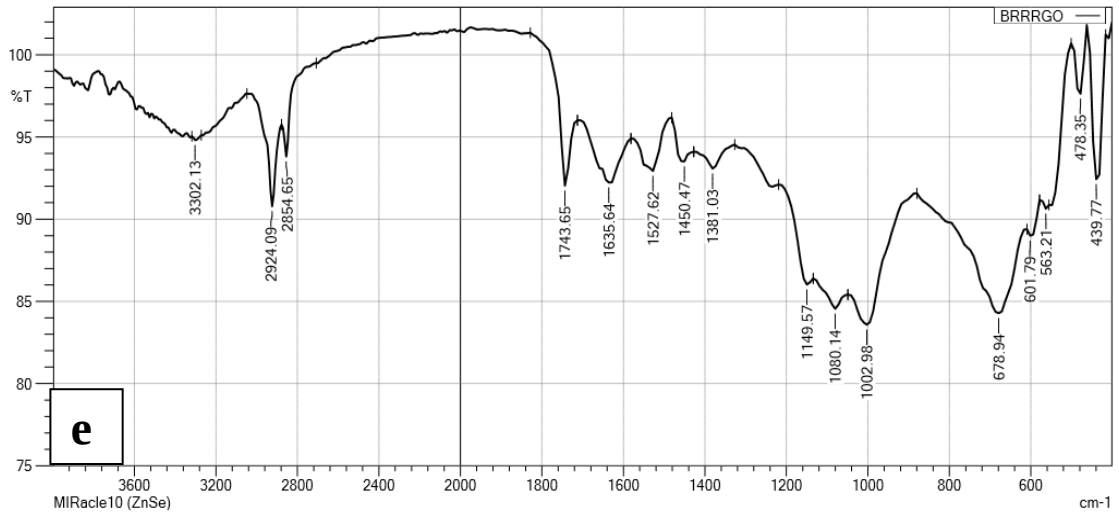
BRRRGO
%T
100
95
90
85
80
75
3302.13
2924.09
2854.65
1743.65
1635.64
1527.62
1450.47
1381.03
1149.57
1080.14
1002.98
678.94
601.79
563.21
478.35
439.77
e
3600
3200
2800
2400
2000
1800
1600
1400
1200
1000
800
600
MIRacle10 (ZnSe)
cm-1

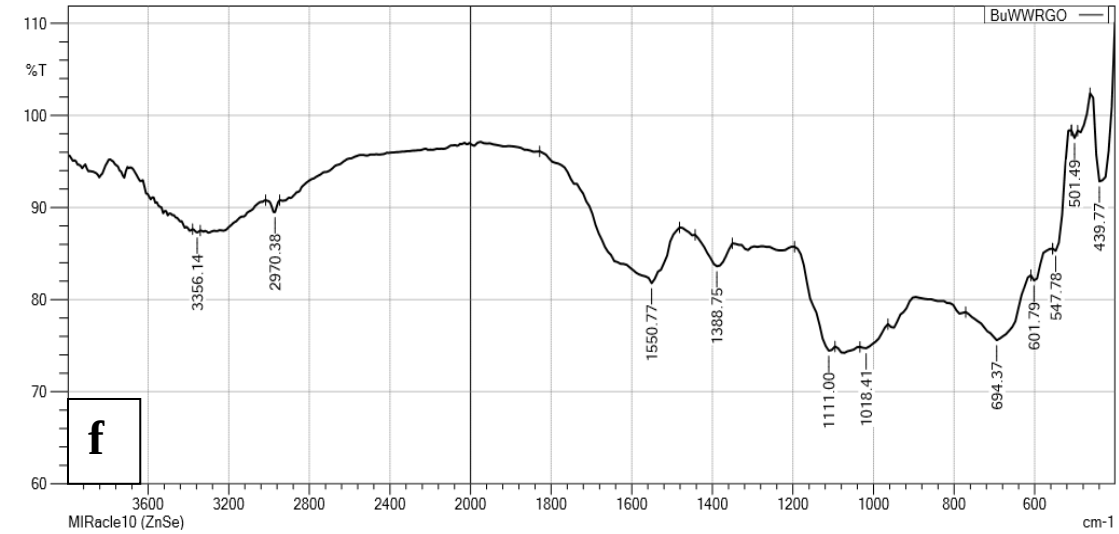
BuWWRGO
%T
110
100
90
80
70
60
3356.14
2970.38
1550.77
1388.75
1111.00
1018.41
694.37
601.79
547.78
501.49
439.77
f
3600
3200
2800
2400
2000
1800
1600
1400
1200
1000
800
600
MIRacle10 (ZnSe)
cm-1

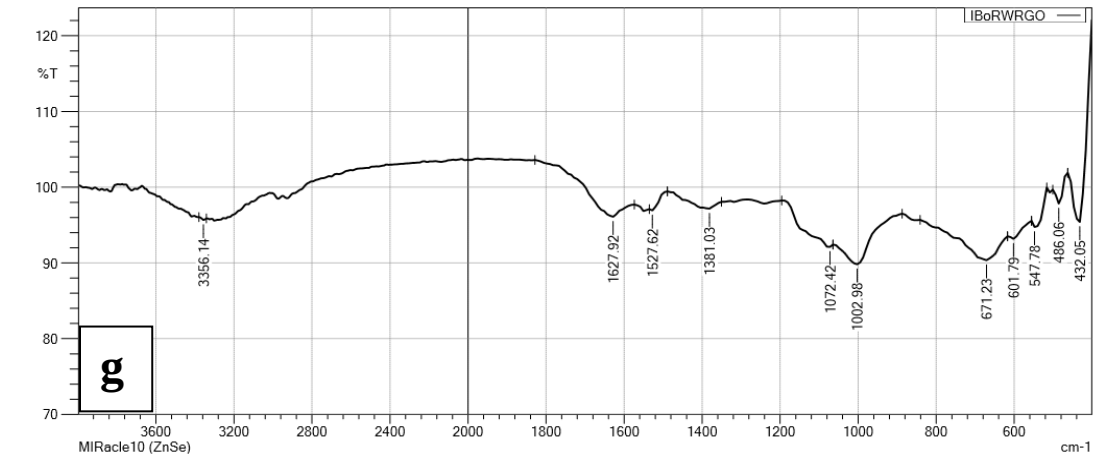
IBoRWRGO
%T
120
110
100
90
80
70
3356.14
1627.92
1527.62
1381.03
1072.42
1002.98
671.23
601.79
547.78
486.06
432.05
g
3600
3200
2800
2400
2000
1800
1600
1400
1200
1000
800
600
MIRacle10 (ZnSe)
cm-1

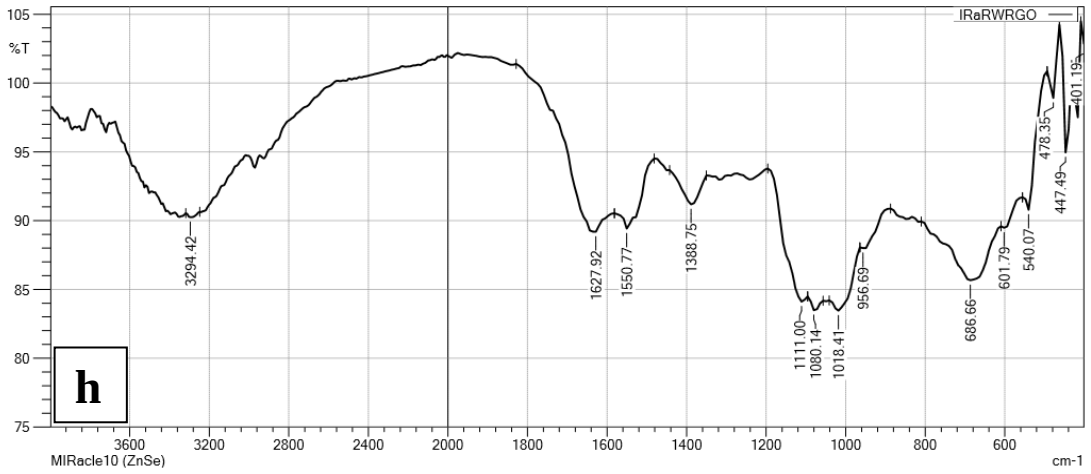
IRaRWRGO
%T
105
100
95
90
85
80
75
3294.42
1627.92
1550.77
1388.75
1111.00
1080.14
1018.41
956.69
686.66
601.79
540.07
478.35
447.49
401.19
h
3600
3200
2800
2400
2000
1800
1600
1400
1200
1000
800
600
MIRacle10 (ZnSe)
cm-1

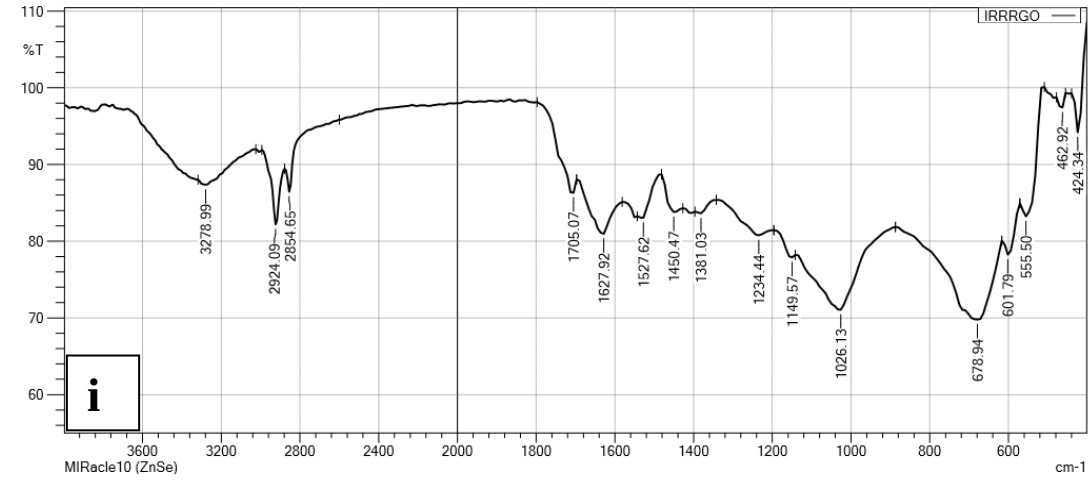
IRRRGO
%T
110
100
90
80
70
60
3278.99
2924.09
2854.65
1705.07
1627.92
1527.62
1450.47
1381.03
1234.44
1149.57
1026.13
678.94
601.79
555.50
462.92
424.34
i
3600
3200
2800
2400
2000
1800
1600
1400
1200
1000
800
600
MIRacle10 (ZnSe)
cm-1

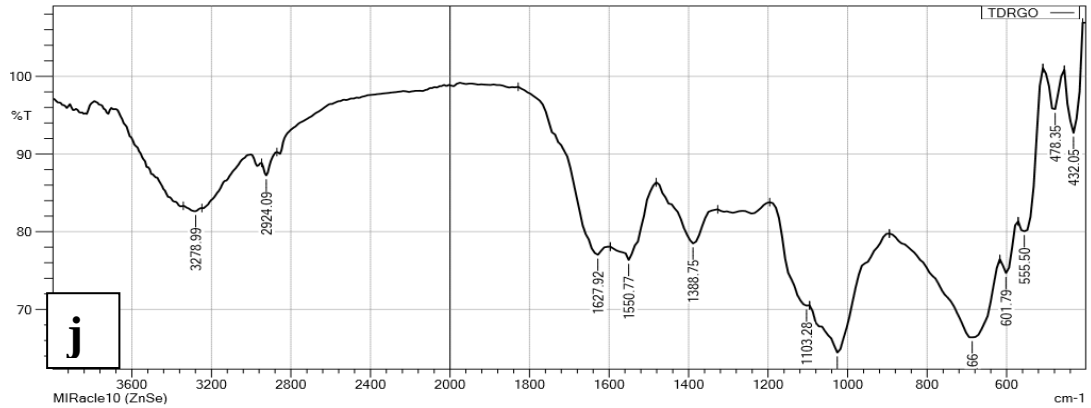
TDRGO
%T
100
90
80
70
3278.99
2924.09
1627.92
1550.77
1388.75
1103.28
601.79
555.50
478.35
432.05
j
3600
3200
2800
2400
2000
1800
1600
1400
1200
1000
800
600
MIRacle10 (ZnSe)
cm-1

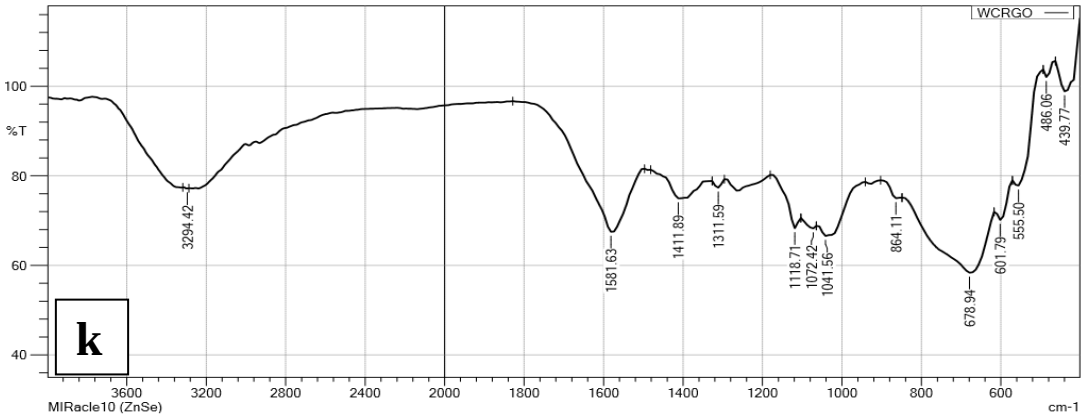

Figure 34: FTIR spectra of (a)GO, (b) IBaRGO, (c) IBrRWRGO, (d) BJRGO, (e) IBRRWRGO, (f) BuWWRGO, (g) IBoRWRGO (h) IRaRWRGO, (i) IRRGO, (j) TDRGO, (k) WCRGO

From the FT-IR spectra, the characteristic GO peaks are observed at 1054.10 and 1315.99 cm^{-1} are assigned to the C–O stretching vibration and C–O–H deformation vibration, respectively. The peaks at 1627.10 and 3430.85 cm^{-1} correspond to the stretching vibrations of C=O and hydroxyl groups, respectively (**Hosseini *et al.*, 2016**). The GO powder varies from that of GO dispersed in water. As a result the characteristic stretching and bending vibrations vary depending on the H_2O molecules absorbed on GO. This might be the reason for disappearance of certain peaks in the GO.

The C=O peak in GO is observed at 1639 cm^{-1}. The disappearance of the peak ensures the formation of the RGO. In the synthesized RGO's the shift in the peak or addition of another peak is observed. Additionally, the peaks observed at 1619 and 1400 cm^{-1} were identified as the C-C stretching mode of non-oxidized graphitic domains and the deformation vibration of tertiary C-OH groups, respectively. Moreover, the peaks at 1224 cm^{-1} were associated with the stretching vibrations of C-O-C and C-O at 1063 cm^{-1}. According to **Esfandiar *et al.*, 2011**, a decrease in the intensity of peaks in RGO compared to GO suggests that oxygen-containing functional groups have been removed. This trend is observed in all RGOs. Specifically, the peak at 3336.71 cm^{-1}, which indicates graphite oxidation, is more prominent in GO but significantly reduced in RGOs, indicating the conversion from GO to RGO. The decrease in the peak at 3336.71 cm^{-1} is particularly noticeable in RGOs.

The FT-IR spectra of GO that was reduced by hydrazine, ascorbic acid, and *Amaranthus hybridus* extract exhibit a comparable pattern (**Faniyi *et al.*, 2019**).

Thus the FT-IR spectra of the synthesized RGO samples reveal the formation of RGO as the spectra is distinct from that of GO. The further morphology, stability and distribution of the synthesized RGOs can be determined by further characterization techniques.

4.6.3 XRD analysis of nanoparticles

4.6.3.1 XRD analysis of GNPs

XRD is utilized for identifying the crystalline structure, phase nature, lattice parameters, and crystalline grain size. The XRD pattern of the GNPs synthesized from aqueous TB fruit extracts are clearly depicted in **Figure 35**. The face centred cubic lattice of TBOSGNP, TBISGNP, TBSGNP, and TBPGNP is unequivocally represented by 2θ of 27°, 27°, 28°, and 27°. The Debye-Scherrer's equation was used to calculate the crystallite size of the NPs (**Table 25**). Based on the significant diffraction observed at 28.1, it appears that zero-valent gold has grown preferentially in the (111) direction. This refers to the formation of solid particles at the molecular scale with a 3D arrangement of atoms or molecules that are evenly spaced.

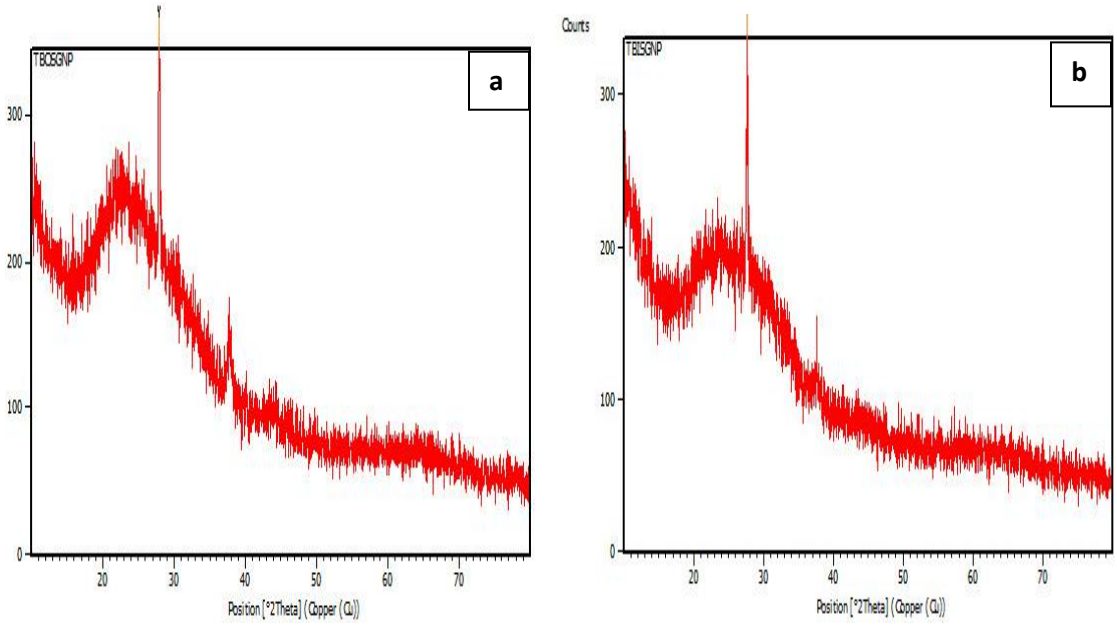

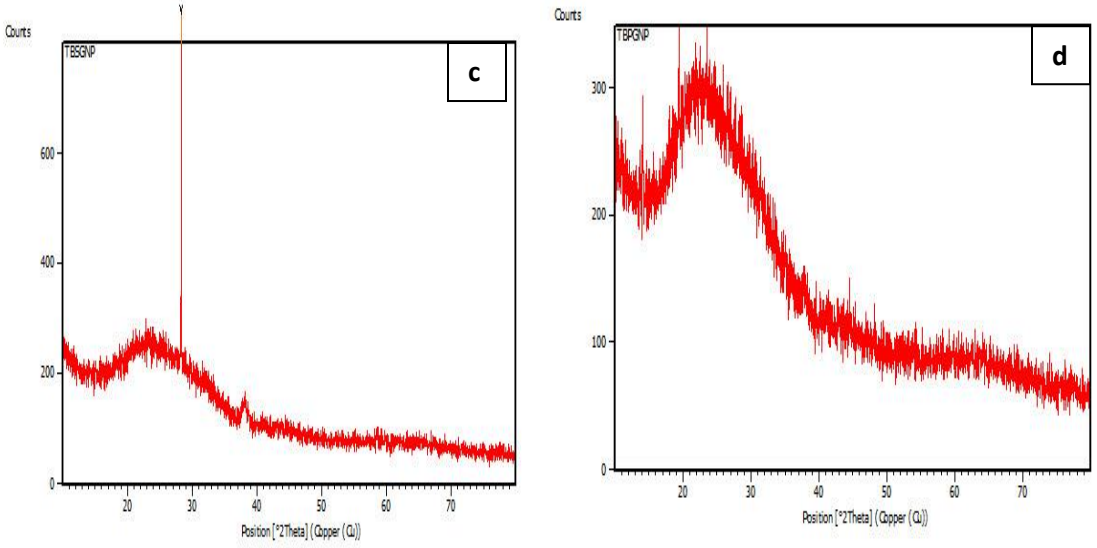

Figure 35. XRD patterns of TB aided GNPS (a) TBOSGNP (b) TBISGNP (c) TBSGNP and (d) TBPGNP

(X-axis : 2theta (deg); Y-axis : Intensity (counts))

Table 25. Calculated crystallite size of the synthesized TB aided GNP

Sample code of GNPs	2θ (degree)	Cos θ	β= FWHM	D=kλ/β Cos θ (nm)
TBOSGNP	27.8841	0.9705	0.0049	27.00
TBISGNP	27.6130	0.9711	0.0056	23.50
TBSGNP	28.2747	0.9697	0.0010	12.60
TBPGNP	27.8314	0.9706	0.0052	25.38

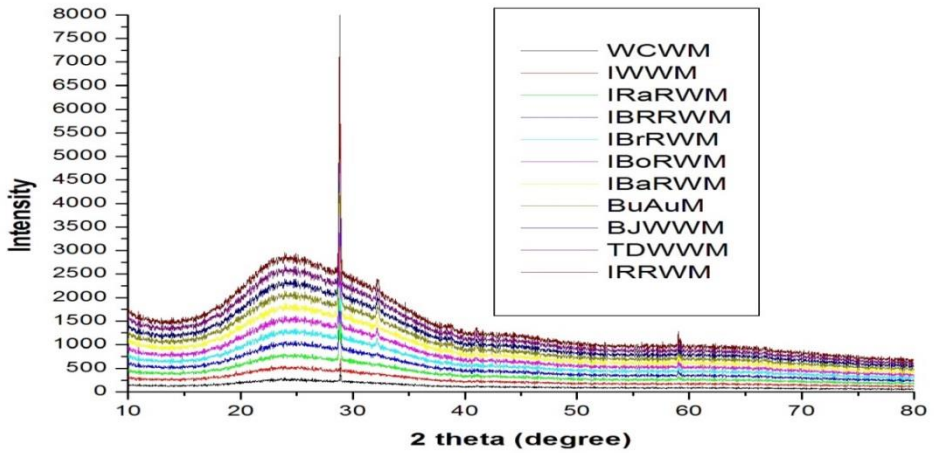

Figure 36. XRD pattern of the cereals and pulses washed water aided GNPs

Similar diffraction patterns were observed for the synthesized NP from cereals and pulses washed water (**Figure 36**). The purity and crystalline quality of GNPs may be validated using XRD, which provides an approximate estimate of particle size using the Debye-Scherer equation (**ullah *et al.*, 2017**). The XRD pattern observed in the present study aligns pure Au nanocrystals reported earlier which matches ICDD PDF card number 00-004-0784 (**Doan *et al.*, 2020**; **Krishnamurthy *et al.*, 2010**).

From the XRD patterns of the synthesized GNP, the crystalline nature is determined. It is also noted that there is no noise in the pattern; this implies the particles are pure.

4.6.3.2 XRD analysis of Silver nanoparticles

The morphology of the synthesized samples was initially analyzed by XRD patterns. XRD results revealed the crystalline characteristics of the synthesized SNPs (**Figure 37**). The absence of AgO_2, Ag_3O_4 peaks in the XRD pattern, implies high purity of synthesized NPs. Strong diffraction peaks are observed for the synthesized SNPs. Diffraction peak at an angle of 2Ɵ 32.3 strongly correlates with diffraction peaks of SNPs synthesized from other plant sources **(Khalil *et al.*, 2014; Shanmugam *et al.*, 2022)**. The average crystallite size (**Table 26**) of the samples was calculated from the 2θ value **(Patil *et al.*, 2017)**. The lesser crystallite size for TBPSNP implies that the SNP is of small size compared to the other synthesized samples. This might be due to the efficient bioreduction compared to the other TB fruit parts extracts. Also in the XRD pattern of TBPSNP, peak broadening can be observed, which further clarifies the size of the crystallites falls in nanometer scale.

Table 26. Calculated average crystallite size of the synthesized TB aided SNP

Sample Code	2θ	FWHM	D(nm)	Mean D (nm)
TBOSSNP	27.977	0.0669	2.230826	1.4880 = 1.48
TBOSSNP	29.0094	0.2007	0.745312	
TBISSNP	27.9133	0.0502	2.972543	2.2380 = 2.23
TBISSNP	32.7803	0.1004	1.503493	
TBSSNP	27.9062	0.1224	1.219112	1.219112 = 1.21
TBPSNP	21.5128	0.9792	0.150538	0.150538 = 0.15

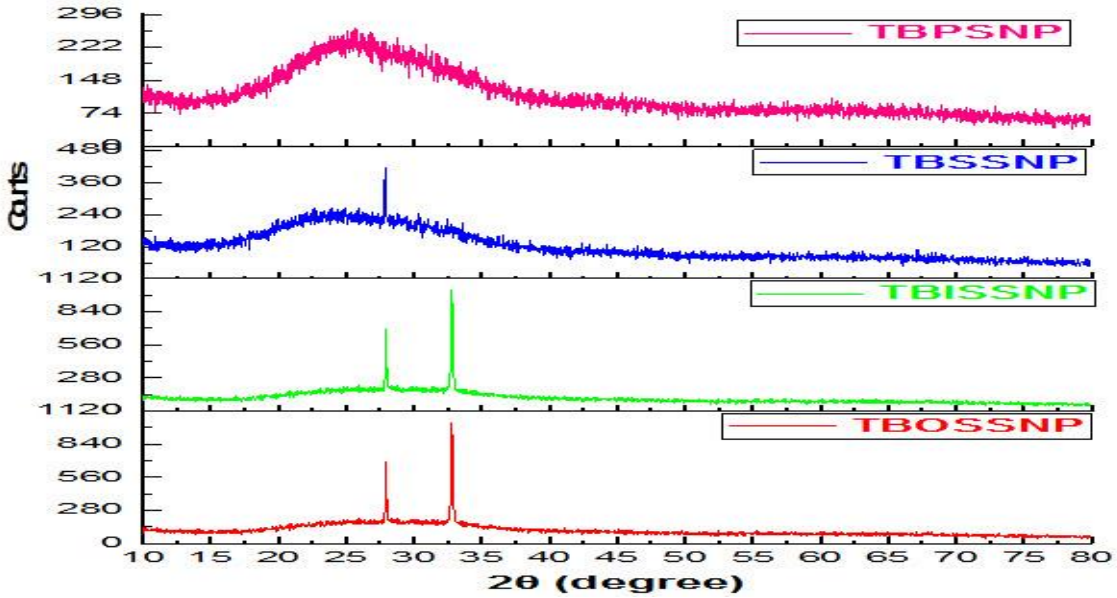

Figure 37. XRD pattern of synthesized SNP from TB fruit parts

(X-axis : 2theta (deg); Y-axis : Intensity (counts))

Similar to TB aided SNPs, cereals and pulses washed water aided SNPs show significant peaks at 27.9^{o}. The weaker peak at 32.7 ^{o} might be due to the organic moieties in the cereals and pulses washed water (**Figure 38**).

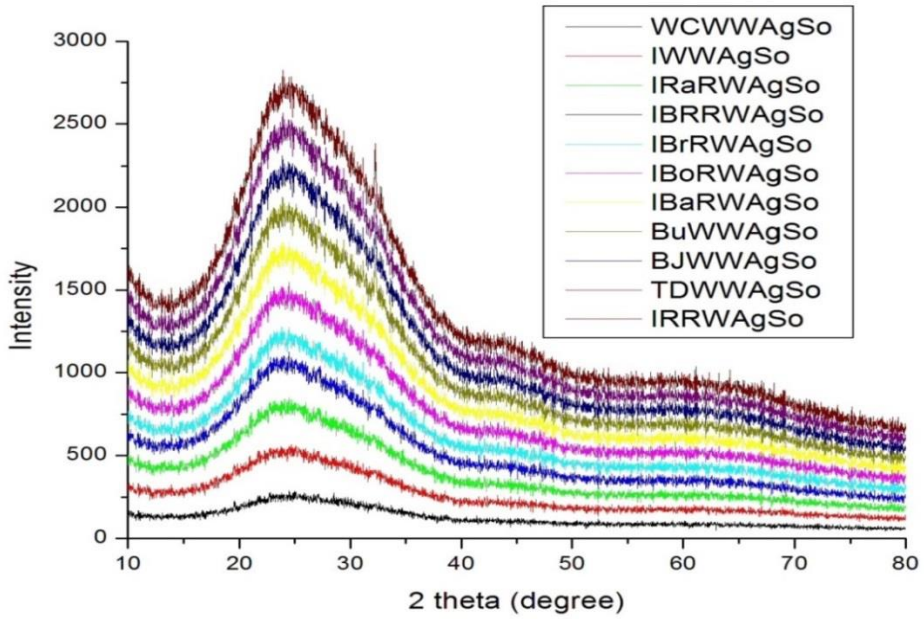

Figure 38. XRD pattern of synthesized SNP from cereals and pulses washed water

(X-axis : 2theta (deg); Y-axis : Intensity (counts))

Kumar and Yadav 2009 ; Jeeva *et al.,* 2014 found crystalline peaks (32.28°, 46.28°, 54.83°, 67.47°, and 76.69°) that were also visible in several other studies where the XRD pattern encompassed the required 2° range and it matches with ICDD file no: 04-0783 (**Dhar *et al.,* 2021**). The stronger planes imply that silver is an important component in biosynthesis. Apart from instrumental peak broadening, the main cause of peak broadening in XRD is the size of particles/crystallites and lattice tensions. The Scherrer equation is employed to determine the latter parameter, along with the broadening of the most intense peak from the XRD data of a particular sample (**Mourdikoudis *et al*., 2018**).

From the XRD patterns of synthesized SNPs, the crystalline nature of the NPs was observed. However the shape and size related morphological characteristics can determine the suitable applications of NPs.

4.6.3.3 XRD analysis of ZnONPs

The XRD is a significant analytical tool for the characterization of ZnONPs. It is a non-destructive technique which determines the crystallinity of the ZnONPs. Diffraction occurs when the waves interact with the regular structure of the samples repeat distance is about the same as that of the wavelength. Among the eleven cereals/pulses washed water aided samples, only six representative samples were taken for XRD analysis.

From the XRD pattern of the synthesized ZnONPs (**Figure 39**) it can be generalized that, the particles are crystalline in nature. Furthermore, the absence of other distinctive XRD peaks other than ZnO peaks suggests that the synthesized NPs were devoid of contaminants. The broad peak at 31^0 and 36^0 indicates the nano crystalline nature of the NPs. The green synthesized ZnONP matches with ICDD number #98-002-9272 (**Sugihartono *et al.,* 2018**).

A distinct line widening of the XRD peaks suggests that the produced material contains nanoscale particles. The calculated peak intensity, position, and width, as well as full-width at half-maximum (FWHM) data, using the XRD pattern analysis with diffraction peaks at 31.84°, 34.52°, 36.33°, 47.63°, 56.71°, 62.96°, 68.13°, and 69.18° are reported for the hexagonal wurtzite phases of ZnO (**Zhou *et al.,* 2007; Khoshhesab *et al.,* 2011**).

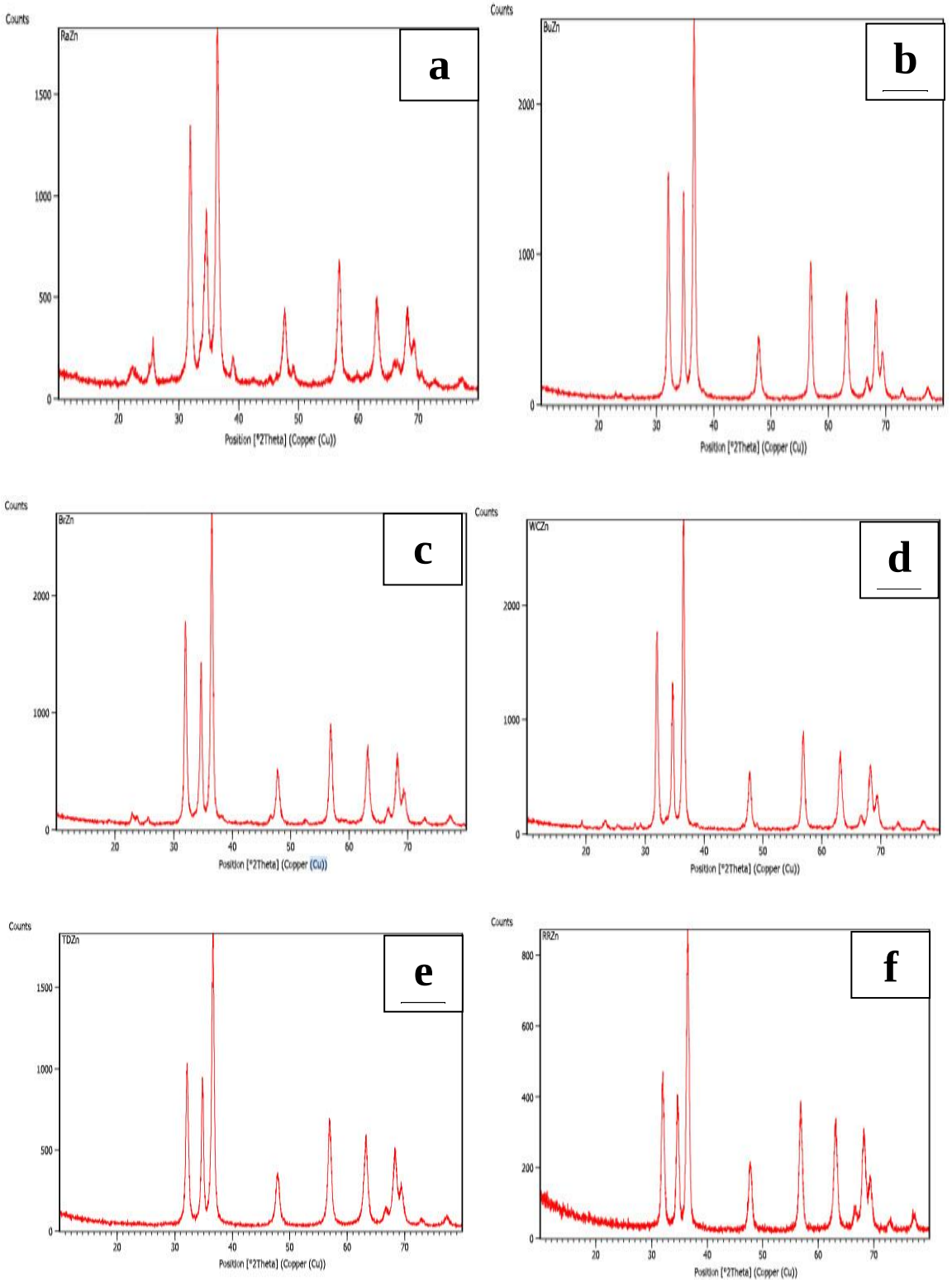

Figure 39. XRD pattern of ZnONPs (a) RaZn, (b)BuZn, (c)BrZn, (d)WCZn, (e)TDZn and (f)RRZn

(X-axis : 2theta (deg); Y-axis : Intensity (counts))

Thus from the XRD pattern of synthesized ZnONPs it is observed that the particles are crystalline in nature. The noise free XRD pattern also implies the purity of the samples. Further characterization studies can help to better understand the morphology (shape and size) of the particles.

4.6.3.4 XRD analysis of reduced graphene oxide

The structural changes in the GO upon reduction by cereals and pulses washed water was determined by XRD analysis (**Figure 40**). A weak diffraction peak near 10.5°, and prominent peaks at 25° and 45 ° are observed in GO. These peaks in GO are due to the layered structure with oxygen containing functional groups in GO. The absence of these peaks upon reduction of GO ensures the formation of RGO (**Jiao *et al.*, 2017**).

Except BJRGO, BuRGO and WCRGO all other samples shows a broad peak near 22° which generalizes that the samples are amorphous in nature and different from GO. This shows the successful reduction of GO by the constituents in the cereals and pulses washed water. BuRGO and WCRGO peaks show crystallinity in the XRD peak. This shows that the GO crystallinity is restored after the reduction process. The peak at around 2θ = 43° due to the slipping out of the alignments of crystal structure from basal planes.

Similar XRD pattern is reported for the RGO synthesized using lemon juice (**Mahiuddin, and Ochiai, 2021**) and *Vernonia amygdalina* extract (**Chufa *et al.*, 2021**).

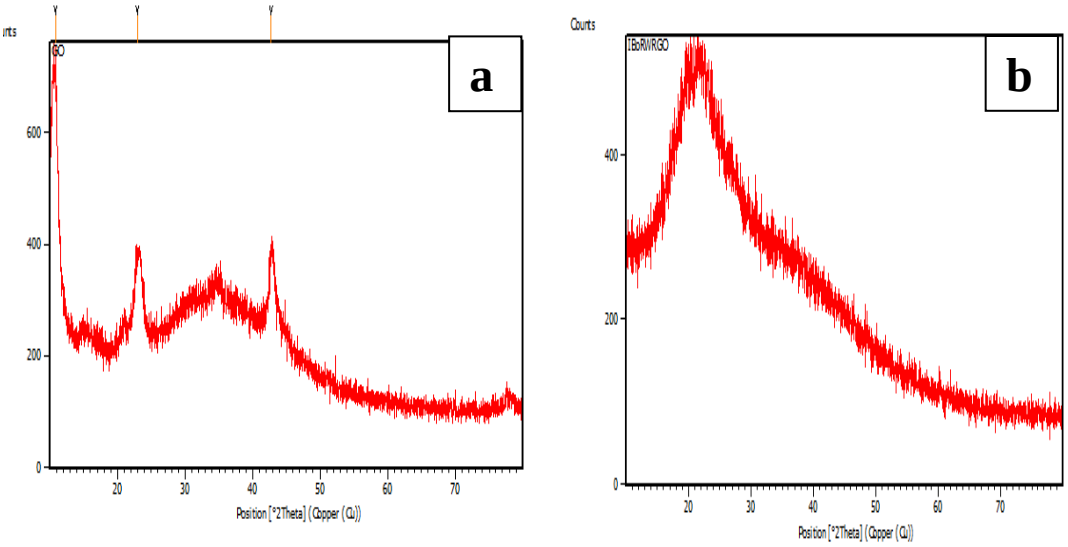

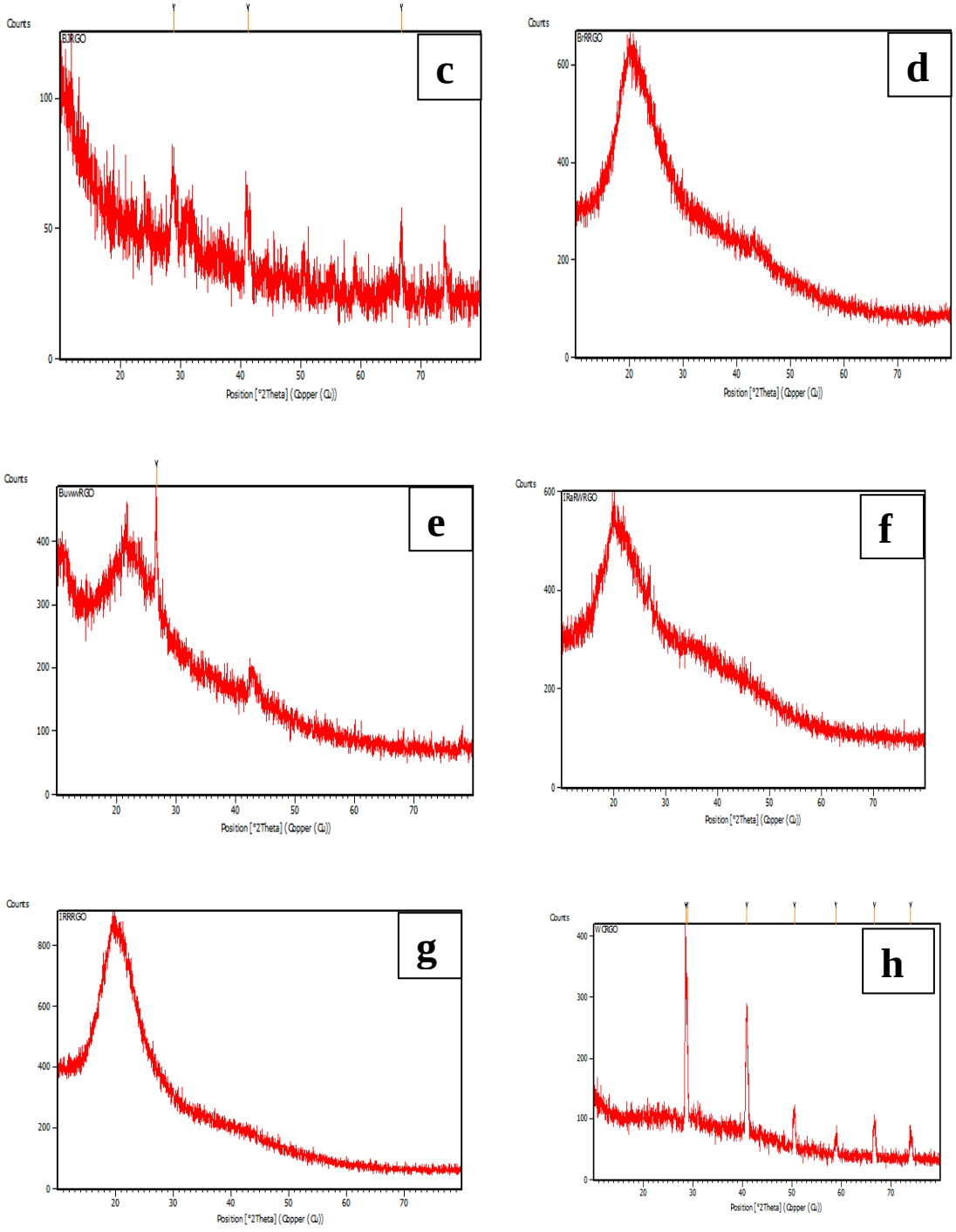

Figure 40. XRD pattern of (a) GO, (b) IBoRWRGO, (c) BJRGO, (d) IBrRWRGO, (e)BuWWRGO, (f)IRaRWRGO, (g)IRRRGO, (h)WCRGO

(X-axis : 2theta (deg); Y-axis : Intensity (counts))

Thus from the XRD pattern of synthesized RGO shows that the formation of RGO (as peaks are different from GO). Further characterization techniques can help to understand the defective sites and morphology of the RGO.

4.6.4 Zeta potential analysis of GNP and SNP

In this study, the stability of the synthesized GNPs and SNPs are determined by the zeta potential analysis. There are no reports on the usage of cereals/pulses washed water aided GNPs/SNPs for biological applications. One of the objectives of the presents study is anti-bacterial and anti-cancer applications of synthesized GNPs/SNPs. Only stable particles can be administered as drug. Thus it is essential to determine the stability of GNP and SNP synthesized using cereals/pulses washed water. Representative samples which show visual stability were chosen for zeta analysis.

It was observed that SNP obtained by solar method and gold nanoparticles by microwave method were comparatively visually stable and hence chosen as representative sample for recording zeta potential. The synthesized ZnONPs and RGOs were visually stable; hence the thermal stability by TGA was carried out for those samples.

The zeta-potentials of NPs are relatively easy to measure and have frequently been promoted as a particle property that must be included in guideline documents for full NP characterization. The goal is to identify the specific properties that affect the outcomes and effects of nanomaterials, to integrate and reuse datasets for multiple purposes, and ultimately, to predict the behaviour of new nanomaterials based on their known properties, including zeta-potential. Several complicating factors challenge the integration and interpretation of this measurement **(Lowry, 2016)**.

The size of the zeta-potential has long been used to predict dispersion stability in the area of aggregation or deposition. Values of zeta-potential greater than ±30 mV were previously thought to be relatively stable against aggregation due to charge stabilization, implying that the electrostatic repulsive forces are strong enough to avoid aggregation. Zeta-potential is highly influenced by particle parameters (e.g. charge density) and solution properties (e.g. ionic strength and composition). Many nanomaterials, such as metal oxides and functionalized carbons, feature surface sites or functional groups that, when distributed in

water, can become positively or negatively charged. The amount and sign of this charge are frequently affected by the pH of a liquid **(Mourdikoudis *et al.*, 2018**).

The synthesized NPs, in the present study show a negative value for zeta potential. This shows that negative charges are distributed around the particles (**Table 27**). From the zeta potential value, among the samples, the order of stability is:

BJWWAgSo< WCWWAgSo< IRaRWAgSo< WCWWM= BJWWM< IBRRWM

Table 27. Zeta potential of GNP and SNP synthesized from cereals and pulses washed water

Sample Code	Zeta potential (mV)
WCWWAgSo	-17.3
WCWWM	-24.1
IRaRWAgSo	-19.5
BJWWAgSo	-5.50
BJWWM	-24.1
IBRRWM	-24.5

From the zeta analysis, it was observed that compared to SNPs, GNPs samples are stable (**Figure 41**). From the graph it is understood that the count of negatively charged particles are comparatively higher than in the SNP samples. This might be the reason for the stability of GNPs. In two GNP samples IBRRWM and WCWWM, two peaks are observed (**Figure 41c & 41f**).

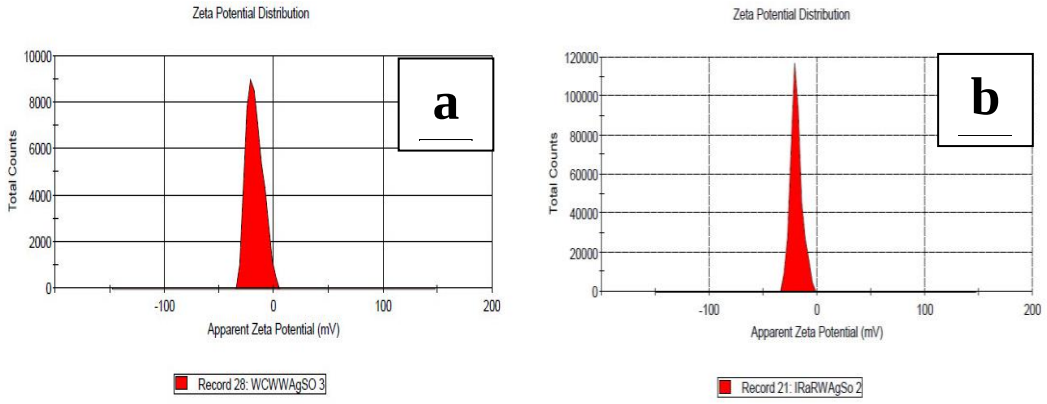

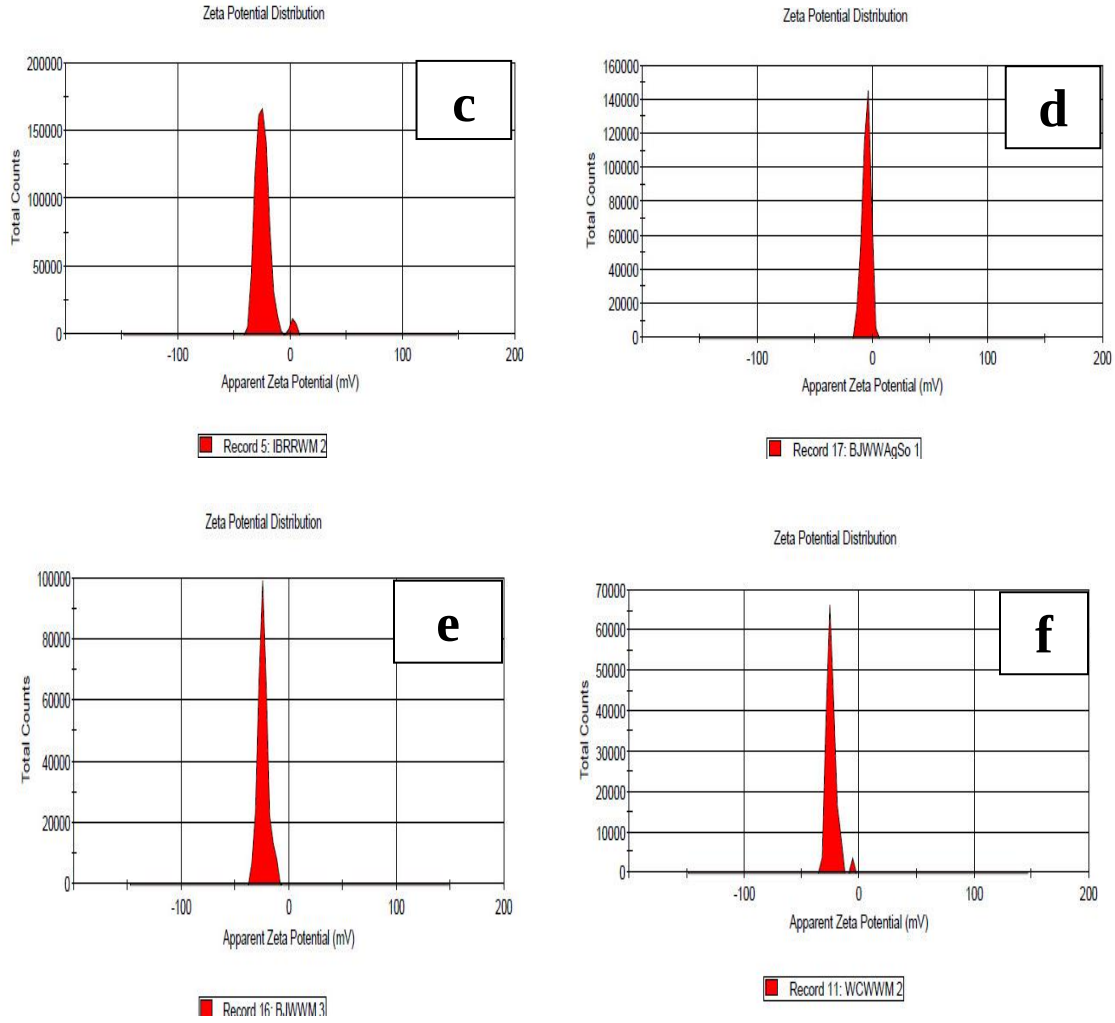

Figure 41. Zeta potential distribution of NPs (a)WCWWAgSo, (b)IRaRWAgSo, (c)IBRRWM, (d)BJWWAgSo, (e)BJWWM and (f)WCWWM

The might be due to the distribution of two different size of particles. In both IBRRWM and WCWWM the small peak have zeta potential nearing to 0 mV, this shows the instability of the particles. It is also observed that in IBRRWM and WCWWM the highest peak has more area of particles compared to small particles. This is the first report on cereals/pulses washed water stabilized GNPs and SNPs.

Thus from the zeta potential values it is observed that compared to SNPs, GNPs are more stable. It is also established that negatively charged particles surround and stabilize the synthesized nanoparticles.

4.6.5 FE-SEM analysis of nanoparticles

4.6.5.1 FE-SEM analysis of GNP

FE-SEM examines the surface morphology and topography; FESEM of TB-mediated GNP (**Figure 42**) also gives the size of NPs. TBOSGNP presents densely packed spherical NPs ranging from 13nm to 25nm in size. We also recorded the data at 30 kV to ensure the stability of the NPs under electrical potential. This suggests that the NPs are stable and do not contain any additional elements at higher kV (as seen in **Figure 42a**). During the sputtering process, any contaminants in the plant residue would have been eliminated.

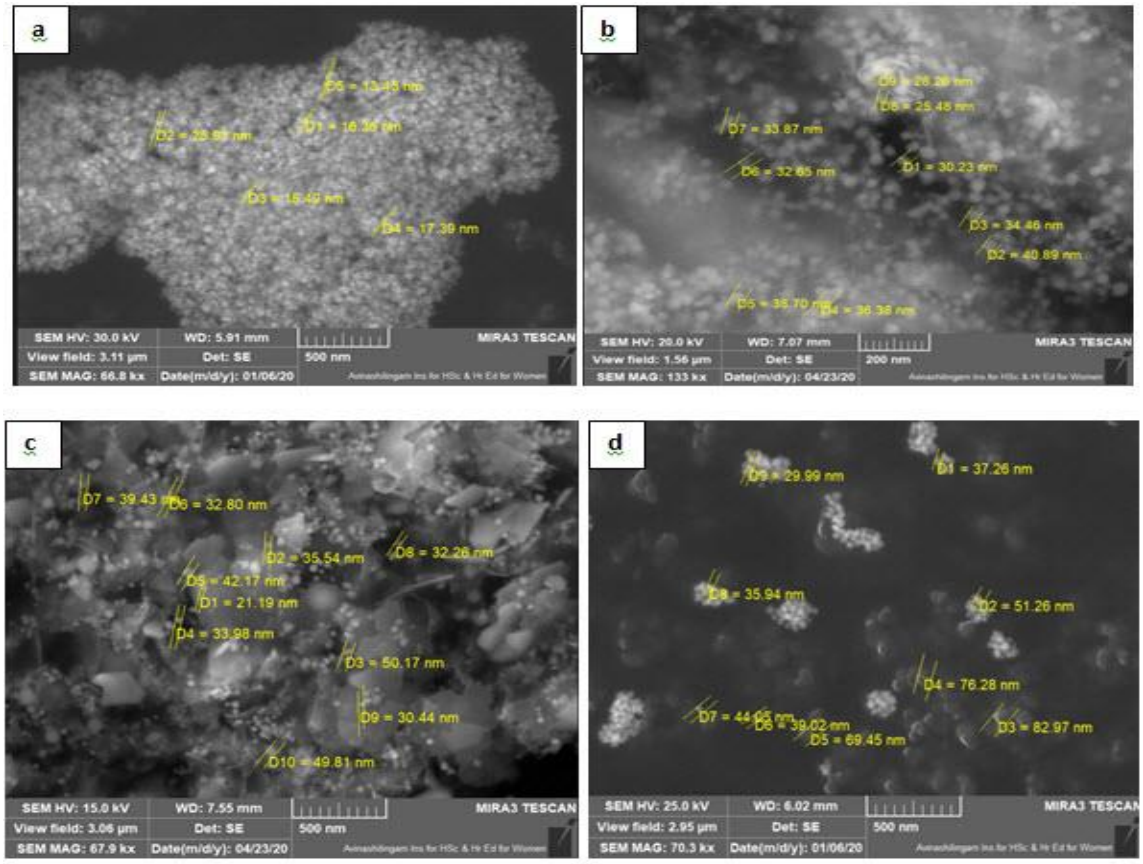

Figure 42. FE-SEM monographs of (a) TBOSGNP (b) TBISGNP (c) TBSGNP and (d) TBPGNP

The particles of TBISGNP have a spherical shape and range in size from 25nm to 40nm. They are capable of withstanding a voltage of 20 kV. Compared to TBOSGNP, TBISGNP has more scattered spherical and hexagonal particles, as shown in **Figure 42b**. TBSGNP, on the other hand, contains a variety of particle shapes such as flakes, triangular,

and spherical NPs. However, these particles are less stable than other GNPs as they can barely sustain 15kV electrical potential. The size of the TBSGNP particles range from 21nm to 49nm (**Figure 42c)**. In the TBPGNP monograph, **Figure 42d** displays perfectly aligned nano balls, which is the ***first report on the nano ball structure*** of gold nanoparticles mediated by TB entire fruit. These nano balls range in size from 29nm to 89nm and can tolerate a 25kV electrical potential, indicating their stability. The efficacy of GNP as possible medicinal agents is demonstrated by the spherical forms of the TB fruit sections mediated GNPs as reported in our published paper (**Chithambharan *et al.*, 2021**).

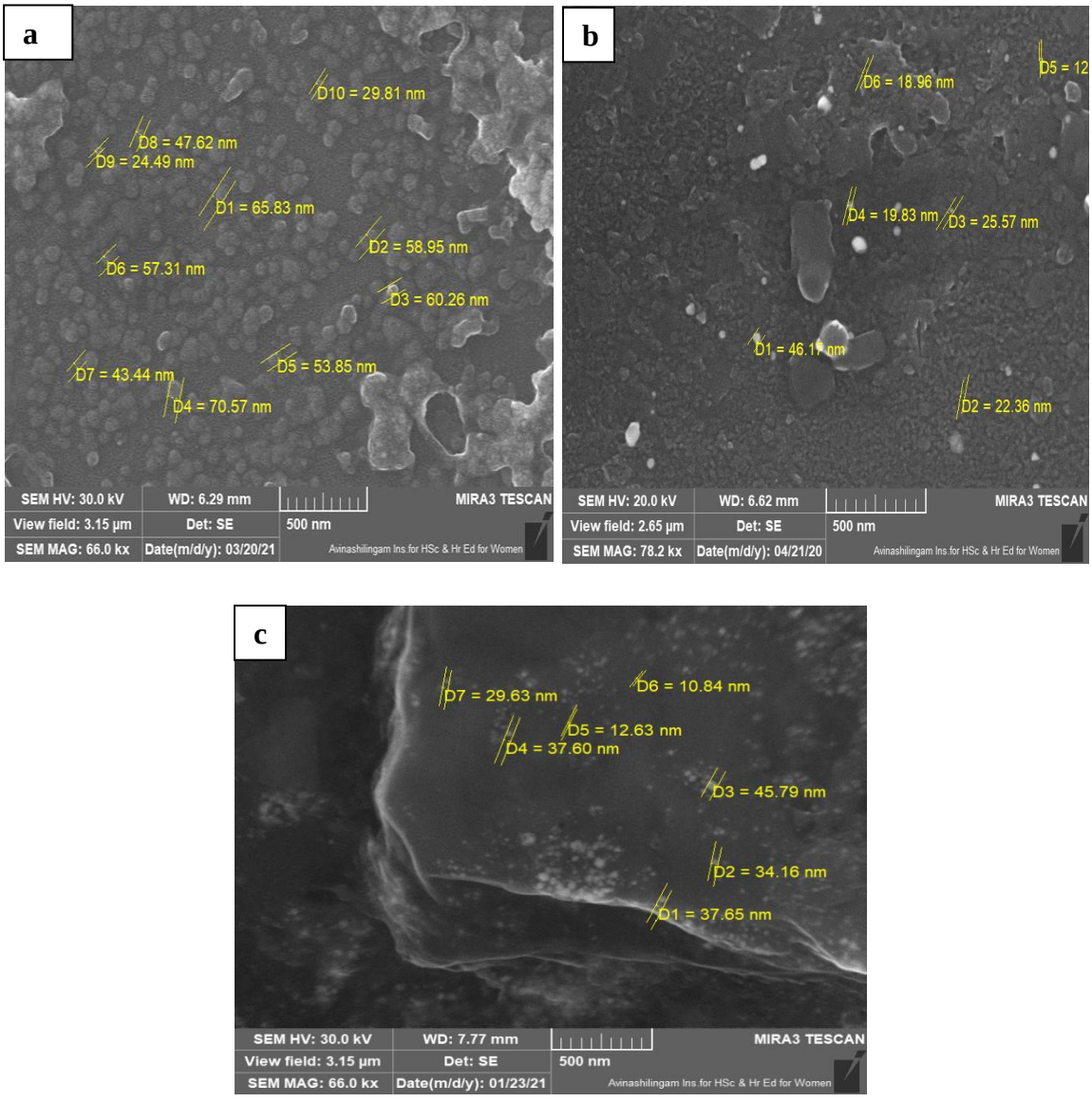

Figure 43: FESEM monographs of (a) IBrRWM, (b) IRRWM, (c) IRaRWM

As the usage of the word 'images' shows similarity index, the word monograph has been used in this thesis to indicate FE-SEM images. Also, as gold sputtering is done, EDS results are not shown here to avoid discrepancy in the sputtered gold and the synthesized gold NPs.

The FE-SEM monographs of GNP synthesized from broken red rice, red rice and raw rice also shows spherical shaped NPs (**Figure 43**). The FE-SEM monographs show the secondary electron interaction on the sample. It is always necessary to understand about the size and shape of NP as they have much importance in applications. So it is always necessary to follow an accurate surface analysis technique before planning for an application. These surface sensitive analytic approaches can be used in two distinct modes. For example, in many cases, merely recognizing the presence or absence of pollutants or confirming the chemical state of elements present in the nanomaterial is extremely beneficial. Such applications predominate in the literature, and their significance cannot be overstated (**Baer *et al.*, 2013**).

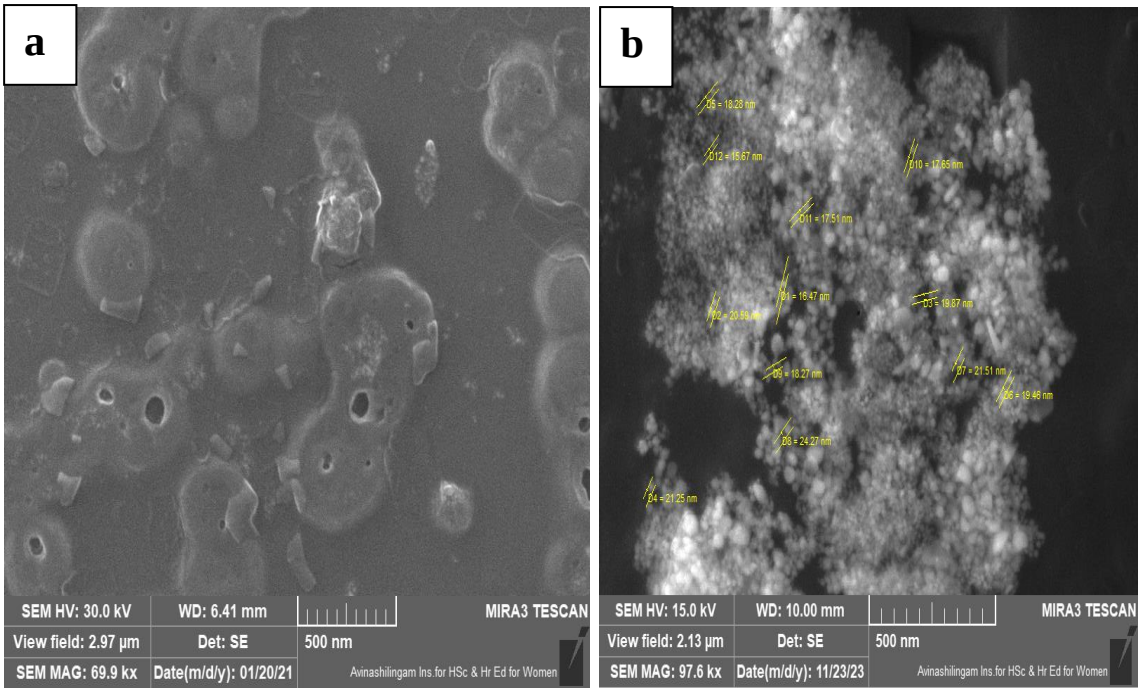

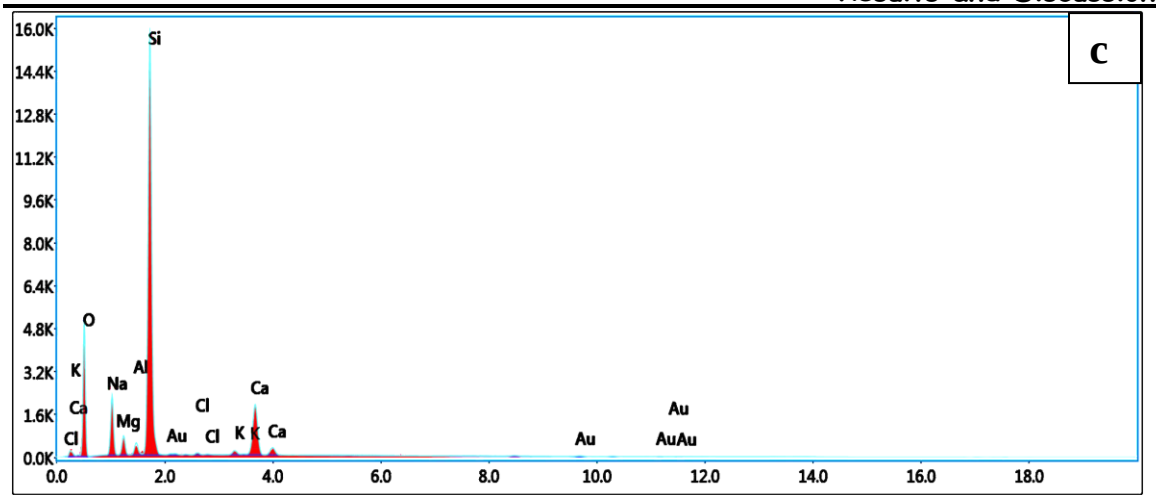

Figure 44. FE-SEM monograph of (a) GCAu, (b) HN28Au and (c) EDS of GCAu

Like TB and cereals and pulses washed water aided GNPs, the FE-SEM monograph (**Figure 44**) of GCAu and HN28Au shows spherical particles. From the EDS spectrum presence of Au confirms the formation of GNPs. Earlier reports on EDS of GCAu indicate the presence of Au, Ca, K, C and O (**Kureshi *et al.*, 2021**). Similar results are observed in this study.

The FESEM monographs of nanoparticles synthesized using four bioreductants reveal spherical nature of the GNP and evidence the size of NPs that aligns with the size calculated from XRD analysis.

4.6.5.2 FE-SEM analysis of SNP

The surface characteristics of the SNPs were further studied using FE-SEM. The SNPs synthesized using TB fruit parts were found to possess spherical shape (**Figure 45**). The representative image of SNP synthesized using cereals/pulses washed water (**Figure 46**) also shows spherical shaped particles All the SNP was found to withstand 20-30kV of voltage. This shows the stability of the NPs; also the clarity of the FESEM monographs are good at applied voltage of 15kVand 30kV. This further infers the stability of SNP. The EDS spectra of the samples further confirm the percentage of Ag present in each of the synthesized SNP. The sizes of the NPs of all the synthesized samples were less than 100 nm.

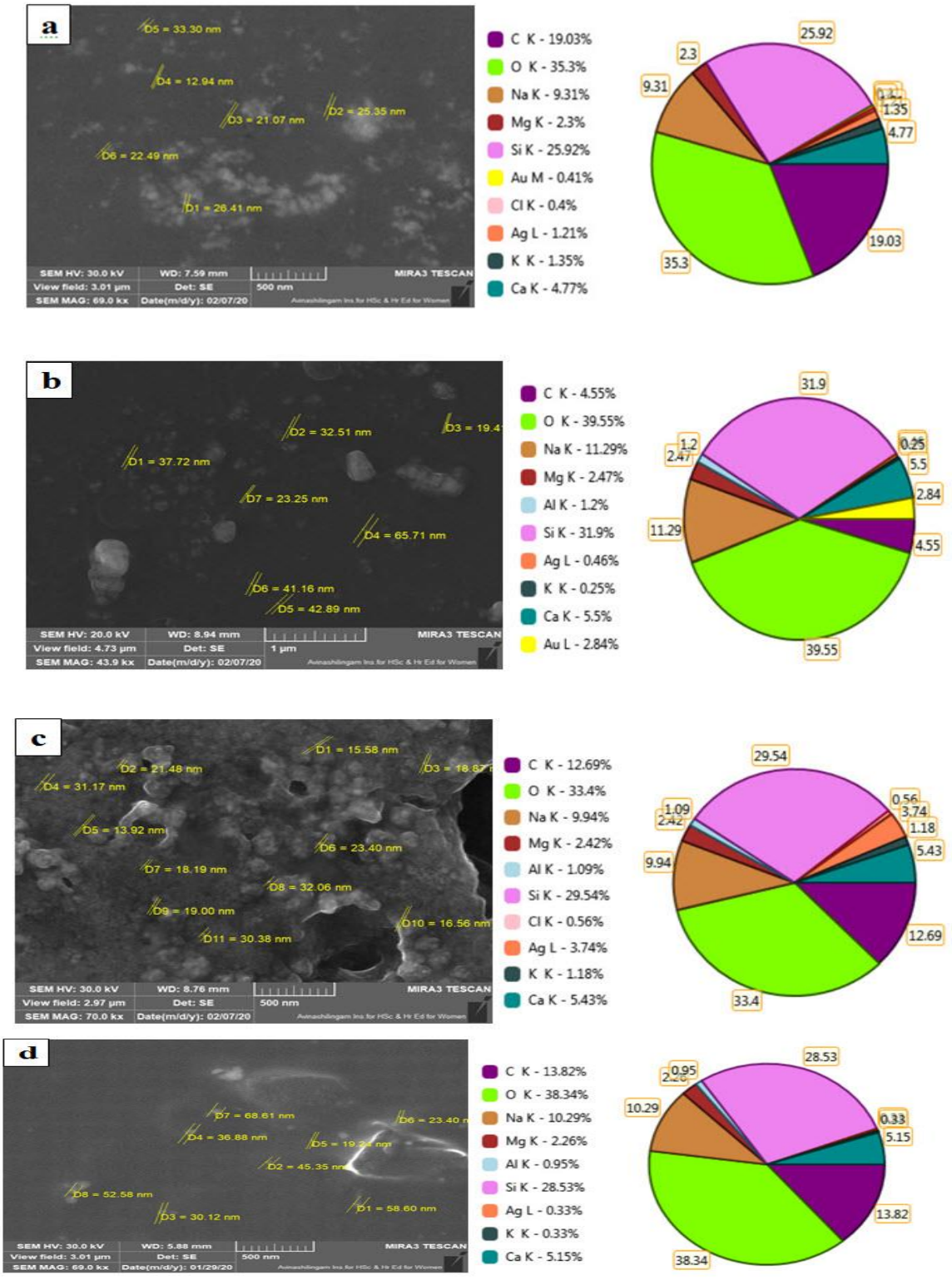

Figure 45. FE-SEM monographs of (a) TBOSSNP (b) TBISSNP (c) TBSSNP and (d) TBPSN

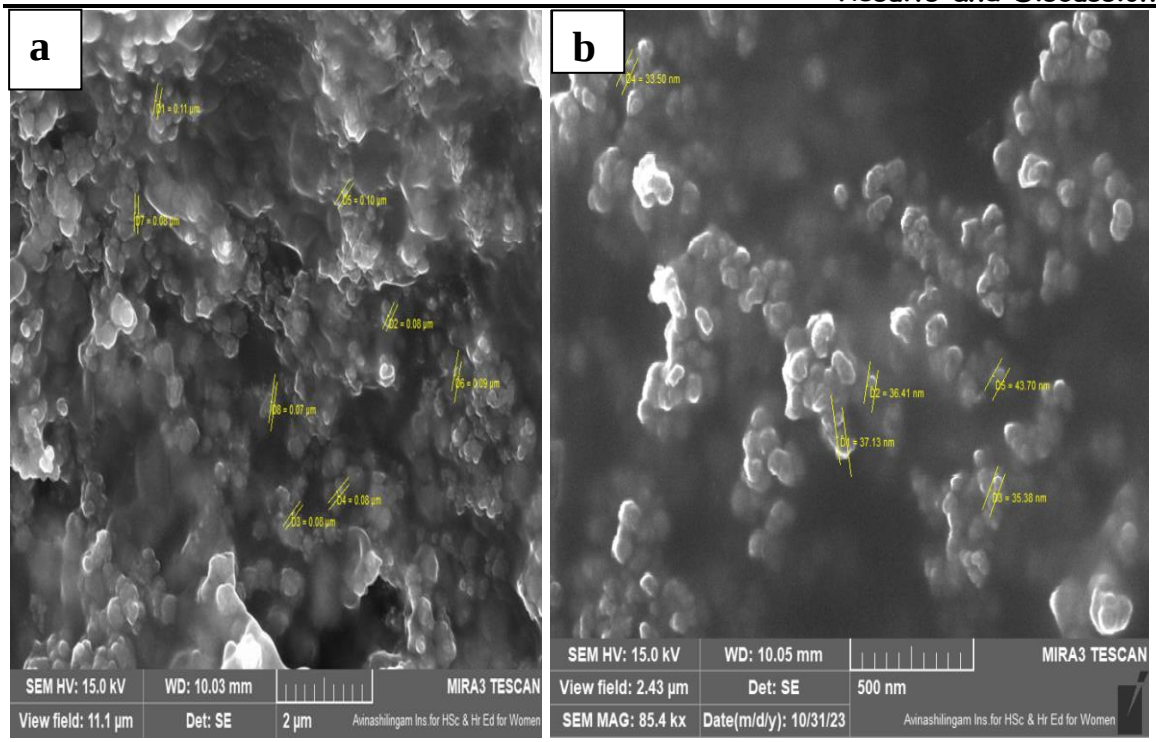

Figure 46. FESEM monograph of (a)IRaRWAgSo and (b)WCWWAgSo

The FE-SEM monograph of the IRaRWAgSo and shows spherical shaped particle, the clear image at 15kV shows the stability of the particles. The images show the uniformly distributed particles. The size of the particle ranges from 70-90nm. This is the first report on morphological determination of SNP synthesized using cereals and pulses washed water.

The result of the present study is correlated with the previously reported studies on curcumin aided SNP with spherical shape (**Khan *et al.*, 2019**) and *Pedalium murex* leaf extracts mediated SNP with spherical shape **(Anandalakshmi *et al.*, 2016**). Earlier reports on TB whole fruit aqueous extract aided SNP by room temperature method and conventional microwave heating method shows spherical shaped particle (**Patil *et al.*, 2017**).

The FESEM monographs of nanoparticles synthesized using four bioreductancts reveal spherical nature of the SNP and evidence the size of NPs that aligns with the size calculated from XRD analysis.

4.6.5.3 FE-SEM analysis of ZnONP

The synthesized ZnONPs using cereals/pulses washed water were also determined by FE-SEM analysis. Among the eleven synthesized ZnONPs, six visually good samples were chosen for XRD analysis and among them three were characterized by FE-SEM analysis.

The FE-SEM monographs of RaZn show the clustered particles which are closely packed. The shape of BJZn and WCZn are found to be spherical. Clear particles are visualized from FE-SEM monograph which are captured at working distance 6.9-10.2 mm; the particles were stable at 15kV. The EDS spectra with 81% Zn further shows the elemental distribution of Zn in ZnONPs. **Figure 47** shows representative images of FE-SEM monographs of synthesized ZnONPs.

ZnONP prepared from *Salvia officials* shows plates and flower morphology **(Alrajhi *et al.*, 2021).** ZnO has been found to grow most easily along the c-axis, aided by the Wurtzite crystal structure. The resulting ZnONPs display significant shape anisotropy, growing parallel to the basal plane. Surface tension effects can cause these NPs to be either crystalline or amorphous, and they may even show a metastable crystallographic phase.

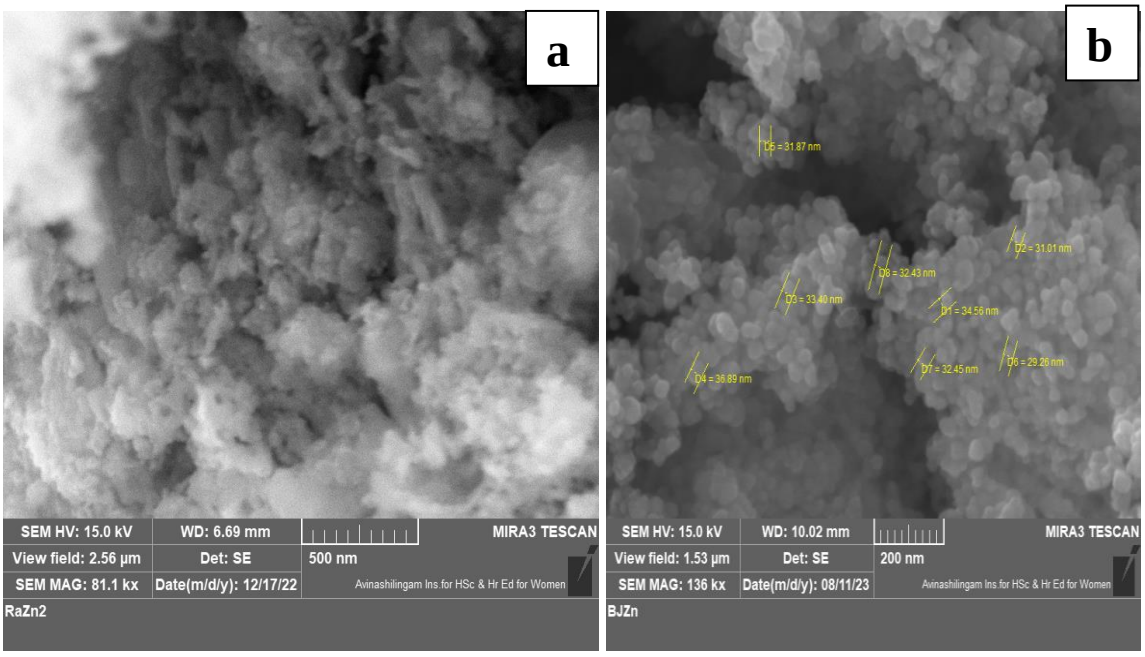

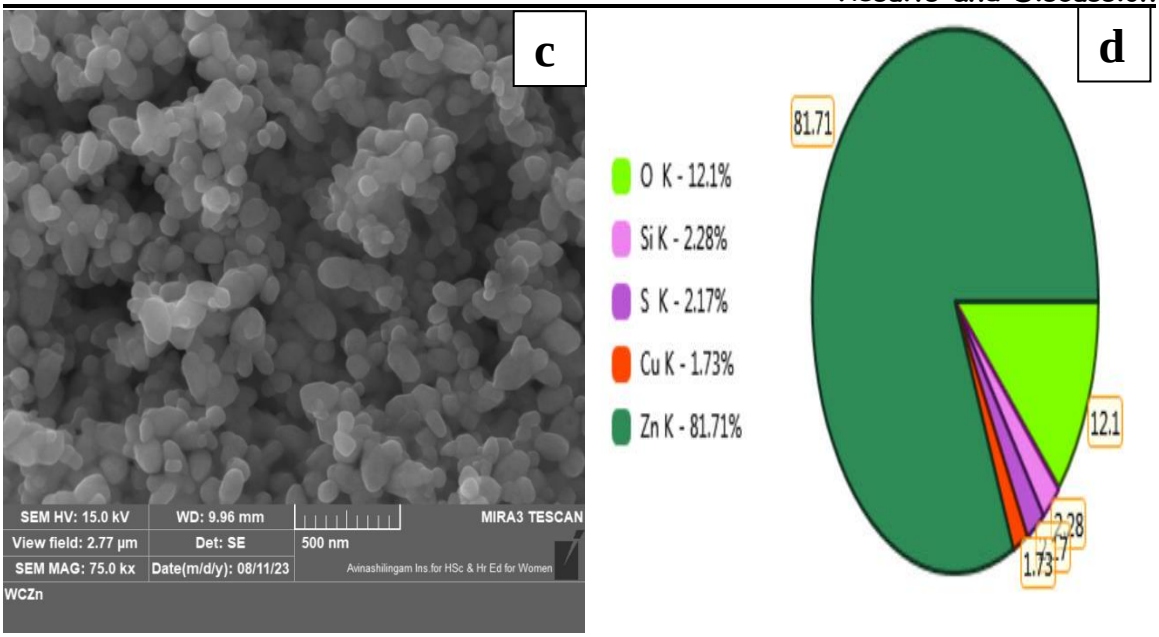

Figure 47. FE-SEM monographs of (a)RaZn, (b)BJZn, (c)WCZn and (d)EDS of RaZn

These unique characteristics make ZnONPs a promising candidate for a wide range of applications, including pharma applications (**Ngom *et al.*, 2016**). The morphology of the ZnONPs depends on pH of the reaction, concentration of extract and Zn source, temperature etc. (**Zeghoud *et al.*, 2022**).

This is the first report on ZnONPs synthesized using cereals and pulses washed water. Thus there are no FE-SEM monographs for comparison. The results show anisotropic particles.

4.6.5.4 FE-SEM analysis of RGO

FE-SEM monographs of BuWWRGO, IRRRGO and BJRGO serve as representative images of the synthesized RGO's. The BuWWRGO shows a wrinkled and crumpled morphology (**Figure 48a**). IRRRWRGO shows a cluster of particles with round edges (**Figure 48b**). At 20kx magnification with working distance 6.9mm, at 30kV applied voltage a transparent surface monograph is obtained. This ensures that the synthesized samples are stable. As the precursors are cereals and pulses washed water, the stability of the RGO at 30kV, as evidenced from higher C and O % ensures the absence of washed water- residues. As EDS is recorded at 15kV, it gives Ca, K, Mg, etc. which might have come from the precursor materials which are embedded with the reduced graphene oxide. Compared to C

and O percentage, the % of O is less, which ensures the successful reduction of GO to RGO by the cereals and pulses washed water (**Figure 49**).

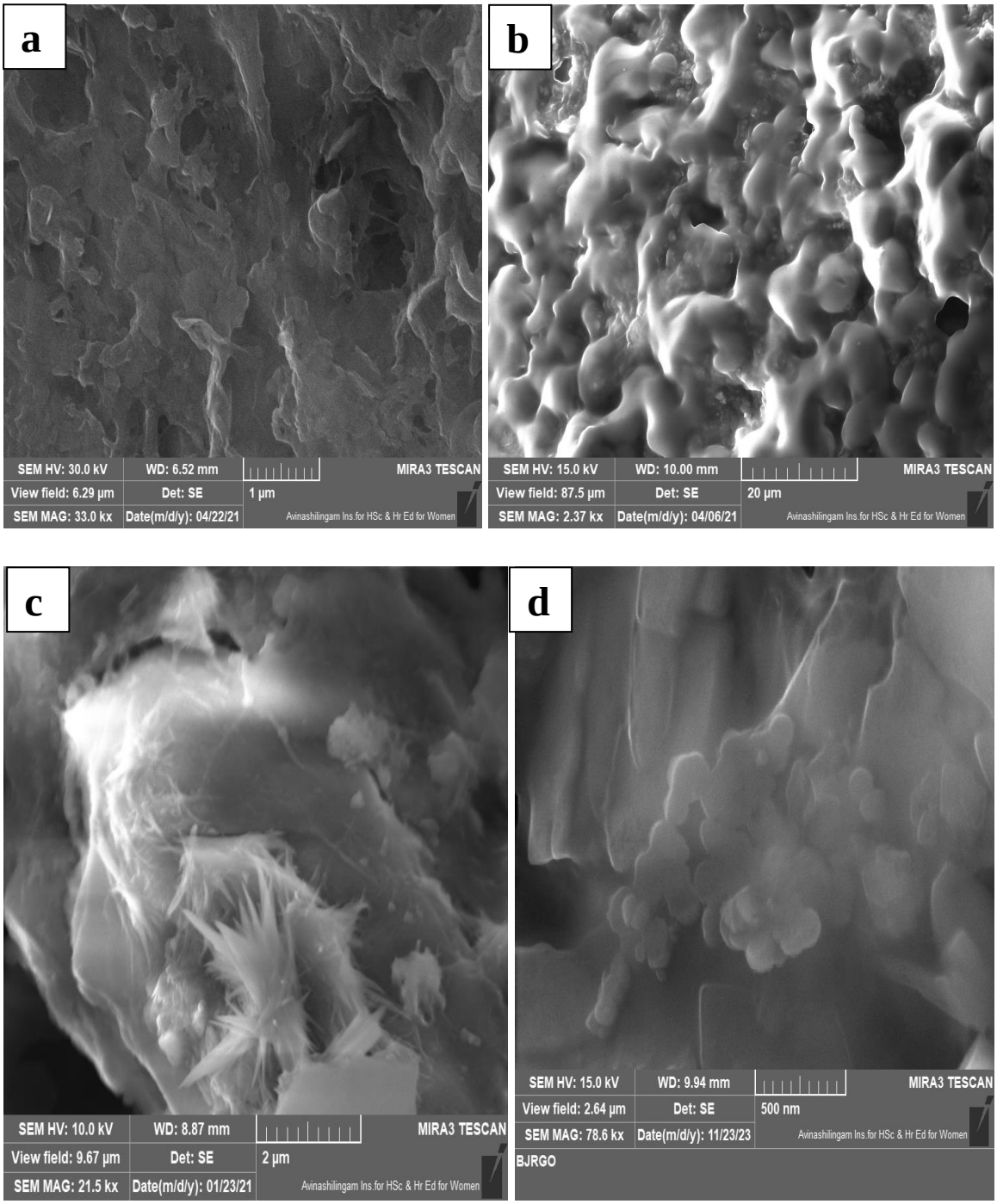

Figure 48. FESEM monograph of (a) BuRGO, (b) IRRRGO, (c) IRaRWRGO and (d) BJRGO

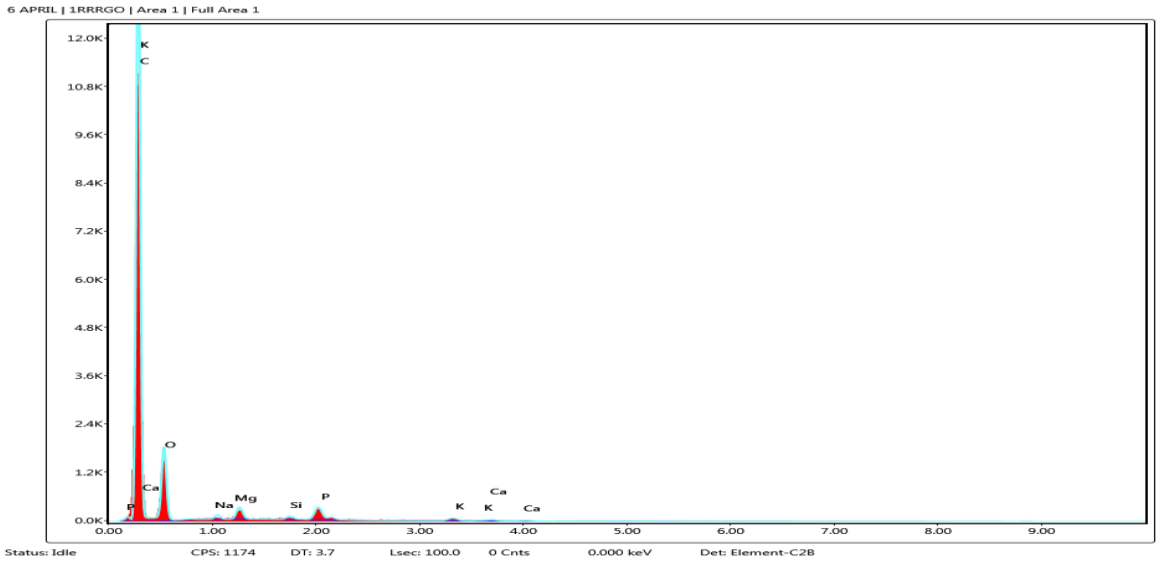

Figure 49. EDS of IRRRGO

It was reported that because of the porous networking architecture, FE-SEM images of GO revealed interconnected, three-dimensional, well-defined graphene sheets with the structure of a loose sponge (**Bykkam *et al.*, 2013**). Furthermore, GO has fewer graphene layers, its FESEM depicts indicate a more open structure and greater dispersion when compared to graphite (**Sharma *et al.*, 2016)**. The synthesized rGO had a uniform shape and smooth surface at higher magnifications, after reduction, the surface displays sinuate structural properties that are characteristic of rGO (**Gopinath *et al.*, 2018).** This could be because of oxygen-containing functional groups in GO have been removed (**Sharma *et al.*, 2016**).

The FE-SEM and EDS of synthesized RGO shows different morphology which depends on the precursors utilized. The EDS results reveal higher percentage of C which ensures the higher carbon content in synthesized RGO samples.

4.6.6 Thermogravimetric analysis of nanoparticles

The TGA measures the weight change of a sample when uniformly heated, providing crucial information on thermal stability and volatile component percentage. The TGA method's temperature fluctuations in weight may be used to identify the composition of NPs, measure the influence of modifications, and test oxidative and thermal stability. TGA including isothermal and non-isothermal techniques was used to conduct dehydration studies. This approach may be used to analyse mass loss due to oxidation, degradation, or loss of

volatiles, such as moisture, within a set temperature range, which often results in a temperature (or time) vs mass (or weight percentage) plot (**Rami *et al.*, 2021**). TGA provide valuable insights into the mass and composition of stabilizers used in nanomaterials. By heating the sample, TGA equipment records changes in mass and temperature, allowing for the identification and quantification of different components. The analysis of the first sample mass is particularly crucial in determining the type and quantity of NP organic ligands present (**Mourdikoudis *et al.*, 2018**).

Among the nanoparticles prepared, gold and silver NPs were not taken for TGA analysis as it warrants minimum 4mg of sample. As the aforesaid both samples were in solution form, TGA analysis was not carried out. TGA was carried out for ZnONP and RGO samples. Among the eleven synthesized RGO samples ten were subjected to TGA analysis, IBRRWRGO which show poor stability by agglomeration visually was excluded from the TGA analysis. Among the eleven synthesized ZnONPs, only four samples (RaZn, BaZn, IWZn and BoZn) which shows good absorption maximum in UV region was chosen for TGA analysis. These four samples were visually stable.

4.6.6.1 Thermogravimetric analysis of ZnONPs synthesized from cereals and pulses washed water

In the present study the thermal behaviour of the ZnONP was determined using TGA analysis. The samples are thermally stable upto 1000^{o}C (**Figure 50**).

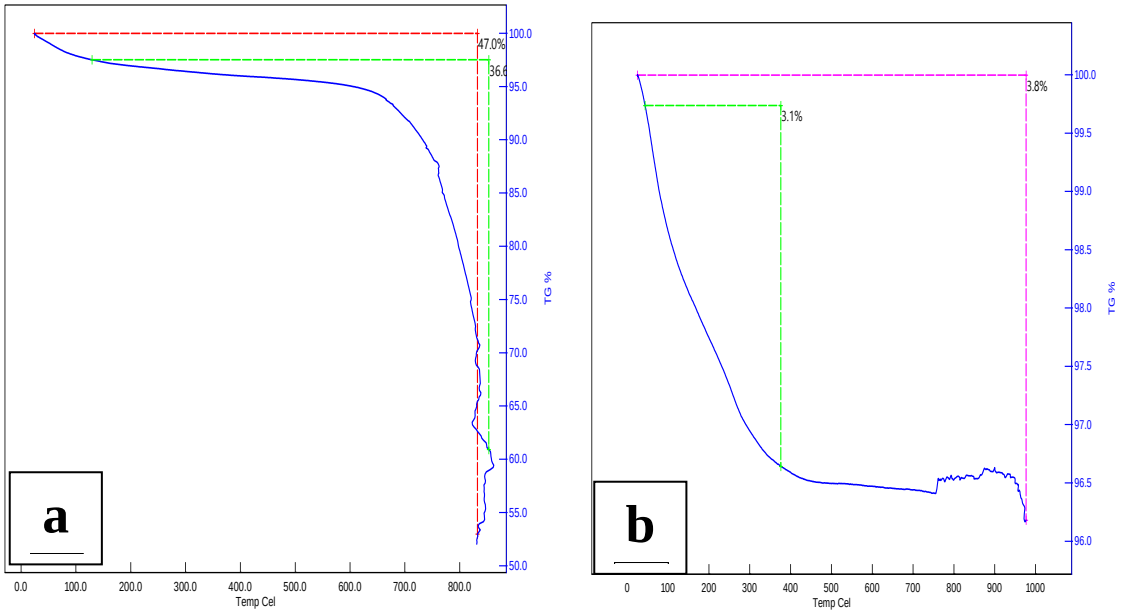

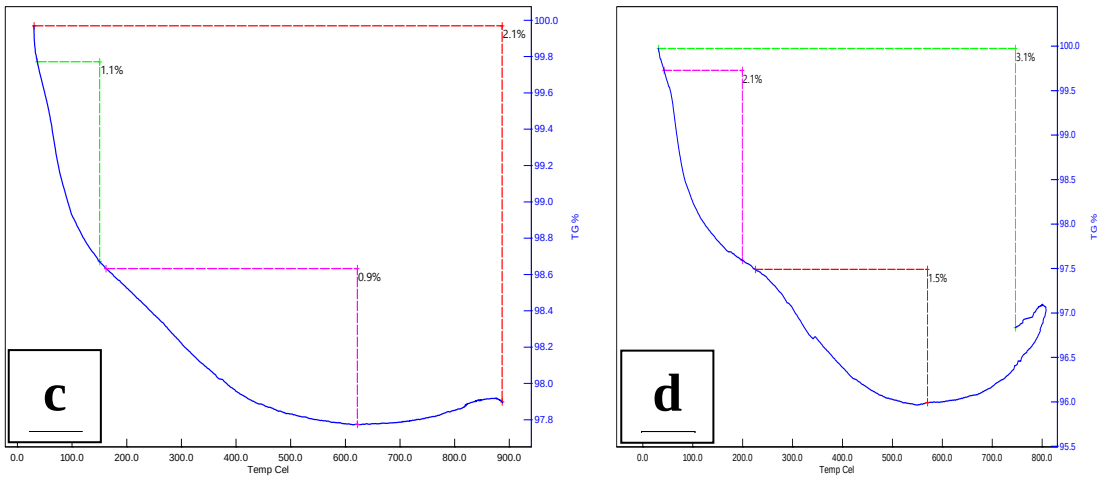

Figure 50. TGA curve ZnoNP (a)RaZn, (b)BaZn, (c) IWZn and (d) BoZn

Most of the samples follow only one step decomposition. Mass loss near 100 ^{o}C attributes to moisture. The loss near 600 ^{o}C corresponds to volatile impurities. BaZn, IWZn, BoZn sample shows 47% total mass loss which is less stable among the ZnONP samples. Other samples such as only 2-3% mass loss. This generalizes that the ZnONP are thermally stable. Based on the TGA and DTA analyses, it has been noticed that there is a significant loss in weight at approximately 200 °C, which is likely due to the removal of moisture and other volatile impurities from the sample. Additionally, the samples (BaZn) experiences 75% weight loss at around 400°C that might be due to the rapid degradation of carbohydrates into combustible products. The DTA curve has a bigger exothermic peak, for all samples, as a result of volatile organic moiety created by the dissociation of the precursor, which reacts with O_2 to yield CO_2 and H_2O. The weight loss seen in the TGA curve in the temperature range 400-600°C confirms the same (**Sagadevan *et al.*, 2019**).

Thus from the TGA analysis of synthesized ZnONPs, the chosen samples are thermally stable; among them RaZn and IWZn show only 2-3% mass loss.

4.6.6.2 TGA analysis of reduced graphene oxide

The thermal stability of the synthesized RGO is determined by TGA analysis. All the samples show two step mass loss. The initial mass loss near 100^{o}C corresponds to moisture in the sample. Further heating of the sample shows a significant mass loss near 300^{o}C -400^{o}C. This might be due to the further reduction of oxygen containing groups in the samples. All the samples are stable upto 1000^{o}C. The total mass loss is less for BJRGO and BuRGO

samples (**Figure 51**). This might be due to the perfect reduction of GO by the BJWW and BuWW.

Reports indicate that GO experienced a significant weight loss of approximately 56.01% as per TGA analysis. The loss in weight up to 100°C was attributed to moisture and interstitial water evaporation, while the loss between 100-250°C resulted from the breakdown of acidic and hydroxyl functional groups.

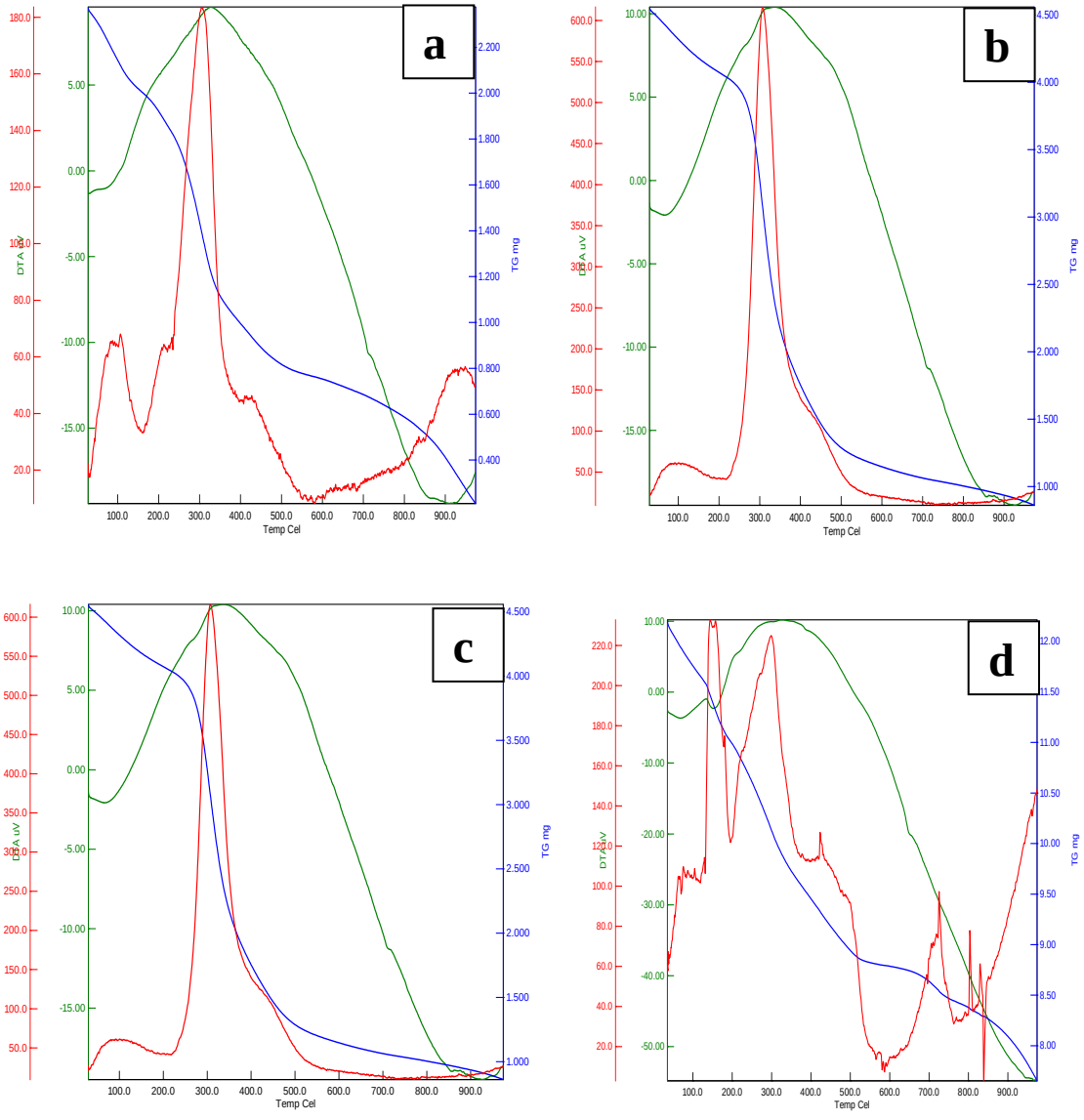

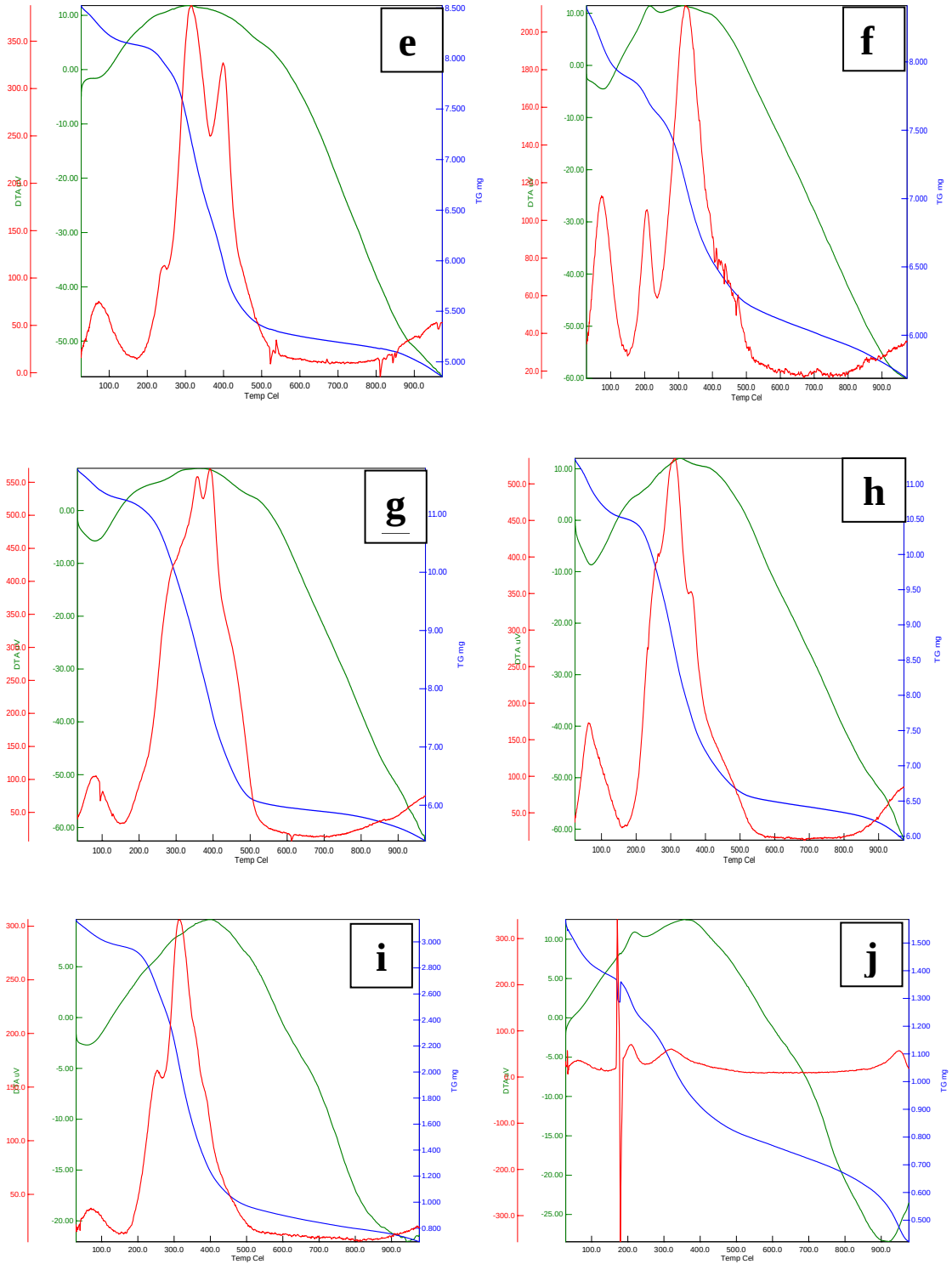

Figure 51. TGA plot of RGO (a)WCRGO, (b)IRaRWRGO, (c)IBoRWRGO, (d)BJRGO, (e)IBrRWRGO, (f)BuRGO, (g)IRRRGO, (h)TDRGO, (i)IBaRGO and (j)IWWRGO

This strongly suggests that GO was highly oxidized during its preparation, which involved a robust acid treatment and the use of H_2O_2 as an oxidizing agent (**Jeong *et al.*, 2009**). It's crucial to note that the weight loss continued up to 800°C, indicating the extent of GO's decomposition (**Wang *et al.*, 2005**).

RGO prepared by exfoliation and reduction method due to smaller amount of oxygen function groups have higher thermal stability than GO (**Loryuenyong *et al.*, 2013**). The outcome of the present study is comparable with the TGA of green synthesized RGO from *Sabdarriffa L* extract (**Alshamsi *et al.*, 2020**), *Citrus sinensis* and *Musa acuminate* peel waste extract (**Olana *et al.*, 2022**).

Thus from the TGA curves of synthesized RGO, the thermal stability upto 1000 ^oC were observed. Among the ten samples, BJRGO and BuRGO shows higher thermal stability with less mass loss (<5%) in both the samples.

4.6.7 Raman spectral analysis of synthesized RGO

Among the eleven synthesized RGO, the best morphology, stability and structural characteristics were observed in BJRGO and IRaRWRGO, and hence were taken up for Raman spectral analysis.

Raman shift of synthesized GO shows D band at 1320.9 cm^{-1} and G band at 1593 cm^{-1} in BJRGO (**Figure 52a**). There is a shift in the peak values of D and G band of IRaRWRGO (**Figure 52b**). This might be due to the distortion in structure upon reduction. The absence of 2G peak ensures the few layered RGOs. It has been proven through research that the G band of GO is wider than that of graphite after chemical oxidation to GO. Furthermore, the intensity of the D band of GO exceeds that of graphite. These alterations arise from the formation of defects, vacancies, and distortions during oxidation, which reduce sp^2 carbon's size in the crystalline domain (**Ferrari *et al.*, 2006; Perumbilavil *et al.*, 2015**). The G-band of RGO is found at 15912 cm^{-1} (**Figure 50b**) which shows that the hexagonal network of carbon atoms with defects has been recovered.

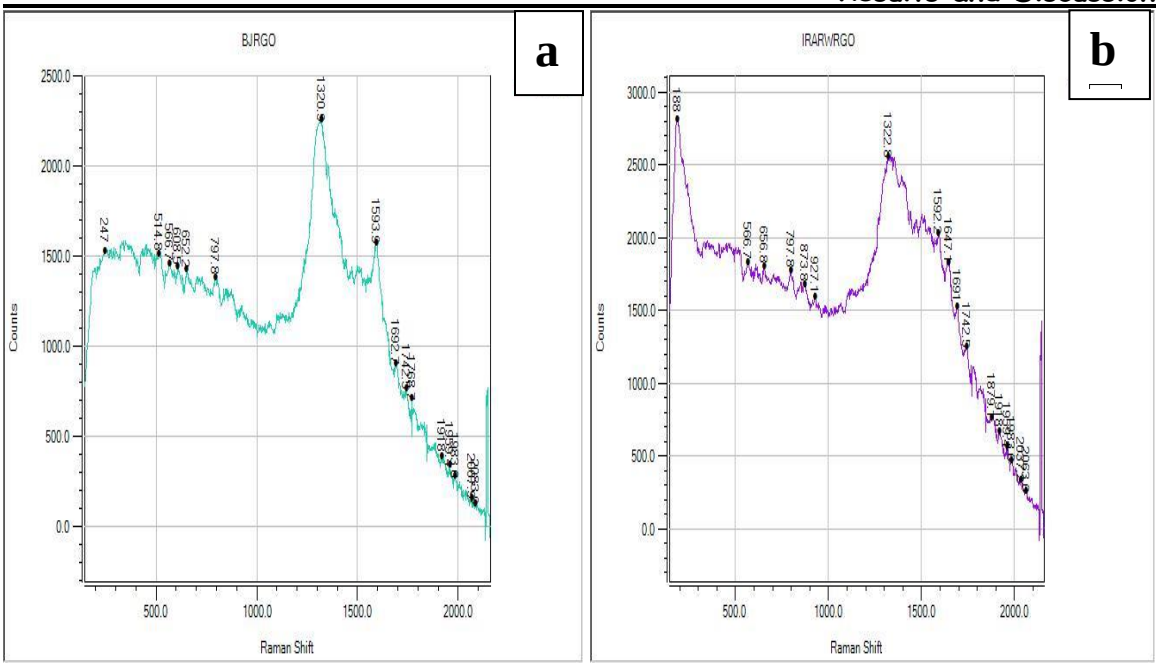

Figure 52: Raman spectra of (a) BJRGO and (b) IRaRWRGO

((X-axis : Raman shift (cm^{-1}); Y-axis : Intensity (counts))

The I(D)/I(G) ratio in RGO significantly increases, which suggests change in the structure of GO with the reduction process, resulting in additional structural defects. However, the presence of the D′ peak and the G peak at 1592 cm^{-1} indicates that the defect status of RGO. Therefore, the higher I(D)/I(G) ratio in RGO indicates fewer faults than GO after the reduction process (**Perumbilavil *et al.*, 2015**).

It is also reported that the efficiency of GO reduction can be enhanced by the factors such as duration of reduction time, concentration of reducing agent, temperature. Optimizing these factors may result in single layer graphene **(Dominic et al., 2021).** The Raman spectra of RGO synthesized from caffeic acid **(Bo *et al.*, 2014)** and *Salvia spinosa* **(Yang *et al.*, 2021)** shows similar peak**.**

From the Raman shift of synthesized RGO samples, it is observed that the RGO are few layered, this supports the FE-SEM monograph of the RGO samples.

4.7 Applications of synthesized nanoparticles

The selected synthesized nanoparticles were explored for applications in the field of pharmacology, biology, cosmetics and nanoswitching/sensors depending on their structural/morphological characteristics and stability (**Table 28**).

Table 28. Applications carried out with the selected synthesized nanoparticles

Nanoparticle	Sample code of Synthesized NPs	Application/assay done	Justification for choosing the sample
GNP	TBOSGNP	• Anti-bacterial activity against clinical isolates • colorimetric sensing of: cyanide, ammonia & melamine	First report on TB fruit part-GNP bacterial activity
	TBISGNP		First report on TB fruit part-GNP bacterial activity
	TBSGNP		First report on TB fruit part-GNP bacterial activity
	TBPGNP		✓ First report on TB fruit part-GNP bacterial activity ✓ Colorimetric ammonia sensing observed ✓ Added as conductive (Au) source in low cost CPE
	IBoRWM	Anti-bacterial studies	✓ Representative sample based on visual stability ✓ First report on anti-bacterial activity
	IBRRWM	• Anti-bacterial studies • Anti-skin cancer studies • DNA binding studies,	✓ Representative sample based on zeta analysis ✓ First report on anti-bacterial activity, anti-cancer and DNA binding studies
	BJWWM	• Anti-bacterial studies, • Anti-skin cancer studies • DNA binding studies • *Allium cepa* toxicity assay	✓ Representative sample based on Zeta analysis ✓ First report on anti-bacterial activity, anti-cancer and DNA binding studies ✓ Best results obtained in bacterial and cancer studies, therefore tested for toxicity
	WCWWM	• Anti-bacterial studies • Anti-skin cancer studies • DNA binding studies	✓ Representative sample based on Zeta analysis ✓ First report on anti-bacterial activity, anti-cancer and DNA binding studies
	GCAu	• Colorimetric cyanide & Melamine • Sensing • Modified CPE/nano switching application in presence of cyanide, low cost CPE for cyanide detection	✓ First report on sensors/nano switching applications against cyanide ✓ Earlier reports on biological activities
	HN28Au	Lotion formulation	✓ Application chosen based on the previous literature reports on protein

			responsible for skin and hair nourishment in precursor ✓ First report on skin care formulation using HN28Au
SNP	TBOSSNP	Anti-bacterial activity against clinical isolates	First report on TB fruit part-SNP bacterial activity
	TBISSNP	Anti-bacterial activity against clinical isolates	First report on TB fruit part-SNP bacterial activity
	TBSSNP	Anti-bacterial activity against clinical isolates	First report on TB fruit part-SNP bacterial activity
	TBPSNP	• Anti-bacterial activity against clinical isolates • Anti-bacterial earphone bud coating against *S.aureus*	✓ First report on TB fruit part-SNP bacterial activity ✓ Observed specific inhibition of *S.aureus*
	IBoRWAgSo	Anti-bacterial activity	✓ Representative sample based on visual stability ✓ First report on anti-bacterial activity
	IRaRWAgSo	Anti-skin cancer activity	There are traditional usages of precursor (raw rice) in skin care, therefore chosen to validate the activity in nano size
	IBRRWAgSo	Anti-bacterial activity	✓ Representative sample based on zeta stability ✓ First report on anti-bacterial activity
	BJWWAgSo	• Anti-bacterial activity • Anti-skin cancer activity	✓ Representative sample based on zeta analysis ✓ First report on anti-bacterial activity, anti-cancer
	WCWWAgSo	• Anti-bacterial activity • Anti-skin cancer activity	✓ Representative sample based on Zeta analysis ✓ First report on anti-bacterial activity, anti-cancer activity
ZnONP	RaZn	Lotion formulation	There are traditional usages of precursor (raw rice) in skin care, therefore chosen to validate the activity in nano size zinc particles.
RGO	BJRGO	Modified CPE for melamine detection / nanoswitching	Compared to other RGO samples, in TGA thermal stability was observed to be high.
	BuRGO	Modified low cost CPE	Thermal stability in TGA observed to be high.

This is the first study on the synthesis of NPs using the cereals/pulses washed water. Thus the possible pharmacological and biological assays were carried out. Among the synthesized ZnONPs, only one representative sample was chosen as additive in lotion formulation, this was one of the objectives of the present study. The further biological applications of ZnONP will be carried out in future. Likewise, upon literature survey revealed the conductive nature of RGO and hence was focused as an objective in the present study. HN28Au particles was utilized as additive in lotion formulation, as there are no reports

with free edge of human nails aided NPs and application, this study focus only on skin care formulation. The further bio activity study will be carried out in future. For detection of melamine, the synthesized NP doesn't show any positive results by colour change. Therefore in this study we have done analytical detection of melamine by FT-IR initially. The detection of leached melamine from the melamine tableware which are incubated with common Indian foods and the toxicity of the leached melamine by comet assay were carried out in this study. This was an awareness study where there was no report on melamine toxicity which was leached from melamine tableware in India.

4.7.1 Anti-bacterial activity of TB dry fruit part-aided GNP against pathogens

Extensive exploration on the review of literature and traditional knowledge on using TB has being detailed in chapter two; the scientific validation for TB fruit administration is previously reported by our research team (**Smina *et al.*, 2021**). However there are no anti-bacterial studies with TB fruit parts, and hence this studys' intention is to identify which fruit part of TB and GNP are best anti-bacterial agents and hence chosen in the present study. We conducted a study to test the antibacterial properties of TB fruit extracts and GNPs made from TB fruit using the well diffusion technique. The results showed that the GNPs made with TB fruit were effective against clinical pathogens as shown in the table provided. We used the antibiotic amikacin as a standard for comparison (which is chosen based on the pathogen chosen in this study). Zone of Inhibition (ZOI) obtained for the samples are shown below (**Table 29**).

Table 29. Zone of Inhibition (ZOI) obtained for the gold nanoparticles synthesized from TB fruit parts

S.No.	Samples/Standard drug (SD)	Zone of Inhibition (mm)		
		***A.pneumonia* (n=2)**	***B.subtilis* (n=2)**	***E. faecalis* (n=2)**
1	SD (Amikacin)	25	24	12
2	TBOS	-	-	10
3	TBOSGNP	-	10	-
4	TBIS	-	-	-
5	TBISGNP	-	-	-
6	TBS	-	-	-

7	TBSGNP	-	-	-
8	TBP	-	-	10
9	TBPGNP	-	14	12

(-) indicates no zone of inhibition; SD-standard drug

A.pneumonia was found to be resistant to both extract and GNP, no zone of inhibition was observed. In the study, it was found that the ZOI 10mm was seen in TBOS and TBP aqueous extracts against the pathogen *Enterococcus faecalis* (**Table 29**). TBP aqueous extract showed a higher ZOI of 12mm against *Enterococcus faecalis*, but TBPGNP proved to be a more potent antibiotic against the pathogen as observed in **Figure 53**. Clinical *Bacillus subtilis* was found to be resistant to TB fruit extract aqueous extracts and the whole fruit aided GNP.

The stability of the capping agents witnessed from FT-IR analysis attributes to bacterial activity in TBPGNP and TBOSGNP. *Bacillus* competes with other organisms for survival (as mentioned in **Figure 53**). TBOSGNP and TBPGNP showed ZOIs of 10mm and 14mm, respectively, indicating that TB-assisted GNP have high efficacy as anti-bacterial agents against clinical gram-positive and gram-negative bacteria.

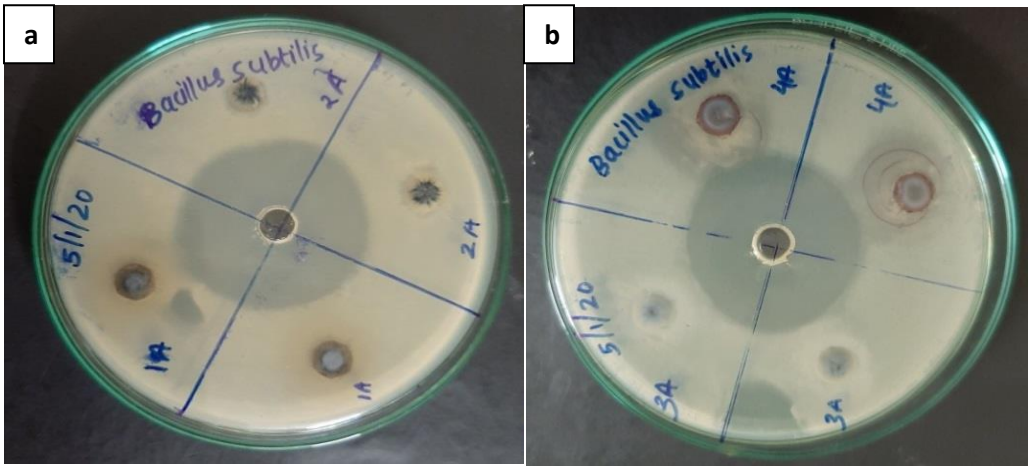

Figure 53. ZOI obtained against *Bacillus subtilis* bacteria (a) TBOSGNP and (b) TBPGNP

It is likely that pathogens found in clinical samples have become resistant to treatment. Our research shows that TBOS and TBP aqueous extracts are more effective in fighting bacteria and have been found to have a ZOI of 100µg/µl against the selected

pathogens. Additionally, GNPs made from these extracts have even more potent antibacterial properties than the aqueous extracts alone. However, our study also discovered that aqueous extracts from TB seed and mesocarp are not effective in fighting clinical pathogens like *A.pneumonia, B.subtilis*, and *E.faecalis* at 100µg/µl of the samples (**Figure 54**). *Enterococcus faecalis is* multidrug resistant bacteria. *E.faecalis* shows resistance to antibiotics by modifying the drug target by decreasing the binding affinity and deactivating the drug like agents (**Miller *et al.*, 2014**). The drug resistance of *E.faecalis* was disturbed by TBOS, TBP and TBPGNP in this study. Only spherical particles showed antibacterial effectiveness against the test pathogens in our investigation. It has been observed that nanostructures improve bacterial cell adhesion (**Patel *et al.*, 2019**).

GNPs are an effective way to combat pathogens. When they bind to the cell wall of the pathogens, the surface charge of the NPs enhances their antibacterial ability. This interaction causes a surface alteration in both the bacteria and the GNPs, resulting in the gradual degradation of proteins, DNA, and mitochondria, eventually leading to cell death (**Lee *et al.*, 2020**). The anti-bacterial effectiveness of TB fruit pieces, when combined with GNPs, can be attributed to the synergistic action of plant metabolites.

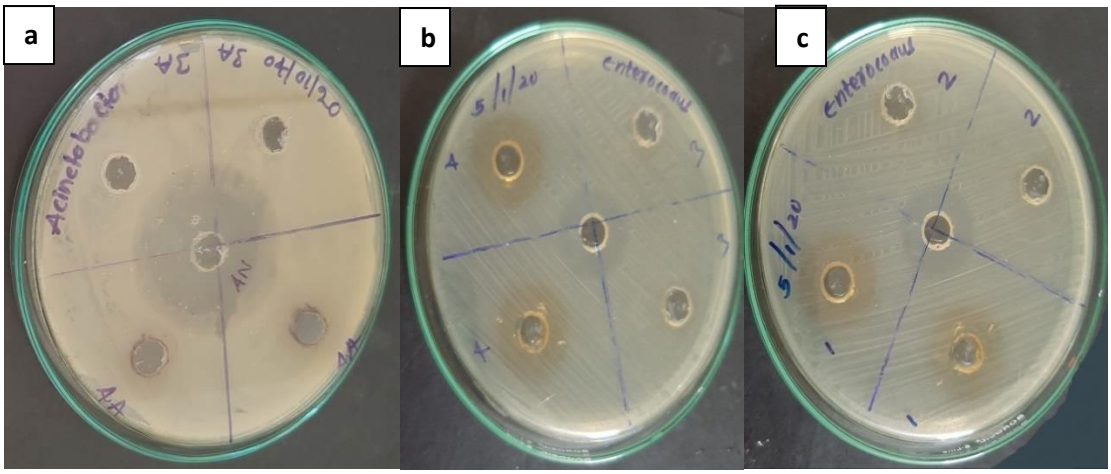

Figure 54. ZOI obtained against *Enterococcus faecalis* bacteria (a) TBPGNP (b) TBP and (c) TBOS

Table 30. Anti-microbial activity reports of TB fruit extracts and nanoparticles

Sample	Extract/Nano material	Microbes	Reference
TB whole dry fruit	Crude extract Methanol	*S. aureus, S.pneumoniae, S. typhi, S.*	**Elizabeth, 2005**

	extract	*typhimurium,E. coli (UTI),E. coli (EP),P.aeruginosa, Y.enterocolitica,C. albicans*	
TB whole fruit	Ethanol extract	*K. pneumoniae, E.coli, E.coli NCTC 13441, E.coli NCTC 13465, E.cloacae E.cloacae NCTC 13406*	**Thirunavukkarasu and** Purushothaman, 2017
TB whole fruit	P.E extract Chloroform extract Aqueous extract	*E.coli, P.aeruginosa, K.pneumoniae, S.flexneri, S.typhi*	**Devi *et al.*, 2014**
TB whole fruit	Gold nanoparticle	*Candida tropicalis, Candida albicans*	**Annavaram *et al.*, 2016**
TB dry fruit parts and Whole fruit	Aqueous extract	*B.subtilis, Enterococcus faecalis*	**Present work**
TB dry fruit parts and Whole fruit	Gold nanoparticle	*B.subtilis, Enterococcus faecalis*	**Present work**

Table 30 displays previous research on the antimicrobial efficacy of TB fruits and TB fruit-based GNPs. As per the literature, all solvent extracts exhibit antibacterial effects on almost all types of microorganisms, whether gram-positive or gram-negative. TB fruit is categorized as a broad-spectrum antibiotic (**Elizabeth, 2005**). The antimicrobial attributes of TB fruit extracts and TB fruit-based gold nanoparticles (**Devi *et al.*, 2014; Annavaram *et al.*, 2016**) have been studied. This is the first investigation that examines the antibacterial potential of TB fruit pieces and TB-mediated GNPs on pathogens obtained from clinical samples.

From this anti-bacterial study, it was observed that TBOSGNP and TBPGNP are effective in inhibiting the growth of clinically isolated B.subtilis and TBOS, TBP and TBPGNP inhibits the growth of clinically isolated E.faecalis. Clinical isolates of A.pneumonia show resistance towards TB aqueous extracts and GNPs. This is the first report on the bactericidal activity of aqueous extracts of TB fruit parts aided GNP against clinical isolates.

4.7.2 Anti-bacterial activity of TB dry fruit parts aided SNP against pathogens

Recent researchers focus on metal-based NPs with built-in antibacterial activity. Since they have shown to have potent antibacterial, antiviral, and antifungal properties, SNP are of particular importance in the fight against infections. SNP have the ability to physically

engage with the surface of different bacterial cells, harm cell membranes, and cause structural alterations that make these pathogens more permeable.

The synthesized TB fruit parts aided SNP were screened for the antibacterial activity testing against clinical isolated microorganisms which could have acquired drug resistance. **Table 31** shows the ZOI obtained.

Table 31. Zone of Inhibition obtained for the TBSNP against clinical isolates

Sample code	Zone of Inhibition (mm) n=2			
	Bacillus subtilis	***Staphylococcus aureus***	***Pseudomonas aeruginosa***	***K. pneumoniae***
TBOSSNP	-	18	-	-
TBISSNP	-	16	-	-
TBSSNP	-	16	-	-
TBPSNP	-	16	-	-
Ciprofloxacin	34	24	34	16

(-) No zone of inhibition

The synthesized SNP sample shows specific inhibition against *Staphylococcus aureus* clinical microbes. Among the synthesized SNPs TBOSSNP shows more inhibition compared with the standard drug of the same concentration (**Table 31, Figure 55**). This might be due to the smaller size of the synthesized NPs as described in the FE-SEM monographs. Also the synergistic effects of the phyto compounds present in the extract might also be a reason for the enhanced anti- bacterial efficiency of the TBOSSNP compared to the other SNP. Plant "capping" phytochemicals usually possess their own antimicrobial ability that can boost SNP action. This particular characteristics of phytochemicals enhance the antimicrobial activity of TB aided SNP against *S. aureus* clinically isolated microbes. The synthesized SNP also can be utilized for the specific *Staphylococcus aureus* infections in the dose dependent manner for ear infections.

The TB aided SNP samples shows anti-bacterial activity against only *S.aureus*, thus MIC and MBC was carried out for the TB aided synthesized SNP. The results show that all the SNP has MIC 500 µg and MBC 250 µg. The drug formulations incorporating the TB aided SNP (500µg) (**Table 32**) can be even effectively utilized for ear infections such as *Otitis externa*.

Specifically, upon intratympanic administration, SNP can, either alone or in conjunction with different antibiotic formulations, eradicate pathogens in the inner ear. This effect is dose-dependent. This is a highly beneficial ability against multi-drug resistant bacteria getting over the limitations of free antibiotics and effectively getting rid of the microorganisms in ear therapy (**Gheorghe *et al.*, 2021**).

Table 32. Minimum Inhibitory concentration of the TBSNP samples against *S.aureus*

Sample Code	MIC (Minimum Inhibitory concentration) µg	MBC (Minimum bacterial concentration) µg
	Staphylococcus aureus (n=2)	
TBOSSNP	500	250
TBISSNP	500	250
TBSSNP	500	250
TBPSNP	500	250

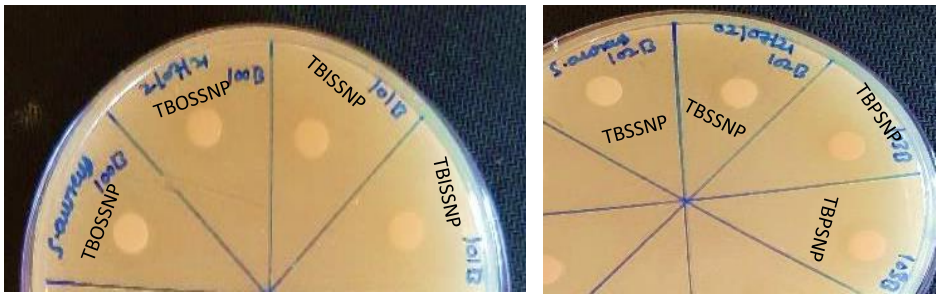

Figure 55. Antibacterial activity testing of synthesized SNP against *S.aureus* microbes

Recent researches show that nanoparticles and nano structured materials can be effectively utilized for *otitis externa* condition. External formulation developed with norfloxacin loaded nanocubosomes shows management of *otitis externa* in rabbits **(Al-Mahallawi *et al.*, 2021)**. Additionally, ceragenin-conjugated nonspherical gold nanoparticles are being able to eliminate the microorganisms responsible for otitis media which create biofilms **(Prasad *et al.*, 2021)**.

4.7.2.1 Mechanism of Anti-bacterial action of TBOSSNP against clinical isolates

Although the exact mechanism of action of is not yet known, there are a number of theories explaining the antibacterial, anti-inflammatory, and anti-cancer activities of SNPs. SNPs exhibit effective antibacterial activity via a variety of mechanisms, such as the

generation of free radicals, which increases membrane permeability by creating holes or channels in it, and the disruption of cell proteins by binding with thiol and amino groups, which results in membrane damage and the disruption of cell proteins **(Hanna *et al.*, 2022)**.

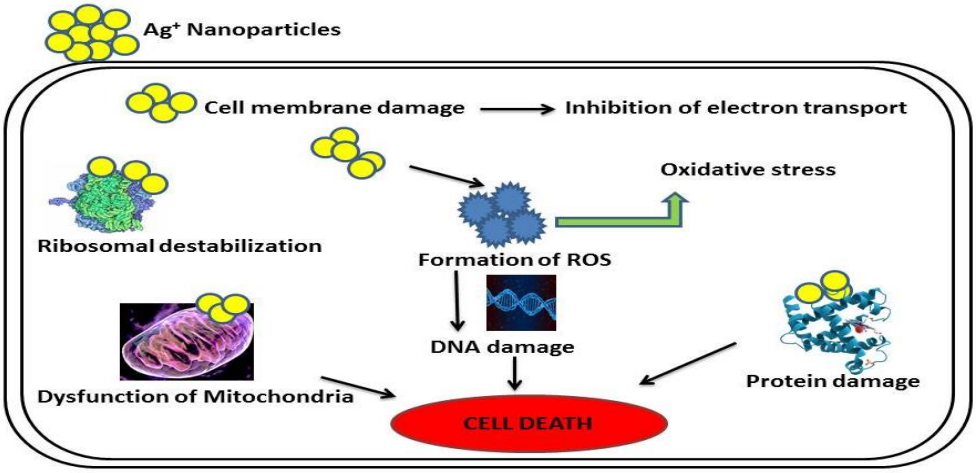

Figure 56: Proposed bactericidal mechanism of SNP

NPs are known to have a significant surface area that either penetrates the cell or attaches to the cell wall **(Siddiqi *et al.*, 2018)**. This disruption in membrane permeability causes the membrane to become porous **(Kambale *et al.*, 2020),** which causes further leaking of cell content. Additionally, the development of membrane holes causes NPs to diffuse into the cell, where they bond with sulphur- and phosphorus-containing proteins, inactivating proteins and DNA **(Vijayan *et al.*, 2018)**. Another theory contends that the release of Ag^{+} ions during the oxidation dissolution process is what causes SNP's antibacterial action. The main interaction between the oxidised silver ions from SNP and the thiol groups of several enzymes and proteins is to interfere with the respiratory chain and damage the bacterial cell wall. Additionally, due to the inhibition of DNA replication and ATP synthesis, silver ions promote the creation of reactive oxygen species, which is thought to be the primary factor in the majority of cell death **(Liao *et al.*, 2019)**. The synthesized SNPs in the present study show a *S. aureus* inhibition that might follow a similar mechanism.

4.7.3 Anti-bacterial earphone buds coated with TBOSSNP

TBOSSNP which shows good ZOI against *S.aureus* was coated on the sterilized ear buds. The hydrophobic surface of the ear buds were prone to physical abrasion by probe sonication. Plasma treatment is a well-researched technique for changing the surface properties of materials with minimal impact on their bulk properties. Through plasma

treatments, materials can be rendered hydrophilic by adding highly reactive species to their surface. Many reactive species are present in it, including positive and negative ions, UV photons, electrons, excited molecules and atoms, and free radicals. These reactive species have the ability to rupture covalent bonds in polymers and initiate a variety of surface chemical processes. The change in properties depends on the air which is passed in the plasma chamber and the other reaction parameters **(Owad *et al.*, 2022)**. Manufacturing industries will perform plasma treatment, as it changes the hydrophobic surface to hydrophilic surface.

For this study oxygen is passed in the plasma chamber. After plasma treatment within 45 minutes TBOSSNP was drop casted over the ear bud surface (**Figure 57**). The humidity or water vapor in the air, there is a transitory increase in surface energy. The high surface energy of the plasma-treated surface will eventually bond with water vapor, lowering surface energy to that of water. The adhesion of water to a surface will prevent the adhesion of the subsequent coating. Therefore plasma treatment will make the surface temporary hydrophobic.

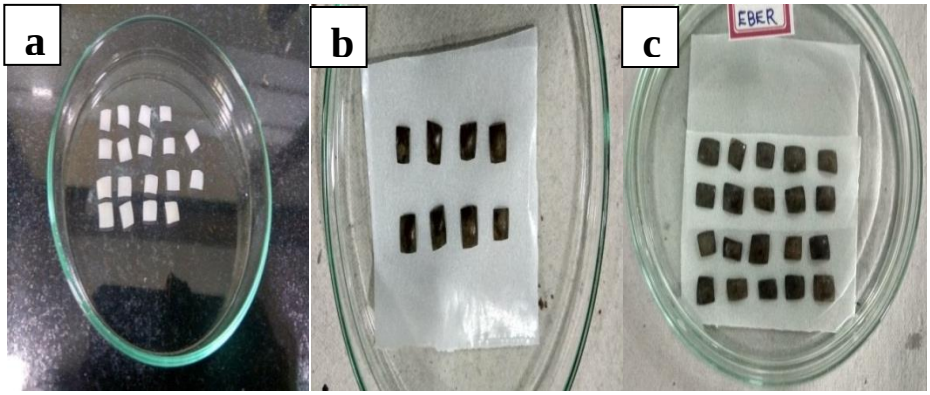

Figure 57. Ear buds (a) EBP, (b) EBC and (c) EBER

To provide scientific validation to the coating, 3D optical profilometric analysis was carried out for ear bud samples. From the **Figure 58a** it is clear that micrometre scale piths are produced in the surface of the ear buds which were subjected to probe sonication; this also indicates the increase in roughness of the surface. After the subsequent coating of materials it was found that the roughness of the ear bud surface decreases. In order to reduce the error, surface profiling for the three cross sections were done. 3D optical profilometre provides deep insights into the surface characteristics of the coated and untreated ear buds. It is well evident from the zeta software enhanced image on EBER (**Figure 58f**) that the

surfaces of the ear buds are well coated. The image also shows that the mixture of epoxy resin and TBOSSNP is also good as the surface is only in one colour (purple) in the scale of 131.71μm.

3D optical profilometre is a non-contact sample profiling techniques which helps to determine the surface characteristics in micrometre level. For coated samples like ear buds this non-contact technique is a boon as it does not disturb the coating during sample analysis. The images are captured with 20x resolution lenses in white LED background. The true colour of the images was captured as such and thus helps to analyze the samples effectively. The intention of epoxy resin for coating was to ensure the hydrophobicity of the surface, which will further help for antimicrobial contamination. Also epoxy coated ear buds are found to have a glossy coating which feels aesthetically good **(Figure 57c**). Mean roughness obtained is mentioned in **Table 33.**

Table 33. Details of ear buds coated with TBOSSNP

Sample code	Description	Mean Surface roughness (μm)
EBP	Ear buds (blank)	1.706 ± 0.16
EBWH	Ear bud- probe sonicated for physical abrasion	10.24 ± 0.32
EBC	Ear bud coated with TBOSSNP after physical abrasion	1.90 ± 0.03
EBBR	Ear bud coated with Epoxy resin after physical abrasion	5.794 ± 0.07
EBER	Ear bud coated with Epoxy resin after physical abrasion followed by drop casting with TBOSSNP	3.498 ± 0.37

Leaching of the coating from the EBER samples were tested by dipping and wiping of the coated ear buds with water. From the decrease in mass after the washing, the quantity of coated materials was determined.

No noticeable leaching was found from any of the coated sample. The triplicate weight before and after the leaching studies of the ear buds reduces the error in the study. It is clear from the **Table 34** that there was no significant leaching from the EBER samples and dipping of the ear buds in water would be a better method of cleaning the surface of EBER rather that wiping with water. The coated ear buds were subjected to anti-bacterial activity testing against *Staphylococcus aureus* bacteria. There was no bacterial growth on the top and bottom of the coated ear buds (**Figure 59**).

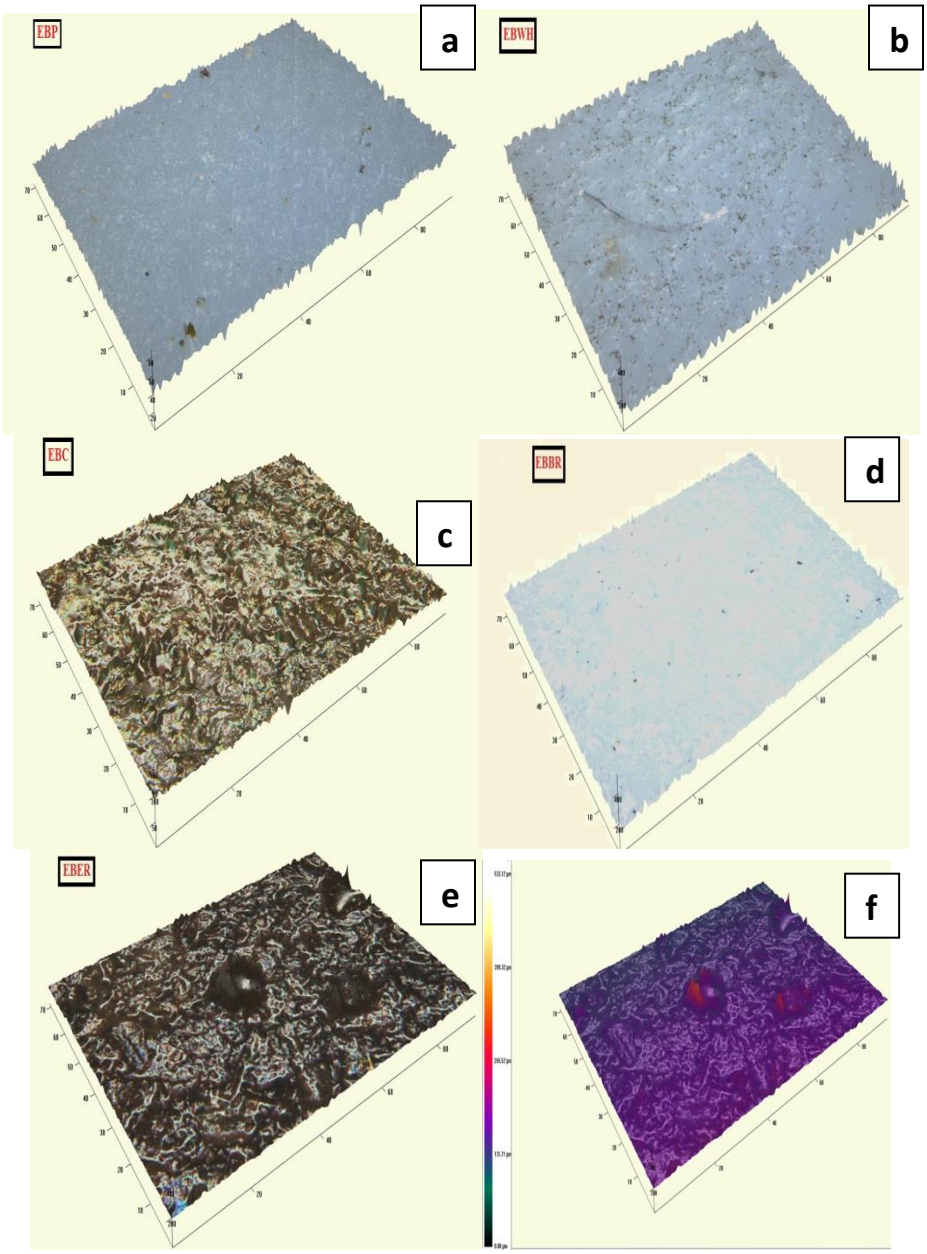

Figure 58. 3D Surface profile of (a) EBP, (b) EBWH, (c) EBC, (d) EBBR, (e) EBER & (f) EBER (software enhanced image)

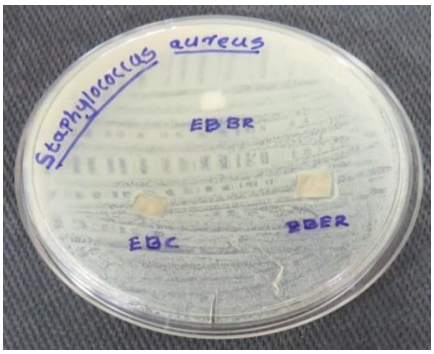

Figure 59. Anti-bacterial activity of coated earbuds against *S.aureus*

This ensures that the TBOSSNP coated surface will not be contaminated with microbes. As the coated samples are stable and set over the surface of the ear buds, they were not able to migrate inside the nutrient agar medium. This might be the reason for the absence of ZOI **(Figure 59**). Absence of ZOI does not imply the non-antibacterial nature of the tested material.

Table 34. Leaching Studies of EBER samples

Dipping method				Wiping method			
Weight of EBER before dipping (g)	**Weight of EBER after dipping (g)**	**Weight loss (g)**	**Mean weight loss (g)**	**Weight of EBER before wiping (g)**	**Weight of EBER after wiping (g)**	**Weight loss (g)**	**Mean weight loss (g)**
0.0140	0.0139	0.0001	0.00006	0.0147	0.0144	0.0003	0.0001
0.0199	0.0199	0		0.0115	0.0114	0.0001	
0.0160	0.0159	0.0001		0.0155	0.0154	0.0001	

Recently antimicrobial earphone buds are available in global markets from the popular brand like LG where they claim ear buds are coated with static antimicrobial material. The novelty of this work lies in the ear buds coated with SNP which specifically inhibit the growth of S.aureus.

4.7.4 Antibacterial studies of cereal and pulses washed water aided GNP and SNP

Anti-bacterial potential of GNP and SNP synthesized using cereals and pulses washed water was tested to determine their potential to inhibit common infection causing gram positive and gram negative bacteria that cause common infection. The samples chosen

are GNP (IBRRWM, BJWM, WCWM, IBoRWM), SNP (BJAgSo, IBoRWSoAg, IBRRWAgSo, and WCAgSo), and their precursors BJWW, IBRRW, IBoRW, WCWW.

For TB aided SNP, four different clinical isolates were chosen, as there are earlier reports on laboratory cultures. This is the first report on antibacterial activity of GNP and SNP synthesized from cereals and pulses washed water; we have chosen laboratory culture of common infection causing pathogens. For this study we used ciprofloxacin as standard.

From the ZoI values and **Figure 60** and **Table 35** it is clear that SNP and GNP synthesized using cereals and pulses washed water are inhibiting the growth of microbes. IBoRWSoAg, BJSoAg, IBRRWAgSo and WCAgSo are equally efficient in inhibition of *K. pneumoniae*. The ZOI is 13mm and on par with the standard ciprofloxacin (100ng/ml) used in this study. *B. cereus* inhibition is better with WCAgSo (ZOI- 15mm).

Table 35. Zone of Inhibition of Cereals and pulses washed water and their GNP, SNP against *Klebsiella pneumoniae, Bacillus cereus, Staphylococcus aureus and Escherichia coli*

Sample Code	Zone of Inhibition (mm)			
	K. pneumoniae	***B. cereus***	***S. aureus***	***E. coli***
IBoRW	10	0	9	0
IBoRWM	11	10	15	9
IBoRWAgSo	13	11	19	12
BJWW	0	9	0	0
BJWM	11	12	12	17
BJAgSo	13	11	14	17
IBRRWM	12	10	13	11
IBRRW	0	0	8	0
IBRRWAgSo	13	13	14	17
WCWW	0	0	9	0
WCWM	12	13	13	11
WCAgSo	13	15	14	15
Ciprofloxacin	21	22	20	20

IBoRWSoAg gives a better inhibition against *S. aureus* than other samples with ZOI-19mm which is very much closer to the value of standard drug (20mm). BJWM, BJAgSo, IBRRAgSo samples are efficient in inhibiting *E.coli* with ZOI 17mm. Comparing SNP and GNP, SNPs has better ZOI values compared to GNPs. This might be due to the presence of Ag in the particles.

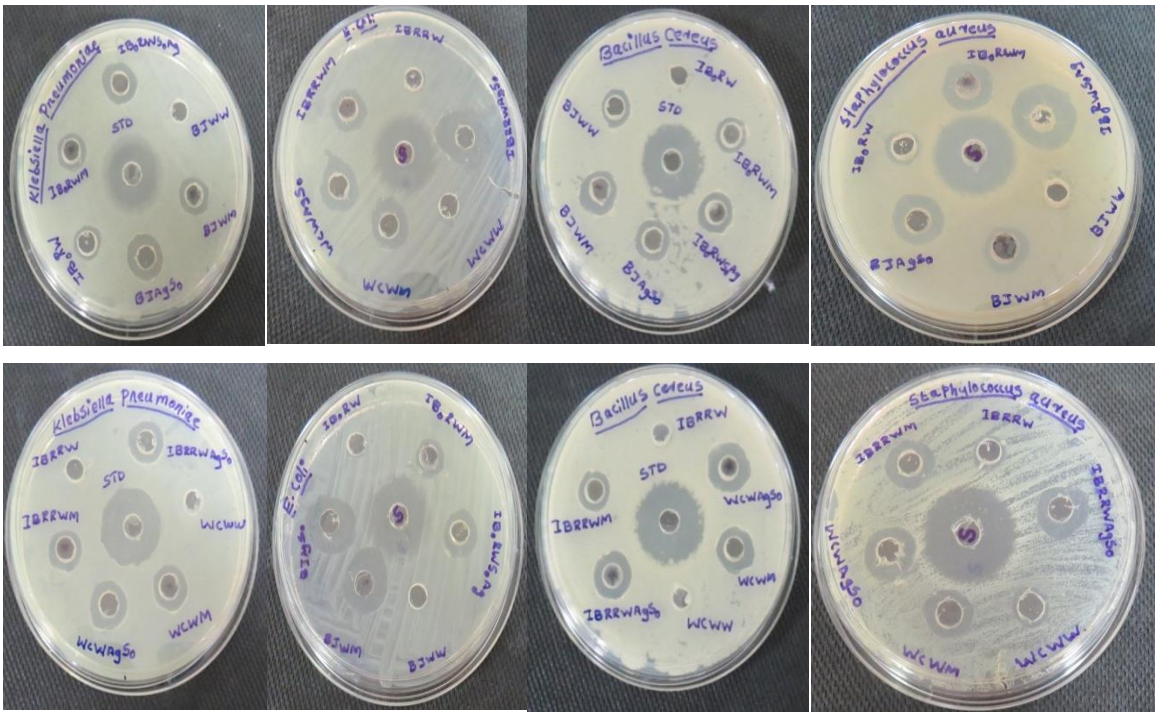

Figure 60. Zone of inhibition formation in agar plates with SNP and GNP against gram positive and gram negative bacteria

From ancient days the anti-bacterial properties of bulk Ag metal is known. In recent days' research focus on SNP and antibacterial efficiency has increased. The plant based biowaste materials were successfully utilized to synthesize SNP and their microbial activity is reported to be more. Unused parsley stems and potato peels aided SNP shows strong antimicrobial properties against *E.coli* and *S. aureus* bacteria (**Wolny-Koładka *et al.*, 2022**).

Comparing the bacterial activity of synthesized GNPs and SNPs using cereals and pulses washed water; it was found that SNPs have more potential to inhibit the bacterial growth than GNPs.

From the anti-bacterial activity studies, it can be generalized that the synthesized GNPs and SNPs using TB fruit part extract and cereals and pulses washed water shows comparable activity with that of standard drug against common infection causing pathogens. As an outcome of the study, we were able to fabricate an anti-bacterial ear buds coated with TBOSSNP which inhibits ear infection causing bacteria S.aureus.

4.8 Anti-cancer activity of GNP and SNP synthesized from cereals and pulses washed water against A375 skin cancer cell lines by MTT assay

Several biomedical applications of GNPs and SNPs are reported. It is most important to determine the cytotoxic activity of the NPs. In this study, cytotoxic activity of SNPs (BJAgSo, IRaRWSoAg, WCAgSo), GNP (IBRRWM, BJWM, WCWM) and their precursors BJWW, IBRRW, IRaRW, WCWW are carried out against A375 skin cancer cell lines as these NP samples possess better stability and morphology compared to other synthesized NPs in this study. The results were compared with doxorubicin which is a standard drug.

From the results obtained (**Table 36**), it was observed that cytotoxicity is concentration dependent; the increasing concentration of NPs decreases the development of cancer cell, and similar trend was followed in the standard drug sample. The cytotoxicity of IBRRW, BJWW, WCWW and IRaRW on A375 cell lines was less compared to their NPs. This implies the lesser anti-cancer efficiency of washed water towards A375 cell inhibition. Half minimal inhibitory concentration (IC_{50}) of the samples was calculated for the GNPs, SNPs and their precursors.

Table 36. IC_{50} (µg/ml) of samples against A375 cell line

Sample code	IC_{50} (µg/mL)
IBRRW	157
IBRRWM	**70**
BJWW	132
BJWM	**75**
BJAgSo	**83**
WCWW	182
WCWM	**72**
WCAgSo	110
IRaRW	160
IRaRWAgSo	**85**
Doxorubicin(standard)	**17**

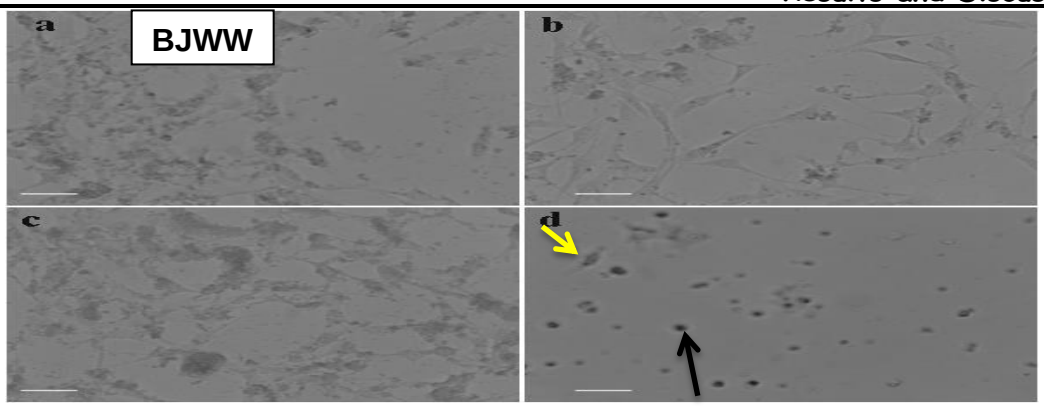

Figure 61. Surface of A375 cell line treated with BJWW after 24h (a) 50 µg/ml, (b) 100 µg/ml, (c) 200 µg/ml and (d) 250 µg/ml

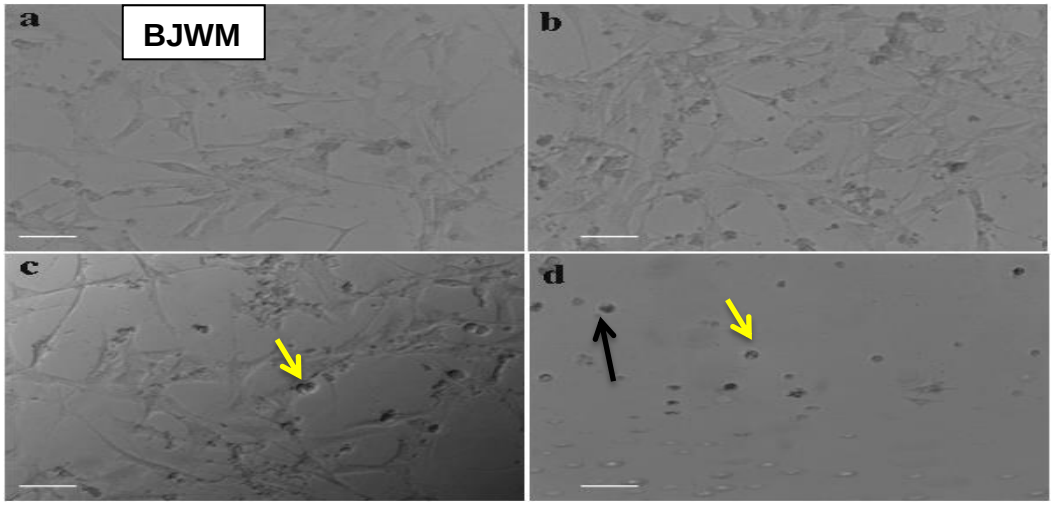

Figure 62. Surface of A375 cell line treated with BJWM after 24h (a) 50 µg/ml, (b) 100 µg/ml, (c) 200 µg/ml and (d) 250 µg/ml

In all the samples maximum cell death occurred at 250 µg/mL. The disruption caused on by membrane blebbing in the stability of cell membranes and the impact of NPs on their cytoskeleton is a result of cytotoxic activities. From the surface studies of treated cell lines a cell shrinkage (indicated by black arrow) and blebbing (indicated by yellow arrow) can be observed (**Figure 61 & 62**)

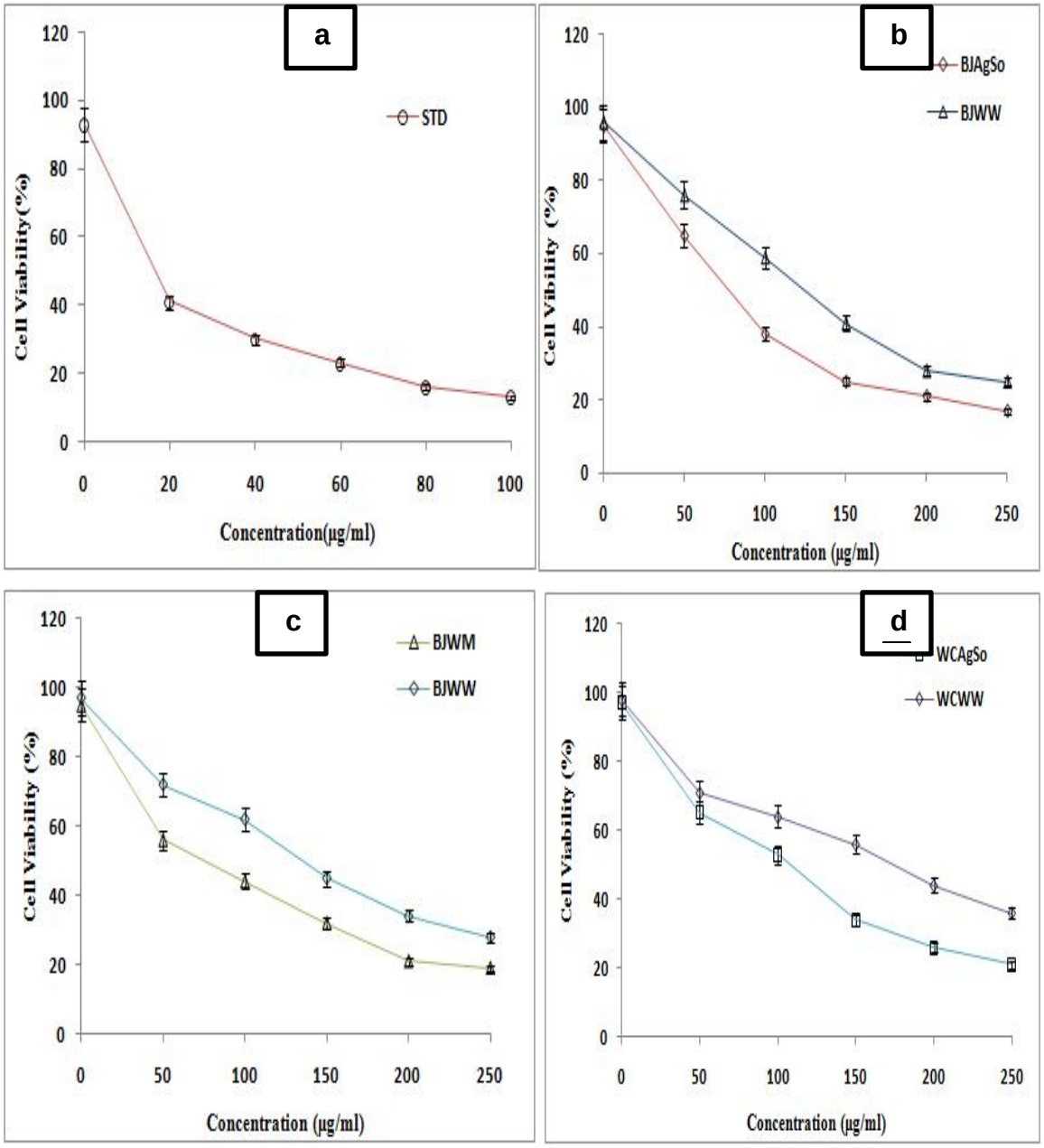
a
STD
Cell Viability(%)
Concentration(µg/ml)
b
BJAgSo
BJWW
Cell Vibility (%)
Concentration (µg/ml)
c
BJWM
BJWW
Cell Viability (%)
Concentration (µg/ml)
d
WCAgSo
WCWW
Cell Viability (%)
Concentration (µg/ml)

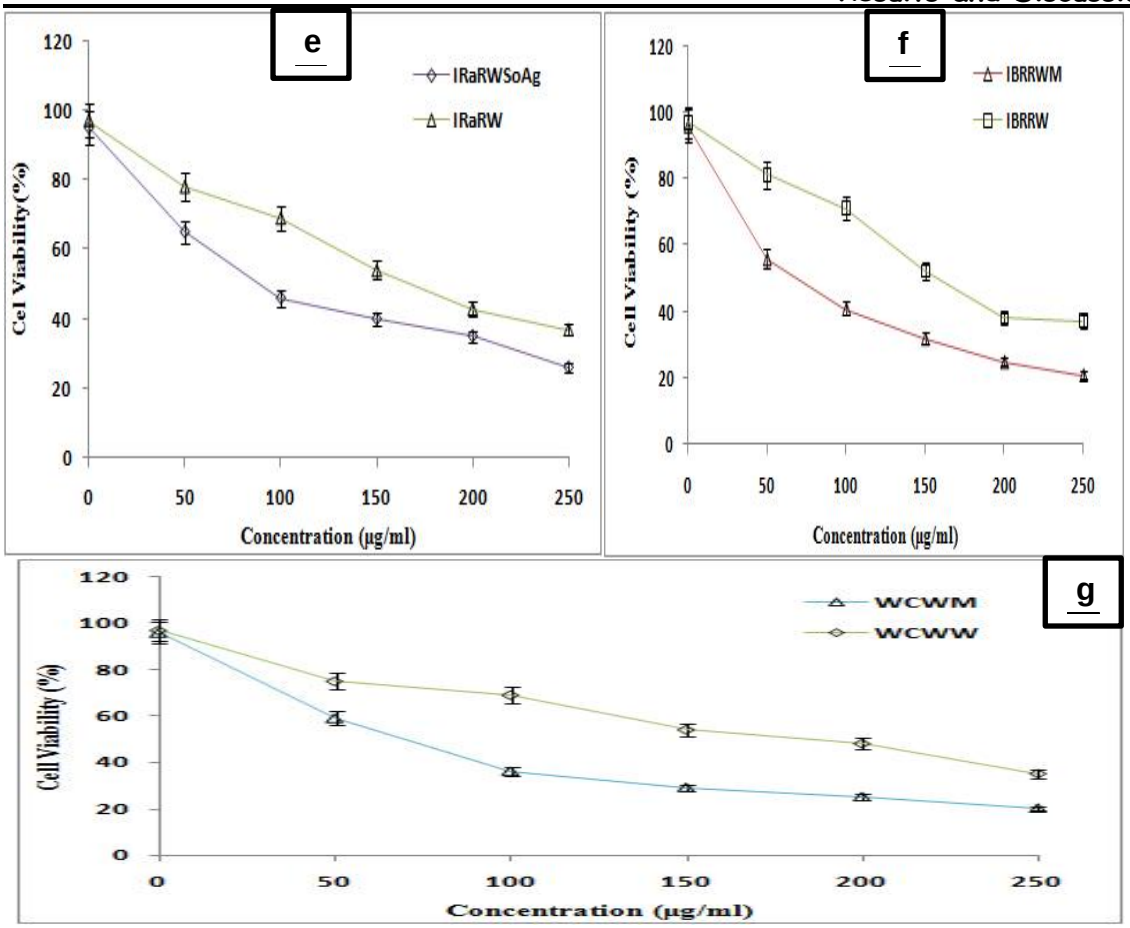

Figure 63. Cell viability (%) of (a) Doxorubicin, (b) BJAgSo, (c) BJWM, (d) WCAgSo, (e) IRaWSoAg, (f) IBRRWM and (g) WCWM treated A375 cell lines after 24h

Comparing the IC_{50} values of synthesized GNPs and SNPs with that of standard, it was observed that GNP is comparable to that of standard. It is also observed that the metallic NPs are 5 times more cytotoxic to skin cancer cell lines than their precursors (**Figure 63**).This might be due to the synergistic effect of Au/Ag metal and the nutrients in the washed water. The results of this study go on par with the previously reported cytotoxic activity of GNP loaded with botulin against A375 cell lines and potent apoptotic effect **(Mioc *et al*., 2018)**.

Melanoma is a deadly kind of skin cancer that has a high risk of metastasizing and intractability. Patients with advanced melanoma are almost usually incurable and have a poor prognosis. Chemotherapy is an integral component of clinical melanoma treatment, but its efficacy is constrained by its adverse effects on healthy tissues. As novel treatment alternatives for melanoma, numerous immunotherapies have recently been discovered;

nevertheless, their efficacies are unpredictable and their side effects are still not trivial (**Zhang *et al*., 2020**).

From anti-cancer study, a biocompatible solution is obtained by the efficiency of cereals and pulses washed water aided SNP and GNP against the growth of A375 cell line.

4.9 DNA binding studies of metallic nanoparticles using UV-Visible spectrophotometer

From anti-bacterial studies and anti-cancer studies it was observed that cereals/pulses washed water aided GNPs and SNPs shows inhibition against common infection causing pathogens and skin cancer cells respectively. Before developing a drug formulation out of these NP samples, it is essential to understand their binding mechanism with DNA.

Many medications that are either in advanced clinical studies are now being used in healthcare field target DNA pharmacologically. It would appear natural, attractive, and theoretically simple to target DNA to control transcription (which controls gene expression and protein synthesis) or replication. Small ligand molecules attach to DNA and cause it to operate improperly or not at all. When altering or inhibiting DNA activity is necessary to treat or control a disease, these tiny ligand molecules operate as drugs. These interactions are studied using a variety of instrumental approaches. Cyclic voltammetry, fluorescence spectroscopy, and **ultraviolet-visible spectroscopy** are some of them.

The DNA-metal interactions have much importance when probing into biological applications of metal NP. The DNA binding studies of selected metallic NPs, GNPs and SNPs when treated with ct-DNA was analysed using UV-Visible spectrophotometric analysis in this study. As the SNPs and GNPs synthesized using cereals and pulses washed water showed good anti-bacterial and anti-cancer results, it is essential to understand the nature of binding of DNA to the metal NP. The binding mechanism also helps to determine the toxicity of the material to the DNA.

The quantitation of the DNA before introducing the drug like sample is necessary to ensure the purity of the DNA. UV-Visible spectrophotometric method is best to evaluate the purity of the DNA. The purity of DNA is ensured from the absorbance ratio A260/280; desirable being 1.8 to 1.9 (**Firdhouse and Lalitha, 2015**). In the present study A260/280 the value obtained is 1.9 ensuring the purity of DNA.

The successive binding of DNA to SNPs and GNPs was observed from the UV spectra. The disappearance of the SPR of the SNPs and GNPs after 30 min at all concentrations (**Figure 64 & 65)** generalizes that the DNA, modified the surface of the GNPs/SNPs and formation of a complex without disturbing the nature of DNA. The ct-DNA absorption will be at λ_{max} 260nm (**Sirajuddin *et al*., 2013**).

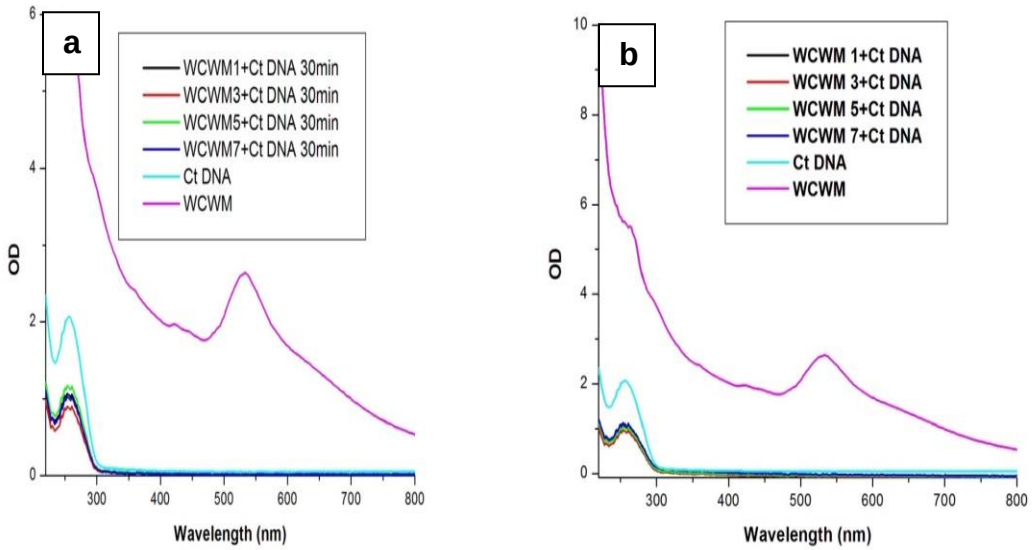

Figure 64. UV-Visible spectra of WCWM - ct-DNA interaction (a) at 30 min (b) at 0 min

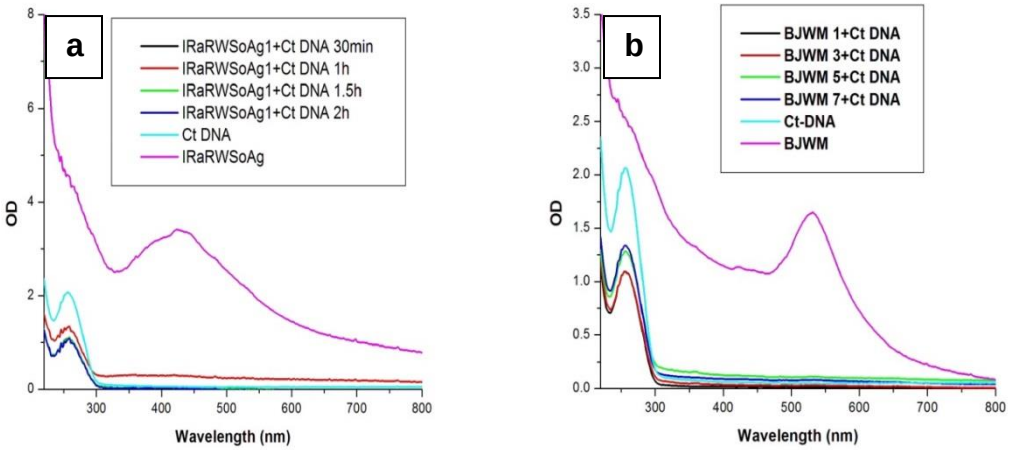

Figure 65. UV-Visible spectra of (a) IRaRWSoAg1 - ct-DNA interaction at varying time intervals, (b) BJWM at different concentrations

In the present study the binding nature of the ct-DNA with SNPs and GNPs (synthesized using cereals and pulses washed water) was analysed. The mode of binding of the DNA towards SNP and GNP was found to be intercalation from the nature of absorption bands.

UV-visible absorption spectroscopy is a powerful tool for studying DNA stability and its interactions with small ligand molecules. With this technique, we can analyze the absorption characteristics of DNA molecules and investigate how drugs interact with DNA. By observing the distinctive absorption band of ligand molecules in the visible spectrum, we can determine whether there is any interaction between the DNA and the drug. By measuring the shift in the position of this band's maximum from when the ligand is free in solution to when it is bound to DNA, we can gain valuable insights into the molecular mechanisms underlying these interactions (**Sirajuddin *et al.*, 2013**).

This indicates that SNP and GNP are bound to the DNA matrix and formed a complex. It is also observed that the OD of DNA peak tends to hypochromic shift as the concentration of GNP/SNP increases. Compounds binding with DNA through intercalation usually results in hypochromism. In the intercalative mode of drug-DNA interaction, a stacking interaction occurs between the chromophore and the DNA base pair. The extent of hypochromism observed is usually proportional to the strength of the intercalative interaction. As the distance between the chromophore and the DNA base pair decreases, the strength of the electronic interaction is expected to decrease as the cube of the distance. This phenomenon is consistent with the combination of the compound's π electrons and the π electrons of DNA bases, leading to hypochromism **(Liu *et al.*, 2002; Sirajuddin, 2012a; Sirajuddin, 2012b)**.

SNPs synthesized using black tea extract shows a strong interaction with ct-DNA and BSA. In fact, the absorption, fluorescence and viscosity data showed that SNP and ct-DNA interaction occurs via an intercalative mode (**Ribeiro *et al.*, 2018**). SNP synthesized from *E. aureum* leaves shows a hypochromic effect on interacting with ct-DNA and isosbestic point which shows a strong binding of SNP with DNA (**Sonia, 2019**).

Results of DNA binding studies show that the synthesized GNPs and SNPs using cereals/pulses washed water do not alter the nature of DNA. The NP bind to the DNA by intercalation mode. It can be generalized that the synthesized NPs can be administered as drug as it does not alter the characteristics of DNA.

4.10 *Allium cepa* root tip toxicity assay for GNP

The characteristics of NPs differ from their bulk. The negative impacts of NPs have to be determined before they are taken up for bio medical applications. NPs are capable of interacting with the intracellular structures and thereby alter their activity and eventually lead to toxicity (**Rajeshwari *et al.*, 2016**) . Therefore in this study the toxicity of the BJWM GNP which has shown good anti-cancer activity and good stability was determined by chromosomal abrasions in root tip of *Allium cepa.*

The *Allium cepa* test has been employed since 1920's, as a bio indicator of environmental contamination. *A.cepa* has been regarded as an excellent *in vivo* model for studying the toxicity of NPs. They also have a stable chromosome number and karyotype, diverse chromosomal morphology, clear mitotic phases, a rapid response to genotoxic materials, and the infrequent occurrence of spontaneous chromosomal damages **(Tedesco and Laughinghouse, 2012**) .

Figure 66 shows the microscopic images of *A.cepa* root tips which are incubated in test solution with different concentrations of BJWM GNPs. The root tips incubated in distilled water doesn't show any chromosomal aberrations; also clear mitotic phase changes are visible **(Figure 66a)**. For this assay $K_2Cr_2O_7$ (100µg/mL) considered as a control.

The elongated, damaged, swelled cells are observed in control **(Figure 66b)**. Root tips incubated in BJWM portray clear, visible mitotic phase at all concentration and reveal its non-genotoxicity (**Figure 66 c-f**). As the concentration increases cell elongation is observed, this might be due to the addition of metal to the cellular system.

The increase in number of large and elongated and polyploid giant cells may form as a result of endoreplication or endomitosis also, chromosomal breaks or other mitotic spindle problems that impair chromosomal separation and hinder cytokinesis in *A.cepa* root tips as a result of metal contamination. In the present study, the above mentioned chromosomal aberrations are not observed, but only elongation of cells are observed for the *A.cepa* root tips incubated in BJWM.

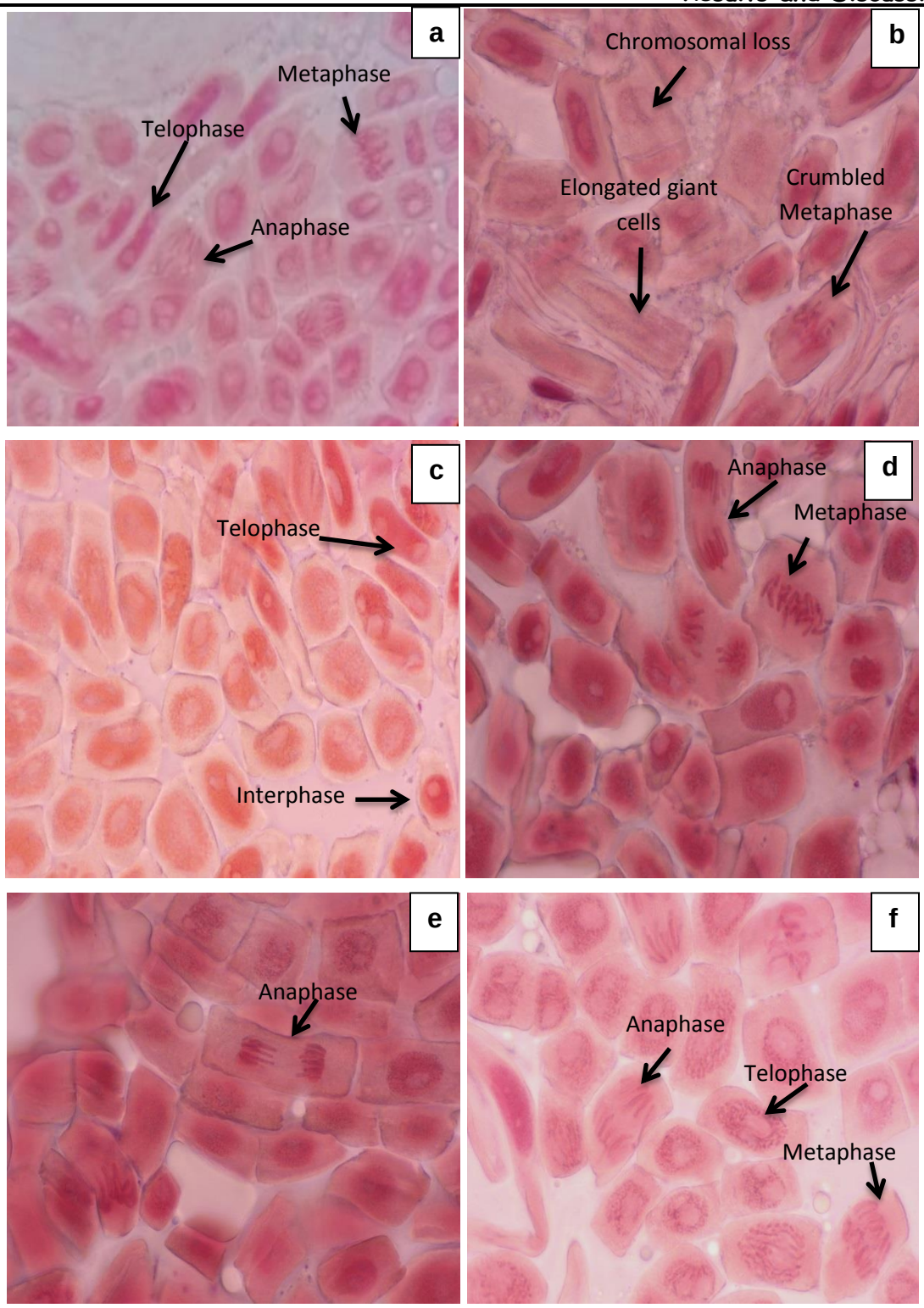

Figure 66. Microscopic images of *A. cepa* root tips incubated in (a) distilled water, (b) $K_2Cr_2O_7$ (100µg/mL), (c) BJWM (12.5µg/mL), (d) BJWM (25µg/mL), (e) BJWM (50µg/mL) and (f) BJWM (100µg/mL)

Chromosome breaks, bridges, lagging chromosomes, chromosomal losses, multi-polar divisions, chromosomal stickiness, delays, and adhesion are the most important aberrations **(Sabeen, 2020**). The mitotic divisions were found to be directly proportional to the concentration of citrate capped GNP (15-40 nm) and inversely proportional to their size (**Rajeshwari *et al*., 2016**).

Yet another report on *A.cepa* toxicity assay treated with manganese oxide NPs and microparticles reported that cytological changes occur in dose dependant manner (**Mangalampalli *et al.*, 2019**) Protein corona-coated vanillin capped GNPs shows less genotoxicity in *A.cepa*.

Thus an inexpensive plant model toxicity assay shows that the BJWM is non-genotoxic.

4.11 Results of Skin care lotion incorporating gold nanoparticle, zinc oxide nanoparticles and their properties

A healthy complexion is especially important since a poor presentation might lower one's self-esteem. Thus in this present study, HN28Au (GNP synthesized from the free edge of HN28) and RaZn (ZnONP synthesized from IRaRW) and was utilized analyzed for sun protection factor and occlusivity studies. The lotion formulations were prepared following the **Indian standards (IS 6608:2004) for skin care products** and tested according to the criteria. The results of the studies are given below.

4.11.1 Analysis of skin lotion incorporating HN28Au

The active ingredients in the lotion formulation is tabulated **Table 37**.

Table 37. Formulation details of lotion prepared using HN28Au sample

Ingredients	Sample code	
	HN28BL	HN28GT
Emulsifying wax (mg)	10	10
Bees wax (mg)	10	10
Cetyl alcohol (mg)	5	5
TiO_2	5	5
Glycerol (mL)	8	8
HN28 (mL)	2	-
HN28Au (mL)	-	2

TiO_2 is a photo active agent. Cetyl alcohol severs as thickener and emulsifier, it will sooth the skin, coconut is the one of the natural source of cetyl alcohol. Hence the choice of the ingredients. The lotion formulations were aesthetically good (**Figure 67**).

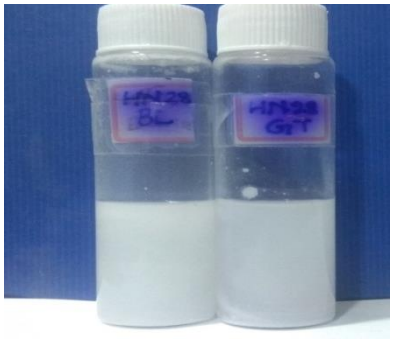

Figure 67. Lotion formulation prepared using HN28Au

The stability of the formulation was good at room temperature and in refrigerator at 18°C. The organic/ oil phase (emulsifying and bees wax) of the formulations combines well with the aqueous phase and stabilizes the formulation. The physico chemical parameters of the formulations are as follows.

Table 38. Physico-chemical parameters of the lotion samples with HN28Au

Sample Code	Colour	pH	Spreadability Mean Diameter (cm) ± SD	Thermal stability
HN28BL	White	6	5.73 ± 0.30	No phase separation
HN28GT	White	6	4.86 ± 0.25	No phase separation
Lotus Sun screen lotion (Standard)	White	6	4.16 ± 0.28	No phase separation

The characteristics of the lotion formulations of this study is on par with the commercially available sun screen lotion. Compared to the HN28 incorporated sample, the spreadability of HN28GT lotion is better compared to the standard sample (**Table 38**). This ensures the consistency of the sample.

The SPF of the lotion formulation analysed by spectrophotometric method in UVB region reveals SPF of HN28GT to be more compared to HN28BL **(Table 39**). The SPF of the formulated samples can be increased by increasing the concentration of HN28Au and any other photo active reagents. It is also appreciable that no other photoactive toxic chemical ingredients are used in these formulations. The validation of the present method was done using a commercial cream of standard SPF 30 as standard. The standard (SPF 30), with *in vitro* SPF calculation studies with Bio spec Nano spectrophotometer shows SPF 22.2271. Synergistic effect of photo protective reagents octyl methoxy cinnamate, octocrylene, avobenzone and dimethicone might have enhanced the SPF of the standard sun

screen lotion. Compared to the standard lotion, in this study, chemicals other than TiO_2 are not used. The addition of few more photo active agents might enhance the formulations of this present study. It is worth to note that 2 mL HN28Au gave SPF 4.33. Thus increasing the concentration of HN28Au might increase SPF.

Table 39. SPF characteristics of the HN28Au incorporated lotion formulation

Sample Code	Wave length (nm)	OD	EE (λ) * I(λ)	$^{320}_{290}$SPF Spectrophotometre = CF*∑EE (λ)*I (λ)*Abs (λ)
HN28BL	290	0.328	0.0150	3.4442 = **3.444**
	295	0.339	0.0817	
	300	0.350	0.2874	
	305	0.344	0.3278	
	310	0.340	0.1864	
	315	0.342	0.0837	
	320	0.346	0.0187	
HN28GT	290	0.457	0.0150	4.3394 = **4.339**
	295	0.453	0.0817	
	300	0.447	0.2874	
	305	0.422	0.3278	
	310	0.401	0.1864	
	315	0.391	0.0837	
	320	0.386	0.0187	
Lotus sun screen lotion (SPF 30)	290	1.964	0.0150	22.2271 = **22.227**
	295	2.206	0.0817	
	300	2.230	0.2874	
	305	2.225	0.3278	
	310	2.244	0.1864	
	315	2.209	0.0837	
	320	2.118	0.0187	

The lotion formulation should equally hydrate the skin. In order to determine the moisturizing effect of prepared lotion formulations, *in vitro* occlusivity studies were carried out. From the occlusivity factor (F) it is clear that the lotion formulations prepared in this study have comparative moisturizing ability with that of the commercially standard (**Table 40**). The keratin in HN28 samples might have enhanced the photo protective and occlusive properties. For a number of dermatological diseases, moisturisers are frequently given as adjuvant therapies and preventative measures. Improved disease control is made possible by the fact that moisturisers appear to be able to correct some of the barrier deficiencies found in disorders like atopic dermatitis. Moisturisers have been researched for their potential as adjuvants.

Table 40. *In vitro* occlusivity of the HN28Au lotion formulation

Sample code	Water loss (%)	F=A-B/A * 100
HN28BL	55.74	44.25
HN28GT	47.57	52.42
Vaseline (Standard)	14.02	85.97
Blank	99.99	-

It has been demonstrated that using a moisturiser as an alternative to active corticosteroid therapy of the skin can reduce the amount of corticosteroids needed without sacrificing therapeutic effectiveness. Although it is hypothesised that the lipid content of the moisturiser may be important, the mechanism behind this is still unknown **(Lundov *et al.*, 2009).**

GNP stabilized with polyvinylpyrrolidone and incorporated in skin care cream doesn't alter the characteristics of GNP like stability, size or morphology (**Majerič *et al.*, 2023**). It is also reported that compared to chemically synthesized nanosilver and nano gold incorporated cream formulation, in nanogold incorporated creams the agglomeration of nanogold was not observed as it possess higher electrokinetic potential than that of nanosilver (**Pulit-Prociak *et al.*, 2019**).

The prepared lotion formulation incorporating HN28Au demonstrates photo protective activity but less compared to standard commercial cream. It is worth mentioning that the formulation is an outcome from a waste material (free edge of human nail), were there is less reported research work.

4.10.2 Analysis of skin lotions incorporating ZnONP from cereals and pulses washed water

To achieve a sunscreen lotion with high SPF, we have formulated lotions with RaZn (ZnONP prepared from the IRaRW) as ZnO has inherent photo protecting activity. Among the cereals and pulses washed water, IRaRW was utilized in this study. There is a traditional knowledge of applying raw rice powder in face for scrubbing and bleaching effects on skin surface. To validate the efficiency of IRaRW and RaZn (IRaRW aided synthesized ZnONP) was utilized in this study.

In the formulations, green synthesized ZnONP, IRaRW, TiO_2 and *Cynodon dactylon* leaf extracts, pumice stone powder were added as photoprotective agents. The emulsifying wax, bees wax and cetyl alcohol are organic/oil phases in which the photo active agents are

dissolved, glycerol acts as aqueous phase and stearic acid acts as a thickener and stabilizer (**Table 41**).

Initial formulations were developed with IRaRW, RaZn and combinations of both. Even though the formulations were stable, SPF was not appreciable compared to standard. Combination of both IRaRW and RaZn shows SPF 7.88 (**Table 42**). Triplicate studies were done for *in vitro* SPF calculation studies; the average of the three is tabulated.

Table 42. SPF of IRaRW and RaZn incorporated formulations

Sample Code	$^{320}_{290}$SPFSpectrophotometre= CF*∑EE (λ)*I (λ)*Abs (λ)
BLANK	6.80
RRL	5.72
RaZnL	6.35
RWZn	**7.88**
Lotus SPF30 (Standard)	22

To improve the SPF, *Cynodon dactylon* (CND) leaf extracts (hexane and aqueous) were incorporated and formulations were prepared. *Cynodon dactylon* is one of the important aspects in ayurveda for skin diseases, jaundice and asthma. CND is also an herbal solution for urinary tract infection, headache and wound healing. There is traditional knowledge on adding CND in food items on a solar eclipse day to avoid the effects of toxic rays (**Panchal *et al.*, 2021; Mangathayaru *et al.*, 2009**). CND leaf aqueous extract was reported to have secondary metabolites such as alkaloids, saponins, tannins etc (**Randive and Jagtap, 2019**).

Table 43. SPF of CND, IRaRW and RaZn incorporated formulations

Sample Code	$^{320}_{290}$SPFSpectrophotometre= CF*∑EE (λ)*I (λ)*Abs (λ)
BLANK	6.80
F6	8.9
CNDL	9.46
CZnL	15.80
F3	14.31
T3	14.58
T4	14.92
RWZnCND	**18.16**
F7	13.29
Lotus SPF30	22

The formulations incorporating CND (hexane and aqueous) extracts along with IRaRW and RaZn formulation were prepared. CND hexane extract with pumice stone was prepared (F3). The formulation was not stable and also the micro particles of the pumice stone were visible in the formulation. The SPF of F6 was not appreciable compared to blank. The pumice stone is rich in K, Na, Ca, Fe, Mg, Mn, Ti and S also it provides abrasions to the skin cell and exfoliates the cells. It was anticipated that mixture of elements in pumice stone would help to improve the SPF of the formulation. It was observed that CND extract and RaZn formulation (CZnL) had an appreciable SPF compared to only CND aqueous extract incorporated formulation (CNDL) (**Table 43**). These formulations were visually stable.

Thus the focus on various combinations by altering concentration in the aqueous phase such as glycerol, CND aqueous extracts, IRaRW and RaZn (F3, T3, T4 and RWZnCND) were carried out. The optimization studies show that the lotion formulation with combination of all the photoprotective agents (RWZnCND) gave SPF 18.16 which is nearly comparable with STD.

Therefore it can be generalized that the combination of the RaZn, IRaRW and CND aqueous extract are best to deliver the photoprotective activity for the formulation. Increasing the concentration of the photo active materials can further increase the SPF.

Thus to determine the fraction of aqueous extract which provide best SPF, from the TLC studies it was determined that ethanol: formic acid fraction shows a band under UV light. This fraction was isolated by preparatory TLC method (**Figure 68**) and incorporated instead of CND extract in the formulation (F7).

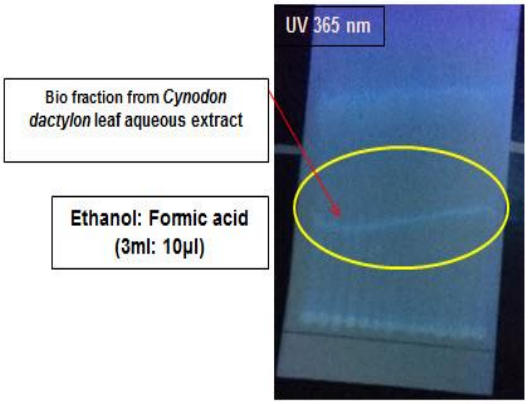

Figure 68. TLC separation of the fraction of *Cynodon dactylon* leaf aqueous extract

It was observed that the SPF of F7 doesn't increase with that of the RWZnCND formulation. Thus it can be generalized that the synergistic effect of all the components in the CND aqueous extract enhances the SPF.

Among the prepared lotion samples, RWZnCND shows best SPF, this sample was analyzed for the *in vitro* occlusivity test. It was found that the sample has around 70% occlusivity compared with the commercial standard, chosen as standard for this present study (**Table 44**). The results imply that the RWZnCND is comparatively efficient as the commercial moisturizer.

Table 44. *In vitro* occlusivity of the lotion formulations using RaZn formulation

Sample code	Weight of water loss (%)	F=A-B/A * 100
RWZnCND	48.05	50.95
Vaseline (Standard)	14.02	85.97
Blank	99.99	-

The moisturizing efficacy of the samples might be due to the synergistic effect of the nutrients present in IRaRW and the secondary metabolites present in the CND extracts and the efficacy of RaZn particles to patch up the pores and hence limit the water permeability.

The samples which have combination of CND aqueous extract, IRaRW and RaZn were subjected to physico-chemical testing (**Table 45**).

Table 45. Physico-chemical parameters of the lotion samples with ZnONP

Sample Code	Colour	pH	Spreadability Mean Diameter (cm) ± SD	Stability	
				Thermal stability	After Centrifuging
BLANK	White	5.96	5.6 ± 0.43	Stable	Stable
CNDL	Yellow	6.53	6.2 ± 0.2	Stable	Stable
RaZnL	White	6.53	6.9 ± 0.23	Stable	Stable
CZnL	Yellow	6.14	6.63 ± 0.32	Stable	Stable
RRL	White	6.18	4.16 ± 0.28	Stable	Stable
RWZn	White	5.70	4.6 ± 0.5	Stable	Stable
RWZnCND	yellow	6.10	5.16 ± 0.2	Stable	Stable
Lotus SPF30 (Standard)	White	6	4.16 ± 0.28	Stable	Stable

Table 41. Formulation details of the lotion prepared using ZnONP synthesized from IRaRW

Active constituents	Formulation											
	Blank	RRL	RaZnL	RWZn	F6	CNDL	CZnL	F3	T3	T4	RWZnCND	F7
Emulsifying wax (mg)	10	10	10	10	10	10	10	10	10	10	10	10
Bees wax (mg)	10	10	10	10	10	10	10	10	10	10	10	10
Cetyl alcohol (mg)	10	10	10	10	10	10	10	10	10	10	10	10
Stearic acid (mg)	10	10	10	10	10	10	10	10	10	10	10	10
TiO_2 (mg)	5	5	5	5	5	5	5	5	5	5	5	5
Glycerol (mL)	8	5	8	5	8	5	5	8	8	8	5	5
IRaRW (mL)	-	5	-	5	2.5	-	-	5	2.5	2.5	2.5	2.5
RaZn (mg)	-	-	4	4	4	-	4	4	-	4	4	4
H_2O (mL)	2	-	2	-	-	-	-	-	-	-	-	-
Cynodon dactylon leaf hexane extract (mL)	-	-	-	-	5	-	-	-	-	-	-	-
Pumice stone powder (mg)	-	-	-	-	5	-	-	-	-	-	-	-
Cynodon dactylon leaf aqueous extract (mL)	-	-	-	-	-	5	5	5	2.5	2.5	2.5	-
Cynodon dactylon leaf aqueous extract (Ethanol: Formic acid fraction) (mg)	-	-	-	-	-	-	-	-	-	-	-	50

(-) absence of the constituent

The results of the samples are compared with the standard SPF (30). The samples were found to be stable at room temperature, higher temperature and after centrifuging for 15 min. The pH of the samples was found to be between 5.7-6.53. Results from the **Table 45** generalize that the prepared lotion formulations follows the Indian standards for skin care cosmetics. The samples with CND are found to have yellow shade (**Figure 69**). This might be due to the colour of the CND extract.

Figure 69. Lotion formulations incorporating RaZn, CND and IRaRW

❖ **Antibacterial activity of the prepared lotion formulations**

It is essential that skin care creams should resist the skin infection causing bacteria and fungi. Thus it is essential to determine the antimicrobial efficacy of the lotion formulations. In this study, the RWZnCND and HN28GT formulations were tested for their ability to inhibit skin infection causing bacteria and fungi. The samples were tested against skin infection causing microbes *Candida albicans and Staphylococcus aureus.* **Table 46** shows the ZOI obtained for the samples.

Table 46. Zone of inhibition values obtained for the formulations against fungi and bacteria

Sample code	Zone of Inhibition (mm)	
	Candida albicans	***Staphylococcus aureus***
Standard (Lotus SPF30)	15	20
Blank	0	0
HN28BL	0	0
HN28GT	**14**	**16**
RWZnCND	**11**	**23**

It is observed that both the samples RWZnCND and HN28GT are efficient in inhibiting *Candida albicans and Staphylococcus aureus.* The blank sample and HN28BL sample doesn't show inhibition towards both *Candida albicans and Staphylococcus aureus*; this might be because the formulation is without any photo active reagents. HN28BL formulation also doesn't show inhibition towards the *Candida albicans and Staphylococcus aureus.* HN28GT is efficient than RWZnCND towards inhibiting *Candida albicans.* The ZOI value is much closer to the value of standard SPF30 cream. RWZnCND has ZOI 23 mm towards *Staphylococcus aureus,* this shows the significance of the formulation than the standard cream of ZOI 20 mm (**Figure 70**). This shows the synergistic effect of the CND leaf extract, RaZn and IRaRW enhance the bactericidal activity of the formulations.

Previous reports on herbal formulations with *Elaeagnus angustifolia* purified extract, sesame oil, and sea buckthorn oil have SPF 21.5 (**Ahmady *et al.,* 2020**). Peel extract from *Hylocereus polyrhizus* rich in phenolic acids and flavonoids demonstrated broad-spectrum UVB and UVA protection with an SPF value of 35.02 at 1.00 mg/mL **(Vijayakumar *et al.,* 2020).**

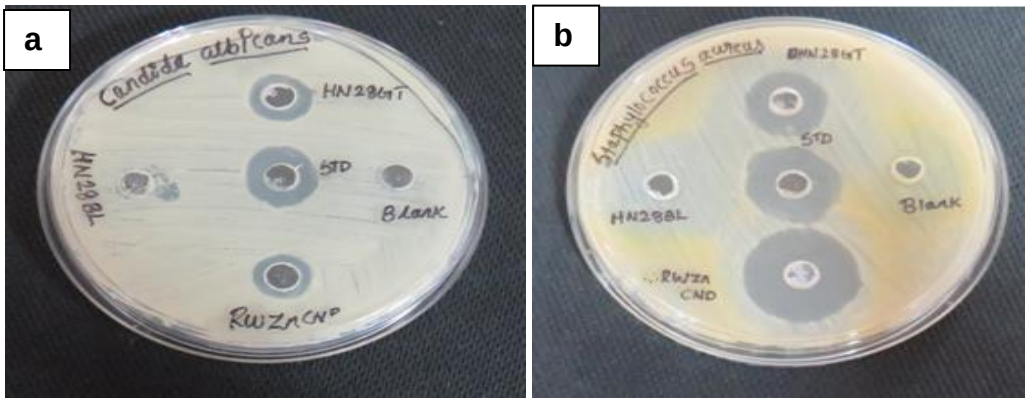

Figure 70. ZOI obtained for lotion formulations against (a) *Candida albicans* and (b) *Staphylococcus aureus*

Clerodendranthus spicatus is utilised to treat renal disease due to its strong anti-inflammatory effects, and its nourishing function reduced UV-induced skin outlooks such coarseness, oedema, and erythema. CS (3.6 g/mL) has an SPF of 16.21(**Wang *et al.,* 2016**). Similar results were obtained in the present study. The secondary metabolites present in CND

leaf extract, the nutrients present in IRaRW and the photo protective activity of RaZn NPs, enhances the SPF, moisturizing nature and bactericidal activity of the lotion formulations.

Lotion formulations incorporating HN28 and RaZn showed an excellent photo protective activity, occlusivity and they are good anti-microbial agents against skin infection causing microbes. However in vivo testing of the formulations has to be carried out for further validation.

4.11 Nano switching/ sensing applications of nanoparticles

As discussed in detail regarding the nano switches in chapter 2, nano switches are the nanoparticles/materials which changes its characteristic nature (colour, size, morphology) when they are exposed to light, electrical impulse, change in pH, chemical reagents etc. Thus initially in this study, the synthesized NPs (GNPs and SNPs) were exposed to different bench reagents and the resulting observations were noted (**Table 47**).

From **Table 47** it is clear that after several trials the synthesized GNPs, TBPGNP and GCAu were selective towards sensing ammonia and CN^- ions respectively.

Our one of the target analyte was melamine, as there are several reports on melamine toxicity; as GNPs doesn't show any switching with melamine, the synthesized SNPs (TBOSSNP, TBISSNP, TBSSNP, TBPSNP, IBoRWAgSo, IRaRWAgSo, IBaRWAgSo, IRRWAgSo, IBrRWAgSo, IBRRWAgSo, BJWWAgSo, IWWAgSo, BuWWAgSo, TDWWAgSo, and WCWWAgSo) were tested with melamine. No colour change was observed. Therefore further validation on switching behaviour of TBPGNP with ammonia, GCAu with CN^- was carried out. For melamine, initial analytical method validation and then by electrochemical sensing of melamine by synthesized BJRGO hence executed.

4.11.1 Colorimetric sensing of ammonia by TBPGNP

In recent days, research on the selective, sensitive and low cost ammonia detection is more. GNPs, due to their excellent optical properties are widely used as sensing probes. Especially due to their LSPR, most often GNP is utilized as colorimetric sensors. The development of a simple and convenient biosensor for detecting chemical and biological substances is critical.

Table 47. Interaction of synthesized GNP with different laboratory reagents

S.No	Reagents used	GNPs																
		TBOS GNP	TBIS GNP	TBSG NP	TBPG NP	IBo RWM	IRa RWM	IBa RWM	IR RWM	IBr RWM	IBR RWM	BJW WM	WC WM	TD WM	BuW WM	IW WM	GC Au	HN 28 Au
1	Melamine	-	-	-	-	-	-	-	-	-	-	-	-	-	-	-	-	-
2	KBr	*	*	*	-	*	*	*	*	*	*	*	*	*	*	*	*	*
3	NaF	*	*	*	-	*	*	*	*	*	*	*	*	*	*	*	*	*
4	NaCl	*	*	*	-	*	*	*	*	*	*	*	*	*	*	*	*	*
5	KCl	*	*	*	-	*	*	*	*	*	*	*	*	*	*	*	*	*
6	$CaCl_2.2H_2O$	*	*	*	-	*	*	*	*	*	*	*	*	*	*	*	*	*
7	$CuSO_4.5H_2O$	*	*	*	-	*	*	*	*	*	*	*	*	*	*	*	*	*
8	Na_2SO_4	*	*	*	-	*	*	*	*	*	*	*	*	*	*	*	*	*
9	$KMnO_4$	*	*	*	-	*	*	*	*	*	*	*	*	*	*	*	*	*
10	D-glucose	*	*	*	-	*	*	*	*	*	*	*	*	*	*	*	*	*
11	$MgSO_4.7H_2O$	*	*	*	-	*	*	*	*	*	*	*	*	*	*	*	*	*
12	Sucrose	*	*	*	-	*	*	*	*	*	*	*	*	*	*	*	*	*
13	Thiourea	*	*	*	-	*	*	*	*	*	*	*	*	*	*	*	*	*
14	$Li_2SO_4.2H_2O$	*	*	*	-	*	*	*	*	*	*	*	*	*	*	*	*	*
15	$SnCl_2.2H_2O$	*	*	*	-	*	*	*	*	*	*	*	*	*	*	*	*	*
16	$ZnSO_4.7H_2O$	*	*	*	-	*	*	*	*	*	*	*	*	*	*	*	*	*
17	Lead acetate	*	*	*	-	*	*	*	*	*	*	*	*	*	*	*	*	*
18	Potassium fericyanide	*	*	*	-	*	*	*	*	*	*	*	*	*	*	*	*	*
19	Ferric chloride	*	*	*	-	*	*	*	*	*	*	*	*	*	*	*	*	*
20	Oxalic acid	*	*	*	-	*	*	*	*	*	*	*	*	*	*	*	*	*
21	Melamine+KCl	-	*	*	-	*	*	*	*	*	*	*	*	*	*	*	*	*
22	Melamine +	*	*	*	-	*	*	*	*	*	*	*	*	*	*	*	*	*

	NaCl																	
23	Melamine+ Lead acetate	*	*	*	-	*	*	*	*	*	*	*	*	*	*	*	*	*
24	Melamine+ Potassium ferrocyanide	*	*	*	-	*	*	*	*	*	*	*	*	*	*	*	*	*
25	Melamine +Potassium dichromate	*	*	*	-	*	*	*	*	*	*	*	*	*	*	*	*	*
26	Melamine + $Na_2S_2O_3$	-	*	*	*	*	*	*	*	*	*	*	*	*	*	*	*	*
27	Melamine + $CaCl_2$	-	*	*	*	*	*	*	*	*	*	*	*	*	*	*	*	*
28	Melamine + Oxalic acid	-	*	*	*	*	*	*	*	*	*	*	*	*	*	*	*	*
29	Melamine + $KMnO_4$	-	*	*	*	*	*	*	*	*	*	*	*	*	*	*	*	*
30	Melamine + acetic acid	*	*	*	-	*	*	*	*	*	*	*	*	*	*	*	*	*
31	Melamine+ Fehlings A	*	*	*	-	*	*	*	*	*	*	*	*	*	*	*	*	*
32	Melamine + Fehlings B	*	*	*	-	*	*	*	*	*	*	*	*	*	*	*	*	*
33	Melamin e+ Dragandroff' s reagent	*	*	*	-	*	*	*	*	*	*	*	*	*	*	*	*	*
34	Melamine + Wagners reagent	*	*	*	-	*	*	*	*	*	*	*	*	*	*	*	*	*
35	Melamine + NH_3	*	*	*	-	*	*	*	*	*	*	*	*	*	*	*	*	*
36	NH_3	-	-	-	+	-	-	-	-	-	-	-	-	-	-	-	-	-
37	EtOH	-	-	-	-	-	*	*	*	*	*	*	*	*	*	*	-	*
38	EtOH + melamine				-	*	*	*	*	*	*	*	*	*	*	*	*	*
39	Soda lime	*	*	*	*	*	*	*	*	*	*	*	*	*	*	*	-	*
40	Barium chloride	*	*	*	*	*	*	*	*	*	*	*	*	*	*	*	-	*
41	Ammonium carbonate	-	-	-	-	*	*	*	*	*	*	*	*	*	*	*	-	*

42	Ammonium chloride	-	-	-	-	*	*	*	*	*	*	*	*	*	*	*	-	*
43	Tollen's II	*	*	*	*	*	*	*	*	*	*	*	*	*	*	*	-	*
44	Tollen's I	*	*	*	*	*	*	*	*	*	*	*	*	*	*	*	-	*
45	Methyl orange	*	*	*	*	*	*	*	*	*	*	*	*	*	*	*	-	*
46	Schiff's reagent	*	*	*	*	*	*	*	*	*	*	*	*	*	*	*	-	*
47	Cobalt nitrate	*	*	*	*	*	*	*	*	*	*	*	*	*	*	*	-	*
48	Potassium ferrocyanide trihydrate	*	*	*	*	*	*	*	*	*	*	*	*	*	*	*	+	*
49	Rhodamine B	*	*	*	-	*	*	*	*	*	*	*	*	*	*	*	-	*
50	Urea	*	*	*	*	*	*	*	*	*	*	*	*	*	*	*	-	*
51	Ammonium ferri sulphate	-	-	-	-	*	*	*	*	*	*	*	*	*	*	*	*	*
52	$(NH_4)_2C_2O_4$	-	-	-	-	*	*	*	*	*	*	*	*	*	*	*	*	*
53	Ammonium acetate	-	-	-	-	*	*	*	*	*	*	*	*	*	*	*	*	*
54	$(NH_4)_2SO_4$	-	-	-	-	*	*	*	*	*	*	*	*	*	*	*	*	*
55	$(NH_4)_2S_2O_3$	-	-	-	-	*	*	*	*	*	*	*	*	*	*	*	*	*
56	NH_4SCN	-	-	-	-	*	*	*	*	*	*	*	*	*	*	*	*	*

+ Sensing with colour change, **(-)** no colour change, **(*)** test not performed

When compared to other sensing approaches, GNP-based colorimetric assays are promising since the entire assay progresses through a simple solution of the target and probes without the need for washing, and the colour change may be viewed directly with the naked eye without the use of specialised instruments. As a result, these technologies greatly simplify operation processes, cut detection times, and significantly lower test cost. Furthermore, such colorimetric assays are easily transferable to smartphone-based devices, which have the potential to be a strong platform for detecting, transducing, and analysing on-line sensing data (**Wu *et al.*, 2016; Smith *et al*., 2016; Li *et al.*, 2018**).

Many traditional colorimetric signal reading methods rely on variations in the colour shade of a solution. While the colour change is visible, the resolution of colour development is insufficient. The precision of the findings observed by the naked eye is reduced when dealing with targets of equal concentrations. A colorimetric sensor with many colours can be built to improve sensor sensitivity by combining high molar extinction coefficients with the LSPR of GNPs. When GNPs are exposed to incident light and the light's oscillation frequency coincides with the oscillation frequency of the free electrons on their surface, LSPR occurs, resulting in considerable photon energy absorption from the NPs (**Ma *et al.*, 2019**).

The synthesized TBPGNP was treated with 1:1 ammonia solution. The immediate colour change to brown was noticed (**Figure 71**). Several other analytes including, melamine, cyanide, ethanol etc were allowed to interact with TBPGNP. TBPGNP was selective towards ammonia alone.

In order to determine whether the TBPGNP particles are interacting with ammonium ions or ammonia gas, another set of experiments were carried out, by adding different ammonium salts to the TBPGNP such as ammonium chloride, ammonium thiocyante, ammonium bicarbonate etc. No significant colour change was observed. Also, TBPGNP was allowed to interact with bases such as NaOH, KOH etc, there was no colour change. This ensures that change in colour of the TBPGNP exposed to NH_3 is not a pH switch mechanism.

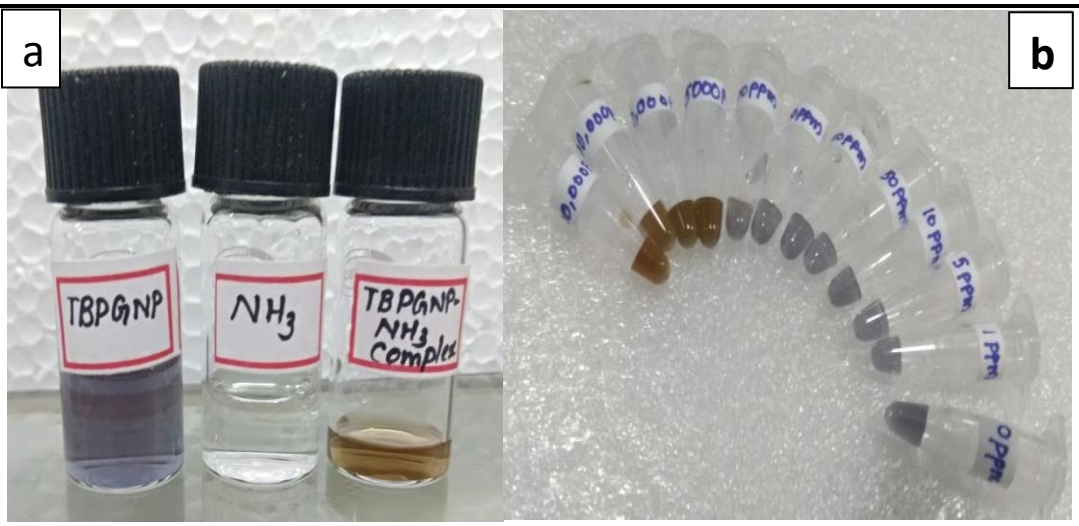

Figure 71. Colorimetric detection of NH_3 by GNP (a) Colour change of TBP on addition of NH_3, (b) change in colour of TBP at different concentration of NH_3

Therefore to prove the change in colour of the TBPGNP is due to NH_3 gas, as mentioned in **Figure 72a** only the vapours of NH_3 was allowed to interact with TBPGNP. After 60 s it was noted the colour of the TBPGNP started changing to brown (**Figure 72b**). This clearly ensures that TBPGNP is selective towards ammonia gas. To determine the lowest concentration to which ammonia can be determined was done by adding different concentration of ammonia solution (0 ppm to 50,000 ppm) to the TBPGNP in different tubes. The sensitivity of TBGNP was upto 5000 ppm of ammonia (**Figure 68b**).

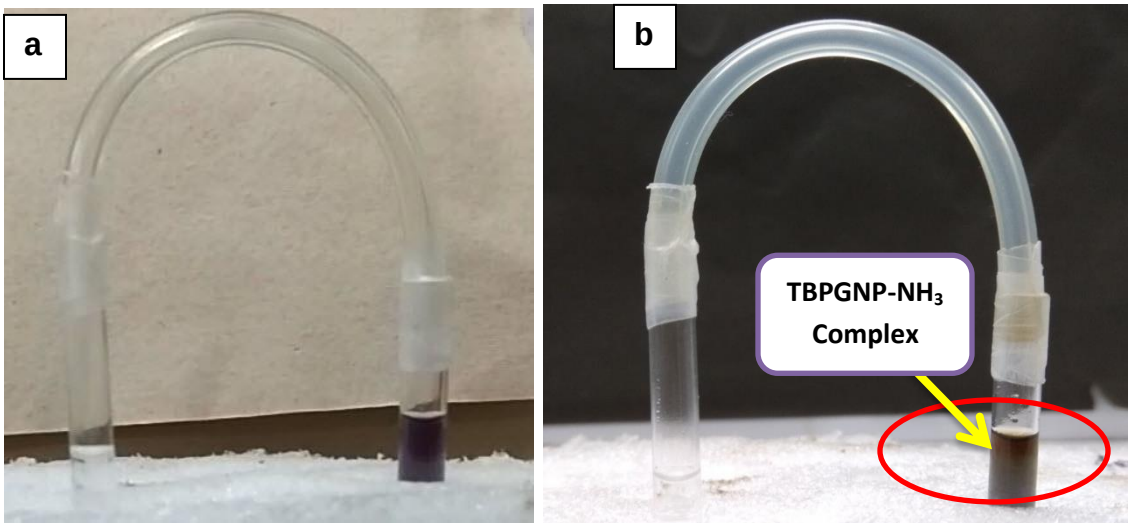

Figure 72. TBPGNP exposed to NH_3 vapours (a) at 0 min, (b) after 60s

From the studies it is obvious that TBPGNP is a self-powered nano switch towards sensing ammonia. The surface stabilized TBPGNP by secondary metabolites such as alkaloids, flavonoids, sterols and tannins present in the TBP extract might have modified the surface and helps to sense ammonia gas. The spectrophotometric analysis of TBPGNP treated with 5000 ppm ammonia reveal absence of ammonia ensuring the formation of Au-NH_3 complex (**Figure 73**).

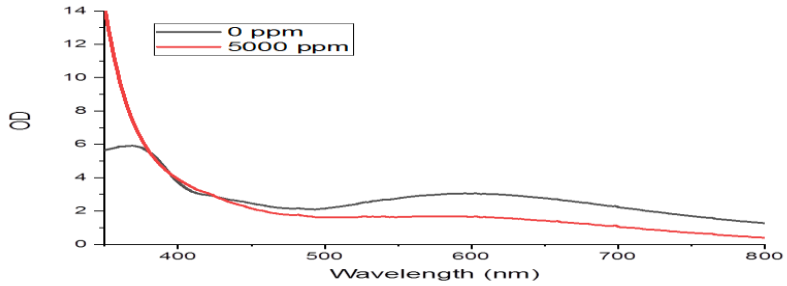

Figure 73. SPR shift in TBPGNP after exposed to NH_3

Upon further validation, as TBPGNP acts as a colorimetric probe, in future facile paper-based sensors can be made. The results of the study show that TBPGNP is a self-powered nano switch.

4.11.2 Colorimetric sensing of cyanide by GCAu

The reaction of GCAu with different reagents shows selective detection of CN^- ions. The selectivity of the GNP to detect CN^- is witnessed as it does not show any colour change when mixed with different reagents. The complex formation between potassium ferrocyanide and GCAu might be the possible reason for the colour change from wine red to yellow-green colour (**Figure 74**).

Figure 74. Colour change of GCAu when reactedwith CN^- ions

Novelty of this research work was presented in NABARD and Nutrition Society of India- sponsored two-day International Web conference on "Food Technology and Nutrition-Prospects for Health" on 28th and 29th January, 2021. This research work was awarded the best oral presentation award.

Unlike TBPGNP, the switching behaviour towards CN^- sensing of GCAu was carried out by electrochemical analysis.

4.11.3 Electrochemical cyanide ion sensing by GCAu@CPE

The use of electrochemical sensors has become an increasingly effective analytical method due to its portability, speed, low cost, high sensitivity, and selectivity (**Niu *et al.*, 2013; Cheng *et al.*, 2013; Rezaei *et al.*, 2015**). Depending on the observed response property, electrochemical sensors can be categorized as potentiometric, amperometric, or conductometric (**Stradiotto *et al.*, 2003; Pejcic and De Marco, 2006**). Recently, GNPs have been incorporated into electrochemical sensors. GCAu incorporated CPE was used as a probe to sense CN^- as colorimetric method shows that GCAu has the capability to sense CN^-.

The electrochemical switching of GCAu on addition of CN^- was optimized with parameters such as scan rate, determination of cathodic and anodic potential, concentration of CN^- ions. Commercially available GCE is expensive. The sensitive nature of the electrode surface will cause noise in the peak if the surface is damaged. Thus this study focused on replacement of GCE with economic and durable CPE.

4.11.3.1 Effect of scan rate on the sensing properties

The CPE modified with 1000 µL GCAu (GCAu 1000) was used as working electrode. To optimise the study, voltannogram were attempted at scan rates 5 mVs^{-1} - 500 mVs^{-1} were carried out. The results (**Figure 75)** clearly show a direct relationship between the scan rate and both the anodic and cathodic peak currents.

Redox peaks are obtained; it is also observed that as the scan rate increase (5 mVs^{-1} - 500 mVs^{-1}) the peak current increases. Electrolysis occurs at the electrode surface to maintain concentrations of oxidized and reduced species. The process is proportional to current and can speed up with an increase in scan rate, resulting in a higher peak current value. This can indicate a diffusion-controlled electrode process.

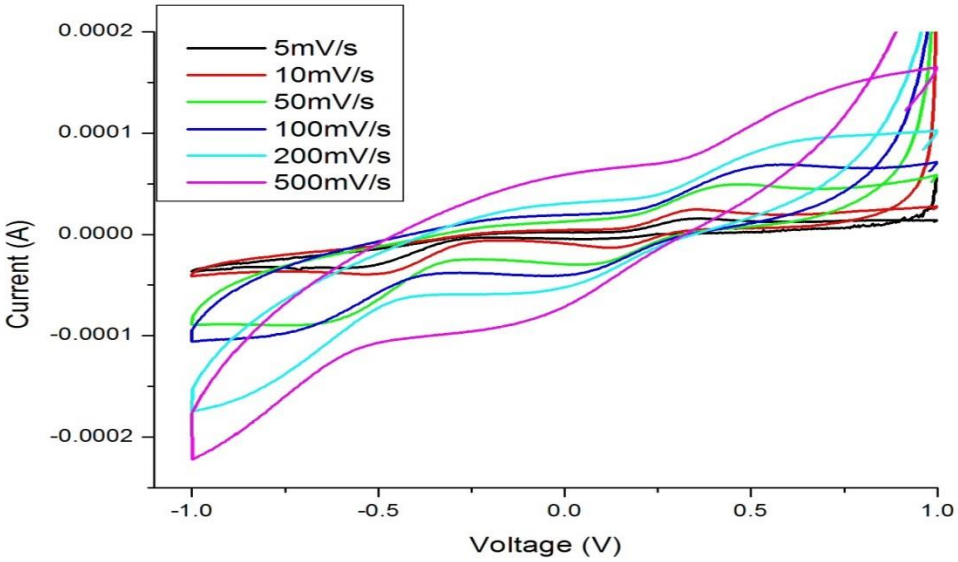

Figure 75. CV plot of 0.01M $K_4[Fe(CN)_6]$ in KCl (0.1M)+ PSB (pH 4) sensing by GCAu1000 electrode at different scan rate

Upon the addition of CN^-, the electrode surface undergoes a reaction with GNPs resulting in the creation of Au-CN complex. CN^- forms a remarkably stable [Au $(CN)_2$] complex with Au(0) through the powerful covalent bonding mechanism that occurs on the electrode surface. This might be the sensing mechanism. In electrochemical reactions, two limiting mechanisms can occur: kinetics and diffusion of the electroactive species. Kinetics governs when species diffusion is rapid, while diffusion (mass transport) controls the phenomenon when kinetics are exceptionally fast, and species enter or leave the electrode surface. The primary factor that controls the electrochemical kinetics is the diffusion of CN^- (**Shamsipur, 2017**).

4.11.3.2 Effect of concentration of CN^- in sensing behaviour of GCAu (1000)

The sensing potential of the GCAu (1000) was determined by having different concentration of CN^- solution from lowest to the highest concentration (100 μM – 300mM). It was found that as concentration increases the peak current values also increases. The redox peak is obtained. Among seven different concentrations of CN^- (100 μM -300 mM), the absence of peak at 100 μM concentrations of CN^- indicates that GCAu is not able to sense CN^- (**Figure 76**).

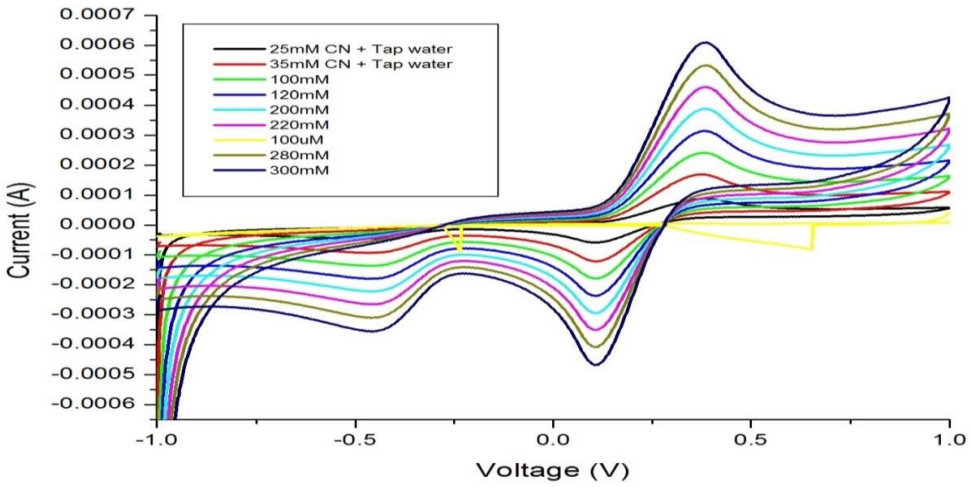

Figure 76. CV plot of different concentration $K_4[Fe(CN)_6]$ in KCl (0.1M)+ PSB (pH 4) sensing by GCAu1000 electrode

To the same system, SCN^-, K^+, Ca^{2+}, Na^+ were added as interfering agents. It was found that there is peak current variation with SCN^- interaction. To the same system, real-life sample such as tap water spiked with 25 mM and 35 mM CN^- solutions was added to check the efficiency of electrode to detect CN^-. Results show that GCAu 1000 was able to detect CN^- in real life samples. As concentration of electroactive species increases the concentration of CN^- increases showing higher peak current. In reversible system as concentration increases, peak current increases. In higher concentration, a reversible behaviour is observed from voltammogram. Higher peak current shows the reversibility. The voltammogram also shows the stability and efficacy of the fabricated electrode.

There are previous reports on cyanide sensing using SNP/carbon nanotube coated on the surface of GCE (**Zhang *et al.*, 2020**) and Ag_2S NP/CPE (**Riojas *et al.*, 2019**); with interfering agents, the electrodes were able to sense CN^-. This study discloses the electrochemical switching mechanism of GCAu towards CN^- sensing.

Thus GCAu selectively senses CN^- by electrochemical method. The GCAu in CPE acts as a sensing and conductive probe.

4.11.4 Results of electrochemical cyanide sensing by low cost CPE in corn sticks (CSC)

The commercial GCE costs around INR 15,500-20,000. The surface of the GCE is sensitive and produces noise if the surface is damaged. An attempt to replace the expensive GCE with modified CPE is executed. During our extensive literature survey, we have come

across "Journal of Chemical Education" (JCE) co-published by the American Chemical Society which focuses on pedagogical and educational relevant contents which will help the educational institutions in low income countries like Africa to execute their chemistry practical sessions effectively at low cost. The contents of the journal inspired us to fabricate an inexpensive electrode.

An attempt was done to fabricate a use-and-throw electrode by filling the modified carbon paste inside corn sticks. The porous materials inside the sticks were scrapped off. The CPE is modified with BuRGO, BJRGO and GCAu. The composite material incorporated electrode on CV shows a conductive behaviour. The peak current a value of CSC doesn't matches with the standard GCE (**Figure 77**). Hence it is recommended that the conductivity studies as electrode material. It is important to note that the there is no noise in the voltammogram of CSC, also without any break the cycle is completed. This makes the low cost electrode a success.

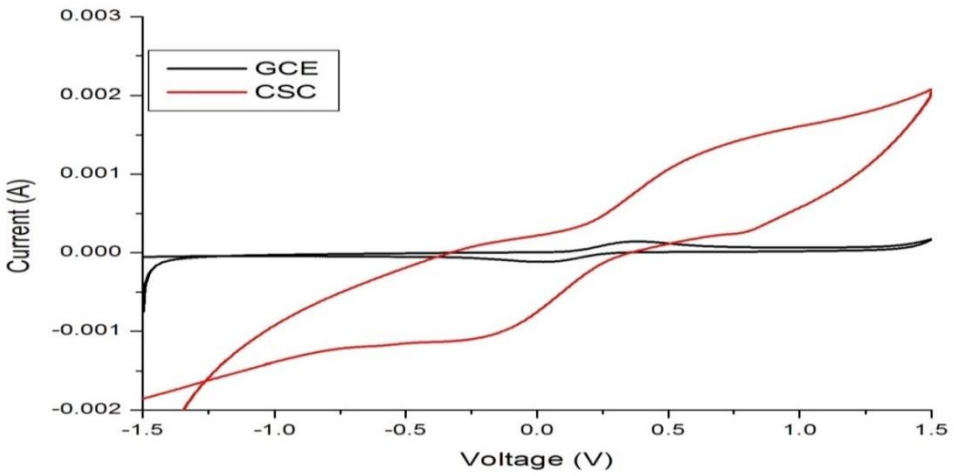

Figure 77. CV plot of $K_4[Fe(CN)_6]$ in KCl (0.1M) and PSB (pH 7.2) at 10mV/s with WE as CSC

CPEs have become increasingly popular as electrodes due to their many advantageous properties. They are both chemically inert and durable, making them suitable for a wide range of sensing and detection applications (**Saad *et al.*, 2019; Kuskur *et al.*, 2019; Beitollahi *et al.*, 2014**). In addition, CPEs are environmentally friendly and non-toxic. If passivation is an issue, the surface can be easily renewed.

Electrochemical detection is a crucial aspect in many fields, but traditional CPEs have some significant limitations that hinder their effectiveness. These limitations include lower sensitivity and reproducibility, slower electron transfer kinetics, lower stability across a wide range of solution compositions, and the need for greater over-potential for electrocatalytic processes. By acknowledging and addressing these limitations, we can develop more effective and reliable electrochemical detection methods that will advance research and innovation in various industries. Fortunately, these challenges can be overcome by using alternative electrodes. Recent studies unequivocally prove that chemically treated electrodes effectively increase electron transfer rate by reducing over-voltage. Nanomaterials-based chemical modified electrodes have emerged as the leading choice due to their heightened sensitivity, amplified response signals and improved reproducibility **(Tiwari *et al.*, 2018; Mouhamed *et al.*, 2018; Sohrabi-Gilani *et al.*, 2018; Oren *et al.*, 2018; Zhu *et al.*, 2018; Nikodimos *et al.*, 2018; Abdallah *et al.*, 2012**). However, the lack of information regarding the long-term durability of these electrodes is concerning. ***This study aimed to address this issue and conclusively demonstrated the feasibility of developing low-cost, eco-friendly CPE*.**

4.11.5 Analytical sensing of melamine leached out from melamine tableware

Melamine is an analyte of our interest in this study, as the literature review reveal that it is potent toxic chemical added in food to increase protein content. There is a research gap on detection of melamine leached out from melamine dinnerware when it is in contact with hot food stimulants. It was also found that the usage of melamine dinnerware is more in India. Thus as an awareness study melamine leached out from melamine dinnerware when incubated in commonly consumed hot Indian cuisines were analysed in FT-IR and the toxicity by comet assay. The reason for choosing FT-IR for analysis is that the synthesized GNPs and SNPs in this study don't show any colour change when mixed with melamine (**Table 47**). FT-IR spectra will provide the functional group that leaches out from melamine.

4.11.5.1 Results of melamine leaching studies

As discussed in materials and methods (**3.13.5.2**) water samples (UMMPW) added to melamine plates broke after 2.47 min in microwave oven, resulting in a loud noise. Upon examination of the fractured plate **(Figure 78b**), it was found that the melamine-formaldehyde resin had broken down and caused irritation to the eyes.

FT-IR of the water sample (UMMPW) demonstrates the presence of melamine indicating that the plates were not safe for use in microwave. It is concerning that there was no warning label on the plates indicating that they should not be used in a microwave. As a precaution, no other food samples were microwaved using these plates in further studies.

Figure 78. (a) Melamine plate before subjected to microwave, (b) Melamine plate after subjected to microwave

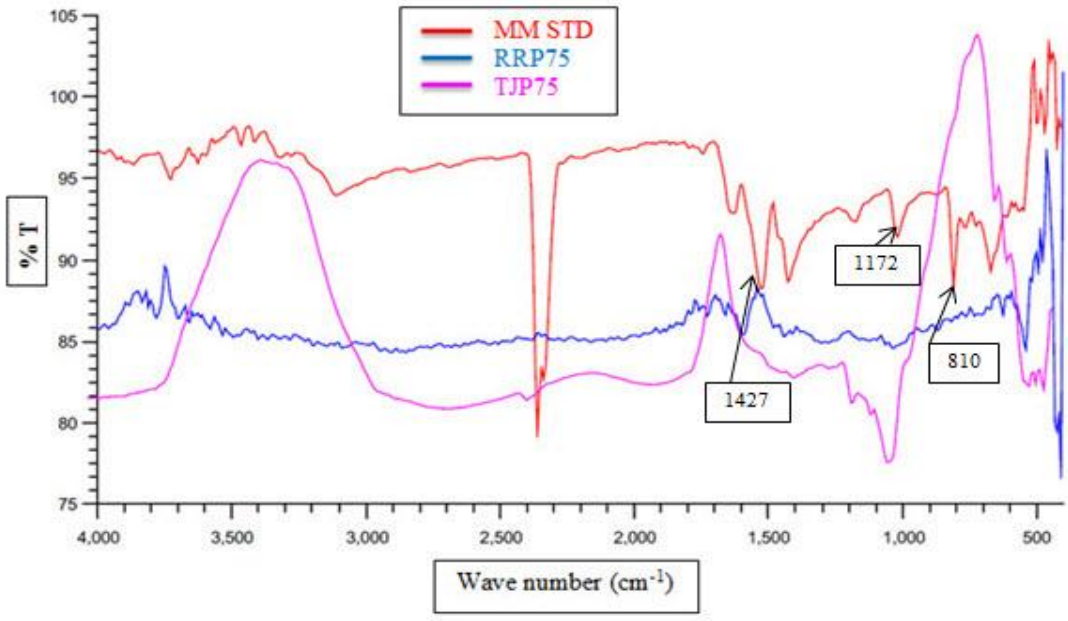

Figure 79. FTIR spectra of the food samples treated in used melamine plates compared to standard melamine

Figure 79 exhibits the FT-IR spectra of melamine (MM STD), hot tomato soup on melamine plate (TJP75), and hot rice porridge in melamine plate (RRP75).The fingerprint region in IR spectra is of utmost importance, as absolutely no two molecules can share identical spectral bands in this area. In MM STD, the fingerprint region unequivocally displays a peak at 763.81 cm^{-1} for side chain out of plane C-N bending, 810.10 cm^{-1} for C-N bending, 1172.72 cm^{-1} for NH_2 rocking, and 1427.32 cm^{-1} for NH_2 wagging. The appropriate peaks in the fingerprint region are solely utilized to determine melamine leaching from food samples.

It is important to note that melamine-formaldehyde (MF) resin is commonly used in most melamine products available on the market. In the production of MF resin, melamine, which is a nucleophile, reacts with formaldehyde, an electrophile. This reaction can occur in almost any pH, but it occurs more slowly in neutral conditions. After reacting with six formaldehyde groups, melamine forms two methyl groups on each exocyclic amine group. Melamine leaching occurs due to a change in pH conditions and can happen when food comes into contact with a melamine plate or when a water sample is microwaved at a temperature of 75°C. FT-IR spectra show that the band at 1149 cm^{-1} corresponds to NH_2 rocking in all spectra. When food samples are incubated in melamine dinnerware at higher temperatures, the group frequency region differs from conventional melamine spectra. This is because melamine in melamine tableware degrades when heated, leading to variation in the group frequency region. According to **Figure 80**, there is no melamine leaching in new melamine bowls.

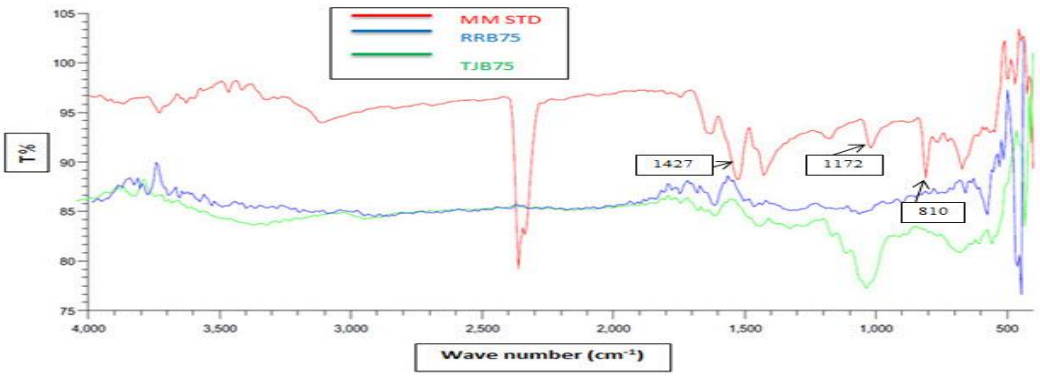

Figure 80. FTIR spectra of the food samples treated in new melamine bowl compared to standard melamine

The studies suggest not to use melamine dinnerware with hot foods, especially plates used over 2 years of period. However, fresh melamine bowls and worn melamine plates do not show melamine leaching at lower temperatures.

From the FT-IR analysis it was found that, the finger print region of the samples matches with MM STD; thus leaching of melamine confirmed. It is hence recommended not to incubate hot food in melamine dinnerware.

4.11.5.2 Results of comet assay determination of DNA damage by leached melamine samples

When food stimulants were incubated in used melamine plates at 75^{o}C, melamine leaching was observed. After being treated with ct-DNA, these samples were exposed to the comet test. The **Figure 81** illustrates the appearance of the comet tail in leached melamine containing food samples. In the presence of an electric field, negatively charged DNA fragments are separated in the agarose gel. DNA migration in the cell is influenced by various factors, which can occur when DNA is damaged. DNA migration increases when DNA strands break due to alkali treatment or specific enzymes.

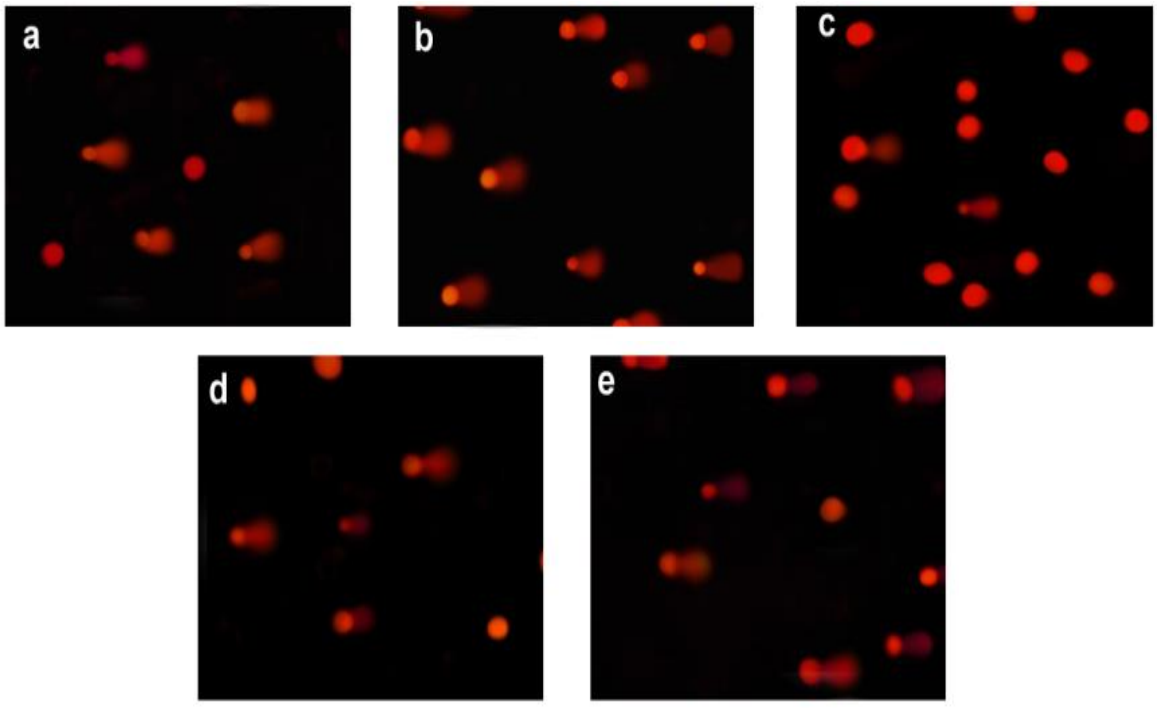

Figure 81. Comet tails for the samples (a)TJP75 (b) RRP75 (c) MMPR75 (d)UMMPW (e)MMSTD

When the concentrations of ethidium bromide dyes are high, the system becomes saturated, so low amounts are usually used. One way to interpret the results of the comet assay is to use the visual scoring technique. This method is quick, simple, and inexpensive because it does not require software programs (**Kumaravel *et al.*, 2009**).

For this study, visual scoring was used, which revealed that all samples damaged DNA as evidenced by the appearance of the comet tail in treated DNA samples. To provide a point of reference, we used a standard melamine solution treated with ct-DNA **(Figure 81e)**. Among the samples, RRP75 (**Figure 81c**) had the smallest tail when compared to others. The other samples showed extensive DNA damage, which could be attributed to the presence of melamine causing DNA migration towards the anode during electrophoresis. The level of DNA damage can be visually categorized on a scale of 0-3 (**Bruschweiler *et al.*, 2016**), with a score of 0 indicating no DNA damage, a score of 1 for low damage (beginning of the tail), a score of 2 for medium damage (visible tail), and a score of 3 for high damage (lengthy tail). Based on the results in **Figure 81**, all of the samples show a score of 3 and their DNA has suffered severe degradation. In **2009**, **Sun *et al***., investigated the harmful interaction of melamine with herring sperm DNA and compared it to ds ct-DNA. They found that the binding mode was electrostatic in nature. This suggests that melamine may interact with DNA phosphates via electrostatic forces, which could be the cause of DNA damage observed in this study. However, it is important to confirm the level of DNA damage caused by melamine by quantifying it in the samples.

From this study, it was found that melamine leaching out from melamine tableware is genotoxic as comet tails are observed in the comet assay

4.11.6 Results of electrochemical melamine sensing by BJRGO@CPE

The synthesized NPs depending on their thermal stability and morphology were categorized for incorporating in the CPE. BJRGO shows excellent thermal stability upto 1000^{o}C in the TGA and lesser mass loss. Next to BJRGO, BuRGO has good thermal stability. The fabricated CPE modified with BJRGO (GSBBJ (5)) was subjected to CV studies for testing its stability and reusability (**Figure 82**). Initially GCE was used as WE (GC1) and CV was run, to the same system GSBBJ (5) electrode was inserted (**Figure 82 GSBBJ1**). After the run again GC (GC2) was used as WE in the same system and then again GSBBJ (5).

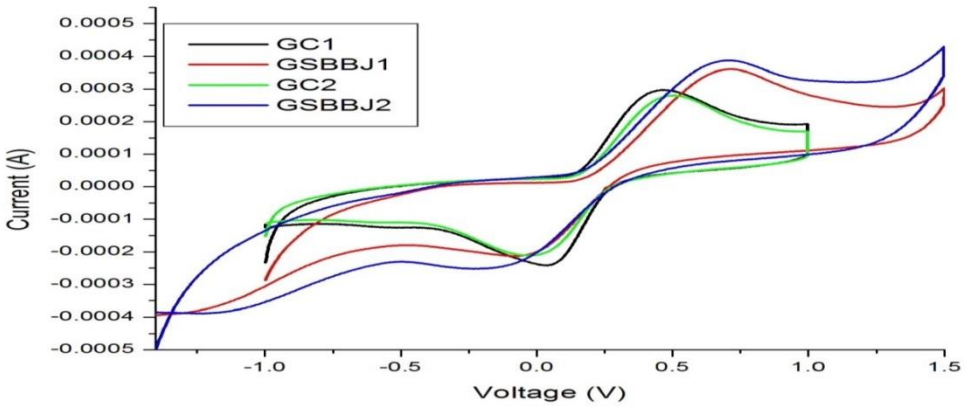

Figure 82. CV plot of standard Glassy carbon electrode and fabricated BJRGO@CPE in 0.01M K_4 [$Fe(CN)_6$] at 10mV/s

It was found that there is no error or noise in the CV peak, which ensures that GSBBJ (5) is not leaching out and stable; to the same system GSBBJ (5) is connected as WE (**Figure 82 GSBBJ2**). There was no change in the peak current values. This ensures the reusability of the GSBBJ (5) with more or less no error in the peak current values. The modification of the electrode with BJRGO causes an increase in the current of the electrochemical probe. This was caused by the electrodeposition of graphene sheets on the electrode surface, which resulted in an increase in the electroactive area of the electrode (**Moreira *et al*., 2020**).

4.11.6.1 Effect of scan rate on the peak current values

It was observed that the scan rate has effect on the peak current and the sensing of the analyte in the system. To optimize the study, scan rate 10 mVs^{-1} - 500 mVs^{-1} was executed. From (**Figure 83**) it was observed that the reaction is irreversible in nature. The cathodic peak is observed at 10 mVs^{-1}, as the scan rate increases, peak broadening happens. At 500 mV/s scan rate the peak vanishes. Therefore further studies are carried out at 10 mVs^{-1}.

It can be generalized that in this reaction, electrolysis occurs only at low scan rate (10 mVs^{-1}). At slow scan rate the electrolyte ions and electroactive species in the melamine solution get enough time to interact which results in cathodic peak. As scan rate increases from 50 mVs^{-1} – 500 mVs^{-1} the interaction for electrolyte ions and electroactive species in the melamine solution is not proper due to less residence time which leads to disappearance of peak.

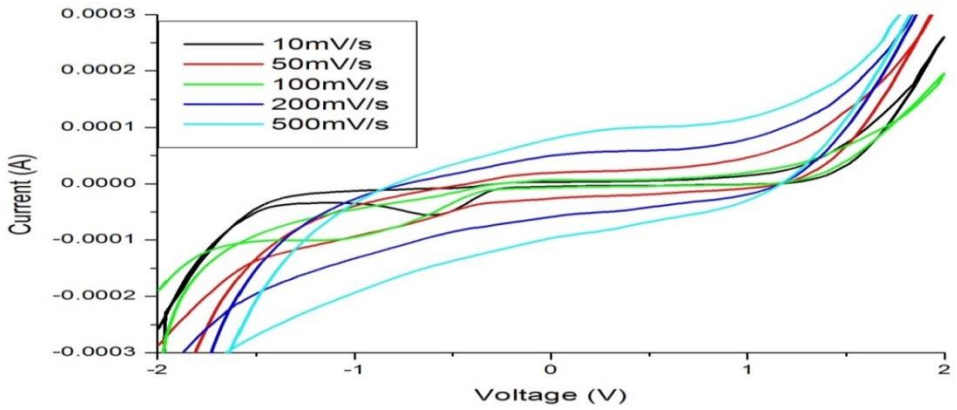

Figure 83. CV plot of 1mM Melamine in KCl (0.1M) and PSB (pH 7.2) at different scan rate

4.11.6.2 Effect of melamine concentration and sensing ability of GSBBJ (5)

It's worth noting that the reaction observed in a voltammetric experiment is heavily influenced by the concentration of electroactive species present in the solution. In order to check the ability of GSBBJ(5) electrode to sense melamine, different concentration of melamine was added to the electrolyte solution from lower concentration to higher concentration (1 nM – 100 μM). It was observed that at lower concentration (1 nM) the peak current reduces (**Figure 84**). As concentration decreases, the reduction peak nears to zero. This might be due to the reduction of electroactive species in the system.

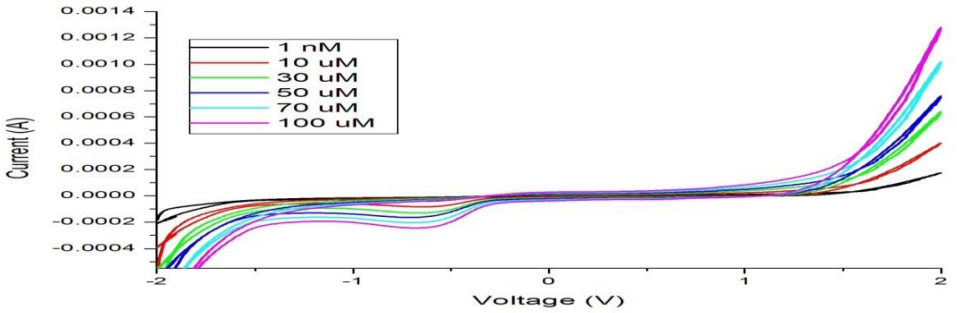

Figure 84. CV plot of different concentration of Melamine in KCl (0.1M) and PSB (pH 7.2) at 10mV/s

At 1 nM concentration of melamine, the reduction peak vanishes, which shows that the GSBBJ (5) is not efficient at lower concentration. **Figure 85** shows that there is no reaction when GSBBJ(5) in only electrolyte medium (without melamine).

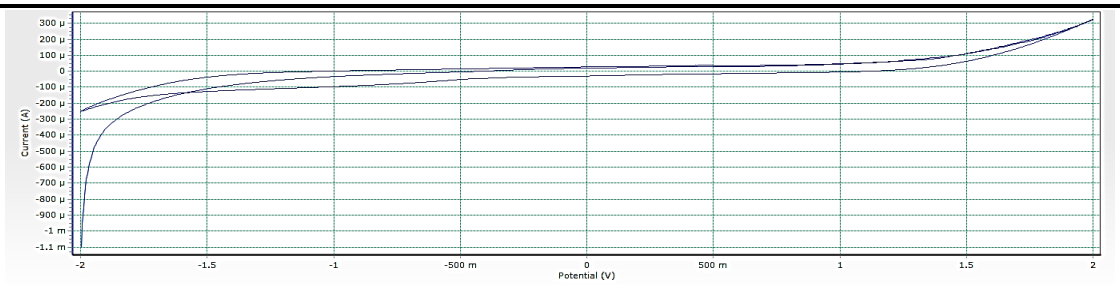

Figure 85. CV plot of GSBBJ(5) vs Ag/AgCl in KCl (0.1M) and PSB (pH 7.2) at 10mV/s

Melamine is a non-electroactive molecule, the possible mechanism of detection of melamine by BJRGO would be as follows: the protonation of NH_2 groups in melamine is possible in PSB solution at pH 7 as PK_a of melamine is 8. These protonated groups might have interacted with the negatively charged groups (-OH) in the electrode surface by electrostatic attraction and promote the electrochemical reaction. The presence of –OH group in BJRGO is confirmed by FT-IR analysis. The H-bonding ability of melamine is previously reported and the triamino triazine group of melamine can form H-bond with thymine base (**Cao *et al.*, 2009**).

4.11.6.3 Selectivity of GSBBJ (5) and real sample analysis

To determine the selectivity of the electrode to the electrolyte, $CaCl_2$ solution, urea solution and lactose were added as interfering agents. To the same solution the processed real milk samples spiked with melamine of two different concentrations were added one after the other. It was observed that interfering agents has no effect on sensing melamine. Due to the addition of interfering agents a noise in the CV plot is observed.

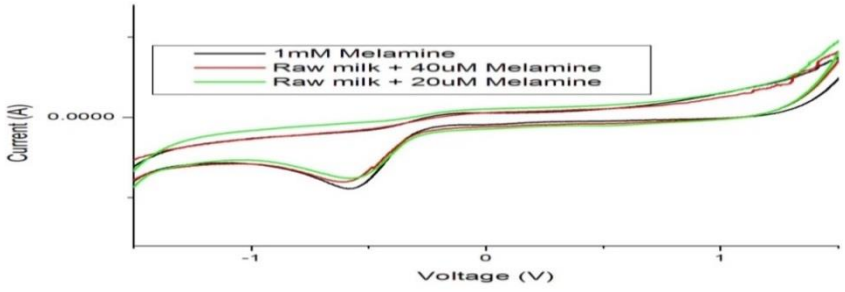

Figure 86. CV plot of GSSBJ (5) melamine sensing of raw milk sample in KCl (0.1M) and PSB (pH 7.2) with interfering agents at 10mVs^{-1}

From the **Figure 86** it is clear that the raw milk sample spiked with melamine can be sensed by the GSBBJ(5) electrode. It is clear from the CV plots that, GSBBJ(5) is selective and sensitive towards sensing melamine. Further studies have to be carried out with more complex voltammetric techniques for detailed clarification. There are earlier reports on melamine detection by RGO/Cu nano flowers modified GCE **(Daizy *et al*., 2019**), ferrocenylglutathione on screen printed electrode (**An *et al.,* 2022**), GNP/graphene/CPE (**Peng *et al.,* 2016**).

From the electrochemical studies, it was found that BJRGO modified CPE act as a conductive probe and was able to sense melamine in real milk samples. The novelty of the study lies in the use of BJWW is discarded as waste. This waste water mediated RGO (BJRGO) was used to detect a notorious chemical melamine even in real milk samples.

4.11.6.4 Impedance analysis of the fabricated electrodes

To determine the electron transport between the electrolyte and the electrode's active surface area, electrochemical impedance spectroscopy studies are carried out. The fabricated modified CPEs GSBBJ(5) and GCAu(1000) were subjected to EIS analysis in 0.01M $K_4[Fe(CN)_6]$ in 0.1M KCl with amplitude 5mV, potential ranges from -0.15V to +0.15V with frequency 0.01Hz to 100000Hz. From **Figure 87** the semicircle observed in the frequency area is a clear indication of the presence of highly active sites with excellent charge transfer pathways. These pathways facilitate controlled ionic diffusions, resulting in an electro active surface of the electrode that is remarkably efficient. This highlights the importance of the semicircle in the frequency area, as it represents a vital factor in achieving optimal performance of the electrode.

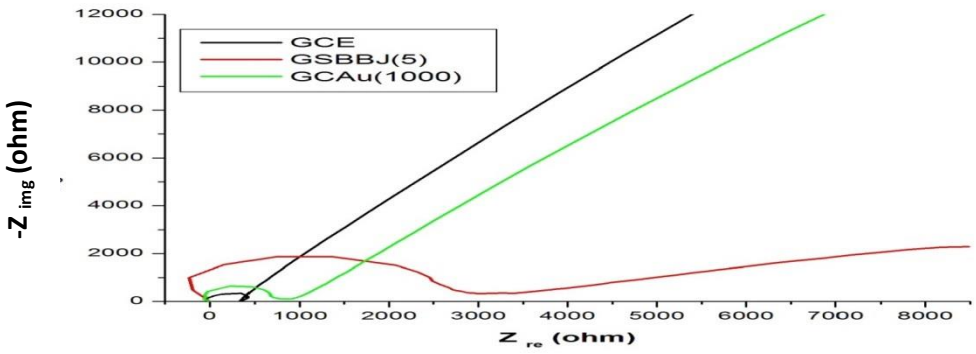

Figure 87. Z_{re} vs Z_{img} plot of GCE, GSBBJ (5) and GCAu (1000) electrodes

The larger semicircle corresponds to the charge transfer resistance (R_{ct}) and the straight line indicates the diffusion limited process. R_{ct} for GCE is ~400 ohm, GCAu (1000) is ~800 ohm and GSBBJ (5) ~2800 ohm. Compared to GCE, the resistance of both the fabricated electrodes are more. Increases in resistance will reduce the electronic conductivity and electro catalytic activity **(Koventhan *et al.*, 2021)** .

From the impedance analyisis, it can be generalized that the GCAu 1000 electrode possess low resistance than GSBBJ (5). However both fabricated CPE electrodes are only nearly comparable with GCE.

From the results of the studies carried out it can be generalized that, the chosen 21 bioreductants, metallic and non-metallic nanoparticles can be synthesized and they possess significant pharmacological, biological, cosmetics and nano switching applications. Novelty of the research work is that the design and development of products according to technology transfer level is carried out for the product such as:

 ***anti-bacterial earphone buds coated with silver nanoparticles***

 ***organic sun screen lotion formulations incorporating GNPs and ZnONPs***

 ***efficient CPEs modified with RGO and GNP for sensing food adulterants.***